Développement d'une stratégie de post-traitement pour l'analyse de la combustion prémélangée : application à une flamme turbulente swirlée.

Pierre-Edouard Bossard

université PARIS-SACLAY

CentraleSupélec

NNT : 2017SACLC037

Post-processing Strategy Development for Premixed Combustion Analysis: Application to Turbulent Swirled Flames

Thèse de doctorat de l'Université Paris-Saclay
préparée à CentraleSupélec

École doctorale n°579 : sciences mécaniques et énergétiques, matériaux et géosciences (SMEMAG)
Spécialité de doctorat: Combustion

Thèse présentée et soutenue à Châtenay-Malabry, le 14 juin 2017, par

Pierre-Edouard Bossard

Composition du Jury :

M. Bruno Renou Professeur, INSA de Rouen	Président
M. Pierre Gajan Docteur d'Etat , ONERA	Rapporteur
M. François Lusseyran Directeur de Recherche, CNRS	Rapporteur
M. Mamoru Tanahashi Professeur, Tokyo Institute of Technology	Examinateur
M. Sébastien Ducruix Directeur de recherche, CNRS	Directeur de thèse
M. Laurent Zimmer Chargé de Recherche, CNRS	Co-Directeur de thèse
M. Franck Richecoeur Maître de Conférences, HDR, CentraleSupélec	Co-Directeur de thèse

Thèse de doctorat

Remerciements

Je tiens tout d'abord à remercier les encadrants de ma thèse. En premier lieu Laurent Zimmer, qui m'a suivi depuis le projet de master, avec qui ce projet de thèse a été mis en place. Il m'a ainsi initié à de nombreuses techniques expérimentales, et sa rigueur ainsi que son expérience m'ont poussé à toujours chercher à obtenir plus des résultats expérimentaux. Je tiens aussi à remercier Franck Richecoeur et Sébastien Ducruix pour leur recul sur les approches employées, et notamment une remise en perspective de ma démarche par rapport aux pistes initiales. Enfin, je tiens aussi à les remercier tous les trois pour leur aide importante lors de la redéfinition de mon sujet de thèse en fin de première année, chose qui n'a pas été facile,et tou au long de mon parcours plus long que prévu.

Un grand merci à Bruno Renou pour avoir accepté de présider le jury. Je tiens aussi à remercier tout particulièrement les deux rapporteurs de mon travail, François Lusseyran et Pierre Gajan, pour le temps consacré à la lecture de mon manuscrit malgré des délais très brefs.
Je tiens aussi à remercier tout le personnel administratif et technique du laboratoire EM2C. Sans eux, il serait beaucoup plus difficile d'avancer dans une thèse expérimentale, nécessitant régulièrement des commandes, des réparations ou la fabrication de pièces diverses. Leur aide permet de résoudre rapidement des situations potentiellement bloquantes.

Je voudrais aussi remercier tous les doctorants et chercheurs du laboratoire, pour la bonne ambiance de travail insufflée, mais aussi les discussions permettant de débloquer les problèmes de certains, ou au moins élargir ses horizons. Une mention plus particulière à tous ceux ayant partagé le grand bureau, que ce soit au début (Béné, Aless, Fred, Tapish, Théo, Raph'), ou plus vers le milieu (Wenjie, Antoine, Meng, Benjamin) de ma thèse.

I must also thank Professor Tanahashi for accepting me in his laboratory during my first year, even though our collaboration was unfortunately cut short. The students of the Tanahashi and Miyauchi lab were all very friendly, and I must thank in particular Shimura, Johchi, Murayama, Ogawa for their precious help conducting my experiments. Working with you was a joy.

Staying in Tokyo, I would also like to thank the guys from the Mushinkan for helping me do something during my weekends, the trainings as well as the chats around beers.

Un grand merci à tous mes proches. Ma famille avant tout, pour m'avoir permis de suivre ce parcours à rallonge avec tout leur support aussi bien matériel que moral, leurs conseils, et leur soutien aussi bien que les coups de pied au cul pour me pousser à faire de mon mieux. Enfin mes amis, même si la bougeotte dans les études n'a pas forcément permis de se voir très souvent.

Voilà, j'espère n'avoir oublié personne, et si c'est le cas, mes excuses, merci à vous aussi, et ne le prenez pas trop mal!

Abstract

Combustion instabilities are one of the major problems encountered in the design of modern gas turbines, as the low equivalence ratio regimes they use to reduce pollutant emissions are very susceptible to these acoustics-combustion couplings. The fundamental mechanisms behind these couplings have been the object of an important research effort, and are now reasonably well understood. However, the prediction and understanding of which particular mechanism drives the instability in a given burner at a given regime is still almost impossible to predict.

The main parameters involved in combustion instabilities are pressure (and more precisely acoustic waves), equivalence ratio and heat release. Knowing the flame position is also important, since flow-flame interactions are a possible source of the fluctuations. The knowledge of these three parameters, and their respective evolution during an instability cycle is needed to more precisely understand their relation to each other. This in turn could allow to find which mechanism(s) drives the observed instability. In order to achieve this however, high repetition rate is needed for the measurements. While the use of microphones gives access to such measurements for the acoustic pressure, the others are more difficult to obtain. Among them, in particular, equivalence ratio is still difficult to measure. This is why one of the objectives of this work is to inspect the feasibility of equivalence ratio measurements by laser absorption in a turbulent swirled air-propane burner.

The other objective of this work is to put forward a post-processing method that, associated to such measurements, can lead to better insights on the mechanisms involved. This method takes advantage of ever increasing access to time resolved data on combustion instabilities, and in particular diagnostics giving 2D or 3D results.

In order to do so, the following manuscript starts with in an introduction giving background information on the possible diagnostic techniques and post-processing methods available for the study of combustion instabilities. In the first chapter, a description of the two stage, propane fueled swirled burner used in the study, as well as the apparatus used for the measurements

used is made. They consist of acoustic pressure measurements by microphones placed in the injection tube and combustion chamber of the burner, OH* chemiluminescence measurements by a photomultiplier tube, high speed flame imaging, OH Planar Laser Induced Fluorescence measurements, as well as laser absorption measurements for equivalence ratio estimation, and high speed Background Oriented Schlieren for the visualization of temperature fluctuations.

In a first analysis step, the average, Power Spectral Density and correlation between the measurements are computed. In particular, the study of the acoustic pressure fluctuations in the burner for various injection conditions allows to choose three sets of injection conditions that exhibit an interesting evolution: for equivalence ratios less than 0.82, the frequency of the observed instability rises with fuel injection and its amplitude remains constant, while for equivalence ratios over that value, the frequency stays stable, but the amplitude diminishes. For that reason, equivalence ratios of 0.74, 0.82 and 0.94 were chosen for further study. Strong correlation between all the measurements was observed at the peak frequency of the instability, at 192 Hz or 212 Hz depending on the injection condition.

In a second step, since a single strong frequency was detected in the system, phase averaging of the various measurements was achieved using the pressure in the injector tube as the phase reference. This study confirmed that while the phase shift between the pressure inside in injector tube and the chamber changes with the equivalence ratio, the phase between the pressure inside the chamber, and the heat release stays almost the same. A study of the OH PLIF images showed that while a strong vortex roll up of the flame can be observed in axial views, the movement of the Inner Recirculation Zone (IRZ), along which the flame is stabilized, is more complex: radial views showed that in the two leanest cases, the IRZ has an elliptical shape that turns around the chambers' axis as well as expand and retract during the instability cycle. The richest case however exhibited a different behavior, where an almost circular IRZ oscillates around a stable angle depending on the distance to the injector. This is also accompanied by a decrease of the instability's amplitude in this rich condition. Background Oriented Schlieren shows that density fluctuations (which can be assimilated to temperature waves) propagate downstream of the flame at a convection speed. Lastly, the equivalence ratio calculation from the absorption measurements was attempted. As it needs a precise knowledge of the length of fresh gases crossed by the absorbing laser, calculation of this length from the PLIF imaging was attempted. However, since the flame is almost exclusively present along the IRZ, a high uncertainty persists on the outer limit of the fresh gases' position. The precision of these measurements was thus lower than expected, resulting in a strong uncertainty on the calculated equivalence ratios.

Lastly, a Dynamic Mode Decomposition study of the system is achieved, and compared to the more classic POD, as well as phase averaging. The DMD gives structures with a sinusoidal time evolution, and optimized for the reconstruction of the observed data field' dynamics. In particular, it is shown that in order to obtain the best computation of the underlying modes, computing and then averaging the DMD from different time series of the same phenomenon, somewhat similarly to a periodogram, is a sound approach. In particular, it is shown that the structures that can be observed in the flame using phase averaging (using the pressure fluctuations in the injector as a reference) are found using only the high speed imaging, and that projecting the pressure and OH* chemiluminescence signals on these modes give the same phase and amplitude evolutions as that phase averaging, confirming the precision of the method.

Résumé

Ce travail de thèse s'inscrit dans le cadre des études sur les instabilités de combustion. Ces phénomènes de couplage entre le processus de combustion, l'acoustique ainsi que l'écoulement dans le brûleur, sont une des difficultés majeures rencontrées dans le développement des turbines à gaz modernes. En effet, afin de toujours réduire les émissions de polluants et en particulier d'oxydes d'azote, les turbines à gaz modernes sont conçues pour fonctionner en régime pauvre partiellement (ou totalement) prémélangé. Hors ces régimes sont particulièrement sujets à ces phénomènes de couplage qui peuvent générer un bruit important, ainsi que réduire la durée de vie de la machine. Bien que les méchanismes fondamentaux impliqués dans ces phénomènes de couplage ont désormais fait l'objet de nombreuses études, il est toujours à l'heure actuelle impossible de prédire précisément les conditions d'apparition de ces instabilités, ainsi que leurs caractéristiques. Les objectifs de cette thèse, sont de proposer une méthode pour appliquer la mesure de richesse par absorption laser à des configurations de brûleur ne disposant pas de plenum, et de mettre en place une stratégie pour le traitement des données obtenues sur un brûleur pour caractériser l'instabilité de combustion qui y est présente. Le brûleur étagé swirlé CESAM ("Combustion Etagée Swirlée Acoustiquement Maîtrisée"), alimenté en propane et présentant de telles instabilités a été employé dans cette étude.

Ce travail de thèse a fait appel à plusieurs diagnostiques: des micros ont été installés dans l'injecteur et la chambre du brûleur pour y mesurer la pression acoustique; un photomultiplicateur a permis de mesurer la chimiluminescence des radicaux OH* produits par la flamme, une caméra rapide a permis de visualiser l'évolution de son positionnement, une PLIF OH a permis de visualiser cette position sur différents plans axiaux et radiaux, un système de mesure d'absorption laser a été mis en place pour mesurer les fluctuations de richesse, et finalement un système haute cadence de Background Oriented Schlieren (BOS) a permis de visualiser les ondes de température générées par la flamme.

Dans un premier temps, une étude des moyennes, corrélations et densité spectrale des résultats obtenus par les différent systèmes employés a été effec-

tuée pour cerner les caratéristiques principales des instabilités de combustion préentes dans la plage de fonctionnement choisie. Tout d'abord, une observation des pressions dans la chambre et l'injecteur en fonction des conditions d'injection a permis de remarquer une évolution dans le comportement du brûleur: pour des richesses inférieures à 0.82 au débit d'injection choisi, la fréquence de l'instabilité présentée par le brûleur augmente avec la richesse utilisée, mais son amplitude reste stable. A l'inverse, pour une richesse supérieure à 0.82, la fréquence reste la même, mais l'amplitude de l'instabilité diminue. Suite à ces observations, les points de fonctionnement à richesse 0.74, 0.82 et 0.94 ont été sélectionnés pour une analyse en détail. Cette première étape a permis de confirmer que toutes les mesures effectuées montrent la présence d'une forte oscillation à la même fréquence, autour de 192 Hz pour la richesse la plus faible, et de 212 Hz pour les richesses plus élevées. De plus, une corrélation importante à ces fréquences entre toutes les mesures confirme bien que toutes les grandeurs mesurées sont impliquées dans le phénomène d'instabilité.

Dans un second temps, les démarches pour obtenir une mesure des fluctuations de richesse dans le brûleur à partir de l'absorption d'un laser infrarouge par le carburant dans les gaz frais ont été effetuées. En particulier, une mesure de la fluctuation de l'épaisseur de gaz frais traversée par ce laser est nécessaire au vu de la configuration du brûleur. Cette mesure étant effetuée à partir d'images PLIF basse cadence, une analyse par moyenne de phase utilisant la pression dans l'injecteur comme référence a été mise en place. Afin de valider sa validite, la moyenne de phase a été employée pour tous les diagnostiques. Cette analyse a permis de confirmer que bien que le déphasage entre pression dans l'injecteur et dans la chambre de combustion dépende du point de fonctionnement, celui entre la pression dans la chambre et le dégagement de chaleur restent quasi identiques. Les films de BOS mettent en évidence pour tous les points de fonctionnement la convection d'une onde de température en aval de la flamme. La moyenne de phase des champs PLIF OH axiaux et radiaux a permis de montrer un comportement de la flamme plus complexe qu'à première vue: dans les trois conditions d'injection, la flamme présente un lâcher de vortex à la fréquence de l'instabilité en pression, mais le comportement de la zone de recirculation interne (IRZ) change. En effet, dans le cas le plus riche, l'IRZ est radialement de forme quasi-circulaire, et oscille azimutalement au cours d'un cycle autour d'une position stable dépendant de la distance à l'injecteur. Pour les deux cas les moins riches par contre, l'IRZ est en fait de profil elliptique, et tourne autour de l'axe de la chambre de combustion. Enfin, le calcul des fluctuations de richesse à partir des mesures d'absorption et des images PLIF a été tenté. En effet, ces dernières sont nécessaires dans la configuration utilisée dans cette étude, car le laser absorbé passe dans la flamme, et le lien entre richesse et absorption ne peut être fait que si la longueur de gaz frais traversé est connue. Malheureusement, la stabilisation forte de la flamme autour de

l'IRZ n'a pas permis d'estimation précise de cette longueur de gaz frais au cours d'un cycle, diminuant fortement la précision des résultats obtenus sur la richesse. Il semble néanmoins que d'importantes fluctuations de richesse soient présentes dans le brûleur.

Enfin, une étude par Dynamic Mode Decomposition (DMD) des mesures haute cadence a été effectuée. Cette méthode d'extraction de modes permet d'obtenir des structures cohérentes à partir de mesures temporellement résolues, mais nécessite l'accès à des champs 2D ou 3D. L'utilisation de cette décomposition sur les films de caméra rapide de la flamme a permis de confirmer que le mode à 192-212 Hz est bien le mode prédominant dans les mouvements de la flamme elle-même, et une projection des signaux de pression ainsi que de chimiluminescence OH sur ces modes permet de retrouver des résultats similaires à la moyenne de phase. Il est cependant montré que pour réellement obtenir des résultats quantitatifs, une approche moyennant des DMD calculées sur différent échantillons de la même mesure de manière similaire à un périodogramme est nécessaire. Des résultats plus qualitatifs sont cependant atteignables en utilisant des échantillons de taille réduite.

Contents

List of Tables

List of Figures

Nomenclature

Latin Characters :

A	Absorbance
A_i	Amplitude of the i $^{\text{th}}$ mode from DMD
B	Matrix containing the temporal information in the DMD
c	Sound speed
c_p	Specific heat
D	Matrix containing the frequency and exponential growths of DMD modes
D_α	Matrix containing the amplitudes of the DMD modes
f	Frequency
f_s	Sampling frequency
I	Intensity of a laser beam
I_0	Intensity of a laser beam before absorption
$\dot{m}_x$	Mass flow rate of species x
N_i	Concentration (in mol/m^3 of the species i)
P	Pressure
P_0	Reference pressure: 20 µPa
P'_{rms}	Root mean square of the pressure fluctuations
T	Temperature
T_2	Amplitude (in Volts) of the signal given by the detector for absorbance measurements of the equivalence ratio
w	Windowing function used in power spectrum estimation
Re	Real part

Greek Characters :

α	Fuel injection staging	Λ	Matrix containing the frequency information in the DMD
α_i	Amplitude of the i^{th} mode from DMD	σ_i	Absorption cross section of species i
ϕ	Equivalence ratio	Ψ_i	i^{th} mode from DMD
Θ	Phase	β_i	i^{th} mode from the Extended DMD
λ	Wavelength		
λ_i	Frequency of the i^{th} mode from DMD		

Abbreviations :

DMD	Arbitrary Units
DMD	Dynamic Mode Decomposition
FFT	Fast Fourier Transform
IRZ	Inner Recirculation Zone
ORZ	Outer Recirculation Zone
PLIF	Planar Laser Induced Fluorescence
PMT	Photo Multiplier Tube
POD	Proper Orthogonal Decomposition
PSD	Power Spectral Density
SPL	Sound Pressure Level

Introduction

Presentation of combustion instabilities

With the industrialization of emerging economies, the worldwide energy demand has been getting higher since the last few decades. Combustion is still the source of more than 80% of the global energy production (IEA (2014)), and is used in applications from electricity production to aerial and terrestrial transportation.

This thesis work treats of combustion problems as encountered in burners of the type found in gas turbines, for electricity generation or aeronautical use. In these particular applications, progress has been made with two goals in mind: to have a better fuel efficiency of the engine, and to reduce the emissions of pollutants. In the aerospace field, the usual design choice made to try achieving the first one is using turbofan engines with a high bypass ratio. The second one has led to a move from Rich-burn Quick-quench Lean-burn (RQL) combustors to Lean Premix Combustors (LPC) in order to drastically reduce the emissions of pollutants, the main one being NOx (Correa (1998)). However, these types of combustors produce flames that can be unstable, and subject to mainly three problematic incidents:

1. Flashback. This is when the flames goes upstream from its expected stabilization points, and into the injector. It can lead to catastrophic damage to the injector and engine destruction.
2. Extinction. This is particularly problematic in the case of aircraft engines, for which in-flight re-ignition can be difficult due to the inlet conditions.
3. Combustion instabilities. This particular phenomenon is the main subject of this thesis, and so will be explained in more detail.

Combustion instabilities are self-sustained pressure oscillations inside the combustion chamber. They lead to an increase in noise level, but also vibrations and heat flux transfer variations, which can reduce the engine's lifetime and even in extreme cases damage it. The phenomenon was first observed in the 1950s in rocket engines, where it led in extreme cases to the destruction of rockets. It has since been observed in various configurations, and has been under study ever since.

The precise mechanisms leading to combustion instabilities can be varied (Candel (2002); Ducruix et al. (2003); Lieuwen et al. (2001); Lieuwen (2003)), depending strongly on the properties of the burner and used, as well as injection conditions. The processes driving the instabilities are mainly interactions between pressure, heat release and equivalence ratio, and their respective effects. However, the mechanisms behind these interactions can be numerous, and have linear or non-linear effect on the combustion instability. For example, vortex shedding (Schadow and Gutmark (1992)) can be shown to have an important effect on the self sustaining of heat release oscillations that can be generated in the burner by various means (Lieuwen (2003)). It can thus be difficult to predict precisely the characteristics of an eventual combustion instability (its frequency, amplitude, limit cycle but also stability).

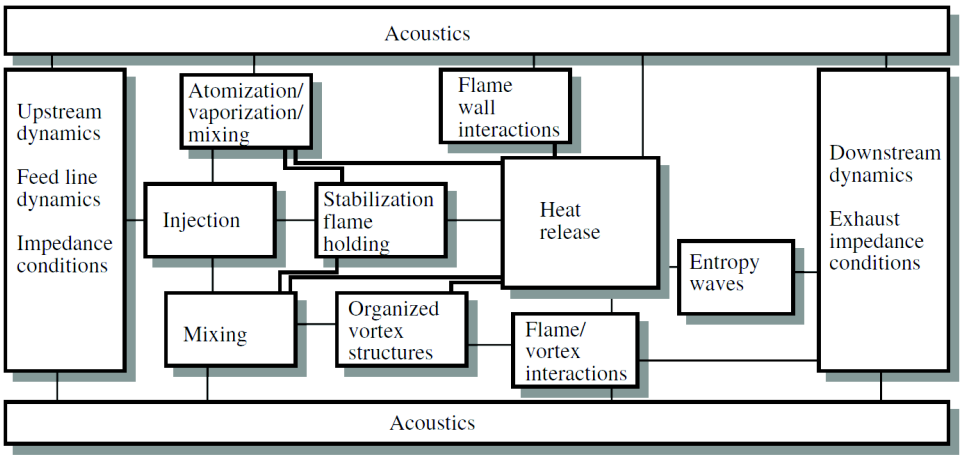

Figure 1: *Basic interactions leading to combustion instabilities (from Candel (2002)).*

The frequency is probably the easiest characteristic to predict: since combustion instabilities are linked to pressure fluctuations, they often correspond to one of the acoustic modes of a part of the burner. This could be (as is the case in the burner studied in this thesis) a longitudinal acoustic mode of the chamber, leading to a low frequency instability, especially in industrial configurations with a big size. However, other acoustic modes can be linked to combustion instabilities, such as transverse modes in the annular configurations found in most gas turbines (Bourgouin et al. (2013); Seume et al. (1997); O'Connor et al. (2015)). As such, the frequencies encountered can vary from a few Hz (typically found in furnaces several meters long), up to several kHz. The precise value however, is still hard to determine predictively, party because the exact frequency of any given acoustic mode depends on the gas temperature (via the speed of sound), and thus the injection conditions of the system.

In the particular case of gas turbines, modern configurations use swirling flows in order to obtain a compact flame. These flows exhibit coherent vortexes even without the presence of a flame (Alekseenko et al. (1999); Providakis et al. (2010)), and the impact of the combustion process on these vortexes is a potential source of instability, as the flame can stabilize around such vortexes (Stöhr et al. (2011)) and thus oscillate at the same frequency. This flame-vortex interaction can be more complex however (Syred (2006); Stöhr et al. (2009); Steinberg et al. (2010); Moeck et al. (2012b); Moeck et al. (2012a)), and the presence of a flame can outright disrupt a coherent vortex structure that was present in the cold flow at the same injection conditions (Legrand et al. (2009)).

A summary of these studies is that combustion instabilities are the results of the couplings between pressure, equivalence ratio fluctuations and flow characteristics in the burner. These interactions however can be complex, as they are due to various mechanisms, whose presence depends on the burner configuration. Moreover, the relative importance of a given mechanism in the driving of combustion instabilities also depends on the injection conditions (burners typically only present instability in a given range of their possible operating conditions).

It is thus important in order to understand the combustion instabilities, to be able to have a quantitative and ideally time resolved access to pressure, temperature and equivalence ratio inside the system, as well as the flame position. In most cases, since vortexes are present, information on velocity is also a plus, but is probably less important in the instability's characterization than the previously cited physical quantities. The main problem has lied here for most studies: since for most gas turbine configurations frequencies in the hundreds of Hertz are observed, measurements at the kilohertz repetition rate or above are needed to precisely describe the different couplings that occur in the burner. The next part will detail the various measurement techniques that allow to obtain such results, with their respective strong and weak points when considering the determination of the fluctuations causing (or caused by) combustion instability.

State of the art on measurement techniques for instability's study

As was said in the previous section, combustion instability is driven by complex interactions, which can be traced back to three elements: pressure, temperature and equivalence ratio. It is thus important, if one wants to understand the instability happening in a given system, to have access to quantitative measurements for them, and since the coupling between them is fundamental, the measurements should ideally be simultaneous. Moreover, in

the case of industrial applications, an important field to study is the triggering and onset of these instabilities, which is yet to be clearly understood. It is indeed difficult to study properly since the time scales involved are very small, and thus high time resolution and simultaneous measurements are needed. Such high speed simultaneous measurements have only fairly recently been available (Stöhr et al. (2011); Böhm et al. (2011); Boxx et al. (2010)).

Efforts have been made along the years to develop new techniques that would allow accurate, precise and fast measurement of pressure, temperature and concentration of species, some of them applicable to combustion study (Docquier and Candel (2002); Ballester and García-Armingol (2010)). They can be broadly divided into two subsets: optical and probe based. They are presented thereafter, for each physical quantity.

Pressure measurement

The measurement of pressure fluctuations as needed for the study of strong thermo-acoustic instabilities is the most easily obtainable in laboratory configurations, as well as industrial ones. This is mainly due to the fact that combustion instabilities are often linked to cavity modes of parts of the burner (usually the combustion chamber, but in some configurations, such as the one used in this study, the injector can also be a cavity), and thus can be considered unidimensional in a first approximation. A measurement of the acoustic part of the wall pressure is thus the only value really needed in this objective and thus microphones can be used to acquire these fluctuations with good precision and temporal resolution. It can be then concluded that the techniques needed for this part of the measurements are classic and already exist.

Equivalence ratio measurement

In the case of equivalence ratio, one wants to either measure it directly, or at least the concentration of the fuel or of a combustion product.

As far as probe based techniques are concerned, there are two types one can use. The first type is based on semi-conductor probes: the electric resistance of the probe is directly dependent on the partial oxygen pressure. This type of probe is used in the automobile industry to measure the injection conditions of the engine (their alternative name in that case is lambda probe). However, the most common of these probes have far too long a response time (typically 100 ms) to monitor variations at the frequencies frequently encountered in combustion instabilities. Research is still made to obtain ever better reactivity from such sensors, and much better response times (down to a few milliseconds) seem to be achievable (Regitz and Collings (2008); Moos et al. (2011); Tragut and Härdtl (1991))), depending on the temperature

they are used at. Another possibility is the use of ionization probes, which exploit the fact that the combustion process produces ions among other things. A tension (inferior to the air's dissociation value) is applied between two electrodes, and the ions produced by the flame allow a current to flow between them. A link between this monitored electric current and the equivalence ratio can then be made (Keshav et al. (2008); Keshav et al. (2010)). The only drawbacks to this type of probe are the perturbation the probe may induce in the flow, and the fact that it can be used only downstream of the flame.

An optics-based solution can be to exploit the combustion process itself: by using captors observing the light naturally emitted by the flame at various carefully chosen wavelengths, information on the relative light emissions by radicals created during the combustion can be used to deduce the equivalence ratio of the flame (Hardalupas et al. (2004); Docquier et al. (2002); García-Armingol et al. (2013)). Indeed, when carefully choosing the monitored species (CH^*, OH^* et C_2^* in the cited studies), one can obtain a monotonous relation between the relative intensities of the bands observed and the equivalence ratio, mostly independent of other parameters like, for example, the strain rate. As an optical measurement method, it requires full optical access to the flame in the appropriate spectral domain. However, as noted by Ballester and García-Armingol (2010), the exact relationship between measured chemiluminescence and equivalence ratio can change depending on the equivalence ratio range observed, and is quantitatively dependent on the measurement system, but also on the configuration studied.

Another useful optical technique is the measurement of Rayleigh diffusion to obtain temperature or equivalence ratio (Schwarz et al. (2010)). This method is based on the fact that Rayleigh diffusion is proportional to the temperature, pressure and concentration of the diffusing species. However this technique has an important drawback: to measure one of these three parameters, the other two need to be known.

Among the techniques that can be used to monitor both equivalence ratio and temperature, Raman scattering has also been used (Meier et al. (2007); Meier et al. (2010); Stopper et al. (2010)). It can give the concentration as well as temperature of several species, but is particularly complex to use due to the various calibrations and post-processing needed.

Lastly, laser absorption techniques can be used, as will be the case in the present study. In this type of measurement, a laser with a wavelength only absorbed by the fuel is used (Li et al. (2011); Lee et al. (2000); Kim and Santavicca (2013); Tomita et al. (2004)). The laser's absorption when passing through the flame can be linked to the concentration of fuel and the beam's geometrical path. The most simple systems use a single laser, offering values

integrated on a line of sight, while more complex configurations can be used to try to apply the technique in more difficult cases (interfering species, aerosol,...) (Klingbeil et al. (2007), to obtain the results on a reconstructed profile (Gillet et al. (2004)), or simultaneously measure other physical quantities (Klingbeil et al. (2009)).

Temperature measurements

Access to the temperature fluctuations can be interesting in the understanding of combustion instability dynamics, and is moreover important in the case of turbine engine applications since their creations by the combustion instability cycle can be a source of combustion noise (Ducruix et al. (2003)). The most common tool to obtain this kind of measurement is the thermocouple, thanks to its ease of use. However, the main problem faced here is the time resolution of the measurement: in order to have access to temperature fluctuations, a time resolution of at least several dozen hertz is needed. However, thermocouples have a response time directly depending on their size, meaning that in practice, thermocouples have a response time at best of the order of the millisecond (Omega (2015)), so it is very difficult to obtain temperature fluctuations occurring at the frequencies needed to properly describe combustion instability cycles.

Another classic measurement method (and one of the simpler optical ones) is the infrared pyrometry. Infrared pyrometers link the emissions of an observed target to its temperature. There are several types of pyrometers that can be distinguished, and which could be used in a combustion environment (Dyne (1953)). The simplest and most common type is the single color pyrometer. This type of sensor measures the target's emissions in a narrow or large infrared wavelength band, and comparing it to a blackbody emission, deduces its temperature. This technique has several drawbacks in the study of combustion instability. The main difficulty is that emissivity of the observed target must be known in order to deduce the temperature from the measurement, and that information for a flame is non trivial since for example it depends on various parameters influencing the flame (such as flame thickness, the concentration of soot particles, pressure,...) (Pastor et al. (2002); Beér and Howarth (1969); Taylor and Foster (1974)). Another linked difficulty is that in the case of combustion instability, the intensity perceived by the captor can vary due to factors other than temperature: movement of the flame in the line of sight, fluctuations in the concentration of emitting gases, or in pressure. Moreover, this type of measurement is easier if the target is a blackbody or a gray body. This is the case of rich, sooty flames where such a measurement could be easier (also thanks to a higher luminosity of the flame), but the lean flames used in modern gas turbines do not emit that type a broadband spectrum, but

instead a band spectrum (mainly from H_20 and CO_2). A more robust type of sensor in this case is the two-color pyrometer: in this case, the emission in two narrow wavelength bands is compared. In most commercially available two-color pyrometer sensors, the ratio of wavelength emission intensities is compared to that produced using Planck's distribution, assuming a black-body or gray body emission. While useful if observing a sooty flame, for a lean combustor it proves unadapted. Thus, for the case of gas turbines, more specialized systems with carefully chosen wavelengths are needed. These can be in the infrared, but ultraviolet is also a possibility (Brown et al. (2008)).

As noted when describing them in the previous section, several of the optical methods giving access to molecule concentration also give a temperature value. The drawbacks were already given there, but to cite them again, they are mainly a low repetition rate of the measurement, a need for good optical access to the studied zone, and for some of them a difficulty to obtain the desired values from the measurements.

As with equivalence ratio, absorption-based methods can be used to measure temperatures (Bolshov et al. (2011)). In this case, lasers emitting at at least two wavelengths are used simultaneously, somewhat similarly to two-color pyrometry. These wavelengths are chosen so that the ratio of absorption between the two can be linked to the desired molecule's temperature. A common choice is water vapor (An et al. (2011); Shimura et al. (2009); Rieker et al. (2007); Rieker et al. (2009)) but other combustion products can be used, such as carbon dioxide (Spearrin et al. (2014); Farooq et al. (2008a)). The temperature value is obtained by measuring the simultaneous absorption of the two lasers and knowing the relation between this absorption ratio and temperature. The lasers used are often diode lasers (Allen (1998)) emitting at the required absorption bands, usually several of them (Hendricks et al. (2005)), but single-diode systems can also be accomplished if the two desired wavelengths are close enough (Farooq et al. (2008b)). The system's acquisition frequency is then mainly governed by the laser diode's ability to scan the wavelength at the desired absorption bands, and can range from a few Hz to several kilohertz (Arroyo et al. (1994)). Since the ratio of absorptions is the only thing needed, there is no dependency on parameters such as the absorption length as is the case for equivalence ratio measurement systems. The only drawbacks of the methods are then that the obtained temperature is a result integrated on the light path of the lasers, and that the measurement is only available in burnt gases because of the usually monitored species.

Lastly, the Background Oriented Schlieren (BOS) can be used to monitor temperature fields. This technique is similar to the classic Schlieren visualization, in that it gives access to gradients of density in the observed field through observation of refractive index gradients (Raffel (2015); Vasudeva et al. (2005)).

Since gases have a temperature-dependent density, a temperature field can be obtained if its value at a reference point in the image is known. In the BOS, the object to study (in the present case a combustion chamber) is placed between a camera and a random or semi-random pattern. The camera is then used to film the deformations of the observed pattern caused by the inhomogeneous density in the chamber, obtained by comparing the film to a reference image. To precisely measure these displacements, PIV algorithms can be used, but other methods can also be employed (Atcheson et al. (2009)). The BOS can thus be a high speed diagnostic, if the camera employed is sensitive enough. Another great advantage of the method is the light requirements in equipment: the background used as reference can be natural (grass, pebbles), and in this case measurements can be made using only a camera (Raffel et al. (2014); Raffel et al. (2000); Mizukaki et al. (2014)). The technique's main limitation is that the measured deformations are integrated on the light path between the screen and the camera: it is then necessary to have symmetry conditions for the observed flow (Venkatakrishnan and Meier (2004); E.D. Iffa and Malik (2011); Zhou et al. (2011)), or multiple fields of view (Goldhahn and Seume (2007); Richard et al. (2002)) if one wants to reconstruct the refractive index field, and from there to obtain a 3D temperature field.

Reasons for choices in this study

The diagnostics used in this work were chosen because they can offer measuring capacities both quantitatively and at a high time resolution, since this will be needed in the present study of an already established combustion instability, but will also be necessary in further studies trying to tackle the hard point that is the onset of a combustion instability in a burner. More precisely, a goal of this thesis is to describe the most precisely possible the differences in the characteristics of the combustion instability present in a burner, depending in the injection conditions.

In order to do that, it is important to obtain high speed measurements of pressure, temperature, and equivalence ratio in the studied burner since they are key parameters. For pressure fluctuation measurements, traditional microphones satisfied these criteria, but as shown in the previous sections, for temperature and equivalence ratio measurements, each method has its advantages and drawbacks. The absorption based technique was chosen as a mean of measuring the equivalence ratio for its relative ease of use, and limited requirement for optical access: for the study of the burner used here it may not be critical, since good optical access to the combustion chamber is available, but for other configurations closer to real turbine applications, this may be of importance. The temperature measurements were made using a Background Oriented Schlieren system which is also simple to use, but

needs perfectly known conditions at the image borders to be able to obtain a quantitative measurement. As the temperature profiles at the walls of the chamber were not available, such quantitative, absolute results could unfortunately not be obtained in the present study, but fluctuations can still be observed.

Lastly, other diagnostics not described previously were also employed. Since the burner used in this study is not cooled, a thermocouple was first used to have an idea of the temperature evolution in the chamber at the typical injection conditions used. A photomultiplier tube was used to monitor light emitted by OH radicals produced by the flame, as a means of monitoring qualitatively the heat release rate. The flame's position was obtained by filming it with a high speed camera. Lastly, low frequency (10 Hz) Planar Laser Induced Fluorescence (PLIF) of OH radicals was also conducted on axial and radial profiles in the chamber to obtain a visualization of the emplacement of the burnt gases during a combustion instability cycle.

More details on the measurements techniques, and the apparatus used in the study are available in chapter 1.

State of the art on post-processing techniques for combustion dynamics studies

Once the data is obtained, it is necessary to use post-processing to extract information on the underlying dynamics of the system. In particular, as was stated earlier in this introduction, combustion instability is characterized by couplings between pressure, equivalence ratio, heat release rate, flame shape,... The objective of post-processing for the study of combustion instabilities is thus to identify any strong oscillation in any of the 1D signals and the main characteristics of these oscillations (frequency, amplitude), coherent structures present in 2D fields, and the links that may exist between these various characteristics. Indeed, knowing for example that pressure oscillations happen at the same frequency as equivalence ratio fluctuations, with a given time shift would certainly help to better understand the mechanism linking the two. The post-processing methods available range from classic statistical analysis (average, mean, standard deviation, correlation,...) and go up to mode extraction methods. These last ones in particular are of the most interest since the development of high speed measurements, as they allow to make sense of the mass of data available. Indeed, with the more common use in research of high repetition rate laser based diagnostics and high speed cameras, the quantity of data available is ever greater, and thus the underlying post-treatment problems that were until now specific to numerical simulations are starting to be felt in the experimental field too.

The variety of post-processing methods available means that choices must be made. In particular, all of them have limitations, either in the type of data they can be used on (number of simultaneous points, periodicity of the signal), or even the explicit or implicit assumptions made on the expected results. Because of this, some care must be taken when establishing the analysis process, to use adapted tools for the particular case. In order to better understand what choices were made in this particular study, where the objective is to characterize the evolutions of the pressure, temperature, equivalence ratio and flame shape in a burner subject to combustion instabilities, a state of the art presenting several of the most relevant methods is useful.

Statistical methods

These are the most widely used tools, as they are simple to use, well understood, and allow to have a first approach of the studied system that may help to chose other, more specialized techniques afterwards. The most common methods are the Fourier transform, mean calculation, and coherence.

A good alternative to the Fourier transform is the Power Spectral Density analysis (PSD). In the present study, Welch's method was used to calculate the PSD of signals, by using the pwelch method from Matlab. Welch's method is based on the use of modified periodograms, where amplitude of the function in each window is multiplied by a window function. This method allows to have less noisy spectra than using only the FFT, and thus can allow to better see features that otherwise may be lost in measurement noise.

Lastly, Cross Power Spectral Density is also useful in the present case, since the relation between several variables in the system needs to be investigated. This method gives a spectrum of complex values, whose modulus $|P_{xy}|$ gives the correlation between x and y at each frequency, and phase $angle(P_{xy})$ gives the phase difference between the two signals.

These methods could already be considered sufficient in determining the frequency, amplitude and delay between several measurements. They however are mostly fit for interpreting 1D signals. If 2D fields are available, using only these methods would lead to a loss of information.

Phase averaging

A classic method for treating coherent signals, phase averaging has its advantages and drawbacks. By using a signal as the reference for a phase calculation, this method allows to obtain an average cycle. The main advantage of phase

averaging is that only the reference signal needs to be taken at an acquisition rate high enough to properly reconstruct that average cycle: it has thus been used numerous times to reconstruct cycles from PLIF or velocity fields obtained at frequencies much lower than the studied phenomenon.

This method however supposes that the signal it is used on really contains a cycle at the desired frequency, otherwise the obtained result may not be physical at all.

Mode extraction techniques

These techniques take advantage of the availability of the data fields obtained from PLIF, Particle Image velocimetry, or chemiluminescence imaging. The goal of these methods is to extract coherent structures (or modes) from the data set used as a reference. In this section, the now common Proper Orthogonal Decomposition is presented, and the first details on the Dynamic Mode Decomposition are given to have a comparison basis. The in-depth analysis of the last one, which was chosen as the preferable method here, is available in chapter 4.

Proper Orthogonal decomposition

The Proper Orthogonal Decompositoin (POD) is by now a classic method of extraction of coherent modes from a given set of data points. It is known under other names in other fields of study (Principal Component Analysis and Karhunen-Loève transform for example). A brief history of the method has been made for example in Berkooz et al. (1993).

The goal of this method is to extract from a set of data points an orthogonal base such as the projection on each component of the base (referred to afterwards as modes) contains the maximum of the energy from the initial signal. The first mode computed will contain most of the energy, and the subsequent modes will contain less and less.

In the study of combustion instabilities, the most interesting use of this method comes from the Extended Proper Orthogonal Decomposition (Borée (2003); Duwig (2010); Stöhr et al. (2011)). The principle is this variant is the following. First, the POD is done on a set of data from a given variable. Modes best describing its energy fluctuations are thus obtained. The Extended part comes from the use of this base on other signals acquired simultaneously to the original set: they are projected onto this base. This allows to visualize the eventual part of a different variable correlated to the fluctuations of the first, which is important in the case of combustion instabilities since they result from various complex couplings.

This method however has a few limits that could be discussed. First, the base is optimized on the energy content. This is probably a good idea in most cases, but in complex interactions, a coherent structure with a fairly low energy content may be of great impact on the overall system. Another thing to take into account is the complete separation of time and space in the method: the modes only contain information about the spatial structure of the mode, and the amplitude for each time step must be computed separately. This has one drawback: the temporal evolution of a given mode can become fairly difficult to interpret if there is no single strong frequency in the phenomenon observed.

As it is commonly used in combustion studies, and is similar in principle to the Dynamic Mode Decomposition, this method was briefly presented here. However, in the present study, that other method was preferred, for its different set of advantages and drawbacks.

Dynamic Mode Decomposition

The Dynamic Mode Decomposition (DMD) is a recent development of mode extraction methods, first introduced concurrently by Schmid (Schmid (2010); Schmid (2011); Schmid et al. (2012)) and Rowley (Rowley et al. (2009)) as a means of analyzing experimental or numerical data in fluid mechanics and combustion study. The goal of this method is to extract complex valued modes from the data set used. The main difference (as far as the method's results are concerned) between DMD and the more classic POD is the temporal evolution of the computed modes: while the POD modes have no fixed temporal evolution and thus can be difficult to interpret in terms of dynamics, the DMD modes have an exponentially increasing or decreasing oscillation at a fixed frequency. Their impact on the dynamics is thus much easier to interpret, as their evolution is simple.

The DMD modes are also constructed not to best approximate the energy content of the signal, but its dynamic: this may have an influence on the results in some cases where the evolution of a phenomenon is not most influenced by a high energy structure, which would thus not be preferentially picked up by the more common POD.

The DMD's drawbacks are linked to the assumptions governing it: the DMD is a linear approximation, and supposes that enough time steps were acquired to be able to fully describe the system's dynamics. The acquisition frequency of the data points must also be uniform, and high enough to be able to describe all the dynamic content. These particular limitations, however, are currently being worked on (Tu et al. (2014); Leroux and Cordier (2016)). Lastly, the DMD decomposes the signal in a series of sinusoidal modes on the time

dimension, and thus suffers from the same problems a Fourier decomposition can have if the underlying dynamics is not sinusoidal: in the case of a triangular fluctuation for example, the fluctuation will be decomposed in an infinite series of modes, introducing some possible errors Duke et al. (2011).

Even though it can have its limitations, the DMD seems promising especially when considering the low number of data points needed compared to other methods and the simple to understand temporal evolution of the computed modes. It will be studied more extensively in chapter 4, giving more insight on the precision and accuracy that can be expected.

Goal and organization of this thesis

The goal of this thesis is two-fold. One of the goals is to measure fluctuations of pressure, temperature and equivalence ratio in a turbulent partially-premixed swirled combustor to study the combustion instability it is subject to. The second objective is to develop a post-processing strategy for the study of such combustion instabilities, that ideally could be used on other burner configurations. In order to achieve that last objective, the problems encountered using even classic analysis methods on a seemingly simple case need to be outlined, and guidelines to the practical use of the Dynamic Mode Decomposition to be given. In order to present the results of this study, the manuscript is divided in four chapters.

The first chapter describes in detail the burner used in this study, and all the measurement techniques used to have access to pressure, temperature and equivalence ratio fluctuations. The post-processing necessary to obtain the physical quantities from the measurement systems' outputs is also given.

In the second chapter, the most classic and simple post-processing of obtained data is made. First, a PSD study of pressure measurements obtained in the injector and chamber of the burner is conducted to obtain a broad study of the combustion instability's sensitivity to injection conditions. From this first approach, three equivalence ratios are chosen to be studied in detail in the rest of this thesis. Once the three conditions are chosen the PSD method, as well as correlations and cross power spectral density analysis, are applied on all the signals acquired in this study. These include pressure measurements, OH* chemiluminescence intensity, but also the laser signals used for absorption measurements as well as broadband emissions of the flame and BOS-measured displacement fields. For all 2D fields obtained (broadband flame emissions, OH LIF at low frequency and BOS displacement fields), the average for each injection condition is given. Thus this first statistical study already gives insight in the instability obtained, and is the basis on

which any further study has to be constructed. In particular, it is shown that the average shape of the flame closes when the equivalence ratio is risen, but that the frequency and amplitude of the instability has two different phases: for $\phi<0.82$, the frequency changes and the amplitude is constant, while for $\phi>0.82$ the frequency does not change anymore, but the amplitude of the observed oscillations is has an evolution opposite to the equivalence ratio.

In the third chapter, phase averaging with the pressure inside the injector as reference is used to construct an average instability cycle in the three chosen injection conditions. The choices made to compute the phases from the reference signal are described in detail, with the effect of all parameters involved. The phase averaging study shows in particular that even though the spectra of the fluctuations obtained in the previous chapter present a strong peak at a single frequency, the amplitude of that main cycle is subject to important dispersion along time. The OH PLIF measurements show that most of the flame's movements are concentrated in the IRZ. Its geometry and evolution during an instability cycle are very dependent on the injection conditions, leading to different flame response. The calculations and assumptions necessary to obtain equivalence ratio fluctuations are presented. Even though the results are not as good as expected, the method is sound and may be attempted on other burner configurations. Lastly, the BOS measurements show that temperature fluctuations are almost certainly present during the combustion instability, and these fluctuations are convected in the chamber at all injection conditions.

Lastly, in the fourth chapter, the groundworks for the practical use of the Dynamic Mode Decomposition and its Extended version are given. In particular, a sensitivity study is conducted with a synthetic signal presenting a single sinusoidal mode. This study allows to determine the optimal numbers of oscillation cycles to be used to conduct the analysis is given (it was found that results are largely independent of the acquisition rate, provided it is high enough), as well as the inherent precision and accuracy of the method. The DMD's use on experimental data shows an inferior stability in the results compared to the synthetic case. A solution given to enhance this precision is the averaging of the results obtained on several calculations done on different sets of data points obtained during the same test run, similarly to a periodogram. When using the DMD and EDMD on the experimental results, a comparison is made with the results obtained using phase averaging, and show very good agreement. This confirms that the average cycle can be reconstructed using the DMD and small amounts of data points.

Chapter 1

Experimental setup and diagnostics used

In this first chapter, a description is made of the CESAM burner, used in the present study. The injection is carried out using two identical stages, in which both air and propane can be injected. The chamber is made of refractory concrete, with two side windows made of quartz. This chapter also describes the systems used for monitoring the pressure, heat release rate, equivalence ratio and temperature fluctuations in the burner. It finally presents the data processing that was necessary to obtain the physical values from the detectors' signals.

1.1 The CESAM burner

The CESAM burner (Fig. 1.1) was developed at EM2C laboratory by Dioc (2005), with subsequent modifications during the PhD theses of Tran (2009) and Lamraoui (2011). The burner is composed of two identical stages, in which air is injected tangentially (Fig. 1.2). Propane is injected in each slot perpendicularly to the airflow through a series of 3 holes each 1 mm in diameter. The small size of the holes helps in injecting propane with a high momentum into the airflow in a jet-in-crossflow configuration, enhancing the mixing process. The air and propane flow is injected into a central mixing tube with a 30 mm diameter, the tangential direction of that injection creating a swirling motion. Estimates of the swirl number (defined as the ratio of the axial flux of angular momentum to the axial flux of axial momentum) give values of about 0.6 in previous studies (Dioc (2005); Lamraoui (2011)). However, the mixing is not perfect and usually the burner runs in a partially premixed regime. To further prevent risks of flashback into the premixer, a small portion (about 5.5 %) of the total air flow is injected along the axis of the system at the back of the injector (Fig. 1.1) through a perforated plate backed by a cavity that also helps in controlling the inlet impedance Scarpato et al. (2012); Scarpato et al.

Type	Air (radial)	Air (axial)	Propane
Reference	F-206AZ-AAA-44V	F-202AC-FAC-44V	F-202AC-AAA-44V
Max. flow	100 Nm^3/h	12 Nm^3/h	4 Nm^3/h
Typical flow used	10 Nm^3/h	1.15 Nm^3/h	0.35 Nm^3/h
Precision	$\pm$0.15 Nm^3/h	$\pm$0.017 Nm^3/h	$\pm$0.006 Nm^3/h
Repeatability	$<$0.2 Nm^3/h	$<$0.024 Nm^3/h	$<$0.008 Nm^3/h

Table 1.1: *Characteristics of the mass flow controllers. Precision is given for the typical flow value used. The measurement of the actual output of the mass-flow controllers allows to ensure the error for each measurement.*

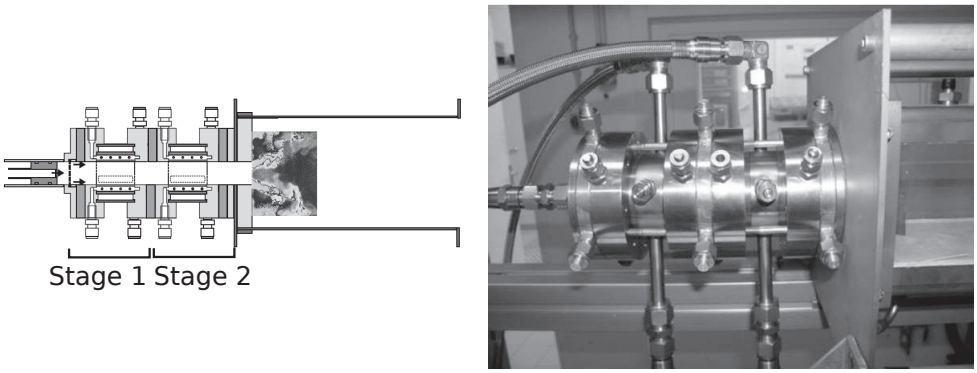

Figure 1.1: *The CESAM burner. On the left, a cutout schematics showing the two injection stages and a view of the chamber, and on the right a photo of the injection system*

(2012). In this study, the cavity has been suppressed by setting its length to 0 mm. There are several ports built inside the injector, giving the possibility to integrate microphones for acoustic pressure measurements inside the injector.

Injection of air and propane is controlled by a series of mass flow controllers (Bronkhorst El-Flow), whose characteristics are given in detail in table 1.1 . For each stage, one mass flow controller regulates air, and another propane injection. The flow is then divided in two to obtain a top and bottom injection of air and propane for each stage. Each feeding line is about 1.95 m long. Another mass flow controller regulates the axial air injection. All these mass flow controllers are linked to a command and control unit (Bronkhorst E-7000) placed in a separate room. The piloting of the burner can be done as is, but to ensure a better stability of the piloting (and give the possibility for controlled evolution of the mass flows in further studies), the command unit is linked to a Labview platform with the ability to control the system. The fluids are stored in pressurized tanks separated from the installation by several filters and security valves.

The injector is installed on a combustion chamber with a square 9.5 x 9.5 cm^2

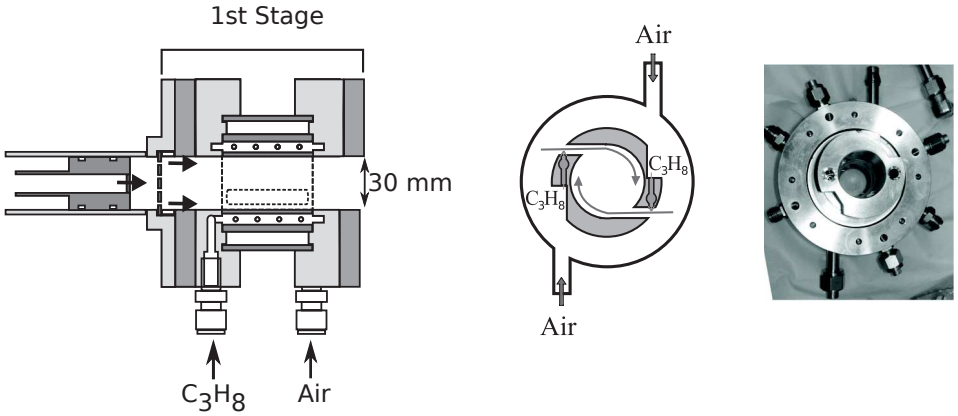

(a) Axial schematics (b) Radial schematics (c) Photo

Figure 1.2: *Injection system of the CESAM burner. Both propane and air are injected tangentially to create a partially premixed, swirling flow.*

cross-section, composed of two parts. The first part, in which the propane-air mixture enters, includes side walls made of quartz to allow optical access, while the top and bottom walls are made of concrete. In the setup used for most of the study, small quartz windows are integrated in the concrete at the injection point to allow the use of diagnostics such as LIF or PIV. This part of the chamber is 49 cm long. Another version of this chamber, only used briefly in this study, possesses three holes for the integration of microphones, or in one case, of a thermocouple. At the end of that section are successively bolted three steel sleeves, each 12 cm long and with the same section. They include a water cooling system, and access ports for microphones. The total length of the chamber is thus 85 cm. A global view of the CESAM burner with the chamber and sleeves can be seen in Fig. 1.3. The air flow then goes out of the chamber into the atmosphere, where a funnel leads the burnt gases into a chimney for evacuation out of the room. The orientation of the axes used in the present study is also indicated, the origin being the center of the injection point.

The flame is swirl stabilized, compact, with an inner and outer recirculation zone stabilizing it. In most regimes, it is V shaped, and starts somewhere inside the mixing tube. The exceptions are when the equivalence ratio is set too low, leading to a detached flame, and when it is too high and the flame takes a tulip shape and seems stabilized almost entirely inside the injector.

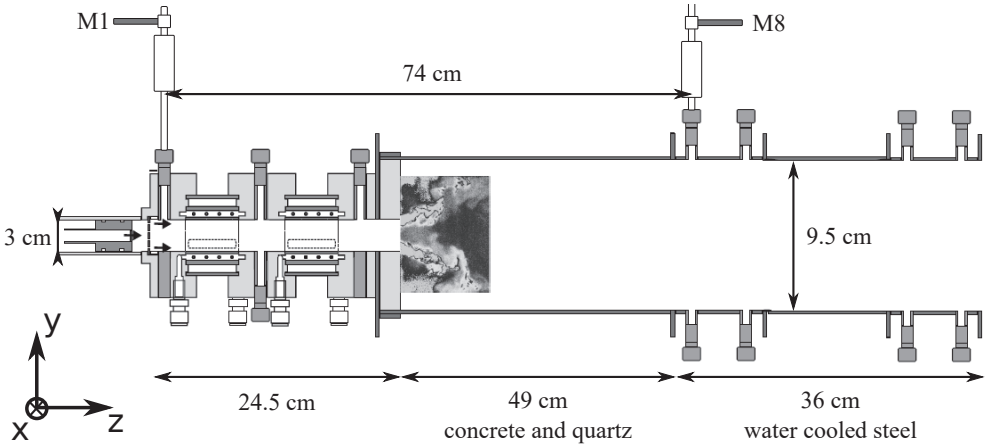

Figure 1.3: *CESAM burner. The figure shows the burner as used, with the injector, concrete chamber and three steel sleeves bolted on. The total length of the chamber is 85 cm. The axes used throughout the study are also indicated.*

1.2 Dynamic Pressure measurements

In the present study, two microphones were used in the burner. They are both 1/4 inch microphones from Bruel and Kjaer. In the injector is installed a 4136 model, and in the chamber a 4938 model (the replacement of the 4136), able to measure fluctuations in the 4 Hz to 70 kHz range. They are linked to Bruel and Kjaer type 2669 preamplifiers, and to a Bruel and Kjaer type 2690-Q54 Nexus. The microphones were calibrated using a Bruel and Kjaer model 4231 calibration system: it emits a stable signal at 1 kHz and 94 dB (a peak to peak amplitude of 1 Pa), and with a push on a button a 114 dB signal at the same frequency, allowing to check the measurement linearity.

In all measurements made in this study, a microphone is placed at the back of the injector, and will be referenced as microphone M1, and another is placed on the top port of the first sleeve at the end of the combustion chamber. It will thereafter be referenced as microphone M8. These two microphones allow to monitor the evolution of the pressure waves inside the central tube of the injector (M1) and in the chamber, far from the flame (M8). A previous, detailed study of the acoustic properties of the burner (Lamraoui (2011)) showed the global shape of the acoustic modes in the burner. Knowing the global shape of the modes, fewer microphones have been used in this study to concentrate on other diagnostics.

Since the temperature inside the chamber can be very high due to the burnt gases, the microphones have to be put on wave guides made of steel, and with a water cooling system to isolate the microphones from these high temperatures which could damage them. The wave guides are made of a straight tube, with

a socket for microphone insertion, and a double layering with a water flow for cooling. After the microphone insertion, the wave guides are attached to long tubing (several meters) to allow for dissipation of the acoustic waves without reflections. Both the metal and plastic tubes have an inner diameter of 6 mm ensuring that no reflections appear in the system due to a change in the cross section. Figure 1.4 shows the schematics of the system. Because of the necessity of using such waveguides, the microphones do not register the acoustic pressure directly at the wall, and a delay appears between the measurement by the microphone and the actual pressure fluctuation in the chamber. This delay is given by the length l_0 between the center of the chamber or injector and the microphone, and the speed of sound in the wave guide c_0, by the formula:

$$\tau_0 = \frac{l_0}{c_0} \tag{1.1}$$

The gas composition and temperature are supposed constant in the waveguide here. These propagation times are calculated for each of the microphones to take them into account, especially when comparing with signal fluctuations from other diagnostics.

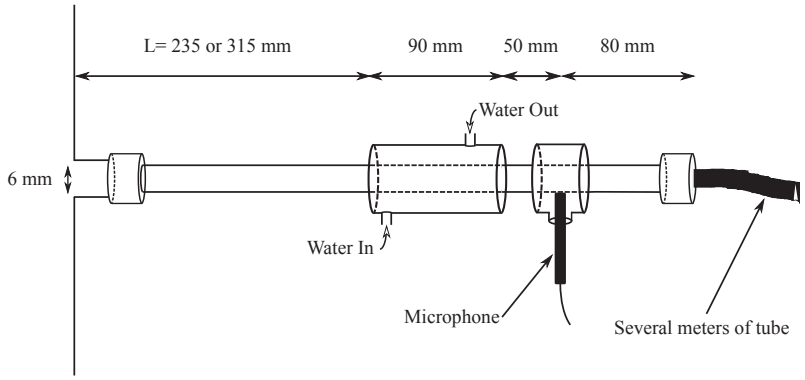

Figure 1.4: *Schematics of the type of wave guide used to plug microphones to the combustion chamber and injector. L is 23.5 cm for microphone M1 in the injector, and 32.5 cm for microphone M8 in the chamber.*

The signal obtained from microphone M1 is used as the reference signal throughout this study, to be able to make comparisons between the various diagnostics used. Usually the acquisition of the signal is done at a sampling frequency of 16384 Hz on a duration longer than 4 s (depending on the needs of the diagnostics used simultaneously, from 4 s to 64 s) to allow for a good detection of the various signals recorded simultaneously, but also to obtain a good spectral resolution when using classic spectral analysis tools such as Power Spectral Density (PSD), which uses PSD averaging to statistically converge the spectrum.

1.3 Heat release rate measurements

1.3.1 Chemiluminescence

The light emitted naturally by flames at low equivalence ratio is due to the emission of excited radicals. They are unstable intermediate products of combustion, generated at an excited state. They return to their ground state either by collision with other molecules, or by spontaneous emission of a photon following the process $D* \rightarrow D + h\nu$, with D the concerned molecule, h the Planck constant and ν the frequency of the emitted photon. As they are produced by chemical reaction, these de-excitation emissions can be used to monitor the combustion process.

In this study, the spontaneous emission by OH* radicals produced by the combustion of propane was observed using a photomultiplier. The photomultiplier was fitted with a bandpass optical filter at $\lambda = 310 \pm 30nm$, which allows the observation of the emission in several bands of OH*. The photomultiplier was placed near the focal point of a 15 cm diameter quartz lens (Melles-Griot, focal lens f=300 mm) pointed at the flame to collect the global emission of the flame.

The chemiluminescence was observed as an approximation of the instantaneous heat released by the flame, even though the quantitative information cannot be deduced from such a simple observation, as the relation between them is non trivial (Haber et al. (2001)).

1.3.2 Natural light emission recording using a high speed camera

In order to have a good understanding of the global flame dynamics, the light emitted by the flame was recorded with a high speed camera (Photron Sa-5) equipped with a 50 mm lens (Nikkon). Images taken with a filter for observing CH* radical chemiluminescence showed a very low signal. Moreover, the protective glass in front of the sensor is not transparent to UV so observation of OH* emission is not possible. The goal was to describe the global shape of the flame at a high enough frequency to capture the dynamics of the flame itself by using analysis tools such as the Dynamic Mode Decomposition (DMD). Natural light images were taken at a frequency of 7 kHz. The images are 640x600 pixels, with a pixel pitch of 178 µm/pixel in both directions. The shutter is opened for 83.35 µs, and the aperture is set at f/D=1.4.

1.3.3 Planar Laser Induced Fluorescence

Planar Laser Induced Fluorescence is a diagnostic taking advantage of the fluorescing properties of a given species when submitted to laser radiation with a specific wavelength. The laser beam is shaped through optics to generate a light sheet. The excitation wavelength is chosen so that it triggers the fluorescence in the chosen species.

In the present case, it was decided to proceed the monitoring of the OH radical. This chemical species is produced during the combustion reaction and has a fairly long life span at high temperature. This makes it a good tracer for the reaction zone and burnt gases, which are of interest in the present study since they allow to see the profile of the flame along different planes (unlike chemiluminescence which gives a line of sight integrated result), and to build a map of the fresh and burnt gases repartition.

1.3.3.1 Experimental setup

The laser used here is a dye laser, associated wih a Nd:YAG laser as the pump. The dye is rhodamine 6G diluted by methanol. This system gives pulses at a frequency of 10 Hz. The laser sheet is formed using two UV optics: a cylindrical lens, and a spherical one. The cylindrical lens (Newport CSV 025AR.10) has a focal length of -25 mm, and the spherical lens (Newport SPX 055AR.10) has a focal length of 300 mm. They generate a laser sheet 50 mm wide (the diameter of the spherical lens), with a variable thickness since there is no third lens. The thickness at the center is about 300 µm, and at distances of about 50 mm from the center, the thickness is about 900 µm.

The images are captured by a Princeton Instruments Intensified camera, equipped with a 105 mm UV lens (UV Nikkor) on which a filter is fitted. The camera is linked to the laser by its timing generator, and the delay between the reference signal from the laser and the opening of the shutter is set using the camera software (Winview). The shutter opening is set at 50 ns, making it possible to collect the fluorescence signal without any spurious spontaneous emission that would flaw the image.

Two types of profiles were registered with PLIF: axial and radial. For the axial profile, the laser sheet was generated horizontally, and then a square mirror (Newport 20SD520AL.2) was used to direct it vertically through the quartz windows in the floor and roof of the combustion chamber. The camera was then set perpendicularly to the chamber axis. In the case of the radial profiles, the laser sheet was generated directly in the proper direction, through the quartz side walls of the burner. Since the camera cannot be put perpendicularly to such a laser sheet because it would then lie in the burnt

gases, it was positioned with an angle to the sheet, and a Scheimpflug system was used to be sure that the images taken were well focused. A schematic view of the two positions is shown in figure 1.5. Image correction had to be employed on these images, and the algorithm will be described in section 1.3.3.3.

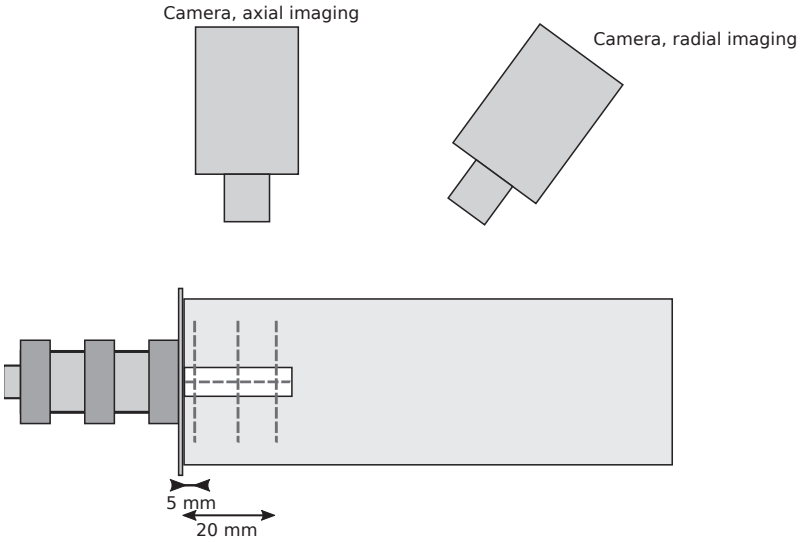

Figure 1.5: *Schematics of the setup for the two types of planes studied with PLIF, radial and axial planes. For the axial setup, the camera is perpendicular to the plane, for the radial measurements there is an angle, and the camera lens is put at the Scheimpflug angle to ensure focus on the whole field of view.*

1.3.3.2 Calibration of the laser wavelength

In order to collect a fluorescence signal from the excited OH radicals produced by the flame, the laser beam must be emitted at a particular wavelength. At the temperature range obtained in burnt gases, several options are available, and the choice is mainly oriented towards the fluorescence power obtained for a given laser power input. Since its is critical to obtain a strong fluorescence signal, a calibration of the laser is needed.

This calibration was conducted by using the laser on two different but close wavelength ranges, measuring the average registered signal output on the camera in each range, and comparing it to a theoretical spectrum obtained from simulation. The goal was to stimulate the $Q_1(6)$ transition of the (1,0) rotational band, at 282.93 nm. As it turns out that setting the laser software at the expected wavelength resulted in excitation around the $Q_1(1)$ transition at 281.91 nm, the experimental scan and simulation were conducted at these two wavelengths.

The simulation was made using the software LIFBase (Luque and Crosley (1999)), for the stimulated emission of the OH radical. The software allows to simulate spectra taking into account various parameters, the most important one in our case being the temperature, since the radical is present in hot gases. The simulation was thus conducted at several temperatures. The comparison spectra (see figure 1.6) shows the simulation results obtained for a temperature of 1700 K and atmospheric pressure, but temperatures were tested up to 2000 K, the expected adiabatic flame temperature in the present conditions. The software also allows to make a convolution to take into account the effect of the instrument, and a 0.1 nm slit function as used.

On the experimental side, an operating point corresponding to an equivalence ration of 0.82 was chosen. The laser was scanned around the two wavelengths with a 0.005 nm step. For each wavelength, 100 images were taken, and the output of the laser measured using a powermeter, since the accurate detection of fluorescence peak intensity depends on the stimulating power. The LIF intensity at each wavelength was calculated by taking the average on a 5x5 pixel zone in the center of the inner recirculation zone near the injector, where the fluorescence signal is strong.

The scanning was made as to obtain more than 5 peaks on each of the two bands, to ensure the accurate knowledge of the emission wavelength of the laser. A horizontal shift of the experimental results to best fit the simulations led to a correction of 1.1 nm of the wavelength given by the laser software. This correction was made by using the relative intensities of the spectra, from the $Q_1(1)$ and $Q_1(6)$ peaks. The results once the proper shift on the experimental data is done are shown in figure 1.6.
It is then possible to set up the laser precisely at the $Q_1(6)$ excitation wavelength, which will allow a strong fluorescence from the OH radicals.

1.3.3.3 Image correction

The PLIF images were taken in two configurations: axial and radial measurements. For the axial measurements, as the laser sheet cuts the chamber on its longitudinal symmetry axis, observation by placing the camera perpendicularly to the sheet is possible. In this configuration, no particular geometrical image correction is required. The choice was made to normalize the intensities in each image so that the minimum is set at 0 and the maximum at 60000.

For the radial measurements however, such a configuration is not possible. The camera had to be set up at an angle with the laser sheet, and thus a Scheimpflug system had to be used. This allows to have an image focused on the laser sheet, but introduces image deformations that must be corrected.

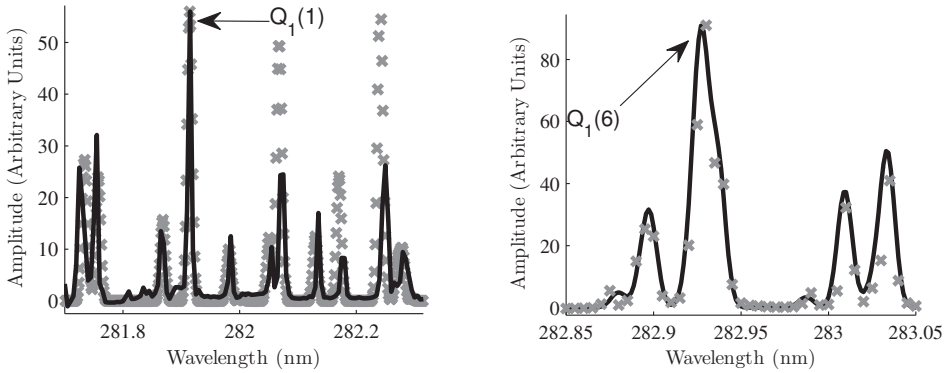

(a) Around the Q1(1) transition (b) Around the Q1(6) transition

Figure 1.6: *Measured (cross) and simulated (plain line) fluorescence spectra centered on the $Q_1(1)$ (left) and $Q_1(6)$ (right) rotational bands. The experimental spectra are obtained by averaging PLIF ouput in a small part of the IRZ over 100 images, while the simulation is done using LIFBase 2.1.1 at a temperature of 1700 K.*

The strategy for image correction is the same as in Providakis (2012). The perspective correction is made in two successive steps: first a correction of the perspective deformation, then a correction of the horizontal pixel pitch deformation.

The deformation of the perspective creates an angle β between the horizontal and lines that should be horizontal in the corrected image. This angle evolves linearly with the vertical position in the image, and so is approximated by a first order polynomial function $\tilde{\beta}$ from measurements on the calibration grid. This function gives the angle slip for each line of the image. The goal is then to obtain from the original image an intermediary image where all horizontal lines are parallel, with no deviation angle. If the original image is called A, and the image corrected in such a way is B, the relation between them is:

$$B_{i,j} = A_{\xi(i,j),j} \tag{1.2}$$

where i and j are the vertical Y and horizontal X positions respectively, and $\xi(i,j)$ is defined as:

$$\xi(i,j) = tan(\tilde{\beta}(i)) \times \delta X_j + Y_i \tag{1.3}$$

where Y_i is the i^{th} line, and δX_j is the distance between the j^{th} column and the reference column. The image B is then characterized by horizontal lines with a constant vertical pixel pitch.

The next step is the correction of the pixel pitch evolution along the horizontal axis. The pixel pitch depending linearly on the horizontal position, the pixel

pitch evolution is also computed by fitting a first order polynomial function $\tilde{g}$ to measured pixel pitch at several points along an horizontal line of B (the choice of the line doesn't matter, since all lines in the image have the same pixel pitch evolution).

If the minimum pixel pitch is noted g_0, then the algorithm used here builds an image with a constant pixel pitch g_0, resulting in a bigger image than the original if the pixel pitch variation is high.

If the relative deviation to the desired pixel pitch is noted $\tilde{g}$, it is defined as:

$$\tilde{g}'_j = \frac{|\tilde{g}_j - g_0|}{g_0}$$

It is used as a weighting factor in the creation of new columns in the final, corrected image. For an image B with N_j columns, the new number $\tilde{N}_j$ of columns is calculated from the original number N_j by using the formula:

$$\tilde{N}_j = round(N_j + N_j \times \tilde{g}_j) \tag{1.4}$$

To construct the final image C, it is then necessary to use dN_j, defined as:

$$dN_j = \tilde{N}_{j+1} - \tilde{N}_j \tag{1.5}$$

The image used here has only small variations in pixel pitch, so in this case dN_j is equal to either one or two. If its value is one, it means that the value in the new column is the same as in the original one. If, however, its value is two, this means that the corrected image C contains one more column than the original at this place. The $\tilde{N}_{j+1}$ is then the same as the $\tilde{N}_{j+1}$, and a new column whose value is the average of the two considered columns in the original image (N_j and N_{j+1}) is injected. Thus, the columns k of C are calculated by the following equations:

$$\begin{aligned} C_{i,k} &= B_{i,j} && \forall dN_j = 1 \\ C_{i,k} &= \frac{B_{i,j} + B_{i,j-1}}{2} \\ C_{i,k+1} &= B_{i,j} \end{aligned} \Bigg\} \quad \forall dN_j = 2 \tag{1.6}$$

The output of this image correction process is shown in figure 1.7, where the results obtained for an image of a grid placed 20 mm away from the injector are presented.

1.3.3.4 Fresh gas position calculation

One of the interests of PLIF in this study is the calculation of the length of fresh gases seen along the path of a laser beam. This will indeed be required,

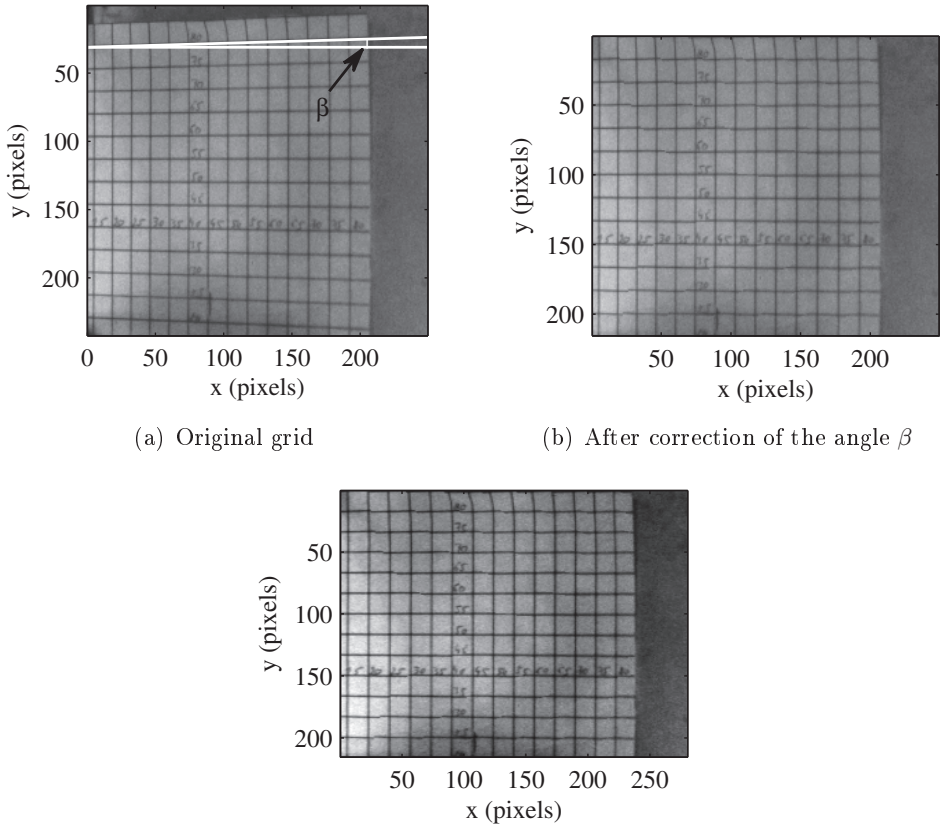

(a) Original grid

(b) After correction of the angle β

(c) Final corrected grid

Figure 1.7: *Illustration of the process of grid correction: (a) the original grid image, (b) after correction of the angular deformation of the horizontal lines, and (c) once the pixel pitch has been corrected. The grid is marked every 5 mm, from the left and bottom of the chamber.*

to be able to associate a measured absorption to an equivalence ratio (section 1.4). The OH PLIF can be used for such a measurement because of the relatively long life of OH radicals, which still exist in the burnt gases some time after their creation, and thus are expected to still be present in the inner and outer recirculation zones of the flow.

The visualization of the flow with the axial measurements allowed to see that the signal in the ORZ was very low close to the injector, that is why the equivalence ratio measurements are made 10 mm after the injection. Since the laser beams goes horizontally through the combustion chamber, the PLIF measurements to consider are radial images taken 10 mm from the injector, where the laser beam is placed. The resolution for these images, after the corrections

presented in section 1.3.3.3 are applied, is 0.37 mm/pixel vertically, and 0.40 mm/pixel horizontally. The laser beam used for absorption measurements is characterized by a diameter of 2 mm, meaning that its thickness corresponds to approximately 5 pixels.

The determination of fresh gases length was hampered by two problems. The first one is that the injector is clearly seen in all images taken, even though tests made without laser pulse during combustion or with only the laser running showed no signal. It is thus supposed that either the heated concrete is fluorescent at the considered wavelengths, or it reflects a portion of the fluorescence from OH. Either way, it introduces background noise. Tests made to try and subtract an average of that noise from PLIF images, or from an image taken without combustion at a longer exposure time showed worse results than doing nothing, so the background noise is not subtracted from the images. It was however necessary to take into account a strong gap in background signal on the right side of the images, especially since the algorithm used is based on derivatives of the signal. To do so, when computing the derivatives of the intensity in the concerned region, the average of the derivative, mainly caused by that background gap, was subtracted.

The other and main problem encountered in the treatment of the images, is the low level of the signal in the ORZ. This low level in the signal leads to difficulties localizing the boundary between the fresh gases and the ORZ, and is the main source of errors in evaluations of the length of fresh gases.

In order to measure more accurately the length of fresh gases absorbing the laser beam, a 2D algorithm can be used, since the number of lines involved is low. The algorithm makes use of a centered first order scheme of the derivative of the intensity along a line:

$$\tilde{I}'_{i,j} = \frac{\tilde{I}(y_0, j+1) - \tilde{I}(y_0, j-1)}{2} \tag{1.7}$$

with y_0 the vertical position considered, j the horizontal position in the image, $\tilde{I}$ the intensity of the image. More precisely, the relative value of this derivative compared to the value of the point considered is studied. The images are separated into their right and left part respectively to the center of the injector, and treated the same way. Starting from the center of the image, the change from the burnt gases in the IRZ, which have a very strong intensity, to the fresh gases is sought. To do so, the image is scanned until coming across a point (i_0, j_0) where:

$$\tilde{I}'/\tilde{I} \geqslant 0.8 \times \max_{i,j}(\tilde{I}'/\tilde{I}) \tag{1.8}$$

The next 3 pixels are then checked, and the one with the highest value is

selected as the transition.

The search for the outer boundary of the fresh gases is made by comparing $\tilde{I}'/\tilde{I}$ to two thresholds: a low one, set at 10 % and a high one, set at 15 %. When the high threshold is met, the next three points are checked, and the transition from fresh to burnt gases is considered found. When the low one is met, a supplementary condition is added before validating the transition: $\tilde{I}'$ must not change signs in the next two pixels. If no such point is found, the image is considered a failure and rejected.

Once an outer and inner border for fresh gases are found, a check on the remainder of the half image is made to see if there is another zone of fresh gases. This can be the case at low equivalence ratios, where the flame front can cross the line of interest several times.

Because of the low level of signal in the ORZ, the intensity of the fluorescence there can be close to the intensity levels in the fresh gases, and so the noise in the fresh gases or no strong gradient at the limit can lead to erroneous values. To try and eliminate these false results, three rejection conditions are put in place. These are:

1. The ORZ is found too close to the center of the injector to be plausible.
2. The average of $\tilde{I}$ in the ORZ is too close to the average in the fresh gases.
3. The minimal intensity in the ORZ is lower than a given threshold.

In case any of them is met, the image is rejected.

A sensitivity to the threshold values was conducted, to ensure that there is no strong dependence of the results on them. Only the low threshold value and the minimal intensity requirement have a strong impact on the average fresh gas length found on a given test run, and even then it is only a few percents while staying in reasonable values.

1.4 Equivalence ratio by fixed wavelength laser absorption

1.4.1 Principle and setup

In order to determine the equivalence ratio, one has to measure the concentration of fuel in the fresh gases. As detailed on the section on equivalence ratio measurement in the Introduction, there are broadly two types of techniques to do so: by using a probe, or by optical means. Since probes are intrusive and will thus interact with the dynamics of the flow, an optical measurement was chosen. Among the various optical measurement techniques available,

the absorption technique was adopted in this study because of its temporal resolution as well as material requirements. For more details on the various techniques and their respective advantages and drawbacks, please refer to the section about equivalence ratio measurement techniques in the Introduction. However, its use on the CESAM burner did not come without drawbacks, as will be explained in this section.

This technique is based on the absorption at certain wavelengths of molecules, and more precisely on the Beer-Lambert law. On the microscopic scale, absorption takes place when a molecules takes the energy from an impacting photon. This results at the macroscopic level in a phenomenon described in the Beer-Lambert law: if a beam of light with initial intensity I_0 propagates through a medium absorbing its photons, then the intensity after propagation through a length x (m) is given by the formula:

$$I(x) = I_0 e^{-\sum_i \sigma_i x N_i} \tag{1.9}$$

with N_i the concentration of constituting species i $(mol.m^{-3})$, and σ_i the absorption cross section of species i for the considered wavelength $(m^2.mol^{-1})$. If chosen at the right wavelength, so that only one species absorbs the light, the above expression is then simplified and allows to draw a link between the decrease of the beam intensity, and the concentration of the absorbing species.

If only one species absorbs the incident light, it is convenient to introduce the absorbance A.:

$$A(x) = -log\left(\frac{I(x)}{I_0}\right) = \sigma x N_{prop} \tag{1.10}$$

With a single absorbing species (in the present case propane), the absorption is then linearly dependent on its concentration and the length of absorption. Other factors are to be taken into account such as the determination of the absorption cross section, but since fuel is only present in fresh gases, it can be supposed that the temperature is the atmospheric temperature and the cross section is constant.

By assuming fresh gases to be at ambiant temperature and pressure, the total number of molecules in a given volume N_{tot} is calculated thanks to the perfect gas law:

$$N_{tot} = \frac{P}{RT} \tag{1.11}$$

If the absorbance is measured through a known absorption length L, the concentration of absorbing molecules in that volume can be calculated using the equation:

$$N_{prop} = \frac{A}{\sigma L} \tag{1.12}$$

It follows, from the global combustion equation of propane:

$$C_3H_8 + 5(O_2 + 3.76N_2) \longrightarrow 3CO_2 + 4H_2O + 18.8N_2 \tag{1.13}$$

that the equivalence ratio can be derived as:

$$\phi = \frac{N_{prop}}{N_{air}} \times 5 \times 4.76 = \frac{N_{prop}}{N_{tot} - N_{prop}} \times 5 \times 4.76 \tag{1.14}$$

From these formula, it can be seen that in order to measure the equivalence ratio from the absorption of fuel, one needs to know the absorption cross section of the fuel for the considered wavelength, and the length of gas which led to such an absorption. It was explained in 1.3.3.4 how the absorption length could be estimated, since propane is only present in the fresh gases, and in the next section it will be explained how the absorption cross section of propane was obtained in the present system.

The system is composed of an Helium-Neon laser emitting a continuous beam at 3.39 µm with a power of 2 mW (Thorlabs H339). This wavelength is absorbed by propane, and not by the components of air. The laser beam then passes through a toothed wheel (Thorlabs MC1000A), which allows to obtain pulses at a selectable frequency. The modulated laser obtained then goes through a beam splitter. One part goes to a Hamamatsu P4245 detector, to monitor the incoming laser power. The other half of the beam goes through the combustion chamber. It then goes through a lens made of standard glass (focal length f=500 mm). A second Hamamatsu P4245 detector is placed a bit closer than the focal length of the lens. The lens was placed there for two reasons. Firstly, it allows to concentrate the beam on a smaller size to reduce the potential effect of beam steering by the flame (since strong optical index fluctuations are to be expected when going through a turbulent flame). Secondly, the lens itself absorbs a good part of the beam power. This allows to center the detector on the beam, which otherwise is impossible since the detector saturates (this is also the case of the first detector, which is a bit decentered to avoid saturation).

It was however discovered upon analyzing the results of experiments, that using a non centered detector for evaluation of the input power was not wise. The detector signal indeed presents strong oscillations in presence of the flame, which could not be explained by light coming from it since there is a beam splitter and filter between the flame and the detector. It was thus decided to unfortunately discard the data from this detector, since it is not reliable, and only use results from the 2^{nd} detector to calculate absorption.

Since the detector gives the intensity received from a beam with variable intensity (the cutting of the laser by a spinning wheel does not give a real instantaneous pulse), it is necessary to treat the data in order to calculate the intensity

of each pulse, to compute the ratio for measuring the absorbance, and to get the equivalence ratio from these values. Moreover, as will be shown in chapter 3, the flame oscillates and the fresh gases thickness varies along a cycle at the main oscillation frequency. This means, since the ratio between absorbance and concentration of the detected species depends linearly with the length of absorption that a correction for these variations is also necessary.

1.4.2 Calculation of the equivalence ratio

As written in the previous section, the detector gives a roughly sinusoidal signal when lit by the chopped laser beam. This signal is centered around 0 V, and the amplitude of the oscillations corresponds to the impacting laser power. To obtain the pulse intensity, the data was treated as follows. Since the continuous laser beam is chopped at 3 kHz and the detector signal is acquired at 131 kHz, the theoretical length of a pulse in the signal is known. The beginning of the first pulse is the first local maximum in the acquired data. In order to determine the amplitude of each pulse, it is necessary to know the difference between the maximum and minimum of the signal in the corresponding period of the 3 kHz sinusoid. To do that, the extrema for each half-period of the sinusoid is searched, starting from the first maximum. The intensity T_2 of the laser signal for each pulse is then obtained by looking at the difference between a maximum and the following minimum. Likewise, since the pulse is not instantaneous, the time stamp for each pulse was determined as the middle time between the maximum and minimum of the signal. Figure 1.8 shows an example of signal obtained from the detector, and the amplitude obtained from it.

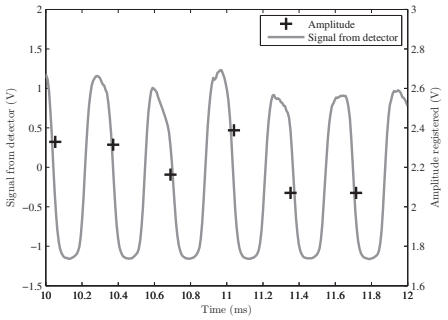

Figure 1.8: *Calculation of the laser intensity: it is the amplitude of the signal given by the detector.*

From this amplitude signal, a direct absorbance measurement can be made if a reference value is available. Throughout this study, for each measurement made with the flame, a first measurement was made without the flame (and more importantly without propane present in the chamber) to provide the background intensity. If that background intensity of the 2nd detector is noted T_{2base} (which

gives the detector output for the considered laser power without absorption), the absorbance can then be computed as:

$$A = -log\left(\frac{T_2}{T_{2base}}\right) \tag{1.15}$$

From this calculation, it follows that the final absorbance measurement is also at 3 kHz.

The next step in the calculation of the equivalence ratio, is the evaluation of the absorption cross section of propane, taking into account the errors from the measurement system. This value was obtained by the following calibration. The combustion chamber was filled with propane at various equivalence ratio values, controlled by the flowmeters. A duration of 45 s passed between the beginning of the injection and measurement, to ensure that the chamber is almost homogeneously filled with the mixture. The absorbance A is then measured, and since the length of absorption (10 cm, the width of the chamber) and concentration of propane are known, a value for the absorption cross section is obtained. The resulting calibration curve is shown in figure 1.9, with experimental points and the uncertainty on them (taken here as the standard deviation of the measurement on 4 seconds). The fitting with a least square method to a first degree polynomial function passing through (0,0) (since for no propane injection, no absorbance occurs) gives an absorption cross section of 21.9 m^2/mol. It can be compared to the value of 20.2 m^2/mol found in Klingbeil et al. (2006), using a similar He-Ne laser. Though the present value seems high, it was obtained in a less well controlled situation leading to potentially bigger errors in the measurement. Moreover, other studies tend to provide slightly higher values. For example, the value of 21.2 m^2/mol obtained with FTIR by Sharpe et al. (2004) can also be considered.
Another use of these calibration measurements is the estimation of the precision of the system. The error obtained on the calibration measurements is indicated in figure 1.10. From these results, it comes that while the standard deviation of the measured absorbance is roughly constant with the equivalence ratio, the higher the equivalence ratio used, the higher the maximum variation observed. This is to be expected, since the measurement system probably has a constant precision, but absorbance is the logarithm of that measurement. Since the absorption length without combustion is the whole width of the chamber, the absorption is much higher at the same equivalence ratio than when combustion occurs. For example, the calibration measurement with an equivalence ratio of 0.80 gives an absorbance of 3, while measurements with a flame at an 0.82 equivalence ratio leads to an absorbance around 0.3. As the maximum variation of the measured absorbance depends on its mean value, it is thus probably better to look at calibration measurements which lead to similar absorption values to measurements in combustion conditions. When considering measurement in calibration conditions, an equivalence ratio of 0.1 would be

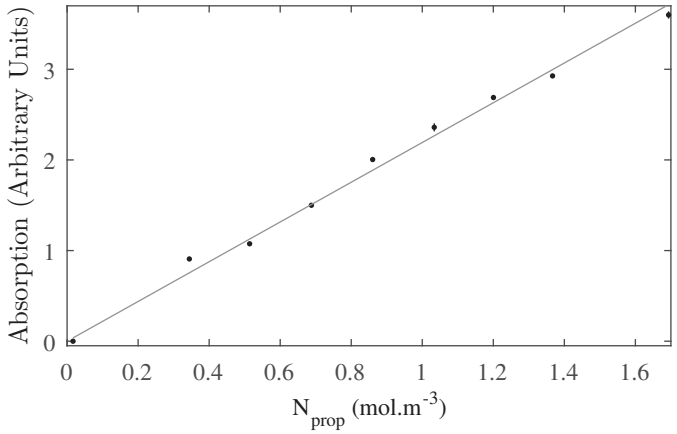

Figure 1.9: *Calibration curve of the system, obtained by filling the combustion chamber with air-propane mixture and measuring the resulting absorption. Standard deviation is given as error bars, but is almost invisible at this scale.*

giving absorbance in the same range of values as the measurements obtained in presence of a flame. Such a low equivalence ratio was not attainable due to the precision of the mass flow controllers used. Calibration measurements made without propane injection give the mean absorbance value the closest to values obtained with combustion: a standard deviation of 0.008, and an maximum error of 0.06 are then to be expected. Considering a precision of 2 standard deviations, the expected precision of absorbance measurements is thus ± 0.16 for the combustion measurements.

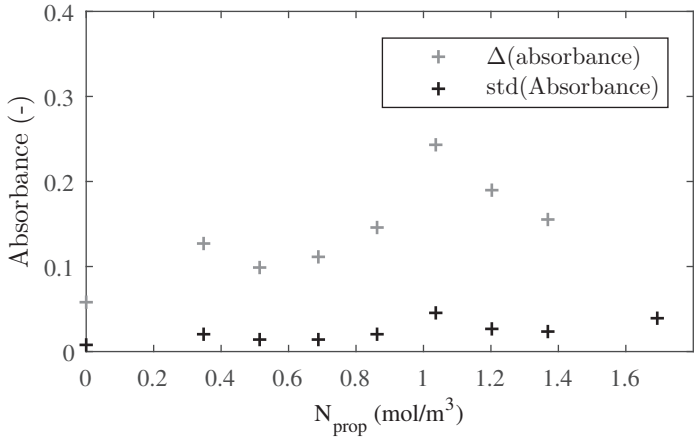

Figure 1.10: *Accuracy of the absorbance measurements obtained during calibration. The maximal error obtained on the measurements, as well as the standard deviation are given.*

1.5 Temperature measurement: Background Oriented Schlieren

1.5.1 Principle and sensitivity estimation

To confirm the presence of temperature fluctuations inside the test chamber, the Background Oriented Schlieren (BOS) method was tested for each operating condition. BOS is a method of the same family as the standard Schlieren visualization or ombroscopy. All these methods are based on the deviation of light when it travels trough a varying refractive index, and on the Gladstone-Dale equation describing the relation between optical index and density in a gas:

$$(n-1) = K(gas, \lambda)\rho \tag{1.16}$$

where K is called the Gladstone-Dale number, and is mainly dependent on the gas, depending more weakly on the wavelength of the light λ. For air, it is taken as 0.23 10^{-3} m^3/kg (value at room temperature). If the density of the gas on the light path changes, the light is deviated, following the equation:

$$\epsilon = K \int_{l_a}^{l_b} \nabla\rho ds \tag{1.17}$$

where l_a and l_b are the points of entry and exit in the volume where deviation occurs. The final deviation ϵ thus gives only an integration of the density fluctuations through the volume, and as it is linked to the derivate of density, boundary conditions are needed.

BOS allows to measure this total deviation. In the present case, the variation in density is mainly caused by variations of temperature in the burnt gases, which we try to measure. This method was chosen here because of its ease of use, even though drawbacks which will be clearly presented in section 1.5.3 will prevent us from accessing the temperature field in this particular configuration.

The principle setup is shown in figure 1.11. A screen with a random background is used as a reference image. By going through a zone (here the combustion chamber) where fluctuations of density occur, the light path is deviated, and exits the chamber with a global deviation ϵ. This means that if without deviation the point Y in the background is associated with the pixel y on the camera, it now appears on pixel $y + V$, and thus is seemingly at $Y + \Delta Y$ on the background image. The goal of the BOS is to measure this deviation V on every image acquired, and knowing by a calibration what ΔY corresponds to it, to calculate the global deviation ϵ. The measurements of this deviation V is made using a software initially developed for PIV measurement, since

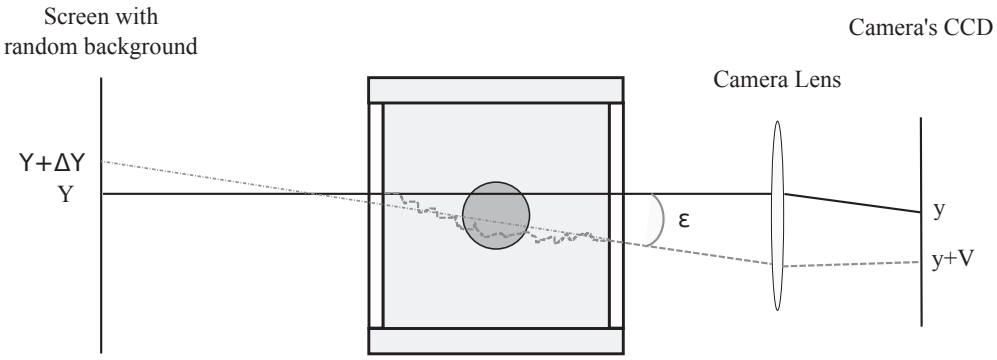

Figure 1.11: *Illustration of the principle of Background Oriented Schlieren.*

the principle is the same: finding the displacement between subsets of a given image.

In order to install a BOS setup, several quantities must be specified. Below is a list of variables that may be adapted, or imposed by the studied flow, the equipment and the room available. The main factors are:

- The minimum deviation ϵ expected in the studied flow.
- The half size of the flow to be visualized Y_{flow}, in mm
- The half size of the screen used Y_{screen}
- The corresponding half size of the image of the screen on the camera y_{screen}
- The pixel size of the camera y_{pix}
- The focal of the lens used f
- The distance X_{back} from the background to the flow
- The distance X_{cam} from the flow to the camera lens

From these parameters, the angular magnification of the system is estimated first:

$$Mag = Y_{screen}/y_{screen} = \frac{X_{back} + X_{cam}}{f} \tag{1.18}$$

The deviation angle corresponding to a given displacement V on the camera can also be calculated. Since this angle is small, it is:

$$\epsilon = \frac{\Delta Y}{X_{back}} = \frac{Mag \times V}{X_{back}} = \frac{X_{back} + X_{cam}}{X_{back} f} V \tag{1.19}$$

A last equation comes from the field of view that should be obtained (ie the screen should cover the entire flow):

$$\frac{Y_{flow}}{X_{cam}} = \frac{Y_{screen}}{X_{cam} + X_{back}} \tag{1.20}$$

The hard constraint in practice will however usually come from the size of the

CCD of the camera, so by re-injecting the magnification relation and rearranging the terms, we obtain:

$$\frac{Y_{flow}}{y_{screen}} = \frac{X_{cam}}{f} \tag{1.21}$$

The two relations 1.19 and 1.21 give the constraints on the system. For a given sensitivity and field of view of the system, once the camera is chosen (and therefore the size y_{CCD} of the sensor, the maximal value for y_{screen}), the remaining variables are f, Z_{back} and Z_{cam}. To obtain a better sensitivity it is best to:

- Use a lens with a long focal length to keep the assumption of parallel rays
- Have a long distance between the flow and the background screen
- Have a short distance between the flow and the camera

The final choice will mainly depend on other constraints, such as the space available near the flow (limiting Z_{back} and Z_{cam}), the necessity to keep the camera away from the flame, etc.

1.5.2 Setup used

Considering the previous explanations on the sensitivity of the system, the setup used in this study is now described.

The background for the identification of the deviations was obtained by using a random pattern printed in A4 format. This pattern was created by generating an artificial Mie image using PIVLab. In order to see it clearly, a LED projector (Nila Boxer) with an affixed sheet of tracing paper for better lightning homogeneity was used to light it up by transparency. The screen was placed 715 mm ahead of the center of the combustion chamber. On the other side of the test chamber, a Photron SA-5 camera was setup, with the lens set at 530 mm from the center of the combustion chamber. It was outfitted with a red LEE filter in order to reduce the range of wavelength observed (and ensure a constant Gladstone-Dale number from the light received). The lens used was a Nikkon 105 mm UV Nikkor, which was the longest focal available allowing to observe the entire chamber (100 mm high) considering the dimension restrictions imposed by the size of the experiment room.

The photron SA-5 has a 1024x1024 pixels detector, each pixel being 20x20 µm. The sensitivity of the system can then be estimated, using equation 1.19. To find the displacement in each image, the commercially available software Dynamic Studio by Dantec was used. The modern algorithms it uses allow to detect reliably even subpixel displacements in an image, ideally up to a tenth of a pixel. By considering a capacity to reliably detect variations of 0.2 pixels,

the sensitivity of the setup setup is then:

$$\epsilon = \frac{Z_{back} + Z_{cam}}{Z_{back} f} y_{pix} = 14 \quad arcsec \qquad (1 \quad arcsec = 4.848 \mu rad) \quad (1.22)$$

1.5.3 Limitations of the technique on this burner

As explained in section 1.5.1, the BOS measures the deviation of a beam of light traversing a field with density fluctuations. The precision of the measurements depends on the capacity of the available setup to detect precise fluctuations in these deviations. However, the main drawback is obvious from looking at figure 1.11: the system detects the deviation resulting from any fluctuation throughout all the space between the screen and the camera. This means that in the present case, the results of the total deviation from the whole chamber will be captured. In order to be able to accurately measure the fluctuations in space, a setup with several cameras would be necessary, as was explored in the thesis work of Todoroff (2013), to obtain several simultaneous fields of view and be able to reconstruct the light space. Without these multiple cameras, only qualitative results can be achieved, especially in turbulent flows.

The other limitation faced here comes from equation 1.17, linking the measured deviation to the actual density fluctuation field (and thus temperature fluctuations). In order to solve this equation, ideally the actual path of the light beam has to be known, as mentioned before. Still, assumptions on the geometry of the flow can simplify the expression. However, boundary conditions on the temperature or density are needed to solve this equation, which we do not have access to here (in particular the wall temperature).

The last limitation of the system is the overall sensitivity: fluctuations of a few Kelvin in a hot flow must be detected, and thus high sensitivity is required. As will be shown in the section devoted to the results in chapters 2 and 3, the deviations in pixels observed on the camera are weak on a great part of the images, and the averaged fluctuations obtained are sub-pixel. The measurements are thus only indicative of the presence of fluctuations, without allowing measurement of their amplitude.

1.6 Summary: diagnostics used

As a conclusion, the various diagnostics used are summed up. The acoustic pressure is available in two points: at the bottom of the injector tube, and 50 cm away from the injector in the combustion chamber. The natural emission of the flame was observed using a high speed camera, with a broad field of view. A series of axial and radial OH-PLIF measurement campaigns at a low repetition rate (10 Hz) was conducted, and an observation of the fluctuations of

density in the burnt gases was conducted using Background Oriented Schlieren. Lastly, the absorption of an IR laser sensitive to the presence of CH bonds was measured 10 mm away from the injector at 3 kHz.
The fields of view of all the diagnostics used in this thesis are given in figure 1.12. The image shown is the average flame obtained from the raw chemiluminescence images at an equivalence ratio ϕ=0.82. All the PLIF setups are given, with the radial ones essentially covering the entire width of the combustion chamber. The circle for the absorption measurement has a diameter of 2 mm (the $1/e^2$ diameter of the laser used).

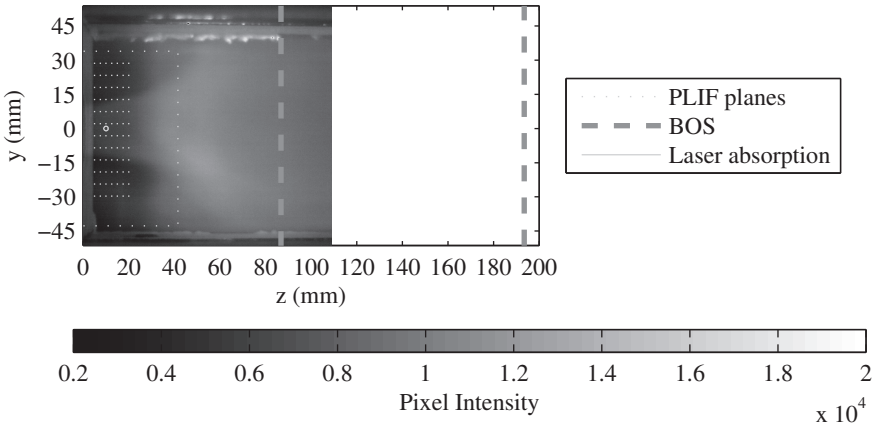

Figure 1.12: *The field of view of the various diagnostics used.*

After presenting in details all measurement and their limitation, one will first present results of the flame from a statistical point of view.

Chapter 2

General analysis of the flame: statistical results

In this chapter, the results are analyzed from a statistical point of view. The various techniques used are classical, and have been described in chapter 1. First, the global temperature evolution of the burner while in use is shown, to explain the timing protocol of the measurements. As will be shown in a second step, the observation of the power spectral density of the acoustic pressure signal in the injector and chamber allows to monitor the instabilities present in various injection conditions, and from these early results a set of conditions to be studied in detail is chosen. In a third section, the calculations on the heat release rate as well as the broadband emissions from the flame confirm that its global dynamics are the same as the acoustics. The average shape of the flame, obtained from high speed imaging, is then shown. Lastly, results linked to laser absorption, available without further post-processing, and the average results of Background Oriented Schlieren, which shows clearly the thermal boundary layer, are presented for the three selected operating conditions.

2.1 Temperature evolution of the bench

Since the CESAM burner is not water-cooled, it is important to determine if the burner is able to reach a thermal equilibrium when operated. Indeed, the heat release by the flame leads to a change of temperature of the walls, which could have an impact on the dynamics of the flame in the burner. It is thus important to know if waiting for the burner to preheat can lead to stable thermal conditions, which would allow to eliminate the influence of that parameter.

As described in chapter 1, the horizontal walls of the burner are made of concrete, while the vertical ones are quartz windows. In order to have an idea of the evolution of the temperature around the walls, a set of concrete walls

different from the ones of the remainder of the study was used. These don't include the quartz windows used elsewhere, and the top wall is pierced by three holes which allow to attach microphones or, in this case, thermocouples. In order to make the measurements, a K-type thermocouple was inserted in the closest port from the injector, which is near the place where the flame is closest to the walls. The thermocouple was held about 1 mm inwards from the wall to try to prevent the measurement of the burnt gas temperature. The temperature obtained in such a manner is of course only a very approximate estimation of the wall temperature, but should allow to draw conclusions on the thermal evolution of the chamber. Measurements were made by starting the cold chamber, and letting it run at an equivalence ratio of 0.82, with $\alpha = 50\%$ and a total airflow of 7.6 g/s, for up to 17 minutes. By that time the radiations emitted by the concrete walls and time needed to cool down the chamber would make measurements with longer time periods impractical.

A typical temperature curve obtained during these tests is shown in figure 2.1. It shows that after ignition (adjusted at t=0 s) the temperature rises sharply. Once the mass flows are stabilized, it continues to rise, though at lower rates. From stabilization until a time of about 5 minutes after it, the increase can be approximated as linear, with a rate of about 0.8 °C/s. This means that in order to consider temperatures to be almost constant, there is a time duration limit for the measurements.

Another point to take into account is the presence of radiation from the refractory concrete, and possibly from burning dust from the concrete itself, leading to a bright orange light in the burner after some time. The evolution of the luminosity of the chamber as seen with the eye is presented in figure 2.2. This puts another limitation when using optical techniques.

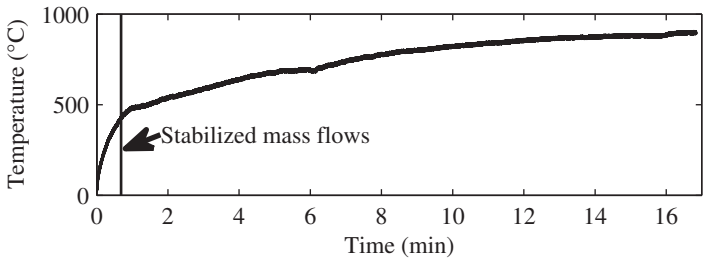

Figure 2.1: *Temperature measured after ignition. The line marks the point at which mass flows are stabilized at their nominal values.*

Because of the limitations on the temperature variations, and to minimize the apparition of light from the concrete walls, it was determined that the timing

(a) t=1min 30s (b) t=5min 30s (c) 10 min (d) 13 min

Figure 2.2: *Photos of the flame at different times after ignition, showing the evolution of illumination. Aperture time: 1/17 s for the first three photos, and 1/20 s for the last one.*

Ignition	t = 0 s
Minimum beginning time for measurements	t = 45 s
Maximum end time of test run	t = 2 min
Waiting time between two runs	30 min

Table 2.1: *Timing of measurements.*

proposed in table 2.1 for the measurements would be a good compromise. Since the longest measurements made had a duration of 64 s, such a timing can be respected. The shorter measurements were made between 45 s and 55 s after ignition, depending on the test conditions (45 s for an equivalence ratio of 0.94, and 55 s for an equivalence ratio of 0.74). Taking into account the growth rate of temperature obtained before, this leads to a difference of about 60 K between the beginning and the end of the measurement, which would correspond to a variation of about 8 % of the expected mean temperature of 800 K during the test run.

The chamber was systematically cooled down by maintaining the cold air flow for about 30 minutes between two consecutive test runs. This is shorter than the time needed to completely cool down the walls (this takes more than one hour), but should be enough to ensure an acceptable variation in the expected mean wall temperature.

2.2 Acoustic response to various experimental conditions

2.2.1 Evolution of the pressure fluctuations with global mass flow

The first global parameter that can be used on the burner is the global air flow. This is also one of the most important, since it imposes the frequency of the potential structures created by the swirling flow. Moreover, since at a given equivalence ratio it dictates the fuel injection rate, it also influences the global

heat release of the system. Most of the previous studies on the system used an air mass flow rate of 14.75±0.05 g/s (Dioc (2005); Tran (2009); Lamraoui (2011)). However, such a high mass flow rate presents several drawbacks for our study, as developed below.

First, since the burner is not cooled, the higher the heat released, the shorter the time available to make measurements before having to shut down for safety reasons. This is most inconvenient when using low frequency diagnostics, which require longer times to obtain a significant number of measurement points. This will be further expanded upon in the next section.

Secondly, the previous study on the CESAM burner (Lamraoui (2011); Lamraoui et al. (2011)) showed that, for the equivalence ratios associated with combustion instability and for this configuration of the chamber, the pressure signal exhibits several simultaneous acoustic peaks, due to a strong decoupling between the injector tube and the combustion chamber itself. This case would prove interesting but complicated to study in a first approach, especially when using phase averaging to reconstruct modes.

Lastly, the chamber cannot directly be lit at such a high mass flow rate. This introduces another uncertainty on the measurements, due to the path used to go from the ignition air flow rate of 7.6 g/s to the final flow rate. The flame may indeed be sensitive to the path chosen to go from one point to the other.

In order to limit these uncertainties, maximize the available measurement time and generate a set of conditions where only one strong mode is present, this study focuses on a 7.6 g/s air mass flow. However, tests were made at other mass flow rate to illustrate the transition from one single mode (presumably a combination of the longitudinal acoustic modes from the chamber and injector) to two strongly separated modes. The sound pressure levels (SPL) measured by the microphone inside the injector are presented in figure 2.3. The equivalence ratio changes slightly from one mass flow rate to the other (from 0.84 to 0.86), as the injection of propane and air on both stages was modified, while the axial injection was kept constant at 0.41 g/s. The study from Lamraoui (2011) at the same high mass flow rate and slightly lower equivalence ratio of 0.83 showed no strong difference in the structure of the pressure spectrum obtained; only the relative height of the main peaks was different. The figure allows to see that even though the equivalence ratio is almost the same, the global shape of the pressure spectrum changes dramatically when doubling the mass flow rate, resulting at high power in two peaks simultaneously present while only one appears at lower mass flow rates.

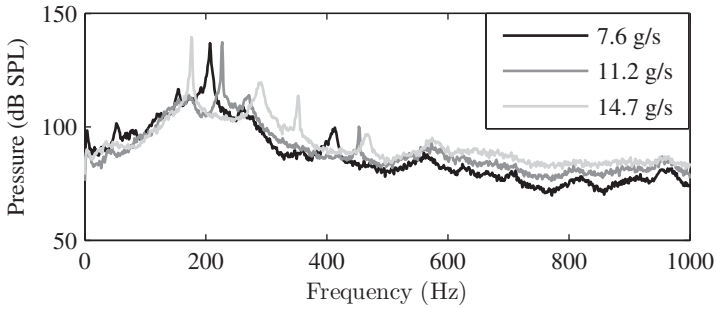

Figure 2.3: *Pressure spectrum (in dB SPL) for the microphone M1 in the injector, at various air mass flow rates for* $\phi = 0.84 - 0.86$.

2.2.2 Evolution of the pressure fluctuations with the staging of the propane injection

One of the parameters that can enter into play in the CESAM burner, is the staging of the fuel injection. As a reminder, it is defined here as (Barbosa et al. (2009)):

$$\alpha = \frac{\dot{m}_{stage1}}{\dot{m}_{stage1} + \dot{m}_{stage2}}$$

Since there is only limited premixing before the injection in the central tube for each stage, there should be two effects of the staging. The first one is the homogeneity of the mixture: a high α means most of the propane is injected far upstream inside the injector, giving more time to air and propane to mix. The second effect is linked to the first one: at high α, the local equivalence ratio being higher on the axis of the injector, this potentially allows the flame to stabilize further inside the injector itself.

In order to study the influence of that parameter on the acoustic modes, variations of the staging factor were made at an equivalence ratio of 0.82 and air mass flow rate of 7.6 g/s which (as the next section will show) is around the middle of the usable range of equivalence ratios for this particular air mass flow rate. The staging parameter α was varied between 35 %, and 55 % by steps of 5 %. The 30 % point is very unstable, the flame is visibly pulsated with successive extinctions and re-ignitions a few times a second. On the opposite, at $\alpha = 60\%$, the flame changes shapes to become a conical flame, which is much more stable and probably stabilized further inside the injection tube. The pressure spectrum (in dB SPL) of the signal from microphone M1 for these operating points is shown in figure 2.4. The data acquisition was made at a frequency of 16 kHz, and the Welch method is used. The segments are overlapping by 50 % and their length is chosen so that the spectral resolution

is 1 Hz. Between $\alpha = 35\%$ and $\alpha = 50\%$, a single main mode is obtained with a frequency that increases with the staging. However, further increasing α, the mode goes back to a lower frequency, and is much lower.

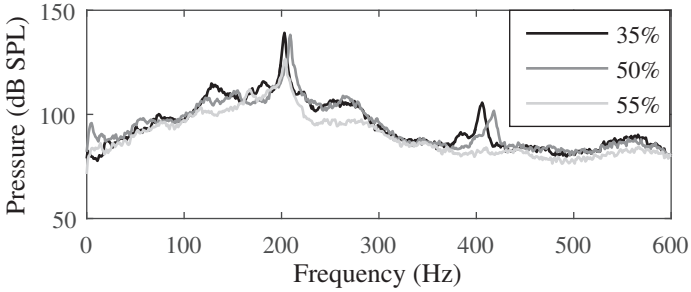

Figure 2.4: *Pressure spectrum (in dB SPL) for the microphone M1 in the injector, at various staging parameters for* $\phi = 0.82$.

This study of the effect of staging shows that it has an influence on the frequency of the main mode obtained within the injector and the chamber, and that the operability range is between 35 % and 55 % for the mass flow rates considered. This is why, for the rest of the study, a setting of $\alpha = 50\%$ was chosen: it is roughly in the middle of that operability range and exhibits a strong acoustic instability.

2.2.3 Evolution of the pressure fluctuations with the equivalence ratio

The main parameter varied in this study was the global equivalence ratio. As stated in section 2.2.2, the staging of the burner is set at 50 %. A series of measurements was made between the two extremes of the operability range of the burner. The lower bound is $\phi = 0.7$, for which the flame is totally lifted away from the injector, and the higher bound is around $\phi = 1$, for which the flame transitions to a tulip shape and seems to stabilize much further inside the injector. The power spectral density of microphone M1 (in dB) for some of the points measured, with the same calculation parameters as previously is shown in figure 2.5. They show a tendency that goes in two steps: for an equivalence ratio $\phi < 0.82$, the frequency of the main mode rises with ϕ, going from 170 Hz to 212 Hz, at a similar amplitude (the figure shows variations between 135 dB and 138 dB, but variations of up to 2 dB in amplitude were observed between measurements at the same settings). Then, for equivalence ratios $\phi > 0.82$, the frequency of the main mode is a constant, but its amplitude decreases when ϕ increases.

The evolution of the pressure fluctuations on more injection conditions is pre-

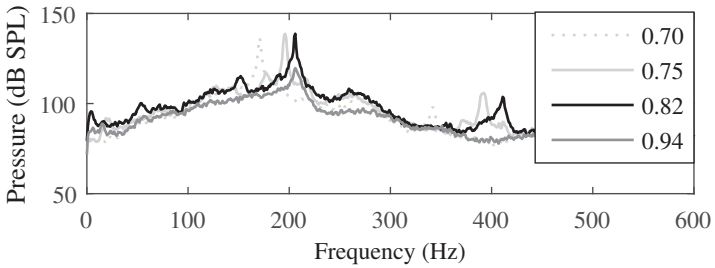

Figure 2.5: *Pressure spectrum (in dB SPL) for the microphone M1 in the injector, at various equivalence ratios for* $\alpha = 50\%$.

sented in figure 2.6, showing more precisely this double evolution. Two different data set were recorded. The Sound Pressure Level is computed directly from the root mean square of the pressure signal in the injector (and not frequency by frequency as the PSD does), and confirms that the transition from a stable amplitude to a decreasing one occurs when the equivalence ratio reaches values around 0.82-0.83. This change in the amplitude evolution is also accompanied by a change in the frequency of the main peak clearly visible on the PSD of the signals (as shown in figure 2.5): the frequency first rises with the equivalence ratio used, and when reaching equivalence ratio values above 0.8 stabilizes around 210 Hz.

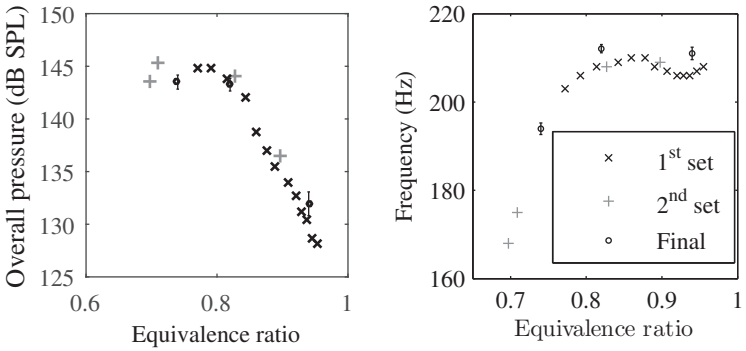

(a) SPL for M1 (b) Peak Frequency

Figure 2.6: *Overall Sound Pressure Level for microphone M1 and frequency of the peak found on the PSD measured in the injector, during two explorations of the usable domain of the burner for* $\alpha = 50\%$. *The subsequent experiment results are also shown, with the standard deviation as error bar.*

This is accompanied with a change in the shape of the flame: it is a V flame for all points considered stable, but the angle closes when ϕ rises, up to the point where the flame becomes a conical flame.

Because of the transitions described here, the following choice was made for

Equivalence ratio	0.74	0.82	0.94
Fuel mass flow (g/s)	0.36	0.40	0.45
Air mass flow (g/s)	7.6	7.6	7.6
Power (kW)	16.6	18.4	21

Table 2.2: *Chosen operating conditions, α=50% for all cases.*

the three points to be studied in detail: the first point at $\phi = 0.74$ is low, but far enough from the lift-off limit that it cannot happen accidentally. The point at $\phi = 0.82$ is at the transition between a change of frequency and a change in amplitude for the main mode, and the point at $\phi = 0.94$ is high, but still far enough from the upper limit to prevent accidental transition during a run. The settings for the three operating points are detailed in table 2.2

As the three points that will be studied further are chosen, a first look at the pressure signal in the injector and the chamber is interesting. As seen in the previous figures, the pressure in the injector is of similar spectral shape at equivalence ratios 0.74 and 0.82. The pattern of peaks seems to be reduced and lost in the broadband signal between equivalence ratios 0.82 and 0.94. The respective sound pressure levels in the injector and the chamber for the three injection conditions are shown in figure 2.7. The spectra for both microphones seem broadly similar, with the main difference being a lower amplitude in the chamber.

As the pressure signals present only one big peak in their spectra at the same frequency, a global way of evaluating the phase delay between them is to use the cross spectral density of the two pressure signals. It was then found that for the equivalence ratio of 0.74, the resulting phase shift is of -35°±3°. At the equivalence ratio 0.82, this phase shift is increased to -63°±3°, and decreases back at the equivalence ratio of 0.94, to a value of -45°±3°.

Lastly, it can be interesting to look at the relative amplitude of the fluctuations in the injector and chamber, taking into account the phase shift between the two. The ratios obtained for the main instability mode are showed in table 2.3. It shows that in the three cases, the injector sees the most important fluctuations, as the pressure ratio is less than 0.21 in all cases. The phase relative amplitude of the modes starts at 0.21 for ϕ=0.74, is reduced to 0.12 for ϕ=0.82, and then increases again to 0.18. This variation however is almost entirely explained by the variations in the phase shift between the pressure fluctuations in the injector and chamber: its values are 35°, 63° and 45° respectively. This means that the ratio of the amplitudes stays almost constant at the three studied injection conditions, but the phase shift varies significantly.

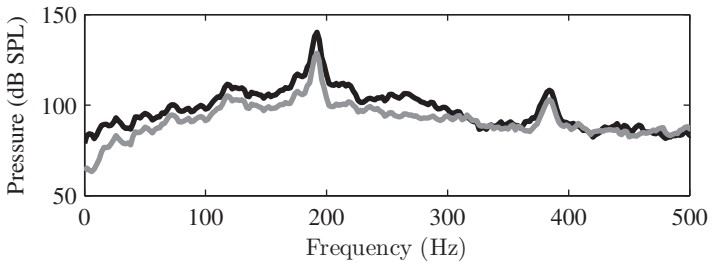

(a) $\phi = 0.74$

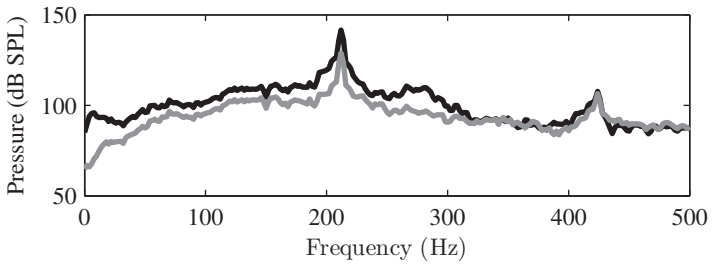

(b) $\phi = 0.82$

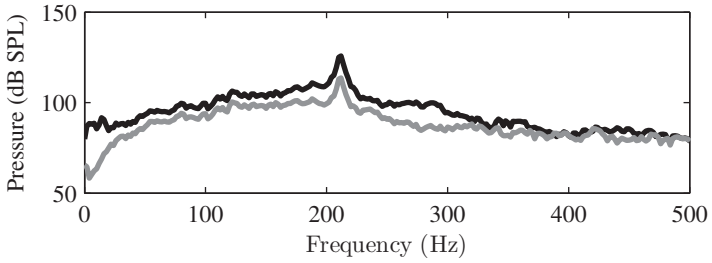

(c) $\phi = 0.94$

Figure 2.7: *Power spectrum of the microphones in the injector (M1, in black) and in the chamber (M8, in gray) for the three equivalence ratio studied.*

2.3 Recording of heat release rate evolution

As described in chapter 1, the heat release rate can be linked to the spontaneous light emissions of excited radicals created by the flame. The photomultiplier used here records the spontaneous emission from the OH* radical, and is expected to present an evolution similar to the heat release rate.

In parallel, a high speed camera was also used to record the flame at a frequency of 7 kHz. To tackle low intensity issues, no interferential filter was

Equivalence ratio	0.74	0.82	0.94
θ (°)	35 °	63 °	45 °
$\frac{\lvert P(M_{chamber})\rvert cos(\theta)}{\lvert P(M_{injector})\rvert}$	0.21	0.12	0.18

Table 2.3: *Ratios of pressure fluctuations amplitudes in the chamber and injector, taking into account the phase difference θ.*

put in front of the objective. Thus, a first task is to confirm whether or not the images from the high speed camera can be assumed to qualitatively represent the evolution of the heat release rate, or only the global shape of the flame.

In order to compare the results from the two systems, two steps are taken. First, the signals from the microphone and photomultiplier are re-sampled down from their original 16 kHz acquisition rate to the 7 kHz acquisition rate of the camera, at the same time stamps. Secondly, a virtual photomultiplier is made by taking the average pixel value on a given region of interest on each image. The selected region for the three equivalence ratios studied is indicated in figure 2.8, and the average flame image is also shown for each case. This region was selected as it covers most of the flame's natural light, while minimizing the influence of light from the heated walls (and more precisely, the insulation fiber used between the concrete and quartz windows). The region also does not extend much in the axial direction to limit the influence of possible soot (more likely in the near stoichiometric case).

The coherence values between the re-sampled signal of the microphone M8 installed in the combustion chamber and the virtual photomultiplier, as well as between the same microphone signal and the re-sampled photomultiplier output are presented in figure 2.9. This coherence between signals was computed using Matlab's mscohere function, and is thus the magnitude squared coherence. More precisely, it is defined for two signals x and y, as:

$$C_{xy}(f) = \frac{|P_{xy}(f)|^2}{P_{xx}(f)P_{yy}(f)} \tag{2.1}$$

with $P_{xx}(f), P_{yy}(f)$ are the power spectral densities of the signals, and $P_{xy}(f)$ the cross power spectral density, all computed using Welch's averaged periodogram method.

The heat release rate inferred from the photomultiplier shows an evolution consistent with the pressure signals recorded inside the chamber: the coherence between the two signals in the 0-1000 Hz range is good, for each of the three injection conditions used. However, the same cannot be said for the camera images. Although the peak associated with the main spectral contribution is visible and has good coherence with the acoustic pressure in the chamber,

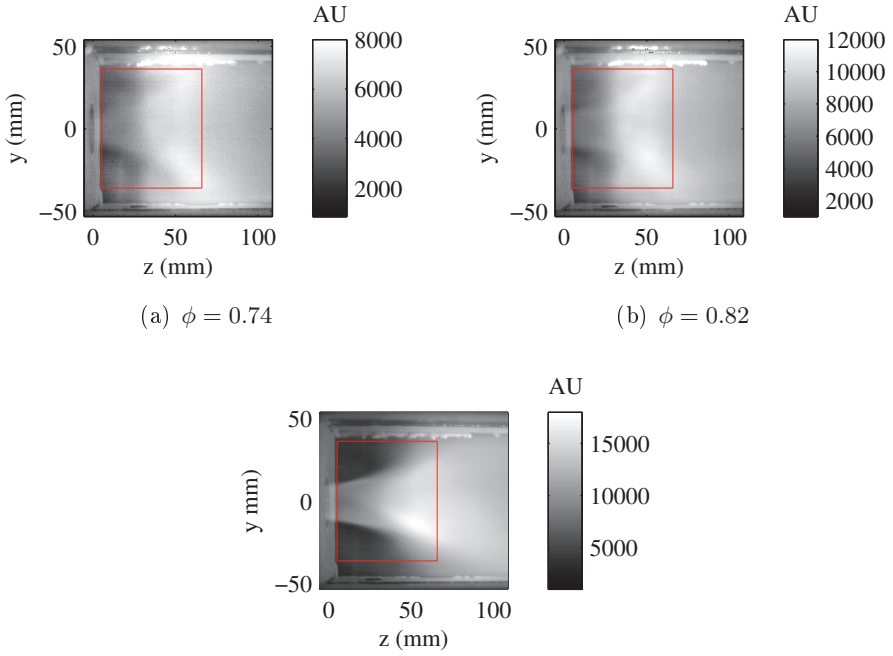

(a) $\phi = 0.74$ (b) $\phi = 0.82$

(c) $\phi = 0.94$

Figure 2.8: *Region of interest used to compute a virtual photomultiplier signal from the camera images for each equivalence ratio. The mean flame image is also shown for reference.*

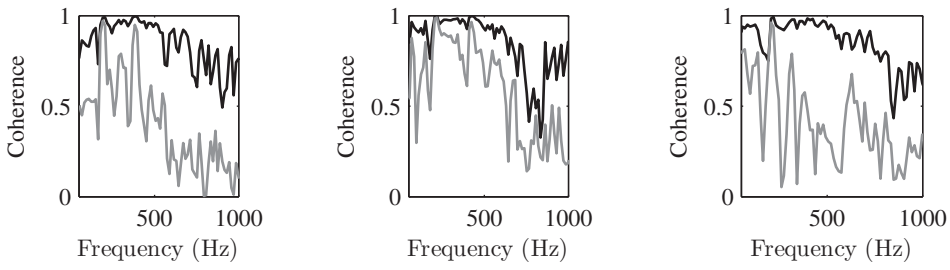

(a) $\phi = 0.74$ (b) $\phi = 0.82$ (c) $\phi = 0.94$

Figure 2.9: *Coherence between the microphone in the chamber and the PMT signal (in black), as well as with a virtual PMT (in gray) created by averaging the pixel value on part of the high speed camera images. Microphone and PMT values down-sampled at 7 kHz.*

outside this range the coherence is fairly low. This means that unfortunately, the camera signal cannot be used to reliably describe the heat release rate obtained from OH* radical emissions. This is a surprising result that may be due to constraints in the camera sensor itself. More probably, it may be due to the fact that in absence of a filter in front of the camera, the contributions due to other sources of light add different components that are not directly correlated to the heat release rate or pressure fluctuations inside the chamber.

In the following, the PMT signal will only be used when heat release rate evolutions are necessary.

2.4 Average shape of the flame

Since in the CESAM burner the combustion tends to occur at the inner interface of the fresh and burnt gases, most of the OH radicals production occurs there, and the PLIF allows to easily monitor the Inner Recirculation Zone in the system. This is a good indicator of the flame shape, and can be compared to the global images taken by the high speed camera, even though the low repetition rate of the PLIF (10 Hz) only allows to use mean and phase averaged images in this case.

The mean axial PLIF image is shown in figure 2.10, without any binarization. As the laser power on each shot as well as the repartition of the power inside the sheet were not monitored, amplitudes have to be taken as a qualitative indication only. This mean image shows that for the three injection conditions studied here, the average shape of the flame changes: the higher the equivalence ratio used, the lower the angle of the flame. This is partly due, as will be shown in the next chapter, to strong pulsations of the flame in the first two cases, that are not as large for the highest equivalence ratio.

The mean profiles taken at various distances from the injector are shown in figure 2.11. Note that there was no correction for the light intensity fluctuations of the laser. Indeed, the intensity for most of these radial profiles is higher in the bottom region compared to the upper one. From these profiles, it seems that the IRZ is broadly circular for equivalence ratios of 0.74 and 0.82 near the injector, and flattens in the vertical direction at longer distances. However, as will be shown in the next section, instantaneous images do not show this circular feature. In the case of the equivalence ratio of 0.94, the shape seems circular too, with some inwards part on both sides. The position of these two features seems to shift with the distance. It occurs in a clockwise direction on the images, which is incidentally the rotating direction of the swirling flow. As will be showed in the next chapter, this property is also found in the mean instability cycle for this particular case.

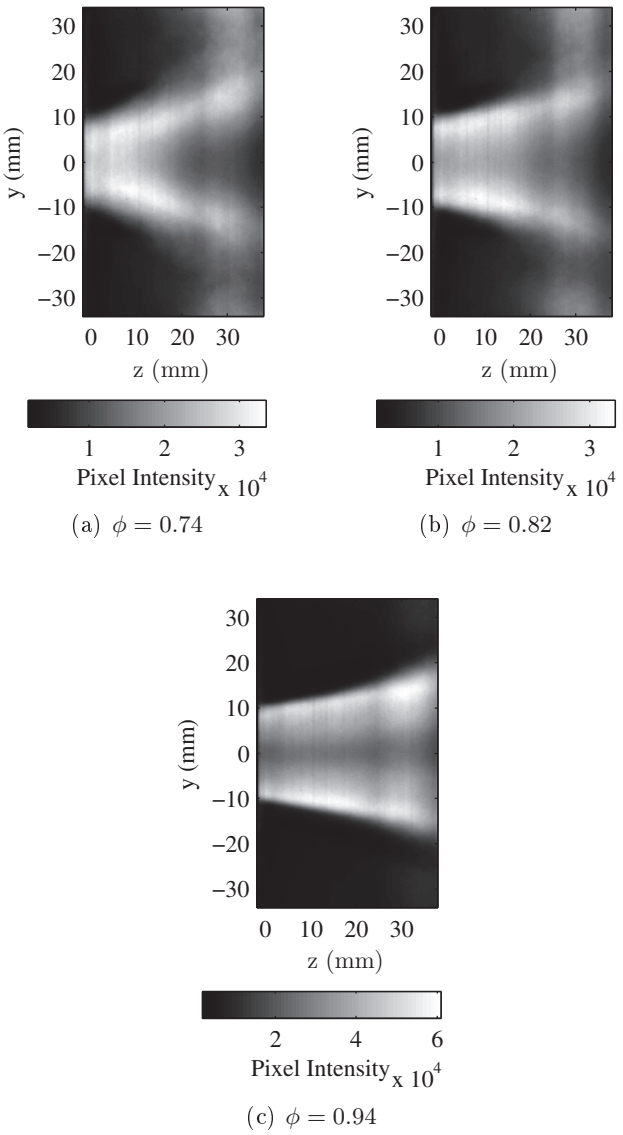

(a) $\phi = 0.74$ (b) $\phi = 0.82$

(c) $\phi = 0.94$

Figure 2.10: *Average image of axial PLIF for each equivalence ratio studied. The flame angle reduction is slightly visible, but the axial length is too short to see it properly.*

The global change in average shape of the flame is even more visible on the direct flame imaging from the high speed camera, because its field of view is larger (figure 2.12). In these images, the first two cases seem almost identical in shape, which was not the case when analyzing the IRZ profile. The total flame light emission seems to be the main difference between them. For ϕ=0.94, the flame clearly shows a lower spread angle. The presence of a light x shaped feature in the middle of the flame is also remarkable. This change of light in the average shape of the flame can be explained by noting the particular shape of the IRZ at these conditions (see figure 2.11). Considering that the flame is shaped as the inner recirculation zone, then at the points where the IRZ goes inwards, the line of sight integration from the camera's axis is expected to be stronger.

2.5 Measuring the equivalence ratio and temperature fluctuations

2.5.1 Equivalence ratio

As exposed in chapter 1, the diagnostic used to measure equivalence ratio during operation is based on the principle of absorption. The primary output signal of the system gives the absorption of the infrared laser, which can then be converted into equivalence ratio if the length of mixture crossed by the laser beam is known. As each step of the process has its own uncertainties and could lead to loss of information, it can first be interesting to look at the dynamics of the absorption of the laser.

Since the laser is chopped at a rate of 3 kHz, the temporal resolution of the absorbance measurement is high enough to describe properly the dynamics in the 0-1 kHz range which is the main focus here. The PSD of the absorbance, shown in the figure 2.13, presents a peak at the frequency of the main acoustic instability, accompanied by a weaker peak at double that frequency. This peak at double frequency is also weakly visible at the equivalence ratio of 0.94, while it does not appear on the microphone signals. Its absence in the acoustic pressure signal at the high equivalence ratio could be simply due to the fact that it is drowned out in the broadband noise.

The absorbance signal itself, unfortunately, is very noisy. Fluctuations are due to equivalence ratio variations, but also to any modification of the flame shape, which may vary a lot between two measurements. Therefore, when analyzing the correlation using the coherence (as defined in equation 2.1) with the microphone in the injector, presented in figure 2.14, one can see that the only strong coherence (close to 1) is obtained at the frequency of

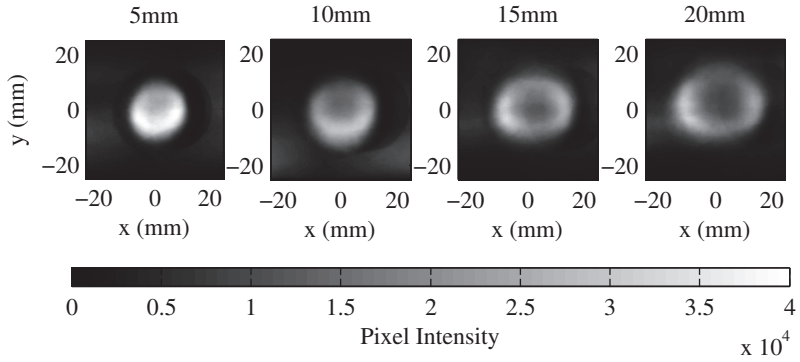

(a) $\phi = 0.74$

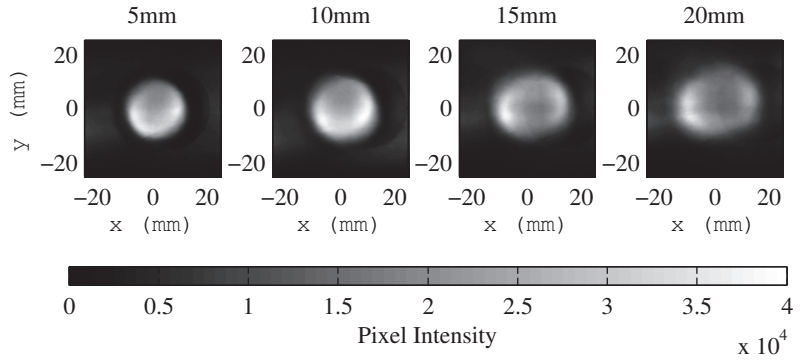

(b) $\phi = 0.82$

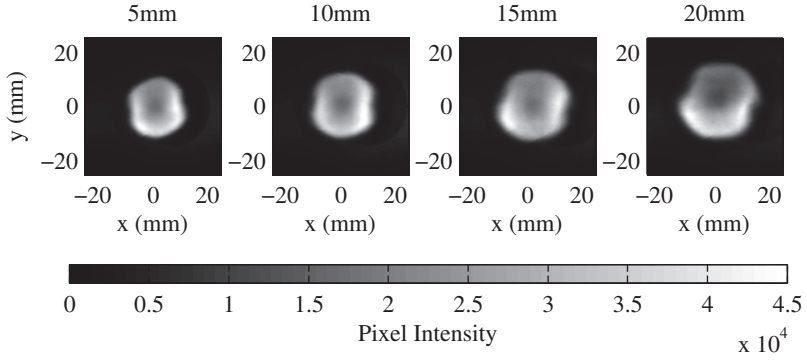

(c) $\phi = 0.94$

Figure 2.11: *Average images of radial PLIF for each equivalence ratio studied, at z=5, 10, 15 and 20 mm away from the injector.*

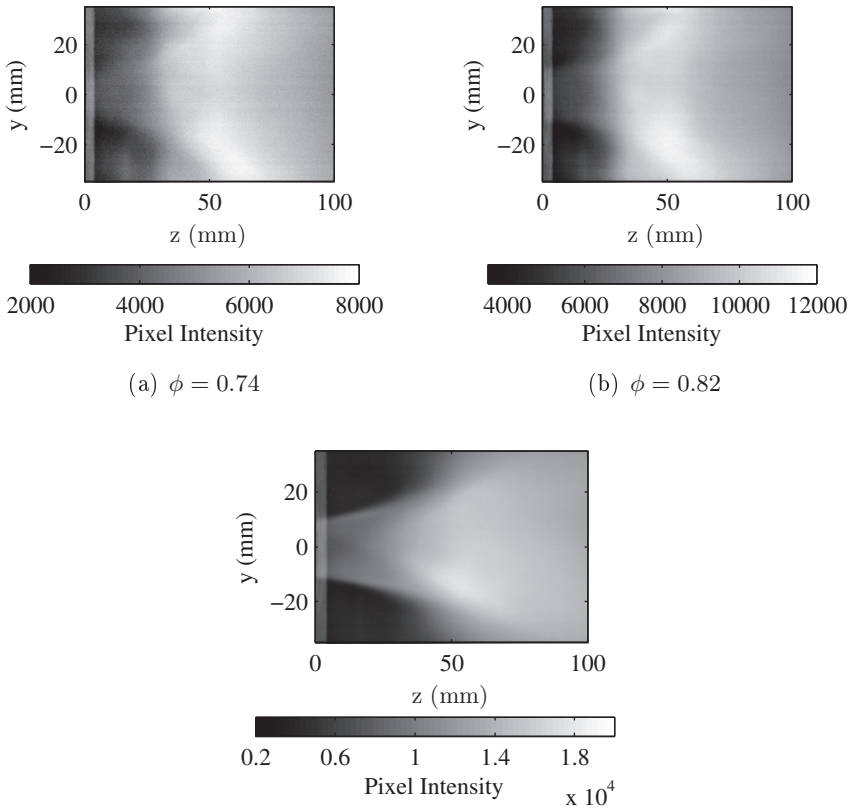

(a) $\phi = 0.74$

(b) $\phi = 0.82$

(c) $\phi = 0.94$

Figure 2.12: *Average images extracted from high speed imaging of the flame for the three equivalence ratios.*

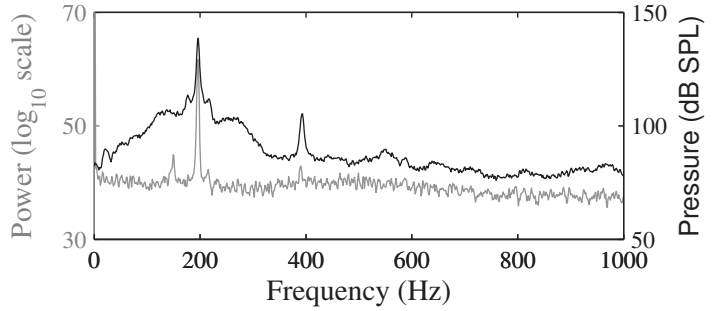

(a) ϕ=0.74

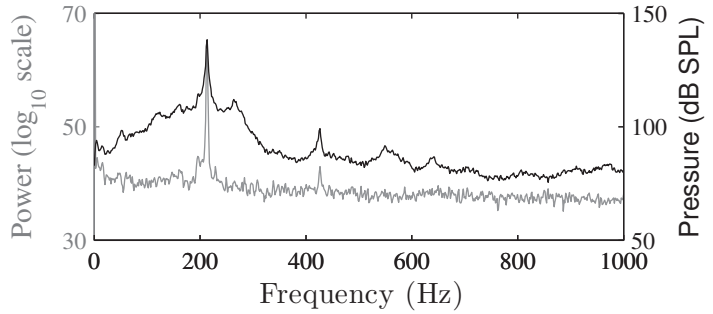

(b) ϕ=0.82

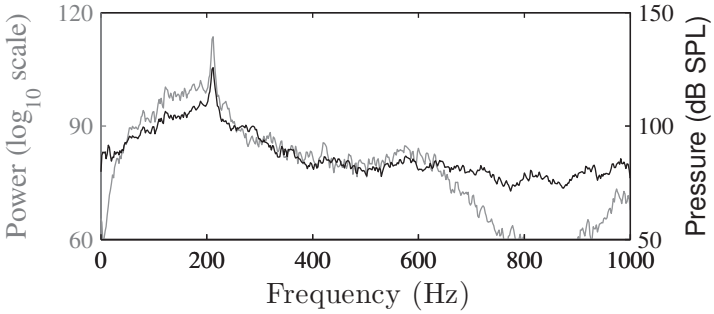

(c) ϕ=0.94

Figure 2.13: *Power spectral density (PSD) at the different equivalence ratios. The PSD of the microphone (in black) is presented in dB (SPL) as previously, and the PSD of the absorbance (in grey) is scaled in similar fashion:* $20log_{10}(absorbance/20e^{-6})$. *The factor in the logarithm is to ensure good visibility of both curves on the same graph.*

the main perturbation. It can be noted, that non negligible correlations are also obtained at the doubled frequency, but also in the 120-150 Hz region. However, as with the pressure oscillations, the amplitude of the oscillation at the main instability is much greater than at the other frequencies. This confirms that the main pressure oscillation, which has been shown to also be linked to the global pulsation of the flame, can also be linked to absorption fluctuations. Whether this correlation is due to fluctuations in the absorption length (and thus the flame shape) or to fluctuations in fuel concentration needs to be confirmed, and will be detailed in chapter 3.

A statistical approach can also be used to ascertain the timing of these fluctuations relative to pressure fluctuations, by calculating cross correlation or cross spectral density between those signals (figure 2.15). These calculations show that the phase difference between the pressure inside the injector and the absorbance changes with the equivalence ratio. It varies from -100° for an equivalence ratio of 0.74, to -180° for the equivalence ratio of 0.94. Even though the measurement at 3 kHz gives a low phase precision of ±12.7° for these measurements, the change is still significant. In particular, there seems to be a switch between the case at low equivalence ratio, where the absorbance and pressure signals are more or less in quadrature, and the case at higher equivalence ratio, where they are in phase opposition, while the intermediate equivalence ratio lies between those two values.

2.6 Temperature

As explained in chapter 1, a Background Oriented Schlieren technique was also applied. The field of view is chosen to limit the influence of chemical reactions and therefore starts 100 mm inside the combustion chamber, whereas average images previously shown ends at 100 mm. Even though the results obtained are only qualitative, they are nonetheless interesting as they confirm the presence of temperature fluctuations downstream of the flow, and can give information on the phase shift between these fluctuations and the pressure fluctuations in the system.

The results are only qualitative due to several constraints. First, the limits on the sensitivity available with the system used led that most displacements detected are sub-pixel and as such not very precise. Secondly, the highly 3D nature of a turbulent swirl flow makes the interpretation of line of sight diagnostics such as BOS sometimes difficult because of complex 3D interactions. And lastly, linking the measured displacements to a temperature would require knowledge of the conditions on the borders of the images, which is unfortunately not the case here: neither the mean temperature profile inside

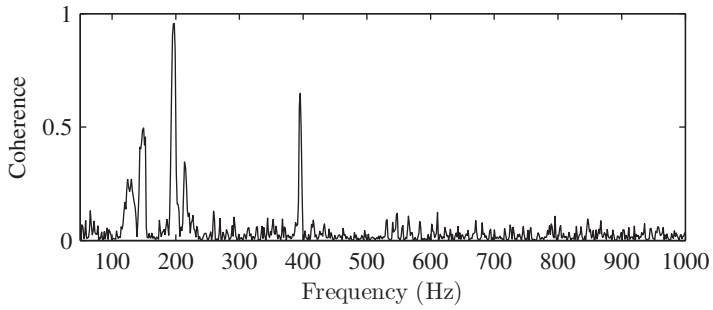

(a) ϕ=0.74

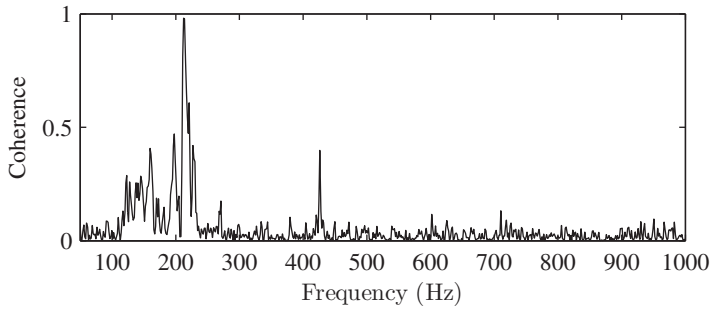

(b) ϕ=0.82

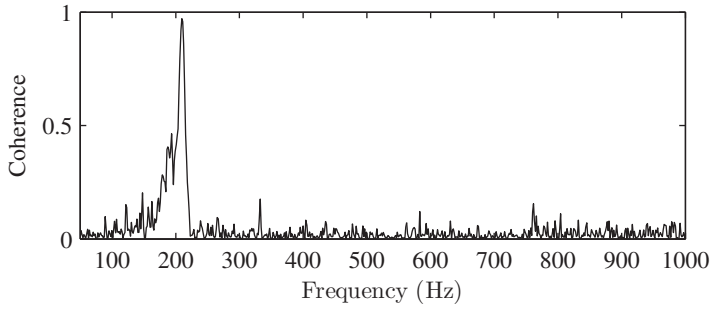

(c) ϕ=0.94

Figure 2.14: *Coherence between the absorption measurement and the pressure in the injector tube, at the different injection conditions.*

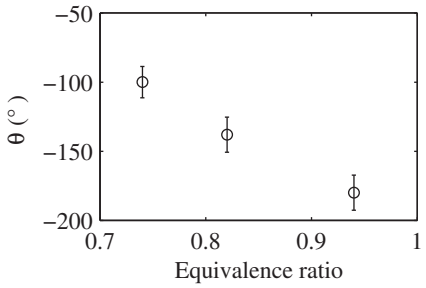

Figure 2.15: *Evolution of the phase difference between the absorption measured by the laser system, and the microphone inside the injector.*

the chamber, nor the wall temperatures are known.

The average values obtained for displacement, both vertically and horizontally are given in figure 2.16. As said earlier, in the biggest part of the flow the displacement observed is subpixel in both directions. However, these averages allow to see that the thermal boundary with the walls is visible on both upper and lower walls for all conditions, and at ϕ=0.74 and 0.82, a horizontal gradient of temperature seems to exist along the chamber too. It does not seem to be present anymore at ϕ=0.94. This may be due to a faster thermalization of the chamber at higher equivalence ratios, or to a longer plume of the flame (in the ϕ=0.94 case, part of the blue afterglow of the flame is in the field of view of the camera).

In order to further exploit these results, a power spectral density analysis of the horizontal displacement was made. Only the horizontal component was chosen, as it is the one that would be linked to horizontal gradients of temperature. As the observed displacements are sub-pixel, they are expected to be noisy. In order to try reducing that noise, the data analyzed is the average of 9 vectors around the chosen positions, each vector having a spatial resolution of 1.72 x 1.74 mm. These positions were along the central axis of the chamber, at z= 100, 145 and 190 mm. The PSD analysis was done with Hanning windows of 1024 points, giving a spectral resolution of 6.8 Hz. The 50% overlap of these windows ensures that 6 windows are used to obtain the spectra shown in figure 2.17. In the three cases, the horizontal deviation presents a strong peak at the frequency expected from the pressure fluctuations. However, as the distance from the burner increases, the peak is lost. At ϕ=0.74, the peak is still visible at 145 mm from the injector but is progressively lost to a mass of content between 50 Hz and 150 Hz. The same conclusion is drawn for ϕ=0.82, but the peak at 145 mm from the injector has a lower frequency (down from 212 Hz to 185 Hz). For the richest case, the peak is quickly lost. The degradation of the results is however to be expected: the further away from the injector, the lower

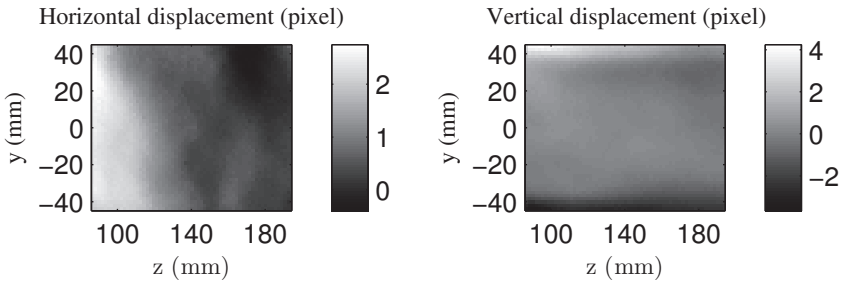

(a) ϕ=0.74

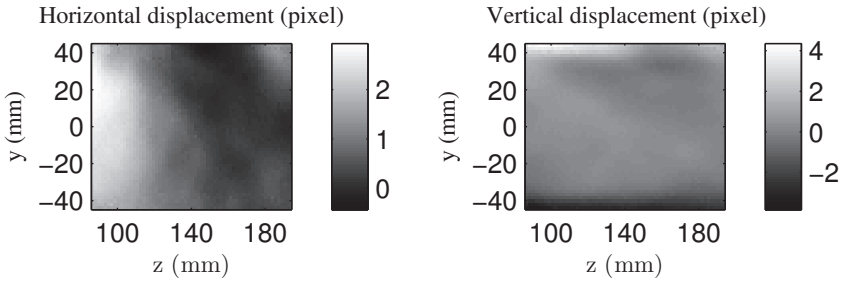

(b) ϕ=0.82

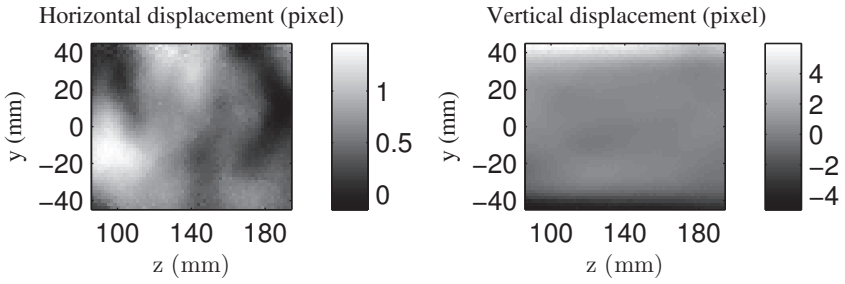

(c) ϕ=0.94

Figure 2.16: *Average displacement observed with the BOS setup for the three equivalence ratios. Left: horizontal displacement (in pixels); Right: Vertical displacement (idem).*

the calculated displacement is, and thus the more prone to errors the results are.

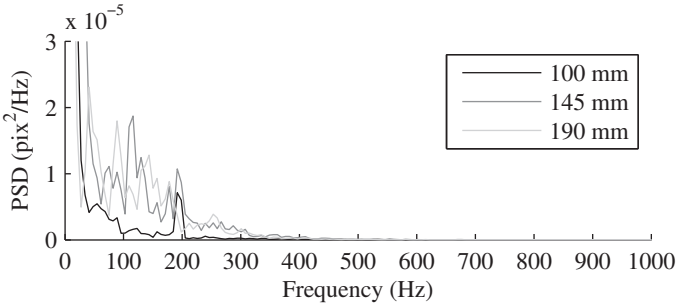

(a) ϕ=0.74

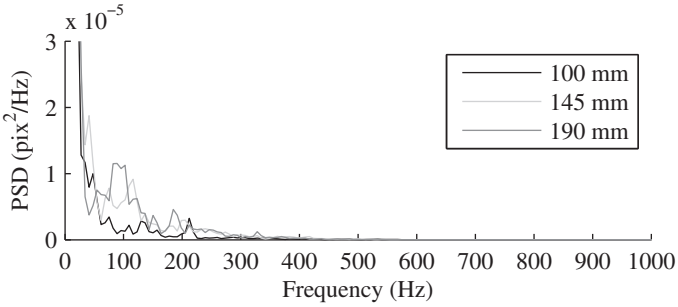

(b) ϕ=0.82

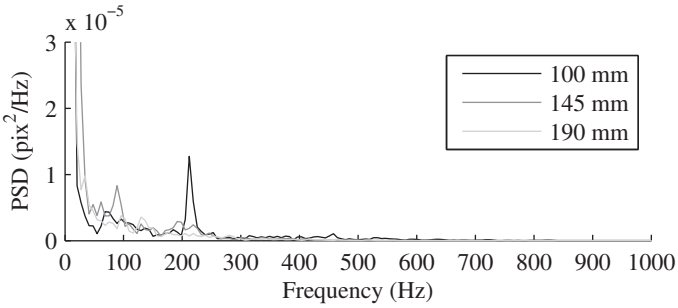

(c) ϕ=0.94

Figure 2.17: *PSD of the horizontal displacement observed with the BOS setup at various distances from the injector for the three equivalence ratios.*

To confirm this statement, the coherence between the horizontal displacement and the pressure inside the chamber was computed for each position for the three conditions. The value of the maximum coherence on a 0-1 kHz range, and the frequency at which this coherence is obtained for each of the three equivalence ratios studied are plotted in figure 2.18. For clarity of the results, only the values for a maximal coherence higher than 0.7 is shown, the other

values are set to 0. It can then be seen that a strong correlation to the pressure fluctuations is linked to the main oscillation frequency. And without surprise, the farther from the injector, the lower the maximum correlation. It can thus be supposed that the peaks observed at lower frequency far from the injector are not linked to the pressure fluctuations inside the chamber.

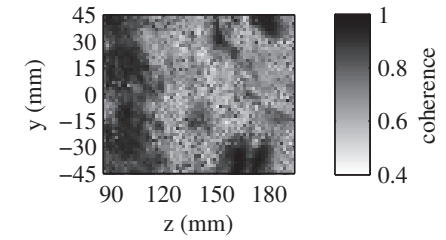

(a) ϕ=0.74, coherence peak

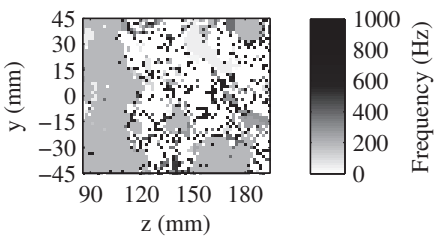

(b) ϕ=0.74, frequency peak

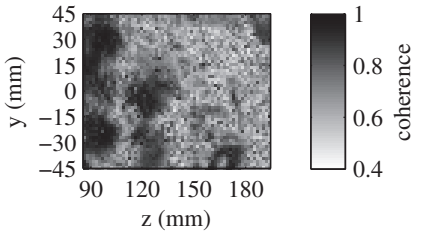

(c) ϕ=0.82, coherence peak

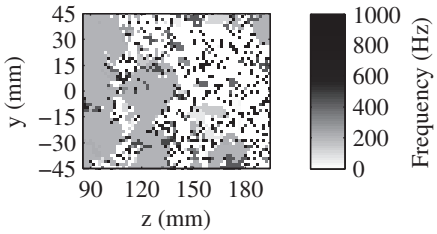

(d) ϕ=0.82, frequency peak

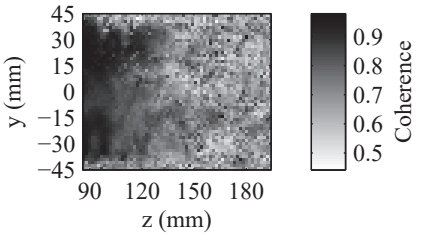

(e) ϕ=0.94, coherence peak

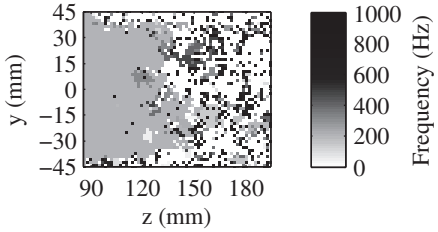

(f) ϕ=0.94, frequency peak

Figure 2.18: *Results from coherence calculations on the BOS displacements and pressure signals inside the chamber. Maximal coherence on the 0-1kHz range is given, as well as the associated frequency.*

2.7 Conclusion

The CESAM burner used in this study is not water-cooled and with quite a high power, and as such all measurements must be made with the same timing

to ensure that the temperature conditions in the chamber are identical. The study with the classical tools that are averaging, PSD and coherence of the various measurements made on the burner allow by themselves to obtain a fairly broad knowledge of the instability occurring in the burner. A strong combustion instability can be found on the entire range of injection conditions explored. For equivalence ratio changes, the evolution of this instability can be separated in two categories: for equivalence ratios lower than 0.82, the frequency changes with the equivalence ratio, but the pressure fluctuations have the same amplitude. And for equivalence ratios higher than 0.82, the frequency is constant, but the amplitude of the pressure fluctuations starts to decrease. For this reason, the three cases (ϕ=0.74, 0.82 and 0.94) are selected to be studied in more detail. The observation of broadband emissions and PLIF of OH radicals shows that the flame gets narrower when the equivalence ratio is larger. The spontaneous emission of the OH* radical is strongly correlated to the acoustic pressure fluctuations, indicating that the heat release rate is strongly linked to the acoustics in the burner. The absorbance of an IR laser by propane in the fresh gases also shows a strong activity at the frequency of the instability, correlated with the pressure fluctuations. However, it is yet unclear if this is due to variations in the equivalence ratio, or in the length of the fresh gases the laser goes through, as the flame changes its shape during the instability. Lastly, the deviations observed by BOS, in regions where the correlation with the pressure fluctuations in the chamber is strong, also vary at the frequency of the instability, suggesting that temperature fluctuations also occur for the same reason.

These results show that various quantities are either driving or altered by the strong instability present in the burner. The tools used up to now allow to determine the frequency and amplitude of oscillations. The cross spectral density can be used to estimate the phase difference between different signals. However, these tools have their limits, one of them being that the evolution during an oscillation cycle is not known, particularly for the PLIF and broadband emissions. The goal of the next chapter is to try and reconstruct the average instability cycle to understand what are the differences between the three studied equivalence ratios.

Chapter 3

Measurement of equivalence ratio fluctuations at the chamber inlet

In this chapter, the method employed to obtain equivalence ratio fluctuations during the instability cycle is described. In order to exploit these measurements, several steps were necessary, as will be developed in the chapter. First, high speed measurements of the absorption at the inlet were carried out. To extract equivalence ratio values from absorption measurements, it is necessary to precisely know the absorption length for each acquisition point. These absorption lengths could be estimated from PLIF imaging, even though in the present case the PLIF images were acquired at a frequency lower than the main oscillation of the flame (and also much lower than the absorption measurement rate). It was thus necessary to implement a phase averaging methodology, as described in the second section, to reconstruct the average cycle for both absorption measurements and absorption length. In the third section, the method developed for phase averaging is validated by employing it on microphone and photomultiplier signals, whose relative phase shifts were already measured in chapter 2 by calculating their cross-correlation. As an other example of its validity, this method is also employed on Background Oriented Schlieren data to measure the convection speed of hot gas pockets that were detected. In a third time, the phase averaging is conducted on both axial and longitudinal PLIF measurements, to build the mean cycles. With this average cycle in hand, the corresponding absorption length is calculated. Lastly, by combining the measured absorption and the calculated absorption length, the associated equivalence ratio measurements is estimated and the final precision of the measurement discussed.

3.1 Context

As was described in chapter 2, the CESAM burner exhibits a strong thermo-acoustic instability at a frequency between 190 Hz and 210 Hz depending on the injection conditions used in this study. In particular, a strong quasi-monofrequential peak is observed in all the microphone signals, showing that a pressure oscillation is present inside the burner. One of the potential agents in sustaining this acoustic pressure instability could be an oscillation of the equivalence ratio occurring at the same frequency.

In order to confirm the presence of this suspected equivalence ratio oscillation, it should be measured, and if possible compared to the pressure oscillations (in frequency, shift between the two cycle types,...). However, the conditions inside the burner used in this study, do not allow to obtain a high acquisition rate using the diagnostics chosen for equivalence ratio measurement, which would allow a straightforward comparison with the acoustic pressure signals.

A solution to this acquisition frequency problem is a conditioned measurement of the equivalence ratio: each measured point of this signal is associated to its place in a pressure oscillation, which then would allow to reconstruct an average equivalence ratio fluctuation cycle at the same frequency as the pressure one. However, this association of a point to its phase in a cycle is not straightforward, so most of the present chapter will be focused in presenting and validating the chosen approach.

3.2 Principle of the equivalence ratio measurement

In this first section, a quick reminder of the principle of the equivalence ratio measurement by fixed wavelength laser absorption is given. The detailed process of absorption measurement can be found in chapter 1.
From the Beer-Lambert absorption law, given an absorbance A and absorption length L, one can calculate an equivalent propane concentration since the laser wavelength was chosen so that propane is the only absorbing species with an absorbance cross-section σ:

$$N_{prop} = \frac{A}{\sigma L} \tag{3.1}$$

As demonstrated in chapter 1, the equivalence ratio can then be computed from such measurements, using the equation:

$$\phi = \frac{N_{prop}}{N_{tot} - N_{prop}} \times 5 \times 4.76 \tag{3.2}$$

One of the main problem to overcome in the present burner configuration is that the absorption length is not constant. This is illustrated in figure 3.1,

showing clearly that since L is the length of fresh gases present between the IRZ and the ORZ for each measurement, it is highly subject to variations. In order to obtain the equivalence ratio values, it is thus necessary to have measurements of both absorption A, and absorption length L. As will be discussed in the remainder of the chapter, if high speed absorption measurements is available, the absorption length was more complex to obtain.

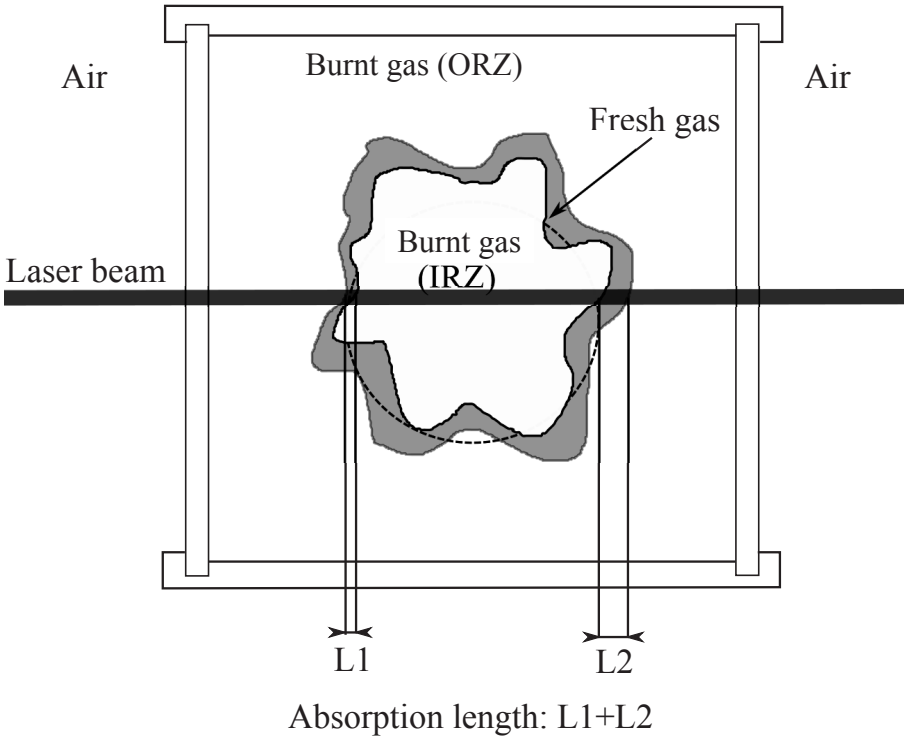

Figure 3.1: *Illustration of the absorption length.*

Since the acquisition frequency of the absorption measurement is sensibly higher than the main instability frequency, it directly gives phase resolved data which allows to obtain for each cycle in the signal its frequency and amplitude. A comparison can then be made with the acoustic instability as described in the previous chapter. On the contrary, the absorption length is derived from PLIF imaging which was acquired at only 10 Hz, much too low to obtain any information on a probable coherent evolution of this length at the same frequency as the instability. A variation of the absorption length at the instability's frequency would have an impact on equivalence ratio calculations, and so it is important to quantify if it exists. Since all measurements were made simultaneously and synchronously with high speed pressure measurements, it is possible to use phase averaging to reconstruct an average instability cycle

from the acquired signals. This will be the focus of the next section.

3.3 Principle and calculation of the phase average

3.3.1 Principle

A classical method to describe a system with a mono-frequency instability is the phase locked averaging method. The principle of phase averaging is to acquire a reference signal at high frequency simultaneously to the desired low frequency data (velocity, an image, etc.). The reference signal is then used to determine when in the instability cycle each acquired data point was taken. The phase of the data point is that position in the cycle translated on a 0°-360° scale. Each data point is then affected to a different phase bin, and an average is computed for each of the bins.

It is thus necessary to precisely determine the phase of each data point. To be able to do this, the reference signal must respond strongly to the instability cycle, and be sampled at a frequency ideally much higher than the observed instability. The resulting precision $d\theta$ on the phase is then given by the sample and instability frequencies as illustrated in figure 3.2, and thus by the relation:

$$d\theta \geq \frac{360 \times f_{inst}}{F_s} \tag{3.3}$$

where f_{inst} is the frequency of the instability, and F_s is the sampling frequency of the reference signal. This is the maximal precision at which a phase average can be conducted. In the case of this study, the lower expected precision is thus around 4.5°, with an instability at 190-210 Hz and a reference microphone acquired at 16 kHz.

Moreover, when computing the phase average, the minimal size of the chosen phase bins is also limited by the acquired signal's length: there must be enough data points in each phase bin to have a meaningful average. Thus, for a given acquisition rate, the closer the resolution $\delta\theta$ of the computed average is to its precision $d\theta$, the longer the signal must be since it requires more individual phase bins.

Once the phase average's resolution $\delta\theta$ is chosen by checking that each phase bin contains a satisfactory number of data points, the limits of the phase bins are constructed. If there are k phase bins, then the i^{th} phase bin is noted θ_i,

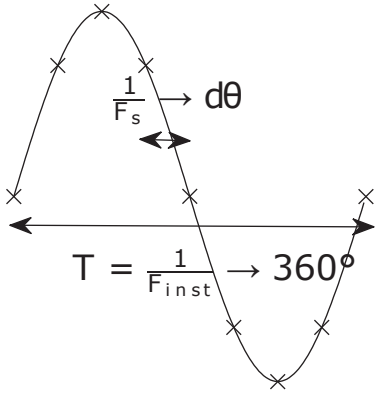

Figure 3.2: *Illustration of the precision of the phase determination on a perfectly sinusoidal signal.*

and defined as:

$$\theta_i = \begin{cases} [0; \frac{\delta\theta}{2}] \cup [360 - \frac{\delta\theta}{2}; 360] & if \quad i = 0 \\ [(i \times \delta\theta) - \frac{\delta\theta}{2}; (i \times \delta\theta) + \frac{\delta\theta}{2}] & if \quad k \geq i > 0 \end{cases} \tag{3.4}$$

Once the points are grouped in their respective bins, the phase average of a signal u can be computed for each value:

$$u_{\theta_i} = \frac{1}{N_{\theta_i}} \sum_{n=1}^{N_{\theta_i}} u_{n,\theta_i} \tag{3.5}$$

where N_{θ_i} and u_{n,θ_i} are the number of points and the n$^{\text{th}}$ value of the signal u in the ensemble θ_i respectively. Similarly, a phase-locked median could be defined by computing the median for each value of θ_i instead of the average, as well as the variation around the total average:

$$u'_{\theta_i} = u_{\theta_i} - \overline{u} \tag{3.6}$$

with $\overline{u}$ the total average of the signal.

3.3.2 Phase determination

As explained in the previous section, obtaining the best precision possible on the phase determination is the most important when computing a phase average. In the present case, the signal taken as reference is the pressure inside the injector, which is one of the fluctuating parameters in a thermoacoustic

instability. It was selected as it is was acquired for all experiments at 16 kHz, a frequency high enough for the data to be phase resolved. The acoustic pressure in the injector was chosen rather than the one in the chamber because of the higher signal level, ensuring a better precision.

One of the simplest ways to get the phase from such a signal would be to use the Hilbert transform. The phase (in degree) of the reference signal $M(t)$ is then the value:

$$\theta = angle(H(M^*)) \times \frac{180}{\pi} + 90 \tag{3.7}$$

where M^* is obtained from M by using a bandpass filter. In the cases studied here, 6^{th} order Butterworth filters around the peak's frequency with various width were tested. The study of this filtering's impact are presented in appendix A, and show that a ± 50 Hz band is a good compromise between noise rejection and signal deformation. The 90° shift is added to respect the convention that will be used from now on for the phase signal: the beginning of the cycle is defined as the point where the value is 0, from negative to positive values.

The filtering is necessary because the Hilbert transform only gives accurate results if the signal is quasi-sinusoidal, and as such is sensitive to noise and insensitive to potential frequency fluctuations. As the instability for the case ϕ=0.94 is of low amplitude compared to the broadband noise, this can prove a severe drawback in that particular case. The figure 3.3 presents the results obtained when computing the phase on two parts of the signal: one where the original signal has a clear instability, and one where the low amplitude of the oscillations makes the determination much more arduous. From this figure, it comes that even on the clear signal, the phase found by the method presents irregularities inside some of the cycles, even though the signal is previously filtered at ± 50 Hz around the instability value before applying the Hilbert transform. This shows that the results from phase averaging using this method have to be considered with care.
For this reason, the method selected in this study is different. It is based on the determination, for each cycle, of the instantaneous frequency value. This frequency is found by searching for the successive points where the signal is equal to 0, and with a positive slope. If the time for each of these j points is noted $t_{period(j)}$, then the associated instantaneous period length and thus frequency can be found:

$$\begin{aligned} \Delta t_{period(j)} &= t_{period(j+1)} - t_{period(j)} \\ f_j &= 1/\Delta t_{period(j)} \end{aligned} \tag{3.8}$$

In order to determine these cycle limits, the calculation is not made on the raw signal, but on a filtered version to eliminate most of the noise, with the

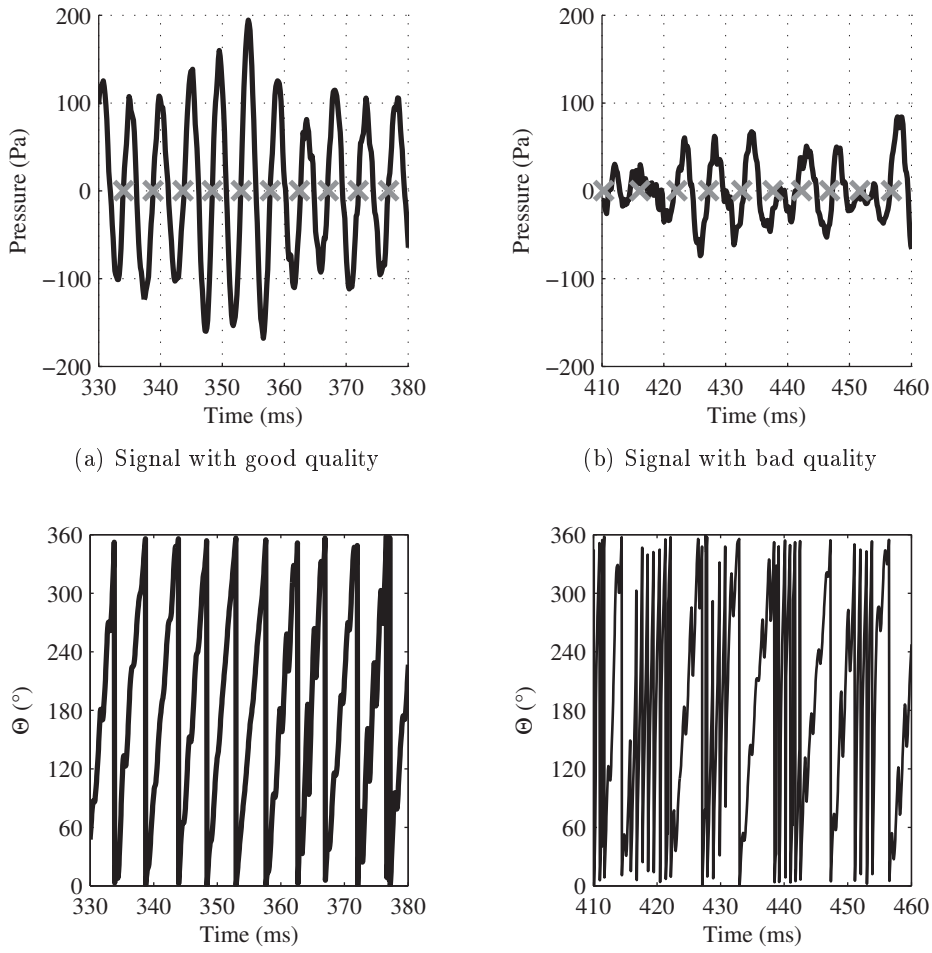

(a) Signal with good quality

(b) Signal with bad quality

(c) Corresponding phase

(d) Corresponding phase

Figure 3.3: *Illustration of the phase calculations using the Hilbert method, from a measurement at equivalence ratio ϕ=0.94: a) and c) show the signal and calculated phase values for a good quality signal, and b) and d) a part of the same measurement where the quality is worse.*

same Butterworth filter at ±50 Hz around the instability frequency as with the Hilbert method. Despite this filtering, variations in the instantaneous frequency can still be found when the signal is locally strongly deformed. To ensure the rejection of problematic values, as illustrated in figure 3.4, a criterion of validation δf of 10 Hz was used: if the instantaneous frequency of the filtered signal is too different from the known instability frequency f_{inst}, it is rejected.

From the convention chosen for the cycle analysis, a phase θ=0° at each time step $t_{period(j)}$ is given. For the data points taken at any time stamp t_i, the phase is then:

$$\theta_i = \frac{360\left(t_i - t_{period(j)}\right)}{\Delta t_{period(j)}} \quad \begin{cases} \forall t_i \in \left[t_{period(j)}; t_{period(j+1)}\right[\\ \forall f_j \in [f_{inst} - \delta f; f_{inst} + \delta f] \end{cases} \tag{3.9}$$

The reason for the filtering and rejection criterion is illustrated on figure 3.4. At equivalence ratio ϕ=0.94, the pressure oscillations inside the injector can sometimes reach low levels of amplitude, in which case the cycles obtained are also far from a sinusoidal shape. As a result, most of these very deformed cycles will be rejected using the current method, ensuring they do not deform the associated average cycle. As such a criterion distorts the reality by rejecting parts of the signal, care must be taken not to use a too strict condition.

A detailed comparison of the results obtained using both methods, as well as the effect of the filter's characteristics on the phase calculation is available in appendix A. The main result of this comparison is that for the highest equivalence ratio setting, even using a narrow bandpass filter leads to bad quality results using the Hilbert transform, since non sinusoidal cycles are present in the signal (filtered or not). This is the main reason for choosing the instantaneous frequency method.

The parameters used for the present study are given in table 3.1. The filter's width is a compromise between eliminating the broadband noise when computing the phase, and not deforming the underlying coherent signal: the results of the study in appendix A show that for severe filtering, the zeros of the unfiltered and filtered signals do not correspond precisely to each other anymore. Identically, the 10 Hz criterion for phase rejection was chosen so as to keep a maximum of data points while ensuring the rejection of spurious results. Lastly, the phase bin width was chosen so that at least a hundred points are present in each phase bin when using the data from PLIF measurements, ensuring meaningful averages in all cases.

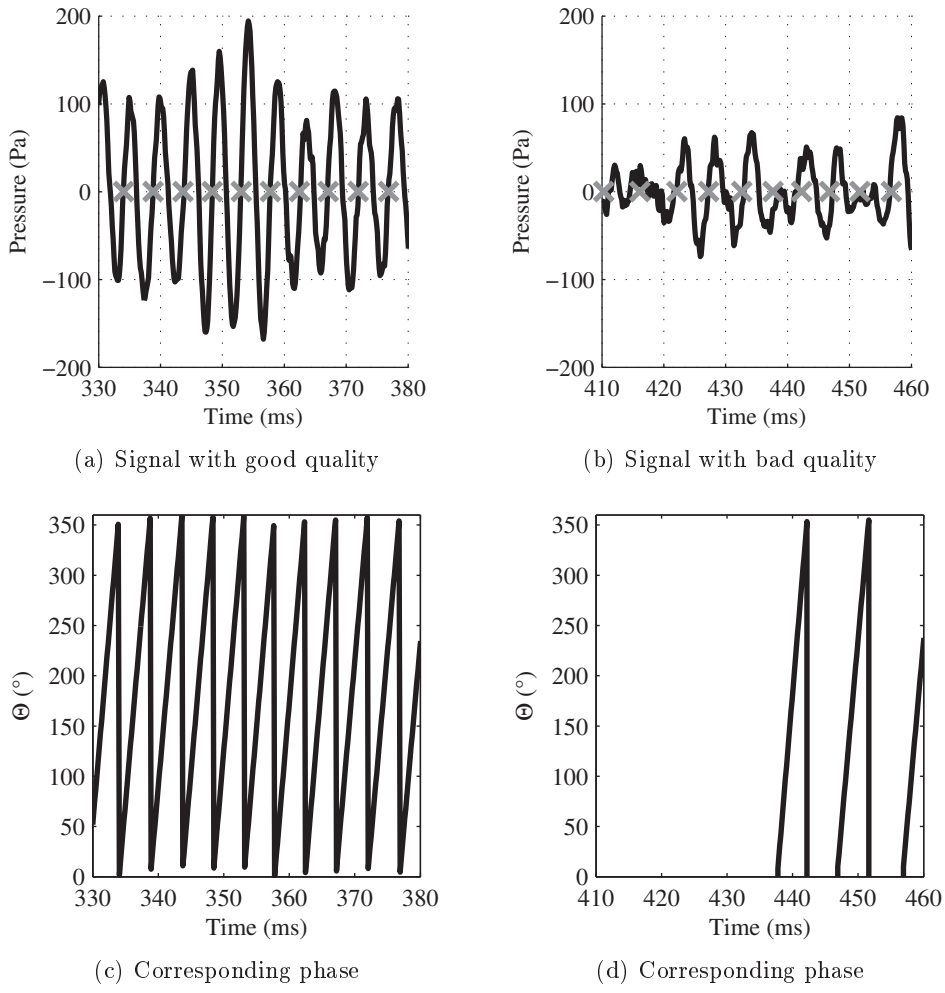

(a) Signal with good quality

(b) Signal with bad quality

(c) Corresponding phase

(d) Corresponding phase

Figure 3.4: *Illustration of the phase calculations, from a measurement at equivalence ratio ϕ=0.94: a) and c) show the signal and calculated phase values for a good quality signal, and b) and d) a part of the same measurement where the quality is low. The gray crosses indicate the cycle limits as found during phase determinations (with a filtered pressure signal).*

Parameter	Value
Width of filter	± 50 Hz
Frequency validation δf	10 Hz
Width of phase bins $\delta\theta$	15 °

Table 3.1: *Parameters used for the phase averaging calculations.*

ϕ	0.74	0.82	0.94
Cross Spectral Density	-35°±3°	-63°±3°	-45°±3°
Phase average	-35°±15°	-60°±15°	-45°±15°

Table 3.2: *Phase difference found, and its precision, between the pressure oscillations inside the injector and chamber, depending on the method used.*

3.4 Evolution of the phase shift between OH* chemiluminescence, injector and chamber pressure.

Using the method described in the previous section, the phase averages are calculated for several signals: the chemiluminescence from OH* radicals as seen by a PMT, and the pressure measurements from the two microphones placed at the bottom of the injection tube and near the end of the combustion chamber, as described in chapter 1. Since the relative phase shifts for these signals was already computed in chapter 2 using cross-correlation, it is used to validate the precision of the phase averaging procedure. It also allows to observe the evolution of these fluctuations during a cycle.

The phase averages obtained for the two microphones are shown in figure 3.5. A lower pressure fluctuation amplitude is observed at the highest equivalence ratio as well as a delay between the two pressure fluctuations for all the injection conditions. The delay's value depends on the operating conditions of the burner. As a reminder, and to better compare, the results that were obtained in the previous chapter using the cross spectral density on the signals are given along with the values found by phase averaging in table 3.2. The profiles found by the phase average presented here were made by calculating the averages on 24 bins of 15° width and are thus less accurate, but seem to confirm these values.

The cycle presented being the result of a conditioned averaging, it is interesting to look at the actual repartition of the measured points relatively to this cycle to confirm its pertinence. A detailed analysis of this repartition depending on the parameters chosen for the phase averaging can be found in appendix A. This study shows that in particular, the repartition for equivalence ratios 0.74 and 0.82 is similar, while for an equivalence ratio of 0.94 the amplitude of the pressure fluctuations can be almost 0 for some cycles. The results obtained on the pressure inside the chamber are given in figure 3.6. The repartition is similar to that observed in the reference pressure signal (i.e. inside the injector), so only the ϕ=0.82 and 0.94 cases are presented, as the 0.74 case is similar to the first one. It can then be seen that the actual instability cycles in the system present a strong variation in amplitude, and for ϕ=0.94 some cycle have a very low amplitude.

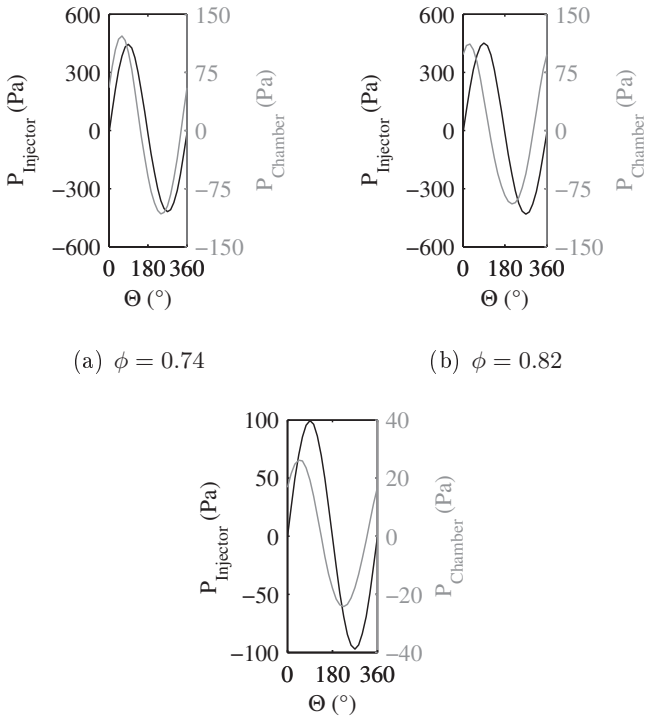

(a) $\phi = 0.74$ (b) $\phi = 0.82$

(c) $\phi = 0.94$

Figure 3.5: *Phase average of the microphones in the injector (in black) and in the chamber (in gray) for the three equivalence ratio studied, at the frequency of the main instability.*

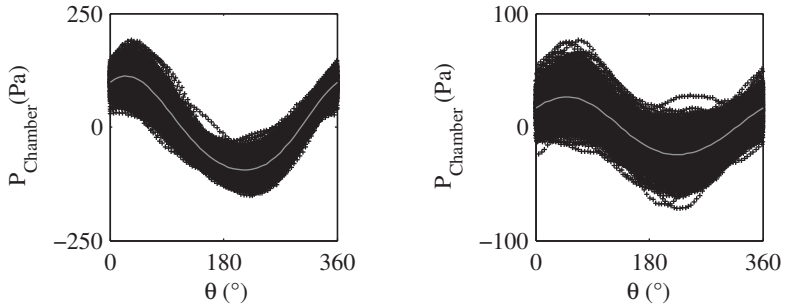

(a) ϕ=0.82 (b) ϕ=0.94

Figure 3.6: *Repartition of the data from the microphone inside the combustion chamber when computing the phase averaging. The line in gray is a phase averaging computed using bins of 15° width, while black crosses represent the individual points used for this phase averaging procedure.*

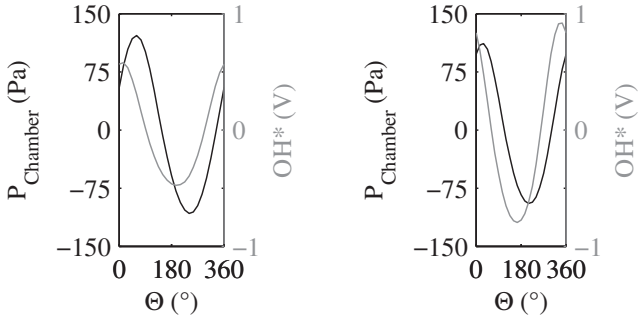

(a) $\phi = 0.74$ (b) $\phi = 0.82$

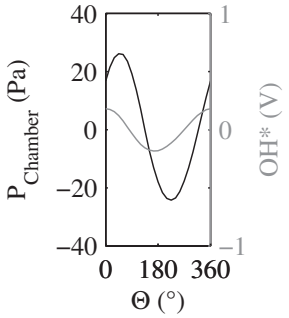

(c) $\phi = 0.94$

Figure 3.7: *Phase average of the pressure in the chamber (in black) and the chemiluminescence emissions (in gray) for the three equivalence ratio studied, at the frequency of the main instability.*

ϕ	0.74	0.82	0.94
Cross Spectral Density	-50° ± 3°	-48° ± 3°	-52° ± 3°
Phase average	-45°±15°	-45°±15°	-60°±15°
Width of phase bins $\delta\theta$	15 °	15 °	15 °

Table 3.3: *Phase difference found, and its precision, between the pressure oscillations inside the chamber, and fluctuations of OH* chemiluminescence, depending on the method used.*

ϕ	0.74	0.82	0.94
Cross Spectral Density	-80° ± 3°	-110°± 3°	-100° ± 3°
Phase average	-75°±15°	-105°±15°	-105°±15°
Width of phase bins $\delta\theta$	15 °	15 °	15 °

Table 3.4: *Phase difference found, and its precision, between the pressure oscillations inside the injector, and fluctuations of OH* chemiluminescence, depending on the method used.*

The phase averaging of the OH* emission, as seen by the photomultiplier, gives an indication on the correlation during an instability cycle between the heat release rate, and the pressure fluctuations. An analysis of the PSD of the PMT signals showed the presence of peaks at both the frequency of the main instability and its double, as detected in the pressure signals. Looking at the results of phase averaging, presented in figure 3.7, in all cases the pressure fluctuation and radical emissions inside the chamber exhibit a phase difference close to 45°. This can be confirmed by calculating the angle with a cross power spectral density as given in table 3.3. The values are so close that this phase difference can be considered constant: the relation between the pressure inside the chamber and the OH* emission is thus probably the same in all three cases. Since the phase Θ was defined from the pressure inside the injector (Θ=0° when the pressure inside the injector goes from negative to positive), then for all the test conditions, there is almost 90° of phase difference between the pressure oscillation in the injector and the chemiluminescence signal, with the emissions from OH* radicals reaching its maximum as the pressure rises above its average value. Correlation and cross spectrum density confirm that result, and all these results are given in table 3.4. The difference observed for the three equivalence ratio is higher (as was the case with the pressure inside the chamber and injector), and suggests that a difference in the instability cycle for the three equivalence ratios comes from the injector-chamber coupling. In particular, the 20° difference observed between ϕ=0.74 and 0.82 can be noted, as it is well in accordance with a phase shift in the rotation of the IRZ present in both these cases, as will be presented later in the chapter.

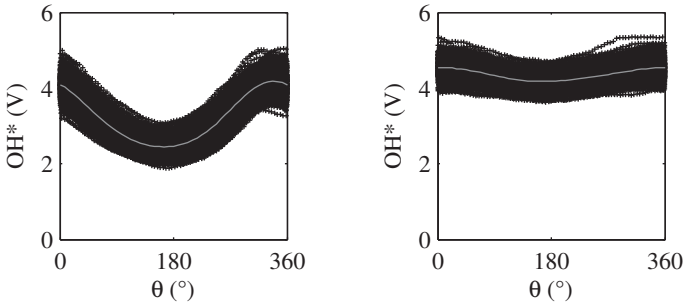

(a) ϕ=0.82 (b) ϕ=0.94

Figure 3.8: *Repartition of the data from photomultiplier registering the OH* spontaneous emissions when computing the phase average. The line in gray is a phase average computed using bins of 15° width, while the individual points used in that phase average are shown in black crosses.*

As with the pressure signals, it is interesting to observe the repartition of the instantaneous measurements along the average cycle, which are shown in

figure 3.8. Since results are similar for both ϕ=0.74 and 0.82 (except for the phase shift relative to the reference pressure), only the latter is shown along with results for ϕ=0.94. The results obtained show almost a band around the phase average for every phase value, whereas the pressure signals presented a lower dispersion when close to the global average. This is probably due to small differences in the instantaneous lengths of the cycles for both signals, and thus is expected. It can be noted however that as was the case with the pressure signals, the amplitude of any cycle can be substantially different from the average cycle presented by the phase averaged cycle.

3.5 Temperature cycles in the burner.

As was showed in the previous section, the phase averaging results obtained on 1D signals are coherent with those obtained by cross correlation. However, an advantage of phase averaging, is that it can also be used on 2D signals, as long as the same reference signal is acquired simultaneously. In this section, phase averaging is thus used on the BOS results, to obtain a better understanding of the temperature fluctuations in the burner.

When phase averaging the displacement fields obtained from BOS, it becomes clear looking at the horizontal displacements that a fairly homogeneous temperature wave is indeed present in the system for the three injection conditions, since temperature fluctuations are the main expected source of observed displacement. The horizontal displacements around the average obtained are shown in figure 3.9. The variations in displacement are very low, under the precision we can expect from the PIV algorithm. The uncertainty on these results is thus quite high, but they seem to confirm that at these distances from the injector, temperature fluctuations can be observed in the combustion chamber.

The wave-like pattern observed has a wavelength of 20±5 pixels in each case (the fronts are quite distorted in some cases and present variations). This translates to a wavelength of 34±9 mm, in each of the three cases. As the frequency of the instability is slightly different for each of them, this means that the temperature fluctuation has a convection speed of 6.6±1.6 m/s at ϕ=0.74, and 7.3±1.8 m/s in the two other cases. As this is far below the speed of sound that could be expected, the convection of temperature fluctuations in the system can be supposed, and needs to be confirmed.

In the three different injection conditions ϕ=0.74, 0.82 and 0.94, the total mass flows are 7.95 g/s, 7.99 g/s and 8.04 g/s respectively. A calculation with GRI-mech 3.0 (Smith et al. (2000)) gives the composition of the burnt gases

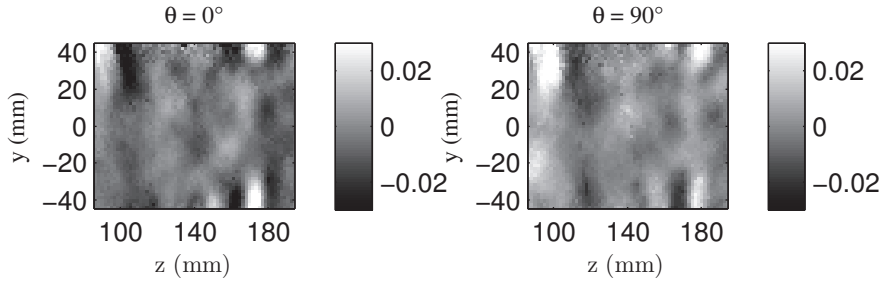

(a) ϕ=0.74

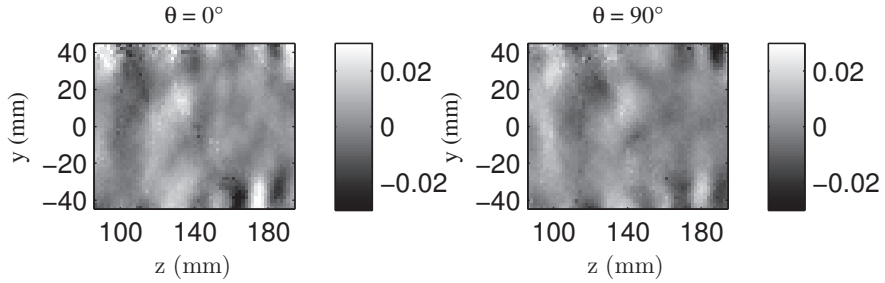

(b) ϕ=0.82

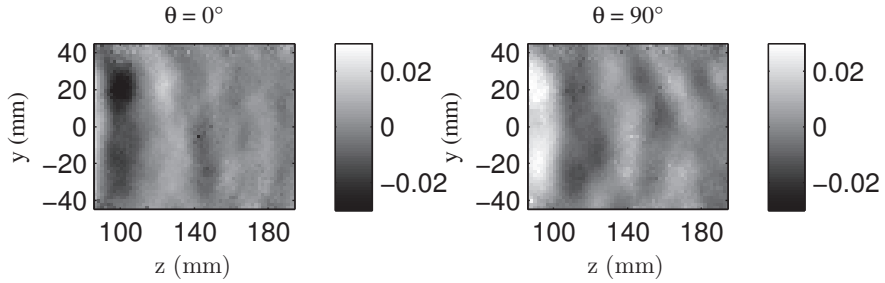

(c) ϕ=0.94

Figure 3.9: *Fluctuations in pixels around the average of the displacements when phase averaging horizontal displacement data with the pressure in the injector as a reference. Note the very low values obtained.*

Equivalence ratio (injection condition)	0.74	0.82	0.94
Adiabatic flame temperature (K)	1928	2055	2208
Molar mass (g/mol)	28.42	28.36	28.20
Density (kg/m^3)	0.180	0.168	0.156
Mass flow (g/s)	7.95	7.99	8.04
Average speed (m/s)	4.9	5.3	5.7

Table 3.5: *Results obtained from the GRI-Mech simulation of the combustion. Density computed supposing adiabatic temperature and perfect gas law.*

as well as the adiabatic flame temperatures in these conditions. From the composition (in mass fractions) of the gases, the global molar mass is deduced. By supposing that the temperature is the adiabatic flame temperature obtained, that the pressure is 1.013 bar and that the perfect gas law can be applied, the burnt gases' density is then computed. Finally, knowing the mass flow rate and the cross section of the burner, an estimation of the average speed in the burner is made. The results from these calculations are given in table 3.5. If the speed is supposed homogeneous in the chamber at the distance from the injector considered, then the obtained values from the calculations are lower than the BOS results suggest: the average speed would vary between 4.9 m/s and 5.7 m/s depending on the case. Since these results were obtained using several assumptions (adiabatic flame temperature, homogeneous speed,...) they are not exact, but give a good estimation of the average convection speed in this part of the burner.

Considering the lack of precision ($\pm$15%) on the propagation speed of the temperature wave and the approximations on the simulation made, it is thus possible to assume that the temperature fluctuations are indeed transported by a convective phenomenon, whose velocity matches the velocity computed taken into account gaseous expansion.

3.6 Evolution of the IRZ shape

On the same principle as the measurement in the previous section, an analysis of the characteristics of the IRZ as measured via OH-PLIF imaging can be made. This can have the major advantage of allowing to observe the evolution of the flame's shape and position using measurements at a low acquisition frequency.

3.6.1 Radial plane measurements

As was seen in the previous chapter, on average the IRZ of the flame seems to be broadly conical. It could then be expected that the strong pressure fluctuations could lead to a flame that would keep a broadly circular shape during an instability cycle. However, this seems not to be the case. In order to show it without any bias due to inhomogeneities in the laser sheet, the radial profile images shown from now on are binarized results. This was done using the Canny method of the edge function of Matlab. This method was chosen as it searches for edges using a low and a high threshold, allowing the detection of the edge of the IRZ even though it often presents strong inhomogeneities in instantaneous images. For images taken radially, 3150 images were available in each injection condition and position combination. The phase averaging was done with bins 15 degrees wide, based on the pressure from the microphone in the injector: the cycle starts when the pressure there goes from negative to positive.

The results of the phase averaging on a radial plane 10 mm from the injector are shown in figure 3.10. From what can be seen there, when averaged along a cycle, the IRZ is not circular but more elliptic for ϕ=0.74 and 0.82. This ellipse seems to change size and orientation during the cycle. For ϕ=0.94, the shape seems to be the same as in the global average, but it oscillates around a central orientation.

In order to better understand the dynamics of the IRZ, it was decided to look at several of its properties. For example, knowing the surface of the IRZ can lead to a better understanding of the opening and closing of the angle of the flame in the axial direction. The phase averaging of the radial images showed that the IRZ tends to be elliptical in that plane for two of the three injection conditions, and almost circular in the third case. It was thus decided that looking at the elliptical fit of the IRZ for each instantaneous image could be relevant, and help describe the movement of the IRZ better than looking only at the phase averaged images. In order to obtain these additional information on the IRZ, the Regionprops function from Matlab was used on the binarized images. The following data was taken from the Regionprops results: centroid position, long and short axis length of the ellipse fit, surface of the IRZ. These parameters were corrected from pixel to physical length by using the pixel pitch in both directions. Since the pixel pitch is not the same in the horizontal and vertical directions, the perimeter of the IRZ was calculated using a custom function.

In order to illustrate the ellipse fit found with the Regionprops function, two random images taken 10 mm from the injector for an equivalence ratio of 0.74 are presented in figure 3.11, with the corresponding orientation of the ellipse, and phase of the image in a pressure cycle. This is the setting for the burner

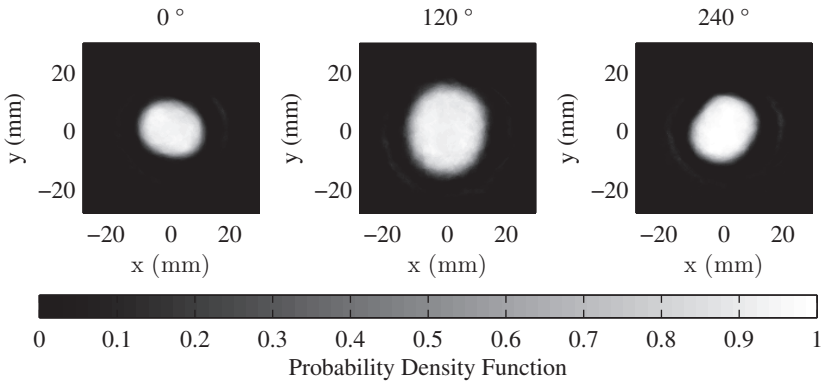

(a) $\phi = 0.74$

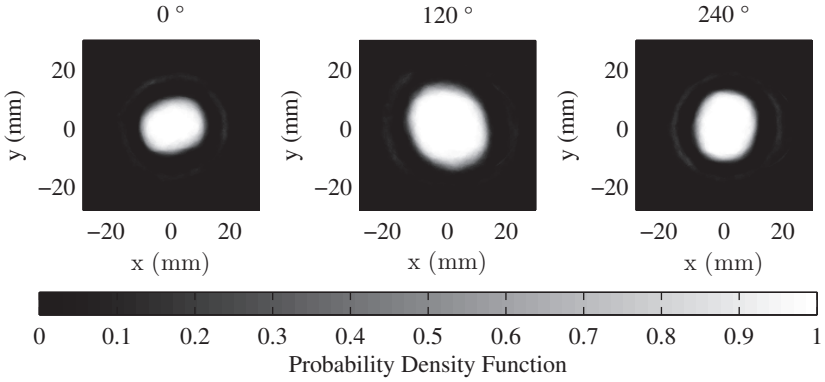

(b) $\phi = 0.82$

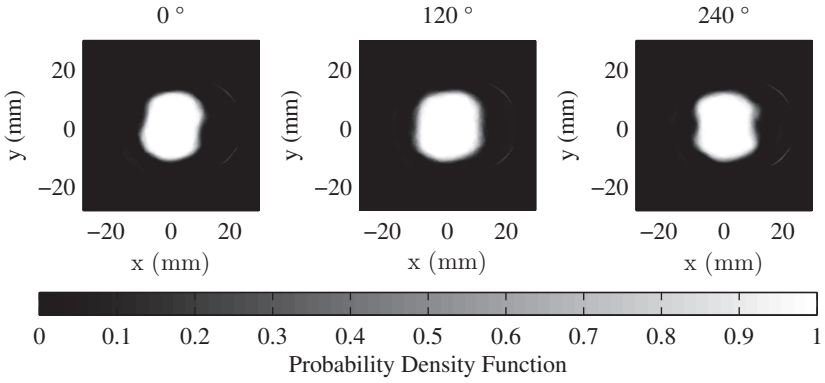

(c) $\phi = 0.94$

Figure 3.10: *Phase averaging of binarized PLIF images taken at z=10mm from the injector. The binarization was optimized to find the IRZ position.*

showing the most deformations in the IRZ, so should be representative of the ellipse fit quality for the whole study.

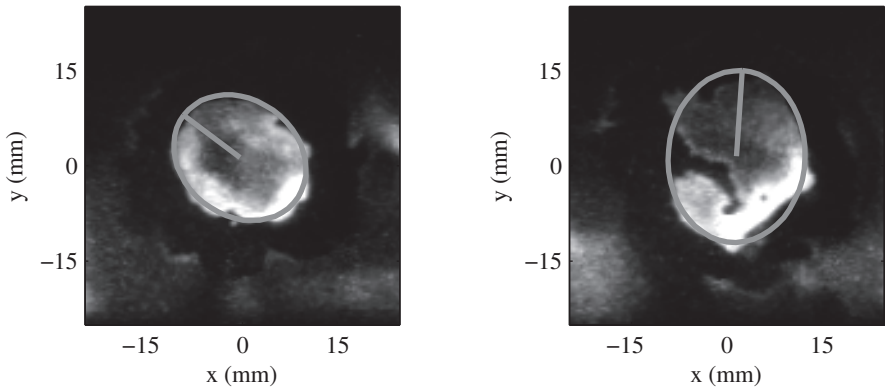

(a) Ellipse's orientation: 142°, θ=41°

(b) Ellipse's orientation: 87°, θ=71°

Figure 3.11: *Two images taken at z =10 mm from the injector for an equivalence ratio of 0.74, and the corresponding ellipse fit (colors saturated for better viewing).*

The evolution of the ellipse fit's orientation for the three equivalence ratios is presented in figure 3.12. For these measurements, taking into account the pixel resolution of the image, the precision of the orientation is at best ±5°(calculated considering an error of one pixel on both the horizontal and vertical positions of the long axis of the ellipse). The computed standard deviation on the different bins used for phase averaging range from 7° to 40°, far greater than these values. The two images selected in figure 3.11 exhibit a difference of about 20° with the phase average of their respective bins. As the ellipse fit found for them does not seem erroneous, it confirms that this higher dispersion of the observed values is due to physical fluctuations of the ellipse orientation.

As expected, the behavior for ϕ=0.74 and 0.82 is the same. The ellipse does a half turn during one cycle of the pressure instability, and this rotation seems to be in block: the orientation is almost the same for all profiles taken between 5 mm and 20 mm from the injector. The difference between the two cases is the ellipse's starting orientation in the cycle, suggesting an evolution in the phase difference between pressure oscillation and flame movement when changing the equivalence ratio. This evolution could suggest that a rotational phenomenon occurs at a frequency near 100 Hz, as a full turn is made in two cycles of the main instability. However, phase averaging at such frequencies does not show such a behavior, and no other acquired signal exhibits a peak at such frequency. This is in fact a phenomenon reminiscent of the rotation observed by O'Connor and Lieuwen (2012): in a system where a preferential direction

is present for the expansion, coherent structures inside the IRZ rotate at half the frequency of a global squeezing of the jet. For ϕ=0.94, it seems that the IRZ oscillates with an amplitude of about $\pm$ 20° around a central orientation which, as well as the phase of the cycle at which the oscillation reaches its maximum, changes almost linearly with the distance to the injector.

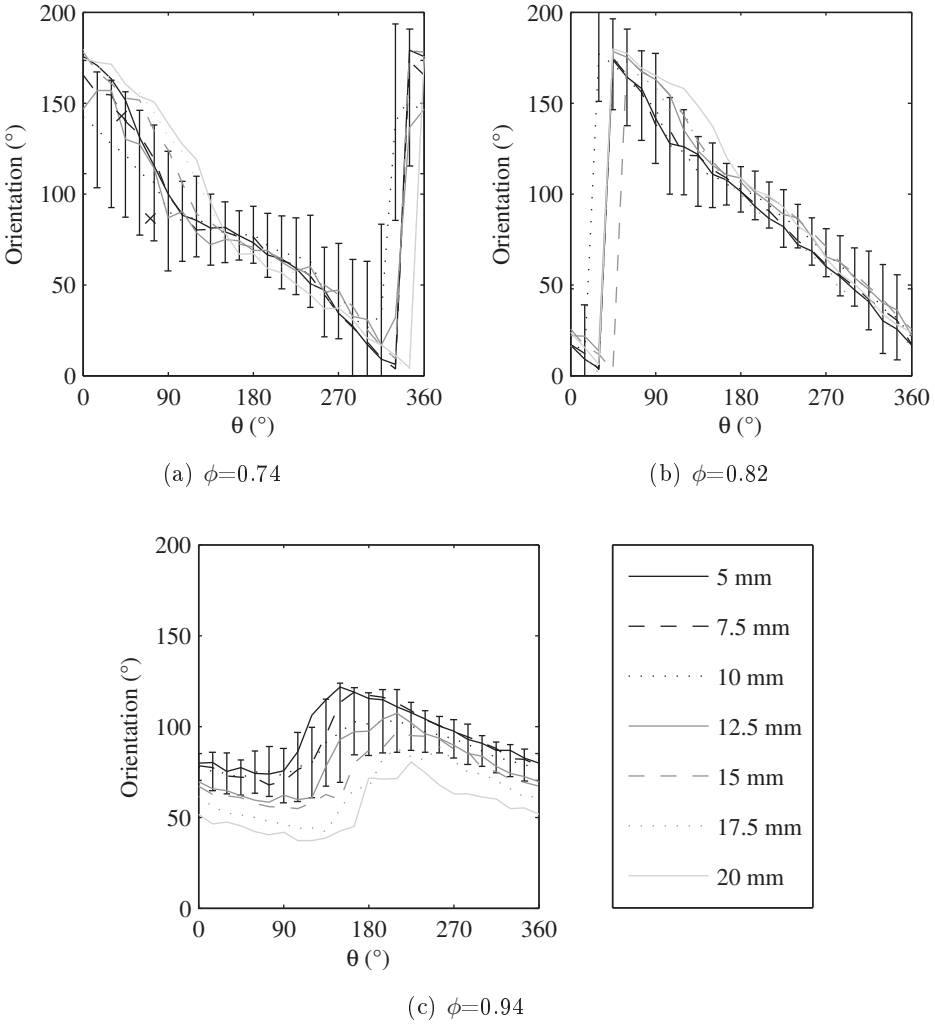

(a) ϕ=0.74 (b) ϕ=0.82

(c) ϕ=0.94

Figure 3.12: *Evolution of the mean orientation of the ellipse fit to the IRZ during a pressure instability cycle. The values for the two images from figure 3.11 are indicated by crosses. Error bars show the standard deviation for the data set at 10 mm from the injector.*

The surface of the IRZ also changes during the instability cycle. More precisely, for ϕ=0.94, the surface of the IRZ, as presented in figure 3.13

evolves symmetrically in both halves of the cycle, almost sinusoidally. For the other two equivalence ratios, the evolution is less sinusoidal. However, the maximum is reached at a similar phase in the cycle in all three injection conditions. Moreover, in all three cases, the phase at which the maximum surface is obtained changes almost linearly with the distance to the injector, suggesting that there is a convection phenomenon. The observation of the axial measurements in the next section will confirm that.

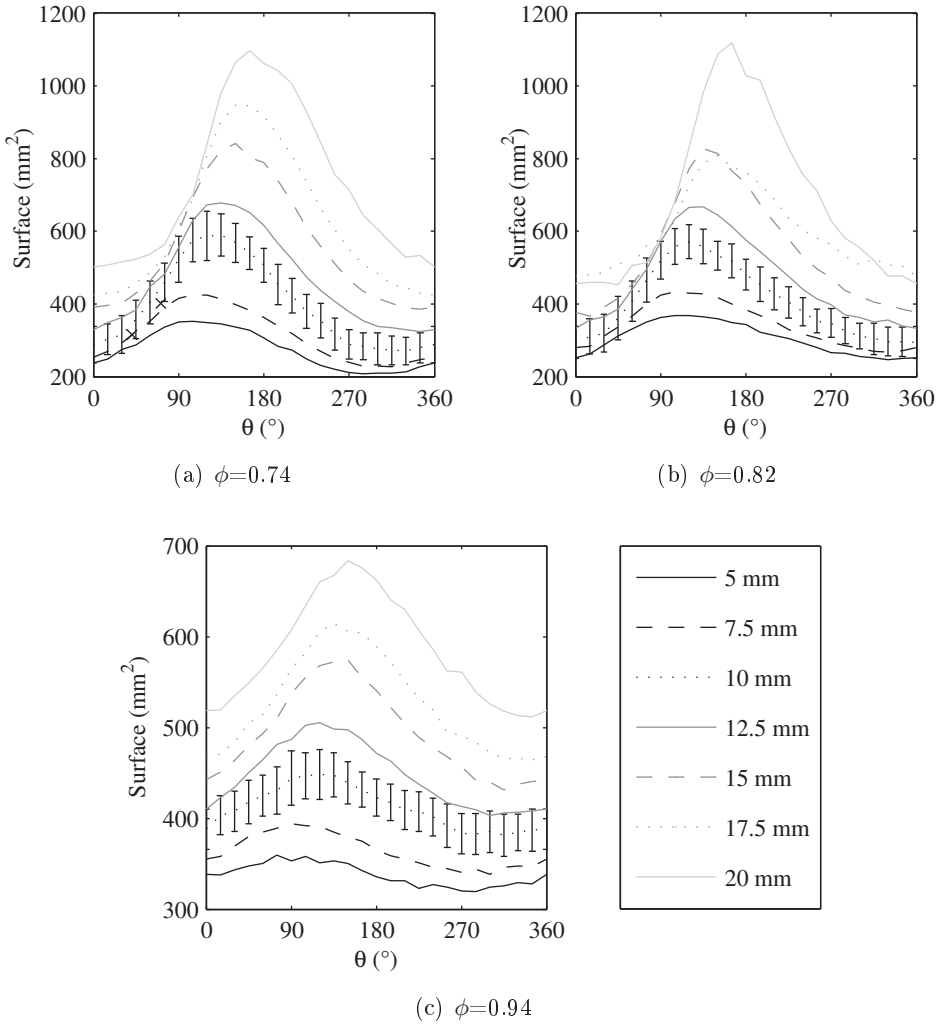

(a) ϕ=0.74 (b) ϕ=0.82

(c) ϕ=0.94

Figure 3.13: *Evolution of the mean surface of the IRZ during a pressure instability cycle, depending on the equivalence ratio and the distance to the injector. The values for the two images from figure 3.11 are indicated by crosses.*

For all three conditions the phase averaged surface to perimeter ratio, presented

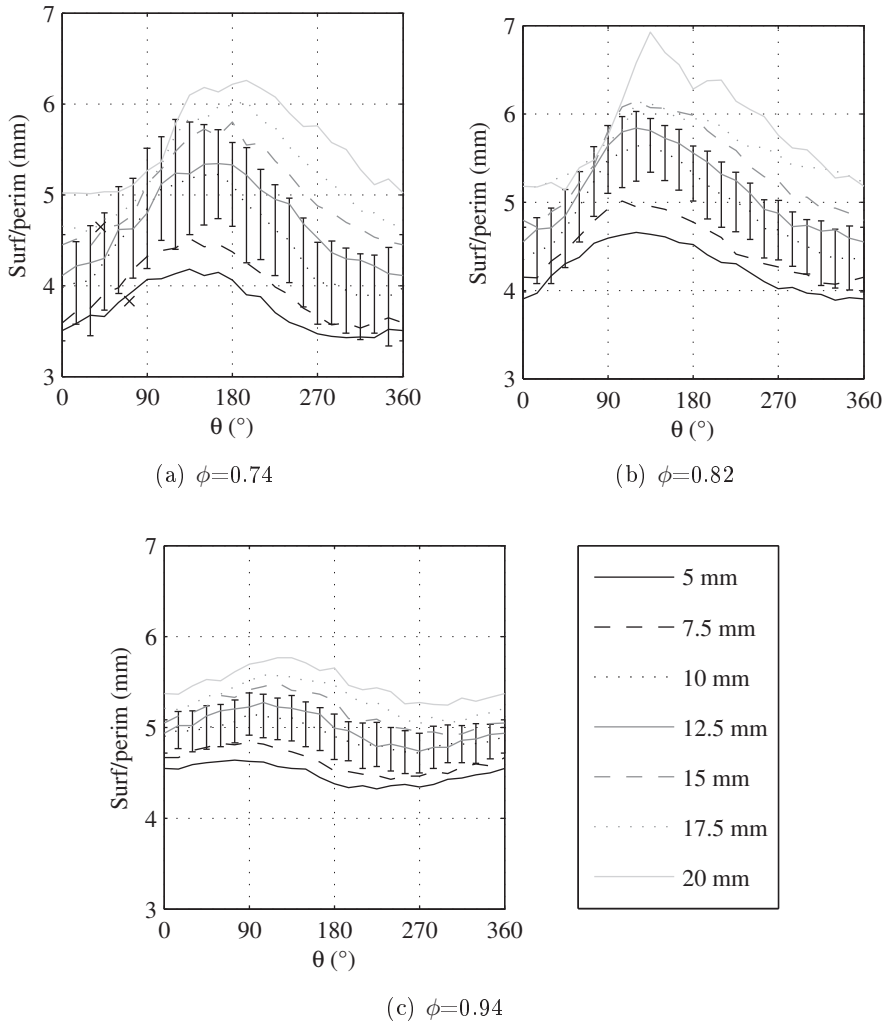

(a) ϕ=0.74 (b) ϕ=0.82

(c) ϕ=0.94

Figure 3.14: *Evolution of the surface to perimeter ratio of the IRZ during a pressure instability cycle, depending on the equivalence ratio. The values for the two images from figure 3.11 are indicated by crosses.*

in figure 3.14, shows an evolution similar to the evolution of the surface itself. The biggest IRZ surface corresponds to the highest surface to perimeter ratio, while the lowest surface corresponds to the lowest ratio, which is coherent with the evolution expected of an ellipse. Since both perimeter and surface used here are those of the real IRZ and not its elliptical fit, it confirms the validity of the approach. Both the short and long axis' length for the fitting ellipse, also evolve in the same way as the surface. A small phase shift between the two could cause a slight change in their ratio, presented in figure 3.15, and so the ellipse may not simply homogeneously be dilated during the cycle, but also slightly deformed. The conditional is used here because of the high fluctuation of the ratio values compared to the phase averaged cycle's amplitude. For ϕ=0.94, the case is a bit more complex. The long axis of the ellipse, shown in figure 3.16, seems more stable the closer to the injector, leading to bigger deformations of the fitting ellipse in that region. Farther from the injector, the same evolution as for the other two injection conditions is seen, with a phase shift between the evolution of both axes of the ellipse fit. It is to note however, that due to the average shape of the IRZ, an ellipse fit is less justifiable in this case.

In conclusion, from this phase average study of the IRZ's radial profile, it seems that for both ϕ=0.74 et 0.82, the IRZ of the flame is acting as a solid conical shape with an elliptic cross section, with variations of both the surface and axis length ratios during the instability cycle. The orientation of this ellipse indicates that it does a half rotation during a full instability cycle, suggesting that it may be due to a phenomenon occurring at a frequency close to 100 Hz. As no pressure peak is present at this frequency, it is unfortunately impossible to really verify this with phase averaging. However, results from other work (O'Connor and Lieuwen (2012)) also suggests that a preferential direction for expansion in the burner may also be the cause of such an evolution of the IRZ shape. The most noticeable difference between the two lean cases is an angle shift of about 20° in the angular position of the main axis for any given phase of the mean cycle. For ϕ=0.94, the IRZ is also broadly elliptical, but with two horizontal slits. The main axis' orientation changes with the distance to the injector, and there is no global rotation of the IRZ. Rather, there is an oscillation of $\pm$ 20°around the main orientation axis during a mean cycle.

3.6.2 Phase average reconstruction of the axial profile of the IRZ

As shown when discussing the global mean of the PLIF images, axial images of the IRZ were also taken. They allow to also monitor the evolution of the IRZ with the distance to the injector, and to make comparisons between the results obtained from PLIF imaging and from chemiluminescence, both on

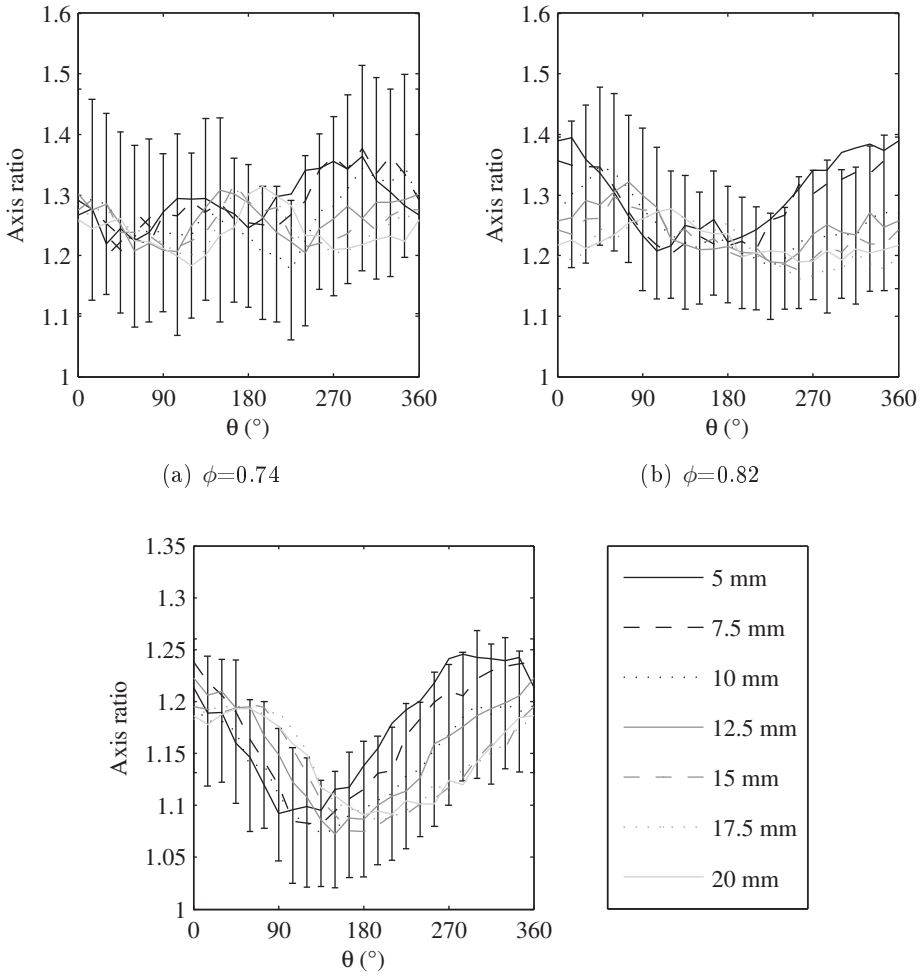

(a) ϕ=0.74 (b) ϕ=0.82

(c) ϕ=0.94

Figure 3.15: *Evolution of long to short axis ratio of the IRZ during a pressure instability cycle, depending on the equivalence ratio. The values for the two images from figure 3.11 are indicated by crosses.*

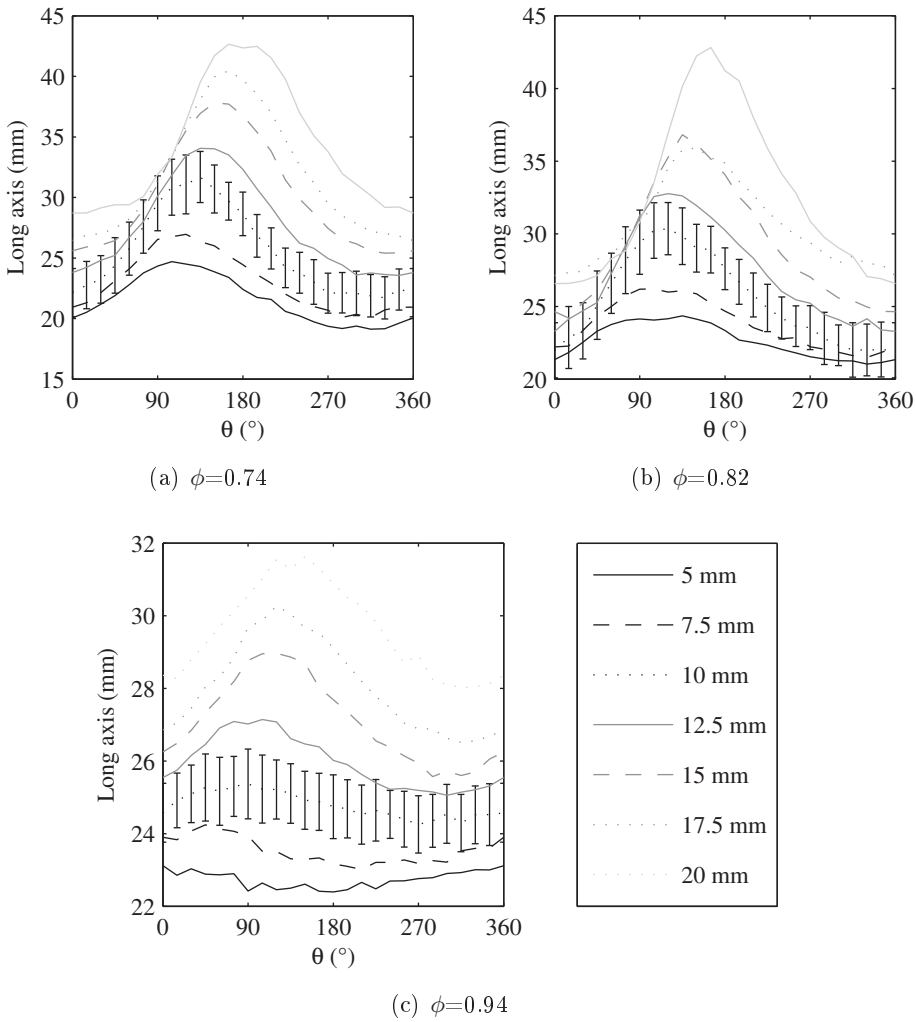

(a) ϕ=0.74 (b) ϕ=0.82

(c) ϕ=0.94

Figure 3.16: *Evolution of long axis length of the IRZ during a pressure instability cycle, depending on the equivalence ratio.*

phase average and modes obtained from the DMD analysis in the next chapter.

The phase averaging results for the axial OH PLIF measurements are presented in figure 3.17. For each setting of the burner, the presence of an opening and closing of the flame during the instability is detected. This opening however is much more marked for ϕ=0.74 and 0.82, as was already suggested by the study of the radial OH PLIF profiles: on top of a higher surface variation observed in the radial profiles in these cases, the turning elliptic shape of the IRZ at these injection conditions ensures that on a vertical profile, a bigger variation is seen than for the case ϕ=0.94. Moreover, the 20° difference in the orientation of the elliptic shape of the core at any given phase value for ϕ=0.74 and ϕ=0.82 is also visible on this set of images: even though the phase average is made using bins 15° wide, a shift of 15° or 30° of the images from the cycle at ϕ=0.82 allows to obtain a profile very similar to the profile at ϕ=0.74 at any calculated phase.

The pulsation of the IRZ is also visible in the high speed images of the flame, and noticeable from the movie without any further processing. This confirms that the movement of the flame (and its IRZ) is indeed at the expected frequency, and not a multiple. The evolution of the flame shape from these images using the phase averaging method is shown in figures 3.18, 3.19 and 3.20. Without surprise, for the part in common for the two measurement types, the results of phase averaging are similar. The overall chemiluminescence images allow to see that the opening and closing of the flame looks in all cases like a vortex shedding. For ϕ=0.94, this phenomenon was not clearly visible in the OH PLIF measurements because it is only strong enough further away from the injection.

The phase averaged profiles from both axial and radial imaging of the flame can thus confirm that in the three cases, the combustion instability is the convection of a strong vortex down the combustion chamber, accompanied by a change in pressure in the burner. There are broadly two dynamics: for the two leaner cases, the vortex shedding is clearly visible from the injection point, and the radial images showed that the IRZ is elliptical and not circular as was first expected. For ϕ=0.94 however, the vortex's effect on the geometry of the IRZ and flame is weaker, and only clearly visible further away from the injection points. Thus, the flame is not only quieter in these conditions, but also more stable.

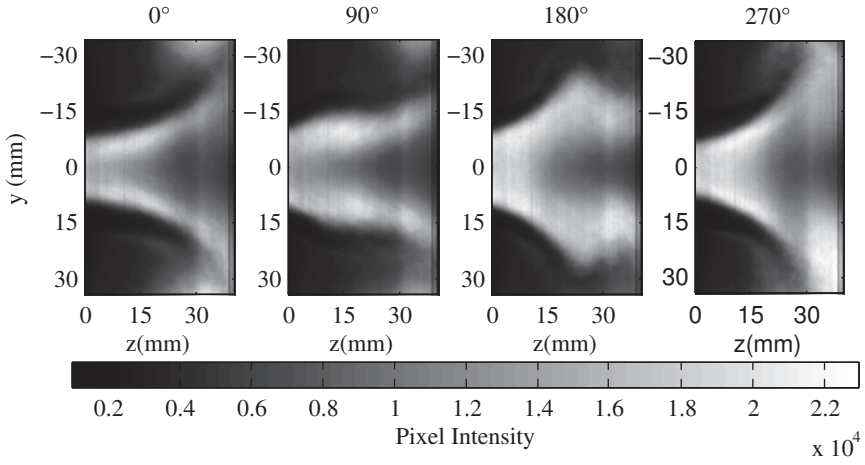

(a) ϕ=0.74

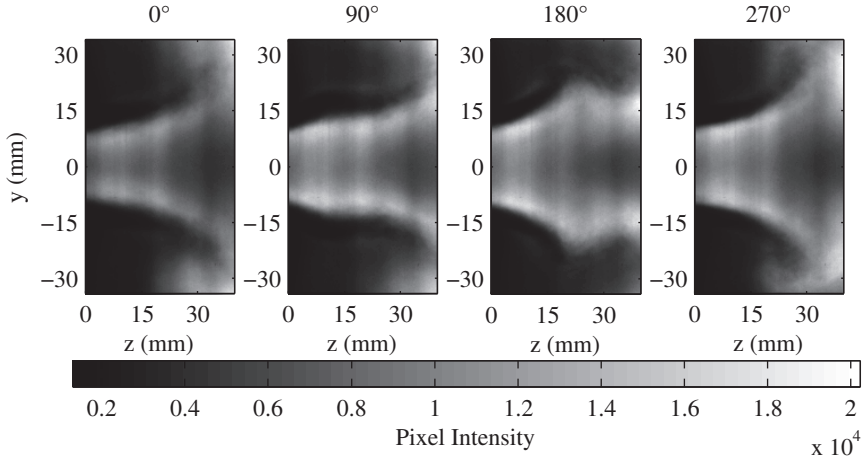

(b) ϕ=0.82

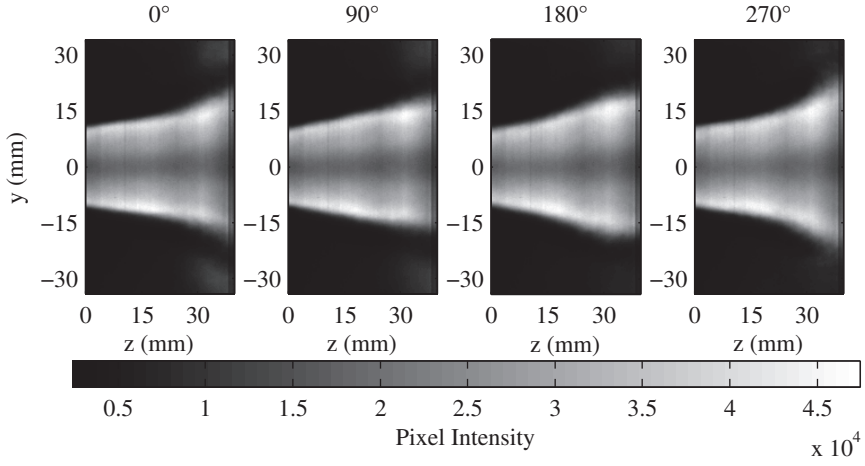

(c) ϕ=0.94

Figure 3.17: *Evolution of the IRZ during a cycle of the pressure oscillation as measured with axial OH PLIF images. The reference is the pressure in the injector.*

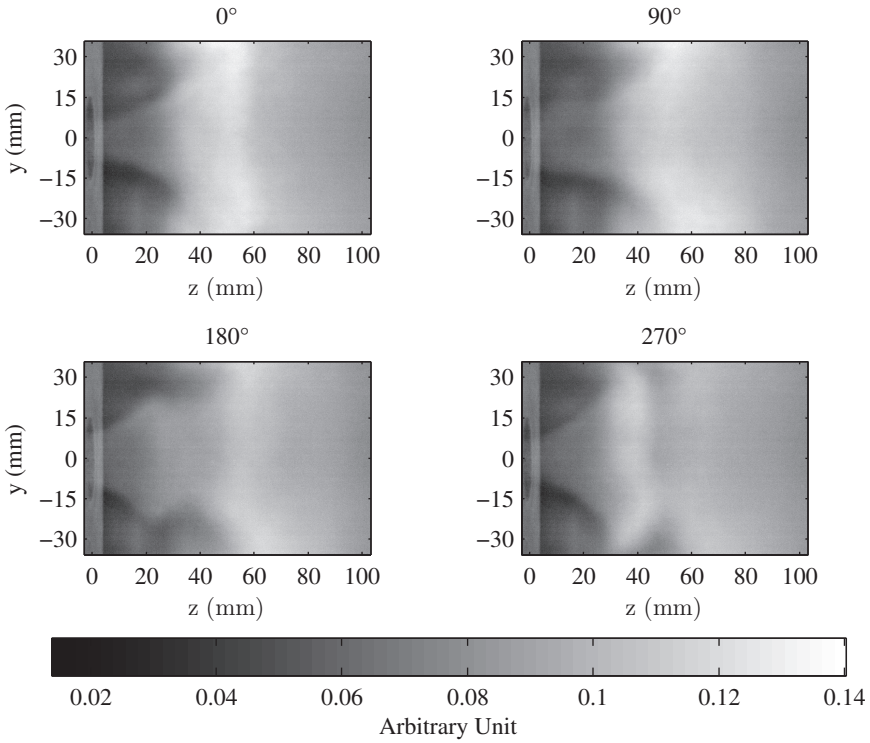

Figure 3.18: *Evolution of the overall chemiluminescence during a cycle of the pressure oscillation for ϕ=0.74, axial view. The reference for the phase is the pressure in the injector.*

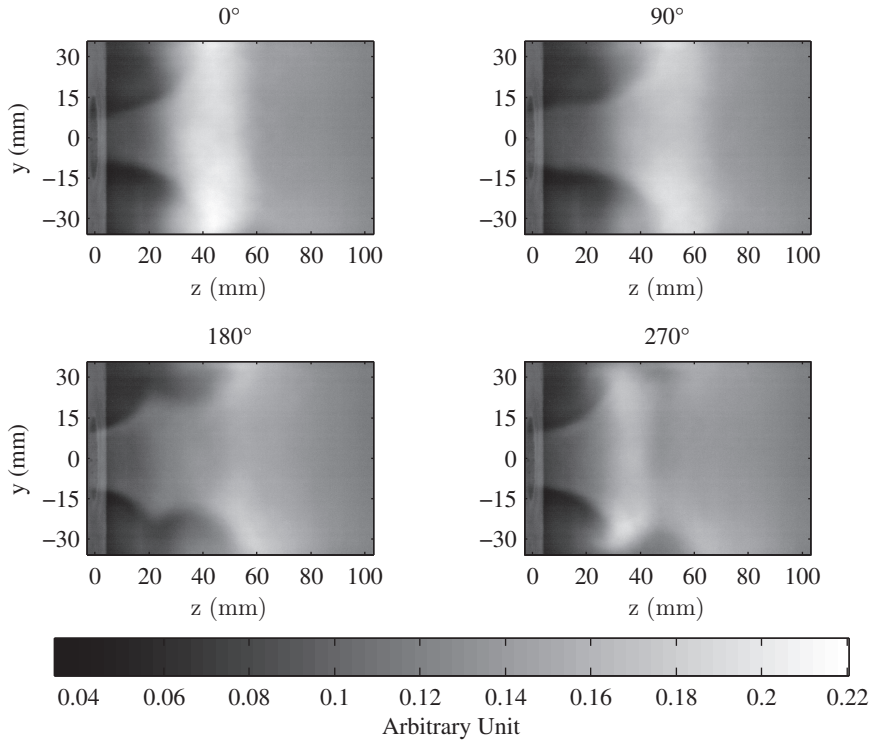

Figure 3.19: *Evolution of the overall chemiluminescence during a cycle of the pressure oscillation for ϕ=0.82, axial view. The reference for the phase is the pressure in the injector.*

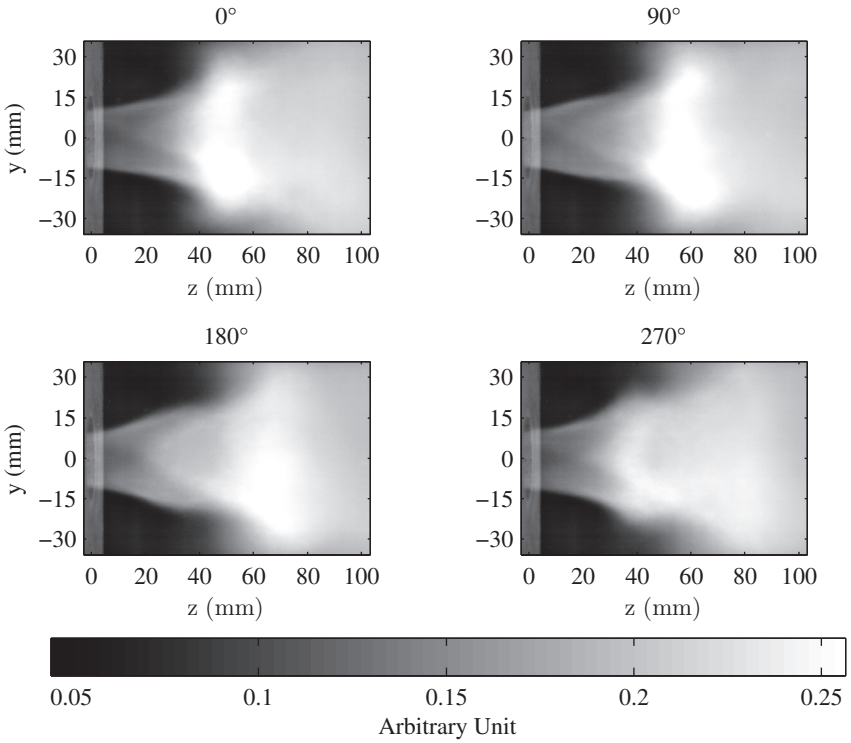

Figure 3.20: *Evolution of the overall chemiluminescence during a cycle of the pressure oscillation for ϕ=0.94, axial view. The reference for the phase is the pressure in the injector.*

3.7 Use of the phase average to obtain the equivalence ratio from absorbance and LIF measurements.

3.7.1 Direct results from the measurement system: absorbance fluctuations

3.7.1.1 General results

As presented in chapter 2, the absorbance signal exhibits a strong correlation with the pressure fluctuations at the main instability frequency. Calculation of the values of the phase shift by both cross correlation and cross power spectral density of the signals gives -100°± 6° for an equivalence ratio of 0.74, -138° ± 6° for ϕ=0.82, and 180°±6° for ϕ=0.94. The measurement at 3 kHz makes for the low phase precision of 25°. The results obtained from phase averaging are presented in figure 3.21: they confirm these calculations.

As with the other diagnostics, the absorbance measurements exhibit variations during a test run of the burner. The results obtained during measurements for each of the three studied equivalence ratios are presented in figure 3.22. The error-bar shows the phase average±standard deviation, with the data points in gray. This shows that even though the standard deviation is greater than the evolution during a given cycle, the data repartition also follows that evolution and thus is physical, similarly to what is observed on the pressure output from the microphones.

The standard deviation represents 15-17% of the phase average value for the absorbance measurements, but seems to be due to physical variations in a given instability cycles' amplitude, as it is in line with the values obtained for pressure and chemiluminescence measurements.

3.7.1.2 Phase bin repartition

As presented in the previous section, visualizing the instantaneous results as a cloud of data gives the impression that the results have a very broad dispersion. Since the calculation of equivalence ratios needs precise measurements of both absorbance and absorption length, further examination of the value repartitions is needed.

The histograms of absorbance, pressure in the injector and fresh gas length (found using a method that will be discussed in detail in the next section) are presented in figure 3.23. The interesting result is that for pressure, the distribution is close to what is expected from a sinusoidal signal for equivalence ratios 0.74 and 0.82. However, this is not really the case for equivalence ratio

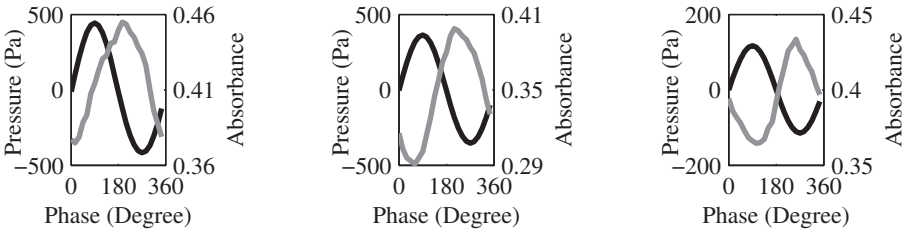

(a) ϕ=0.74 (b) ϕ=0.82 (c) ϕ=0.94

Figure 3.21: *Phase averaged cycles of the absorption measurements (gray) and the acoustic pressure in the injector tube (black), at the different injection conditions.*

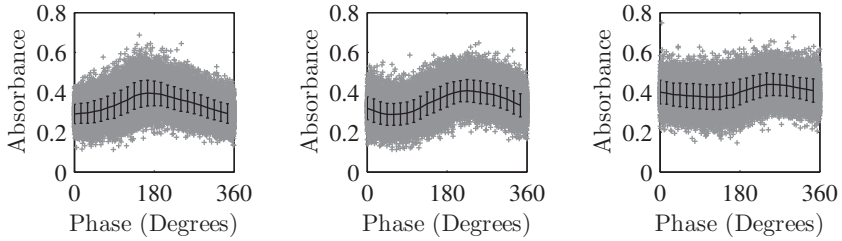

(a) ϕ=0.74 (b) ϕ=0.82 (c) ϕ=0.94

Figure 3.22: *Repartition of the absorbance data points during a test run for each injection condition. The line in black is a phase average computed using bin of 15° width, with the standard deviation for the data set in each bin as error bar.*

0.94, where the global distribution is very close to a Gaussian, with two weak peaks at ±50 Pa. That kind of distribution however, is not found for the two diagnostics used for the equivalence ratio calculations. In the case of the absorbance, the global distribution is close to a Gaussian, while for the length of fresh gases it is closer to a log-normal distribution.

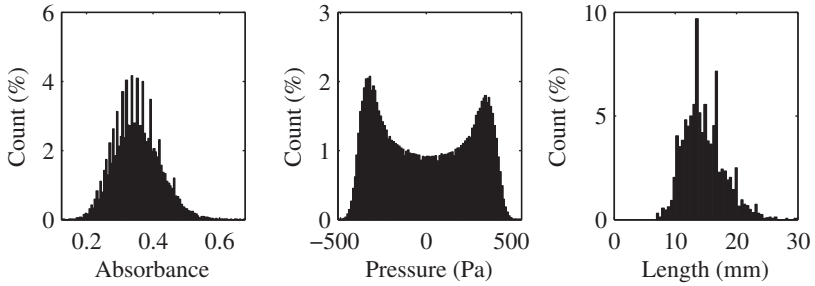

(a) ϕ=0.74

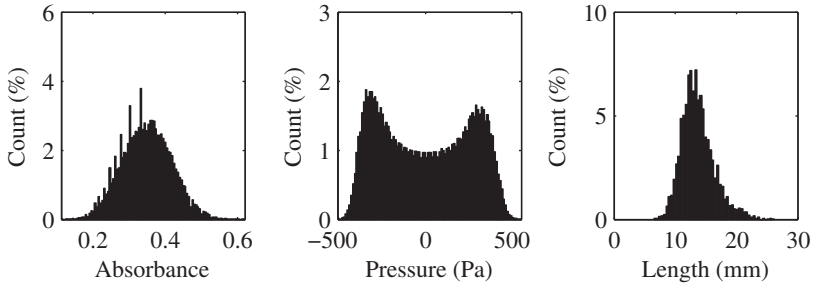

(b) ϕ=0.82

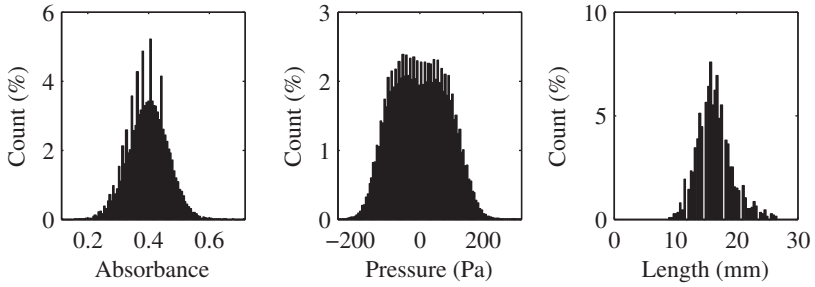

(c) ϕ=0.94

Figure 3.23: *Global repartition of the data points in the three injection conditions: absorbance, pressure inside the injector, and fresh gas length.*

The distribution of values for the absorbance for various phase bins is presented in figure 3.24. For each phase bin (15° wide), the values also have a Gaussian distribution. This confirms the validity of the phase average: even though

ϕ	Relative std (mean)	Relative std (min)	Relative std (max)
0.74	50%	42%	61%
0.82	52%	50%	55%
0.94	84%	77%	93%

Table 3.6: *Characteristics of the standard deviations obtained on the bins used for phase averaging of the absorbance, relative to the averaged cycle's amplitude. The "min" and "max" are the values for the bins containing the minimal and maximal dispersion of values, and mean the average standard deviation obtained.*

the total repartition doesn't look like what is expected from a sinusoidal evolution, for each of the phases a Gaussian repartition around the average value is obtained. The broad dispersion of the data is thus the cause of the change in the total distribution's shape. The standard deviation relative to the amplitude of the average cycle obtained in each condition is given in table 3.6. The table shows the maximal and minimal standard deviation obtained inside the different phase bins, as well as the average of these values. They are quite important: from 50% of the average cycle's amplitude for ϕ=0.74 ad 0.82, up to 80% for ϕ=0.94. This is more than a factor 4 increase when compared to the results obtained for the pressure inside the injector, explaining that the distribution is globally seen as a Gaussian distribution for the absorbance.

3.7.2 Length of fresh gases fluctuations: from radial PLIF

The length of fresh gases the infrared laser went through while making a measurement is an important factor when using absorption to quantify the presence of a species. Indeed the estimated concentration of propane (and thus equivalence ratio) is proportional to both absorbance and length. This means that the evolution of the equivalence ratio may be different from the absorbance alone, if the absorbance and possible fluctuations on the fresh gas length do not have the same phase shift with the pressure inside the injector. A schematic description was given at the beginning of this chapter in figure 3.1, showing a typical case where the laser beams goes two times through absorbing fresh gases. The addition of those two lengths $L1$ and $L2$ gives the total absorption length.

The ideal case would be a configuration where the length is known and fixed, which is unfortunately not the case in the CESAM burner: the flame stabilizes partly inside the injector. It was thus necessary to use the radial OH PLIF measurements made 10 mm after the injector, where the absorption system was also subsequently placed. The method used to estimate the length of fresh gas on any image was explained in chapter 2.

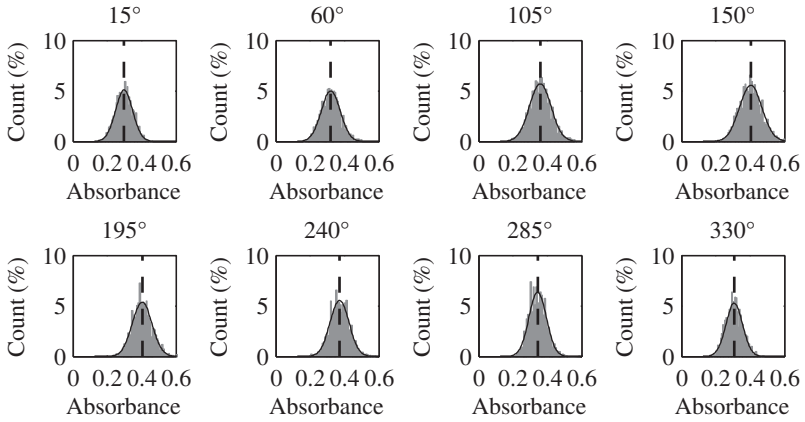

(a) ϕ=0.74

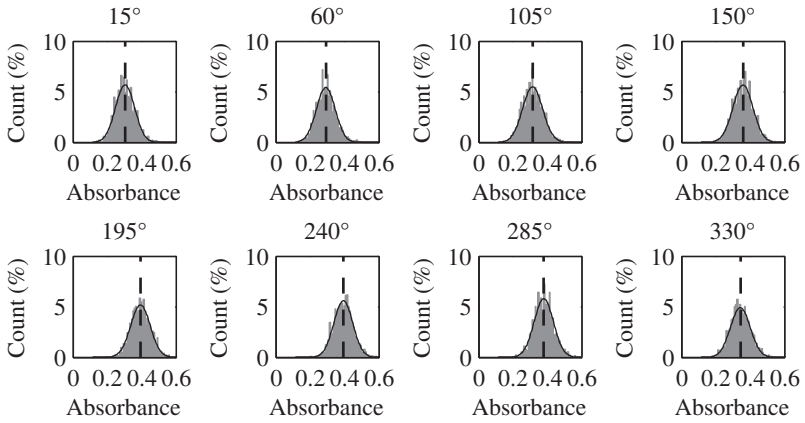

(b) ϕ=0.82

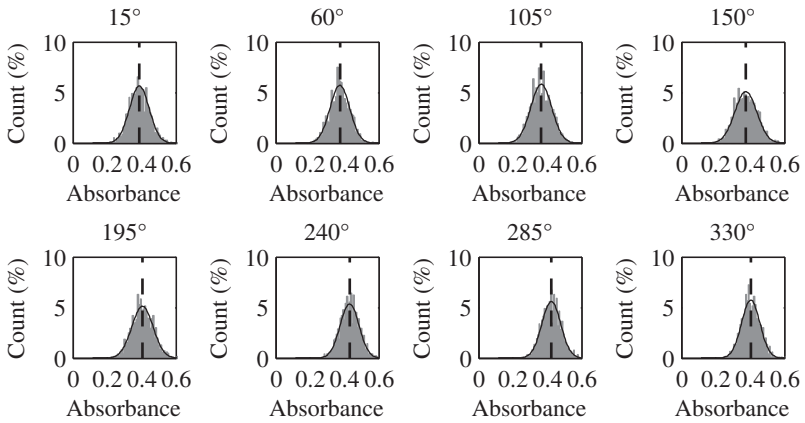

(c) ϕ=0.94

Figure 3.24: *Repartition of the absorbance data points in the three injection conditions. The best Gaussian fit is drawn in black, and a vertical dashed line marks the phase average.*

As the OH PLIF was taken at the low acquisition rate of 10 Hz, the only way to correct the absorbance measurements for fluctuations of absorption length is to compare the phase averages. For the OH PLIF measurements, due to the time constraints on the length of the test runs, only sets of 630 consecutive images are available. Thus the presented images were computed doing the phase average on 10 different measurements, allowing the use of 6300 initial images for each test condition. Due to the low quality of the signal in the ORZ however, not all images are usable so a lower number of images is eventually used.

3.7.2.1 Dispersion of the values in a cycle

The determination of the average absorption length was one of the most problematic parts of the post-processing of the data obtained during the experiments, as the high difference in signal level between the IRZ and ORZ meant that the limit between fresh gases and the ORZ was difficult to determine, and at the highest equivalence ratio, often not clearly visible enough. Thus it is important to show that no strong bias exists in the results, since it is not entirely certain that no erroneous data points are present in the final results.

As a first reminder, the horizontal pixel pitch for the images used to determine the fresh gas length 10 mm downstream from the injector is 0.37 mm/pixel. As a laser crossing the entire chamber at mid-height has to go through two different zones of fresh gases, there is an uncertainty for any image of at least 1.5 mm on the total absorption length. Since the average length found at the three equivalence ratio is between 13.6 mm and 16.3 mm, it results that the expected dispersion is quite high.

Figure 3.25 shows the results of phase averaging obtained for each injection condition. The plots show for each condition a comparison between the phase average, and a phase median (the median of the values in each phase bin) to check the potential effect of erroneous values, which have a big discrepancy, on the results obtained. The error bars show the standard deviation (so the data showed is the phase average$\pm$standard deviation). Finally, to show the bias it could create (notably because of a higher background signal due to the injector's wall on the left side), the averages obtained using only the values computed on the left side, the right side and the sum of both sides for each image are given. These results show that, taking into account the dispersion of the data points, an uncertainty of 5-6 mm seems to exist for the computed absorption lengths.

In order to see the actual repartition behind the big standard deviation, the histograms of the computed values for each phase bin are shown in figure 3.26, along with the best fit found for the distributions. The histograms show

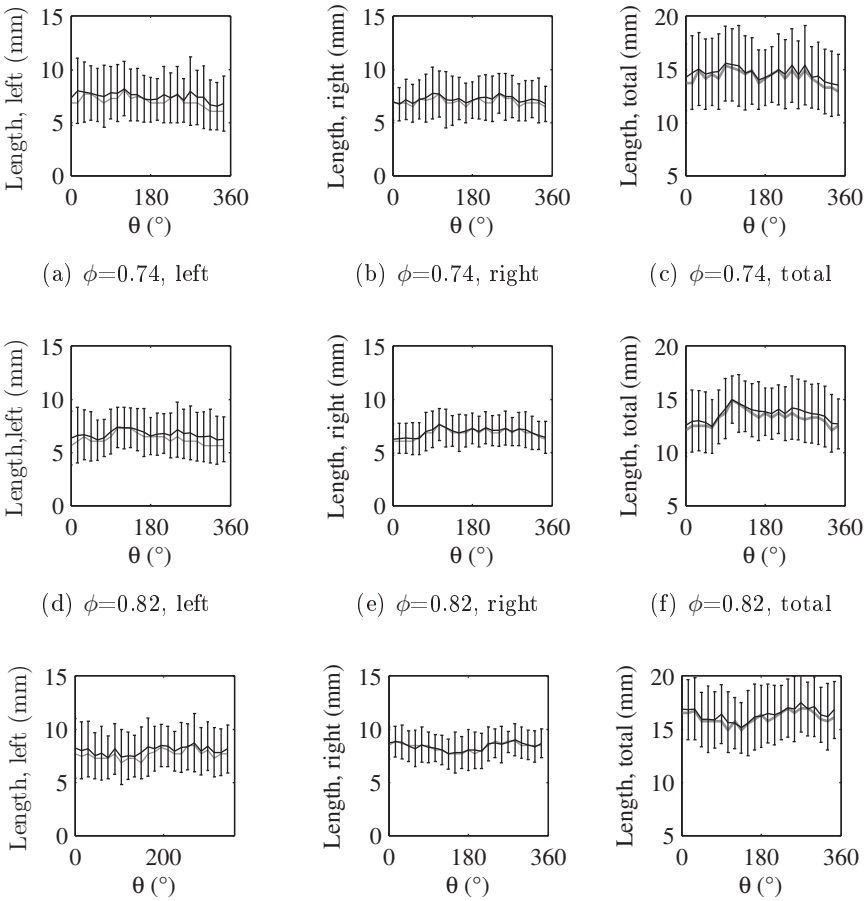

(a) ϕ=0.74, left (b) ϕ=0.74, right (c) ϕ=0.74, total

(d) ϕ=0.82, left (e) ϕ=0.82, right (f) ϕ=0.82, total

(g) ϕ=0.94, left (h) ϕ=0.94, right (i) ϕ=0.94, total

Figure 3.25: *Repartition of the phase averages calculated using the left side, right side and both sides of the radial PLIF images. In black is the phase average computed using bins of 15° width, while in gray is the median for each bin. The error bars are the standard deviation for the data set in each bin.*

ϕ	Relative std (mean)	Relative std (min)	Relative std (max)
0.74	158%	128%	187%
0.82	105%	89%	118%
0.94	116%	99%	132%

Table 3.7: *Standard deviations of the fresh gas length obtained on phase bins used for phase averaging, normalized by the phase averaged amplitude fluctuations.*

that in the case of the fresh gas' length, the best fit to describe the data repartition is not a normal distribution, but a log-normal one. To better see it, 3 of the distributions obtained for ϕ=0.74 are shown in figure 3.27, with the best Gaussian and log-normal fit indicated. In all cases, a slight bias towards high values in the histograms is better taken into account by a log-normal distribution. The fact that the number of points used for the richest conditions is low is seen on the histograms of figure 3.26; only 1546 points are usable after the post-processing, leading to a number of points per bin between 39 and 72. These repartitions indicate that, since a log-normal distribution better describes the results, there may be a slight bias towards high values for the length in this case. Whether this is physical or due to the length's calculation method is unfortunately impossible to determine, even though precautions were taken to eliminate uncertain data points. Since the main interest here is the length fluctuations, the dispersion of the data is as in the previous cases normalized by the amplitude of the phase averaged fluctuation cycle. The maximum and minimum values observed on the phase bins, as well as the average of the standard deviation on all the bins are given in table 3.7. As can be seen in the table, the standard deviation is high, since in no case is it less than 59% of the average amplitude fluctuation. This means that even though the variations observed inside a single phase bin may be low compared to the length of fresh gases, it is still big when compared to the length fluctuations that are expected, casting doubt on the measured coherent fluctuations. The precision of the measurements thus means that the results of the phase average cannot be considered as reliable, since the phase averaged fluctuations observed are lower than the dispersion of data on each phase bin.

In order to limit the effect of the uncertainty on the measurements, and since the laser used for the absorption measurements has a $1/e^2$ radius of 2 mm, the length of fresh gases was computed on several adjacent lines of the PLIF images.

The results of the global phase averaging are presented in figure 3.28, where results for each line of the image around the laser position are presented. It can be seen there that the profile is not as smooth as one would expect from the study of the phase averaging of the IRZ using the same images. The case with the most rejected images in the calculations, ϕ=0.94, uses between 40 and 70 values per phase bin, while for the other two cases, the number is

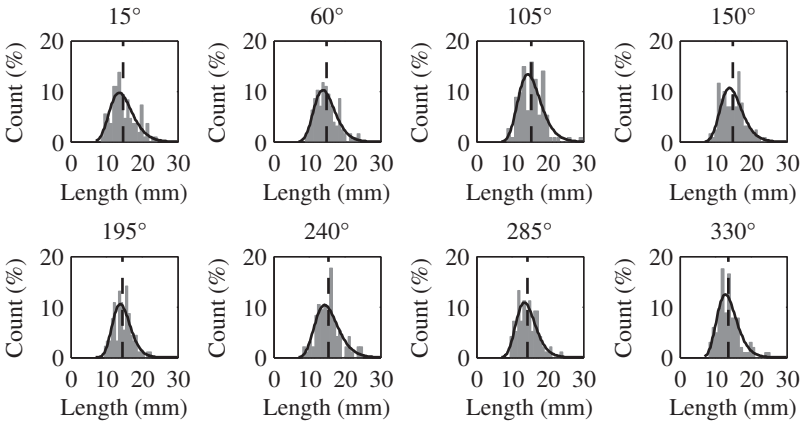

(a) ϕ=0.74

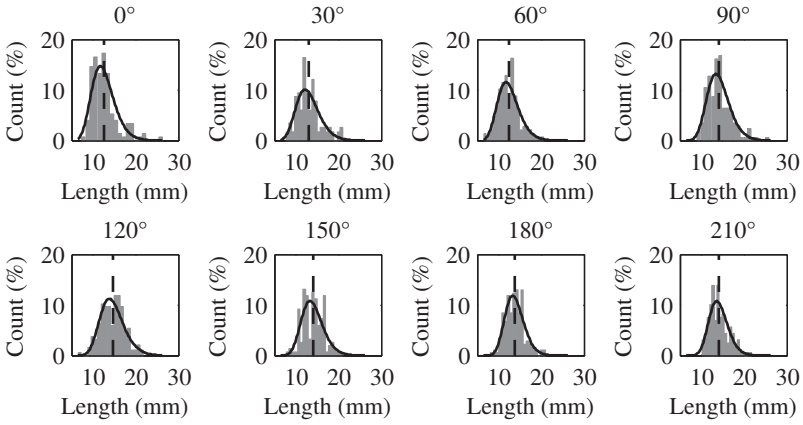

(b) ϕ=0.82

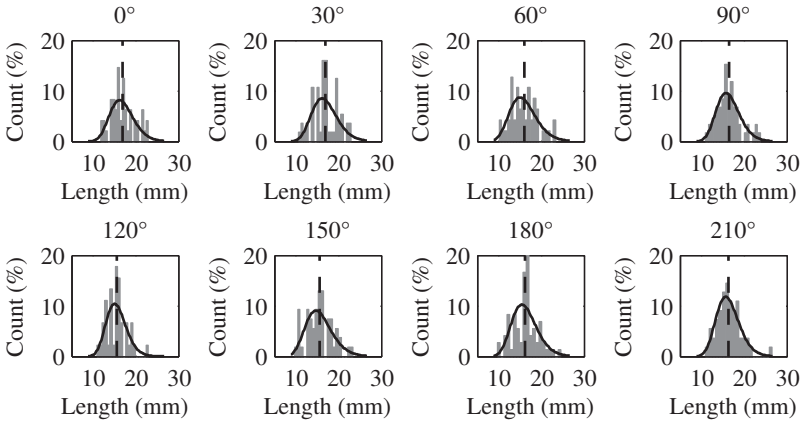

(c) ϕ=0.94

Figure 3.26: *Repartition of the fresh gas length data points in the three injection conditions. The best log-normal fit is drawn in black. The vertical dashed line marks the phase average.*

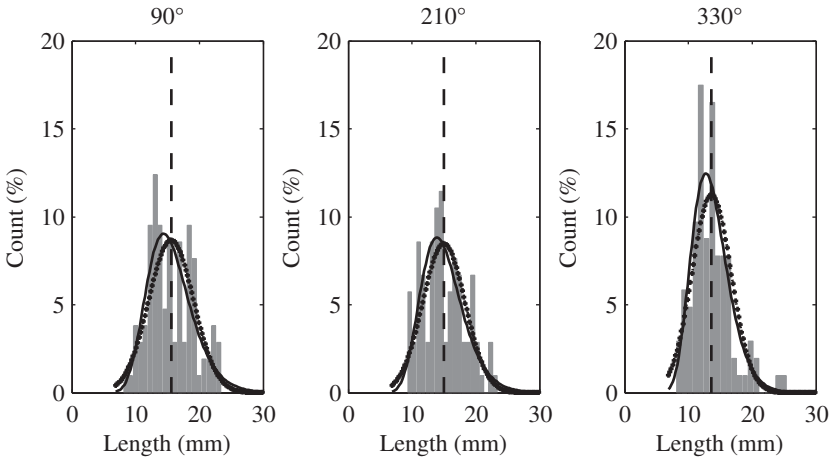

Figure 3.27: *Repartition of the fresh gas length data points at ϕ=0.74. The best log-normal fit is drawn in black, and the best Gaussian fit is in crosses. The vertical dashed line marks the phase average.*

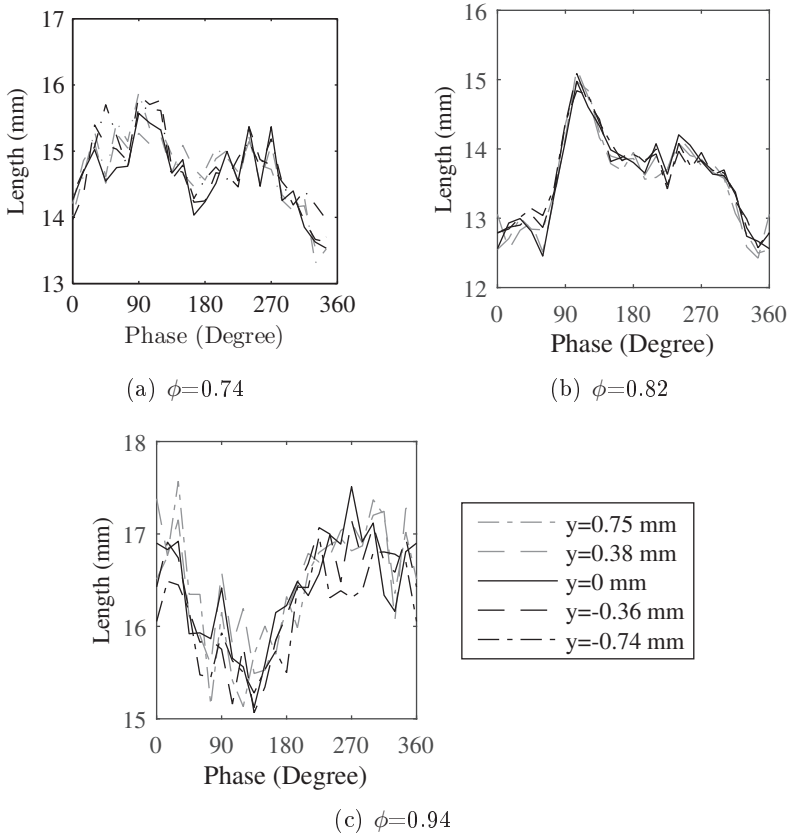

(a) ϕ=0.74 (b) ϕ=0.82

(c) ϕ=0.94

Figure 3.28: *Phase averages of the length calculated for the central lines, at the different injection conditions.*

about doubled. Even though the numbers may seem high, peaks can be seen from one point to the next in the phase averaged cycle, with as much as 1 mm between two adjacent phase values, while the global variation in a cycle is of the order of 3 mm. The results must thus be taken with caution.

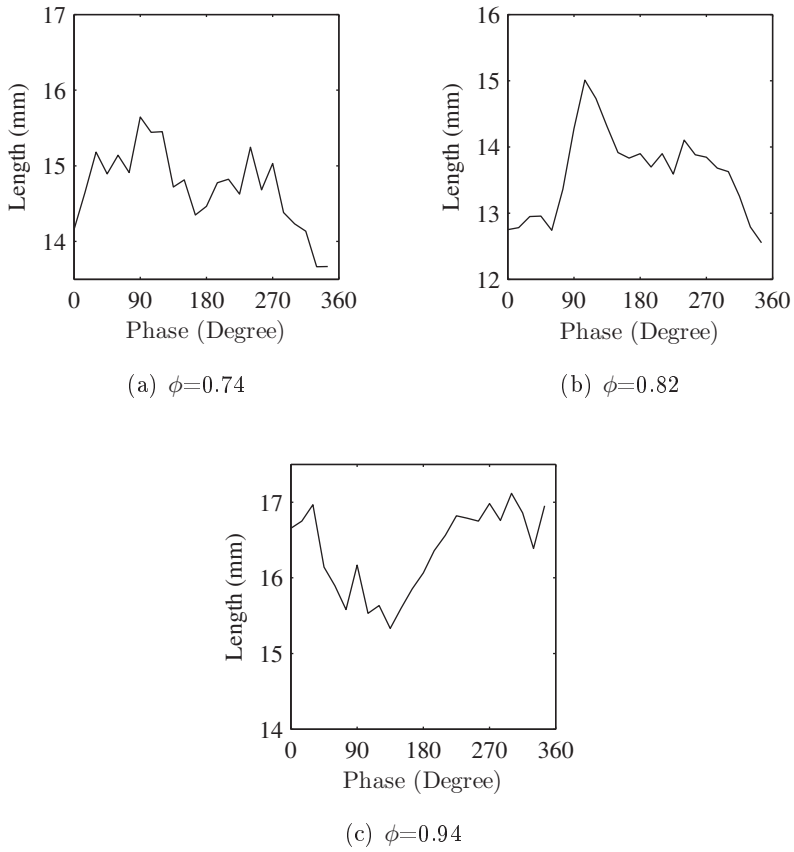

(a) ϕ=0.74 (b) ϕ=0.82

(c) ϕ=0.94

Figure 3.29: *Absorption length calculated by averaging the fresh gas length along the laser's path.*

As the laser goes simultaneously through all these lines at the same time, and since these values are close from one another, a general absorption length can be computed by averaging the results obtained for all the lines. The resulting phase averages are presented in figure 3.29. The statistics on these absorption lengths, summarized in table 3.8, show that the detected variation of that length is about 2 mm for all three equivalence ratios, but the variation in the global average between them is also of the same order, leading to relative variations in length of 10% to 20 %.

Unfortunately, as the profiles are irregular, it is difficult to estimate the

Equivalence ratio	0.74	0.82	0.94
Average absorption length (mm)	14.7	13.6	16.3
Variation in a cycle (mm)	2.0	2.4	1.8
Relative variation (%)	13.4	18.0	10.9

Table 3.8: *Statistics on the phase averaged absorption length.*

phase shift with the reference acoustic pressure inside the injector, to confirm whether absorbance and absorption length variation are in phase, in phase opposition or slightly shifted. The clearest case seems to be ϕ=0.94, where the absorption length is roughly in phase with absorbance fluctuations: both are minimal at a phase of 180°, suggesting that at least a part of the observed absorbance fluctuations is caused by the absorption length variations. In the same way, for the two other equivalence ratios, the absorption length seems to broadly follow the variations of the absorbance, but is not as well defined.

3.7.3 Length of fresh gases fluctuations: from axial PLIF

The previous section showed that the fresh gas length's fluctuations inside a given phase bin are important compared to the length itself. The main source of doubt on the previous calculations is the correct detection of the fresh gases-ORZ limit, which may play an important role in the final dispersion obtained. In order to see if the big variation of the fresh gas length is real, its calculation at the injector position using axial PLIF images is conducted here, since no error on the detection of the outer limits of the fresh gases' domain is possible there.

When using the axial PLIF measurements, the width of the fresh gases can indeed be calculated immediately at the exit of the injector, where the external limits of the fresh gases containing propane is known and fixed: 15 mm from the injector's axis. It is then only a matter of detecting the strong IRZ-fresh gases border to obtain a measurement of that width. The results of these calculations at the injector are presented in figure 3.30. The distributions obtained are narrower than when the calculation is made from the radial images. This is to be expected, as only the position of the IRZ limits have influence here. This is also confirmed by the relative importance of the standard deviation compared to the average cycle amplitude: as indicated in table 3.9, in all cases the standard deviation is under 100% of the cycle amplitude, which is not the case on lengths calculated using the radial profiles. An indication that a slight bias still existed in the calculation using those, is that at the injector the calculated lengths' repartition is best fitted by a normal distribution instead of a log-normal one, which has more high values. These results are thus closer to the normal distributions obtained for both pressure and absorbance measurements.

ϕ	Mean std (mm)	Relative std (mean)	Relative std (min)	Relative std (max)
0.74	2.5	35%	29%	41%
0.82	2	51%	37%	71%
0.94	1.23	81%	65%	96%

Table 3.9: *Standard deviations of the fresh gas length from axial OH-PLIF measurements: mean, minimum and maximum obtained on the different bins used for phase average calculations, and value of the mean standard deviation.*

In the present case, the fact that the external limit for the fresh gases is known and fixed showed that even though the variations observed for samples attributed to the same phase are lower than the results obtained on radial images 10 mm from the injector, there is still a fairly broad distribution of the values in absolute length. The absolute amplitude of the fluctuations is in particular more important at the low equivalence ratios than at the highest value. This was to be expected: from looking at the phase averages of the axial measurements for ϕ=0.74 and 0.82, the expansion of the flame in a cycle starts at the injector, while for ϕ=0.94, the effect happens farther from it. The flame is also more wrinkled the lower the equivalence ratio. The values presented in table 3.9 being normalized by the amplitude of the phase averaged cycle, the richest case seems the most unstable, while in reality it is due mainly to smaller coherent fluctuations of the fresh gas length. In order to illustrate the physical origin of these fluctuations, examples of axial PLIF images obtained for ϕ=0.74 in a single bin (θ=45°) are given in figure 3.31. From left to right, the lengths are lower than the phase average, approximately equal, and higher. These images show that the flame itself can be wrinkled even near the injector and instantaneously exhibiting very different levels of signal in the ORZ. In some cases the PLIF plane shows a disjointed flame in the IRZ at the injector.

Since the measurements at the injector are inherently less subject to errors due to the fixed position of the outer limit of the fresh gases, an attempt to use them for equivalence ratio calculation can be conducted. This requires the proper hypotheses to link the vertical length at the injector to the horizontal length at z=10 mm, which will be given hereafter.

The analysis of the phase averaged radial PLIF images suggests that for the three injection conditions, a link can be found between the length of fresh gases seen in the y=0 mm axis (where the laser for absorption measurements is placed) and the x=0 mm axis, common to both radial and axial measurements. In the lean cases, the ORZ is circular while the IRZ is a turning ellipse: the length in the vertical plane is equal to the length in the horizontal plane with a 180° shift in the cycle. In the case where ϕ=0.94, the images suggest that no phase shift exists between the two as no strong rotation of the IRZ exists.

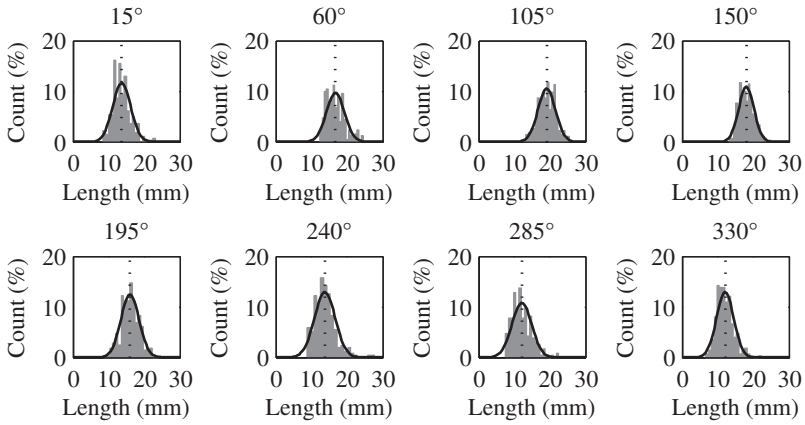

(a) ϕ=0.74

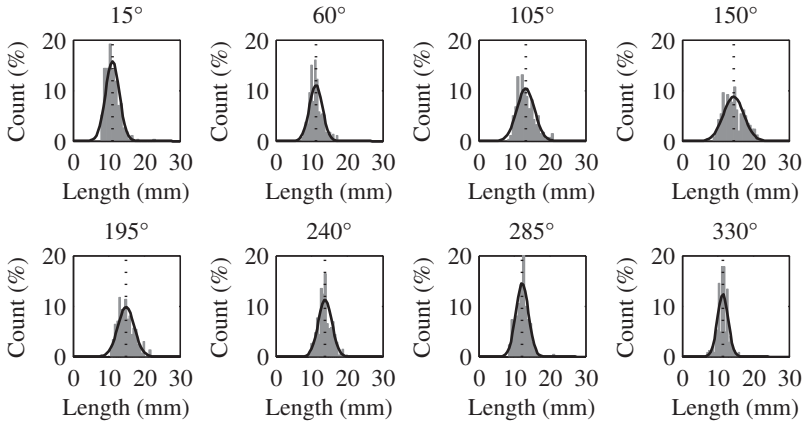

(b) ϕ=0.82

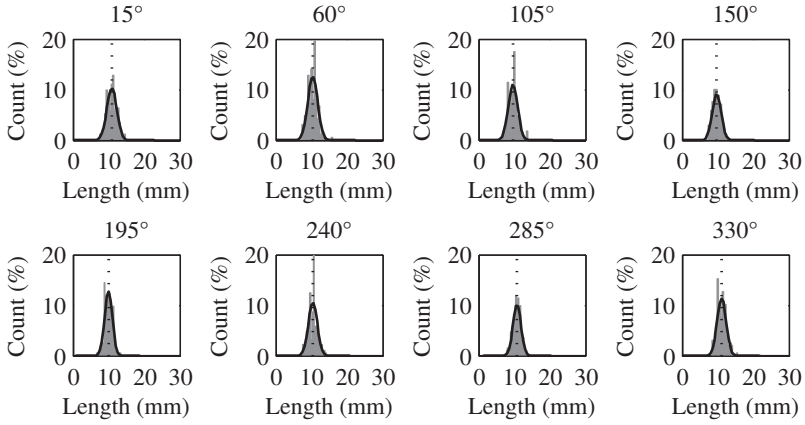

(c) ϕ=0.94

Figure 3.30: *Repartition of the fresh gas length at the injector, data points in the three injection conditions. The best Gaussian fit is drawn in black, and the vertical dashed line marks the phase average.*

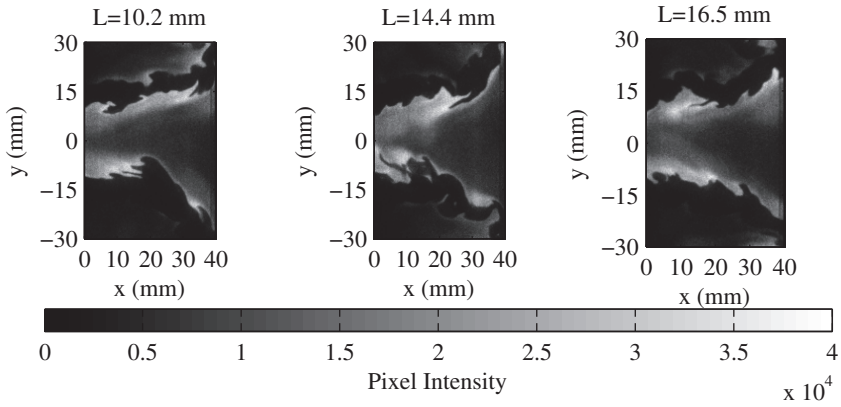

Figure 3.31: *Instantaneous PLIF images attributed to phase θ=45°for ϕ=0.74.*

The length on the vertical and horizontal directions could then be considered equal after phase averaging. The ORZ seems to present small concave slits at the same place that the IRZ does, but not as marked, so the hypothesis of equal lengths will probably lead to a small underestimation of the actual length.

These considerations allow to link the horizontal fluctuations of length to the vertical ones. The next step is linking measurements made in the vertical direction at the injector and at z=10mm. The study of the phase averaged IRZ performed previously is used hereafter. In the lean cases, the orientation of the turning ellipse seems independent of the distance to the injector in the z=5-20 mm zone. The surface of the ellipse itself has a convection speed, but supposing the ORZ adapts to the broadening of the IRZ too, this should not have a strong impact on the width of the fresh gases. For the richest case, as both the ORZ ad IRZ are nearly circular, the assumption is that the length observed will be the same.

The hypotheses just made allow to use the axial PLIF images to compute the length of fresh gases seen by the laser 10 mm away from the injector. As a reminder, these are:

- for ϕ=0.74 and 0.82, the horizontal width of fresh gases 10 mm from the injector is the vertical width at the injector, with a phase difference of 180° due to the half rotation of the elliptic IRZ in an instability cycle.
- for ϕ=0.94, the horizontal width at z=10 mm and the vertical one at the injector are the same.

Using these hypotheses, the equivalence ratio will be calculated in the next section, alongside the results obtained using the radial PLIF images.

Equivalence ratio (injection condition)	0.74	0.82	0.94
Average equivalence ratio (from mean)	0.60-0.66	0.68-0.70	0.63-0.69
Relative variation in a cycle (%)	26-36	33-38	12-14
Average equivalence ratio (from median)	0.62-0.68	0.70-0.72	0.65-0.70
Relative variation in a cycle (%)	28-38	34-39	13-15

Table 3.10: *Statistics on the equivalence ratios obtained with the absorption diagnostic. For each injection condition, 5 different measurements are available.*

3.8 Equivalence ratio fluctuations

3.8.1 Using radial PLIF data

First, some of the results obtained by combining the total phase average of the absorption length from PLIF radial measurements (detailed in the previous section), and the absorbance values from one test for each equivalence ratio are given in figure 3.32. Two results are presented, to illustrate the sensitivity to the absorption length: in black are results obtained by combining for each phase value the phase average, and in gray the median of the length in each phase bin was used instead. The difference between the two values for the lengths can be up to 1 mm. This can lead to differences between the computed equivalence ratio values of up to 0.02. Moreover, the variability in the absorbance measurements between two tests at the same conditions also leads to a variability in the results obtained. The relative variations however are conserved, suggesting that it is mainly a shift in the global value of the signal in this case. The global phase difference between equivalence ratio and pressure in the injector seems to be conserved from the variations observed when looking at the absorbance values (see section 3.7.1).

Statistics on the variations on the average equivalence ratio and relative variation obtained in a cycle depending on the test runs are presented in table 3.10. If the cycle amplitude is considered accurate despite the discrepancy on the global equivalence ratio, the fluctuations in the equivalence ratio at the beginning of the chamber are about 35% at both ϕ=0.74 and 0.82, and a lower 15% variation in the case where ϕ=0.94. There is however an incoherence in the evolution of the computed equivalence ratio: while the mean value obtained for ϕ evolves as expected when changing the equivalence ratio from 0.74 to 0.82, for an equivalence ratio of 0.94, the value obtained is lower than in the two previous cases. As the absorbance exhibits a correct behavior for the three equivalence ratios, but the fresh gas length found using this method is higher for ϕ=0.94 than in the two other cases, the length calculation seems to be the main cause of error here. Since this equivalence ratio was the most problematic for the length calculation using the radial PLIF measurements, such a result is not surprising.

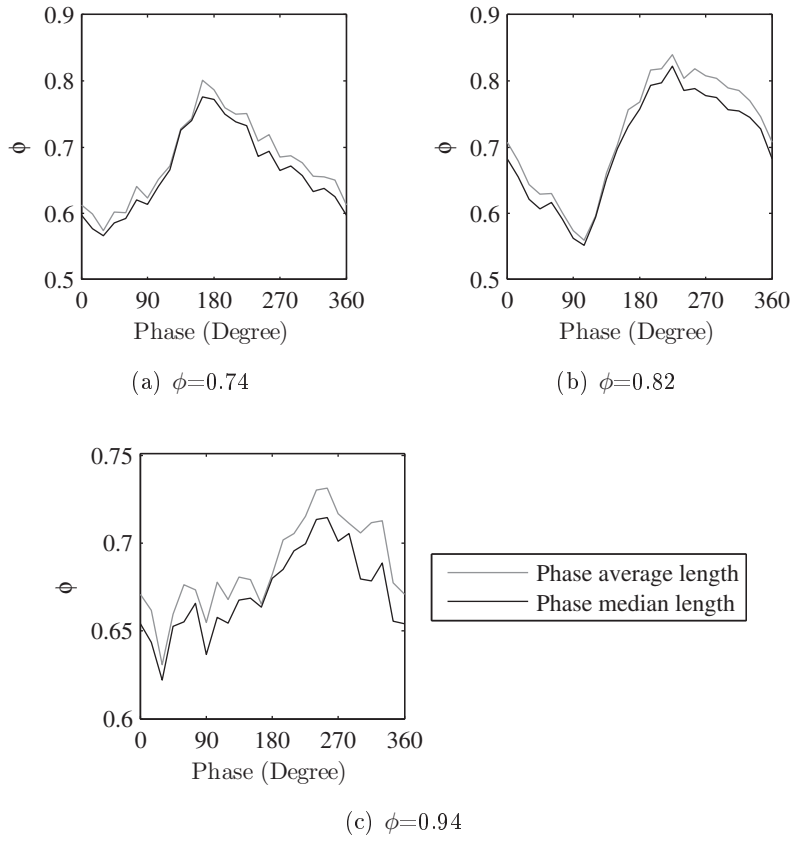

(a) ϕ=0.74

(b) ϕ=0.82

(c) ϕ=0.94

Figure 3.32: *Phase average of the equivalence ratio using radial PLIF data. In black using the phase average of the absorption length, and in gray using a phase median.*

Equivalence ratio (injection condition)	0.74	0.82	0.94
Average equivalence ratio (from mean)	0.57-0.63	0.71-0.73	0.98-1.07
Relative variation in a cycle (%)	45-51	29-33	15-18

Table 3.11: *Statistics on the equivalence ratios obtained with the absorption diagnostic. For each injection condition, 5 different measurements are available.*

3.8.2 Using axial PLIF data

Using the hypotheses described in section 3.7.3, a variation of the fresh gas length crossed by the IR laser can be computed from the axial value at the injector. As a reminder, the corrections to apply are: add 180° to the θ values obtained at ϕ=0.74 and 0.82, and keep the values unchanged for ϕ=0.94.

The results obtained when computing the equivalence ratio from this data are shown in figure 3.33. Since the length found at ϕ=0.94 at the injector is shorter than the values found on the radial PLIF images (which were abnormally high when compared to the other 2 test conditions), there is no more strongly under evaluated equivalence ratio at this condition. The most different profiles from the previous calculated method are obtained at ϕ=0.74 and 0.94. While the change for the richest condition was expected, the change for the leanest case was not. The main change to note is the phase of the equivalence ratio fluctuations: when using the radial PLIF data, the minimum value for ϕ was obtained at θ=30°, while using the axial PLIF data, it becomes θ=90°. This is in part due to a difference in the computed length of fresh gases profiles. Considering that for all measurements obtained on the geometry of the IRZ the two lean cases exhibited only a small difference in phase (in the order of 20°), this result is more conform to what could be expected.

The average equivalence ratio and amplitude of the fluctuations obtained depending on the test run are given in table 3.11. The average equivalence ratios are still not completely recovered using this method, so the results have to be considered carefully. The amplitude of the variations found for the cases ϕ=0.82 and 0.94 are of the same order as found with the other method. In the leanest case however, the amplitude of the fluctuations found is sensibly greater, going up from 35% using the radial data to 47%. This is due to the bigger fluctuations observed in that case at the injector.

3.8.2.1 Equivalence ratio: conclusion

Due to the uncertainties obtained when computing the length of fresh gases crossed by the laser, an important uncertainty remains on the equivalence ratio calculations. Using both the data from radial PLIF (the most correct,

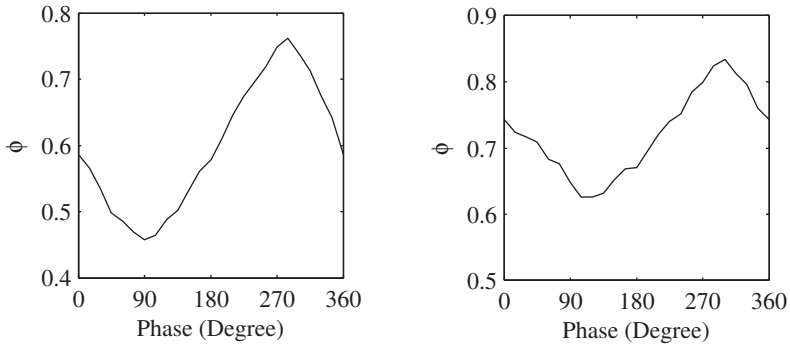

(a) ϕ=0.74

(b) ϕ=0.82

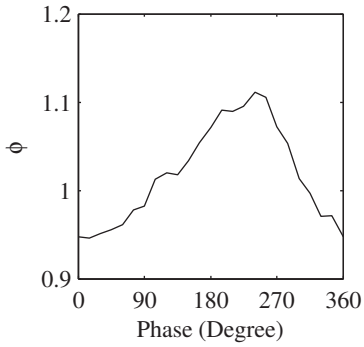

(c) ϕ=0.94

Figure 3.33: *Phase average of the equivalence ratio using axial PLIF data.*

but with potential problems of ORZ detection) or axial PLIF measurements at the injector (whose relation to the actual desired length is only supposed), the average equivalence ratio is unfortunately not found. However, both techniques give similar values for the amplitude and phase shift with the reference pressure signal for the cases ϕ=0.82 and 0.94. When ϕ=0.74 however, the results are less similar: the fluctuations of the length are not the same phase and amplitude-wise, giving different results on the equivalence ratio. If using the radial data, the minimum is achieved at θ=30° and the maximum at θ=165°, while using the values at the injector, the minimum is at θ=90°, and the maximum at θ=285°.

The conclusion is thus that equivalence ratio fluctuations seem to be present, with an amplitude close to 40% in the two lean cases, and with a lesser amplitude of 15% in the richest case. Since the average equivalence ratio wasn't retrieved using this method however, these results are subject to caution.

The method in itself is sound, but unfortunately the V shape of the flame gives in the CESAM burner a weak differentiation between fresh and burnt gases at the limit of the ORZ. With a configuration producing a M flame, where the flame is always present at the limits of both IRZ and ORZ, such a method should work. This strategy would then allow to use the absorption diagnostic in cases such as the CESAM burner presented here, without a plenum allowing to make the measurement at a fixed length of premixed gases. As this kind of configuration without a plenum is closer to most industrial applications, this could be an important step towards measuring equivalence ratio fluctuations at high frequency.

3.9 Conclusion

This chapter described the method adopted to obtain the phase average of the various physical quantities relevant to a better comprehension of the instability present in the CESAM burner. As noted in the description of the algorithm used, care must be taken when choosing the parameters of the phase average: too much filtering of the reference signal will result in changes in the repartition of the measurements, since the cycles are not detected properly. Care must also be taken when interpreting the results: any mode with a frequency close to the frequency chosen for the phase average, its half or its double will have an impact on the results obtained.

In the present case, the cycles exhibit variations in amplitude during any given test run, so the averaging is to be interpreted with some caution. Overall, the cases ϕ=0.74 and 0.82 present similar structure and evolution of the

flame during one cycle, the main difference being in the phase shift between the pressure inside the injector and movement of the flame structure. The IRZ of the flame is elliptical, and combines an expansion/retraction with a rotation at half the frequency of the instability. That expansion of the IRZ is linked to a vortex shedding clearly visible on the high speed films of the flame. The flame near stoichiometry has a different behavior: the IRZ expands much less, with the effect of the vortex shedding only seen far from the injector. The IRZ near the injector is then only oscillating around a stable position, which is dependent on the distance to the injector. The presence in the three cases of temperature waves with a propagation speed close to the expected convection speed was measured by the BOS system.

The attempted measurements of equivalence ratios fluctuations gave results that are unfortunately subject to caution, because of the criticality of the measurement of the fresh gas length crossed by the laser during the absorption measurement. Using several ways of evaluating this length, the average equivalence ratio could not be exactly recovered. However, the fluctuations were found to be consistent, with 35-45% amplitude in the two leanest cases, and 15% fluctuations at ϕ=0.94. This would link the lesser fluctuations of the pressure and shape of the flame to lower fluctuations of the equivalence ratio too in that particular case.

The phase average is very useful in that it allows to obtain a reconstructed cycle with data that do not have an acquisition rate high enough to proceed by any other mean. However, the number of data points acquired will limit the number of bins that can be used in the reconstruction, and thus the precision in the phase calculations. It also forces the dynamics of the reference signal on the treated data. The mode extraction methods can somewhat alleviate these drawbacks in the case where the acquisition frequency is high enough: they find coherent structure in the data itself (preventing an eventual forcing). For this reason, the use of the Dynamic Mode Decomposition will be made on the high speed camera images, and combine with other data.

Chapter 4

From High speed diagnostics to flame dynamics: the Dynamic Mode Decomposition

In this chapter, the post processing technique called Dynamic Mode Decomposition (DMD) and its so-called Extended version will be discussed in detail and applied to the data sets obtained on the CESAM burner. A detailed comparison to the results obtained using the more classic Proper Orthogonal Decomposition (POD) will also be conducted. In a first part, the principles of the DMD and POD, as well as the algorithm used will be discussed. In particular, the choices made to obtain spectra representative of the system dynamics will be explained. A synthetic test case made to be representative of the data set used will be presented, as it is used to benchmark the DMD. The results of this benchmark, as well as the recommendations on an efficient calculation of the DMD are then made. The last parts of the chapter will describe the results obtained on the experimental data, first considering the high speed broadband emission images only, and then adding the influence of simultaneously acquired pressure data.

4.1 Principle and algorithm of the POD, results obtained

4.1.1 Principle and algorithm

Since the advent of high speed image diagnostics and simulations with calculations of unsteady components (Direct Numerical Simulation, Large Eddy Simulation), experiments as well as simulations give access to a wealth of data describing turbulent phenomena. However, extracting the coherent components from this data can be difficult. A solution to interpret the turbulent results is

to look for coherent structures inside the flow. They can be seen as a series of modes, which combined, give the original signal used to compute the decomposition. A classic method to look for these coherent structures, thereafter called modes, is the POD, and was described briefly in the Introduction (p. 11). The algorithm used in the POD calculations presented in this study is detailed here.

The POD modes are computed so that the modal base is orthogonal, and optimized by their energy content. More precisely, if a series of n measurements $v_1 \cdots v_n$ is considered, the POD decomposition gives a series of modes $\phi_{POD,i}$, such as:

$$v_j = \sum_i \phi_{POD,i} \times a_{i,j} \tag{4.1}$$

with each mode $\phi_{POD,i}$ orthogonal to the others. In the present study, the modes were computed using the snapshot method, with the following steps:

- the snapshots $v_1 \cdots v_n$ are assembled in a single matrix V_1^n.
- the correlation matrix R is computed:

$$R = V_1^{n\prime} \times V_1^n \tag{4.2}$$

.

- The eigenvalue and eigenvector of R are computed. They are then sorted in descending values: the eigenvalue corresponds to the energy content of the mode, and so modes corresponding to the highest eigenvalue are the most important in the signal's description.
- The modes are the columns of the matrix ϕ_{POD}, derived from the snapshot matrix and the eigenvector matrix U:

$$\phi_{POD} = V_1^n \times U \tag{4.3}$$

- Finally, the matrix A containing the temporal coefficients of each mode is computed:

$$A = \phi'_{POD} \times V_1^n \tag{4.4}$$

Once this algorithm applied, a series of modes $\phi_{POD,i}$ with their corresponding time evolution vector $a_{i,j}$ are obtained. In this particular study, the POD was applied after removing its average from the image set: this is to prevent the computation of the average during the POD algorithm. Each mode has an energy value attached, and their relative importance can thus be assessed.

As indicated in the introduction, this method has some drawbacks due to the constraints imposed to the modes. The main problem remains interpreting the dynamics for each mode: the temporal evolution for any given mode is not restricted to a given frequency, and as such some modes can have complex content in the frequency domain. A POD analysis will thus give a series of i

modes consisting of a spatial shape $\phi_{POD,i}$, with temporal amplitudes $a_{i,j}$ for each of the j snapshots. If a fluctuation occurs at a single frequency f_{fluct}, then a PSD analysis of the coefficients $a_{1,j}$ of the most energetic mode (ignoring the mode giving the signal's average) is expected to exhibit a strong peak at that frequency. The other modes may also have strong peak at that frequency. This is particularly the case if a coherent structure is convected in the signal, as two modes $\phi_{POD,i}$ are then needed to describe this convection. When fluctuations at several different frequencies occur simultaneously however, the different modes may or may not combine content originating at two different frequencies, making the interpretation more difficult.

4.2 Results of the POD on experimental data

The results presented thereafter were obtained using 32 sets of 400 images series for each equivalence ratio. These specific image sets are the same as those that will be used to compute the DMD later in this chapter, and can serve as a basis for comparison.

First, the structure of the two most energetic modes from the POD results for each equivalence ratio for one of the POD computation is presented in the figure 4.1. In the ϕ=0.74 case, the first negative pattern in the first mode is at z=10-40 mm, with a positive pattern for z=40-80 mm approximately. The second mode on the other hand, exhibits a negative fluctuation for z=0-30 mm, and a positive one for z=30-60 mm. Similarly, in the ϕ=0.94 case, a positive pattern for z=15-35 mm is followed by a negative pattern for z=40-60 mm in the first mode, while the second mode has them at z=0-20 mm and z=30-50 mm respectively. This means that for all three equivalence ratios, the first two modes describe the convection of a single structure. As this mode was obtained by multiplying the normalized mode matrix by the maximum value of the coefficient $|a_i|$, the pixel intensities obtained are overestimated.

The third and fourth most energetic POD modes' shapes are presented in figure 4.2. The shapes are not as clearly defined as for the main instability. In particular, there is no clear evidence of observing the convection of a structure as with the previous modes. But as explained in the previous section, the temporal evolution of the modes has the potential to not be restricted to a single frequency, so further study of the temporal evolution must be conducted.

In order to confirm the POD modes' evolution, the PSD of the temporal evolution of the eight most energetic modes for each equivalence ratios was computed. Since the number of time steps is fairly small (300 points are available), rectangular windows of 200 points and 50% overlap were used in

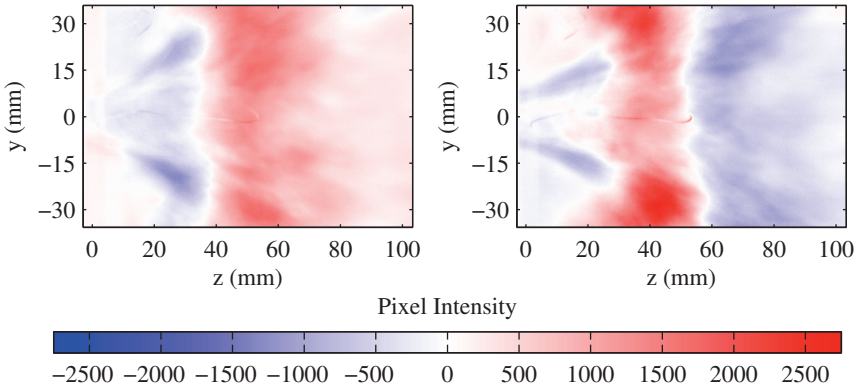

(a) ϕ=0.74

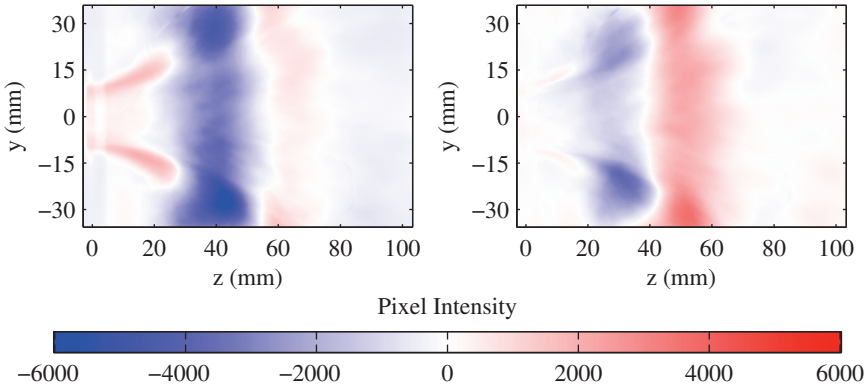

(b) ϕ=0.82

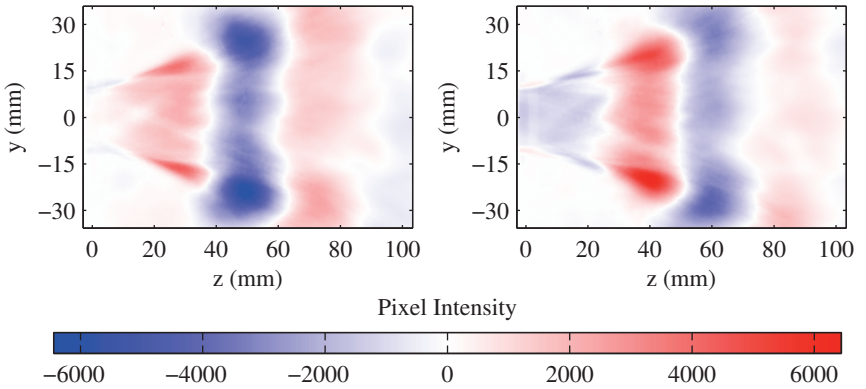

(c) ϕ=0.94

Figure 4.1: *Structure of the first (left) and second (right) most energetic mode obtained from a single POD computation on the experimental data.*

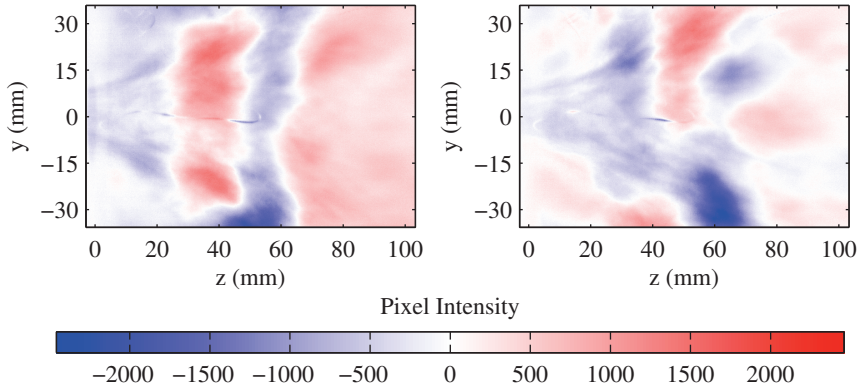

(a) ϕ=0.74

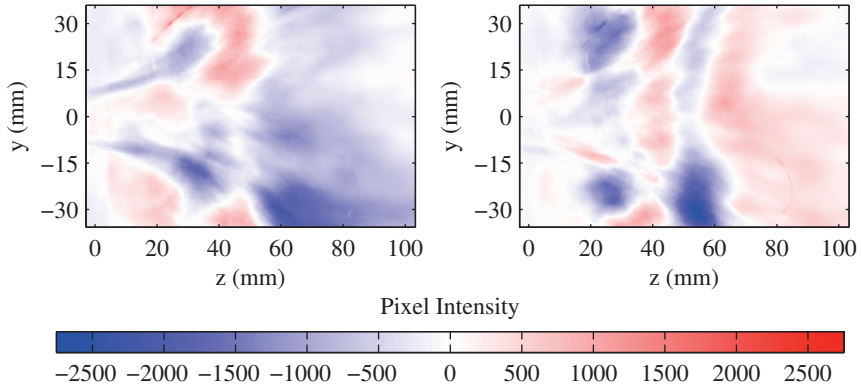

(b) ϕ=0.82

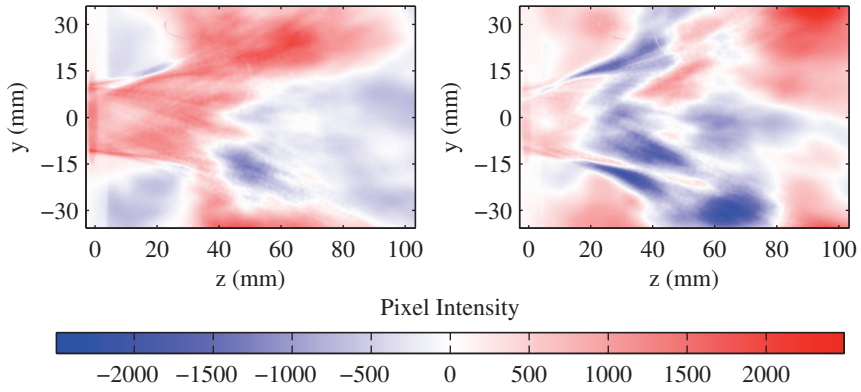

(c) ϕ=0.94

Figure 4.2: *Structure of the third (left) and fourth (right) most energetic mode obtained from POD computation on the experimental data.*

the Welch computation, resulting in a frequency resolution of 27.37 Hz using three periodograms. For each value of ϕ, 32 different POD computations were conducted. In an approach similar to the DMD averaging, the results presented in figure 4.3 are the averaged spectra of the corresponding PSD computations. For each value of ϕ, the amplitude in dB is obtained by taking $10log_{10}$ of the PSD amplitude, normalized by the maximum amplitude on the spectra (thus the maximum is 0). These results show that if the first two POD modes for each equivalence ratio describe a variation at the instability frequency, it is not the only frequency present. And even though the modes 2 to 7 seem to have fairly important content in the 382-400 Hz range at ϕ=0.74, for the two other equivalence ratios this is less true: for ϕ=0.82 all 8 modes seem to have a slight peak in their PSD decomposition at such a frequency, while for ϕ=0.94 no such peak is visible until the 7^{th} mode.

Another notable result is the presence of low frequency content for every mode: this shows that for such low numbers of images, POD is very probably sensitive to evolutions in the signal.

These figures show clearly the difficulty of interpretation of the POD modes: each single POD mode has significant content in several frequency bands, making their interpretation more difficult. In particular, one can see that for ϕ=0.74 the PSD of the 4^{nd} to 7^{th} modes have similar amplitudes at both 380 Hz and 570 Hz: they correspond to a mix of the doubled and tripled main instability frequency. This also means that for each equivalence ratio, the dynamics for a given frequency are divided into several POD modes. To better illustrate this phenomenon, the energy repartition for the main instability frequency is given in figure 4.4, and for the doubled frequency in figure 4.5. They were obtained by integrating the PSD results for all the modes around the desired frequency in a 3 point band. For example, for the main frequency at ϕ=0.74, integration was conducted on a 164-218Hz band. Since 32 different POD calculations were available for each equivalence ratio, the average value is marked by a cross, with the standard deviation as an error bar.

The results show that although the first two modes seem to correspond to the convection of a single structure, they do not have the same energy content in the POD computations for the two leaner cases, and for ϕ=0.94, even though the average value is the same, the standard deviation is slightly lower for the second mode. Moreover, even though for ϕ=0.74 case these first two modes account on average for 82.6% of the energy in that frequency band, the standard deviation suggests that it can go lower than 74.6%, so that only taking these two modes into account on a single POD computation could lead to a wrong understanding of the dynamics at that frequency. That phenomenon is exacerbated for ϕ=0.94, with an average of 73.3% and a higher standard deviation. For ϕ=0.82, the average value of 82.6% with a low

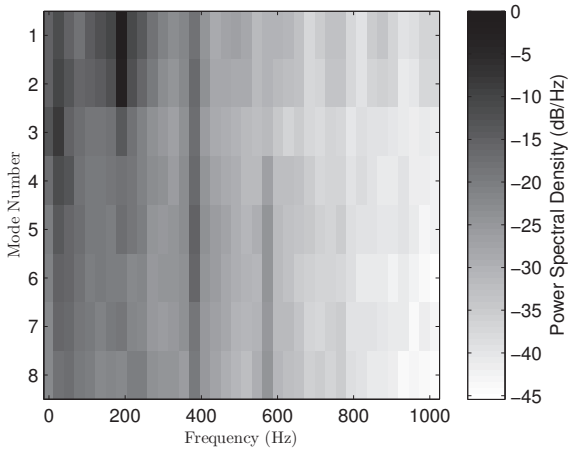

(a) ϕ=0.74

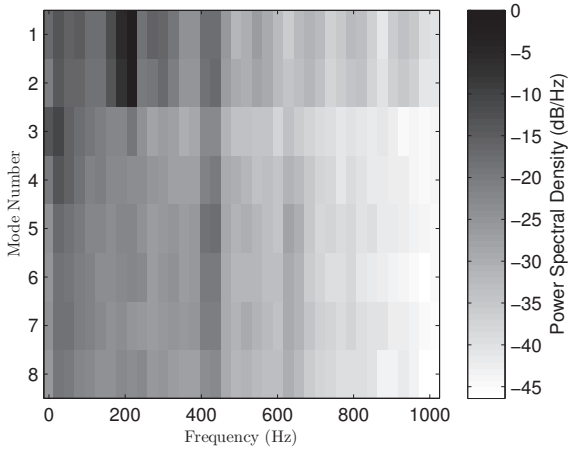

(b) ϕ=0.82

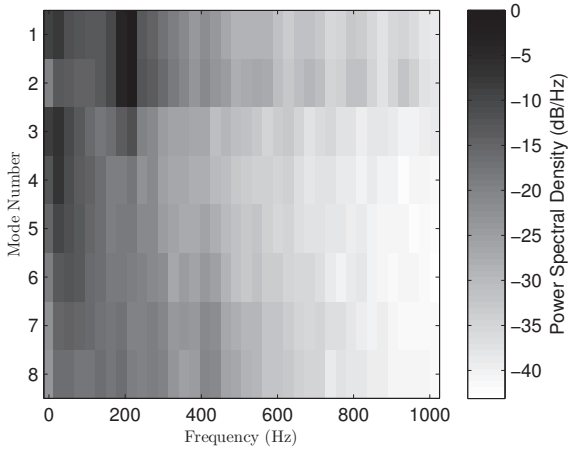

(c) ϕ=0.94

Figure 4.3: *Average PSD spectrum for the first 8 POD modes. For each mode, 32 different PSD computations were used.*

standard deviation suggests that the two modes are more representative.

In the frequency band around the double of the main instability, the results show that for every equivalence ratio, no single mode is predominant.

The analysis of the POD results show that even though the shape of the two most energetic modes seem to describe the convection of a single structure and could be compared to a DMD mode that will be studied later in the chapter, the similarities stop there: in only two of the three equivalence ratios studied, the POD modes accounted on average for the vast majority of the energy content at that frequency, meaning that in particular for ϕ=0.94, more POD modes are to be taken into account. The standard deviation suggests that even for ϕ=0.74, some individual POD computations may show a similar behavior. Moreover, no POD mode was found that would account for a significant amount of the energy around 400 Hz (*i.e.* the double of the main instability frequency). Thus, the POD could not be used to better understand what phenomenon occurs at that frequency, since all modes that have fluctuations at that frequency also exhibit significant fluctuations at the main instability frequency. Lastly, the POD has another drawback: since every mode corresponds to fluctuations at various frequencies, an averaging of POD modes over computations on different images as will be conducted in the DMD is possible, but may associate structures corresponding to slightly different dynamics. The amelioration of the results through averaging is thus probably more limited, with mainly access to averaged spectra.

4.3 Principle and algorithm of the DMD

In this thesis, the choice was made to focus on another method, the Dynamic Mode Decomposition (DMD), which was first introduced concurrently by Schmid (Schmid (2010); Schmid (2011); Schmid et al. (2012)) and Rowley (Rowley et al. (2009)) as a means of analyzing experimental or numerical data in the fluid dynamics field. In this section, the algorithm used in this study will be described, and further details can be found in Schmid (2010) and Richecoeur et al. (2012).

Let us consider a series of n measurements $v_1 \cdots v_n$, for example a time series of images acquired at a fixed frequency. Each of these n measurements consists of m data points (in the case of images, it is the total number of pixels). From these images, the following matrix is constructed:

$$V_1^n = \{v_1, \cdots, v_n\} \tag{4.5}$$

where all the data points taken at a given time step are put in a single column.

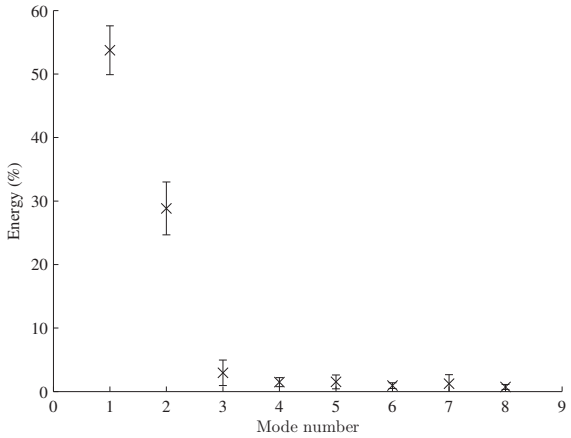

(a) ϕ=0.74

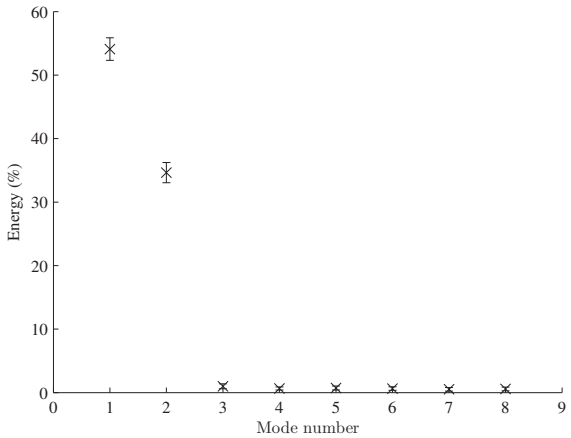

(b) ϕ=0.82

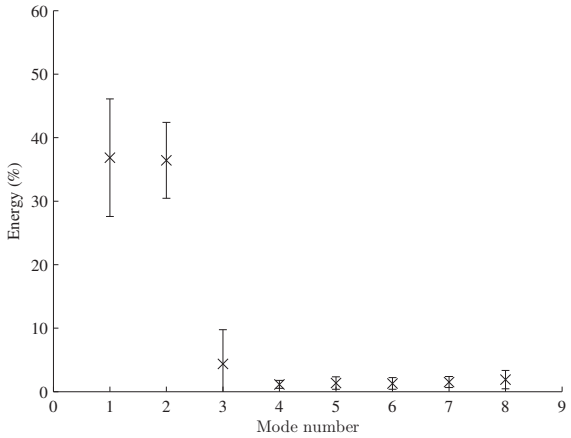

(c) ϕ=0.94

Figure 4.4: *Repartition among the modes of the energy around the main instability frequency (191 Hz for ϕ=0.74 and 218 Hz for ϕ=0.82 and 0.94).*

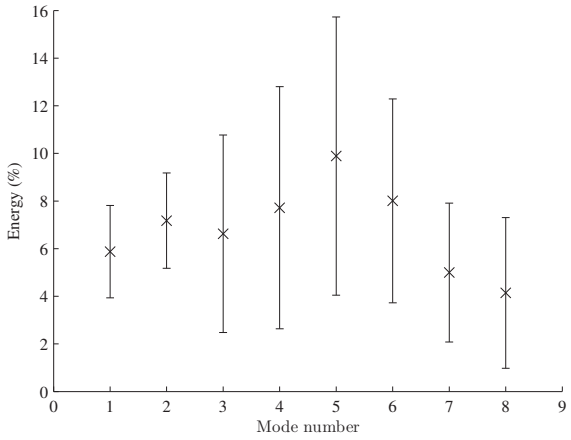

(a) ϕ=0.74

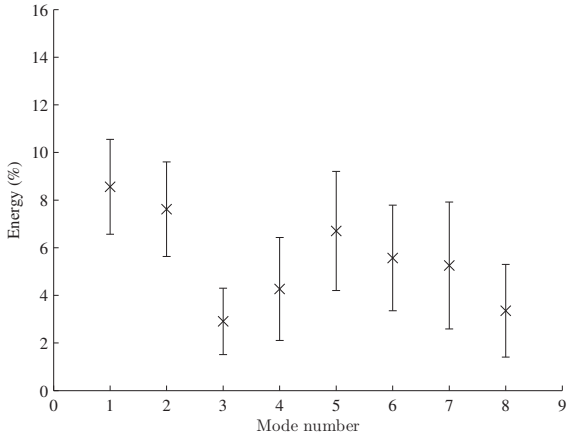

(b) ϕ=0.82

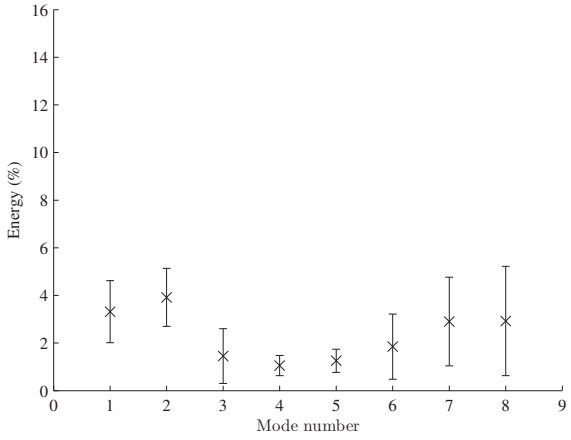

(c) ϕ=0.94

Figure 4.5: *Repartition among the modes of the energy around the double of the main instability frequency (382 Hz for ϕ=0.74 and 410 Hz for ϕ=0.82 and 0.94).*

The goal of the DMD is to find a series of modes which best approximates the system's dynamics, with modes containing each a single temporal frequency. This means that interpreting any given mode is fairly straightforward. A schematic representation of the matrices used and obtained for the DMD calculation, as well as the information they contain, is presented in figure 4.6.

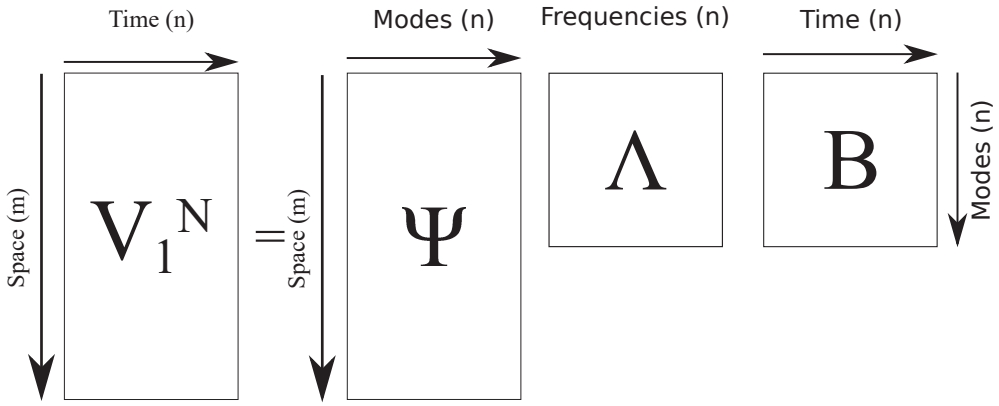

Figure 4.6: *Visualization of the matrices involved in the Dynamic Mode Decomposition, with the corresponding dimensions.*

The Dynamic Mode Decomposition is a linear approximation of the observed system, and it supposes that there is a constant matrix A linking the consecutive snapshots:

$$\begin{aligned} \forall i \qquad & v_{i+1} = Av_i \\ & V_2^n = AV_1^{n-1} \end{aligned} \tag{4.6}$$

Since A is considered as a constant, the measurement can then be expressed as a Krylov sequence:

$$V_1^n = \{v_1, Av_1, \cdots, A^{n-1}v_1\} \tag{4.7}$$

As one can see, this version of the DMD requires a temporal resolution higher than the frequency of the observed phenomena. It has been found in Schmid (2010) that to be able to obtain a good accuracy in the results, a sampling frequency of at least three times the Nyquist criterion is necessary. This means that in this study, its use will be limited to the analysis of high speed camera imaging and the simultaneously acquired pressure and chemiluminescence signals. It can be noted however, that recent efforts have been made to allow the use of the DMD principle on data sets that do not satisfy this high acquisition frequency criterion (Tu et al. (2014)), or even with non uniformly sampled data (Leroux and Cordier (2016)), thus alleviating this limitation.

Since the matrix A contains all the information on the system's dynamics, the goal of the DMD is to extract the relevant information (eigenvalues and eigenvectors) from it. However, in practical applications where the data set is a few hundreds high resolution images containing each m pixels, the $m \times m$ size of A would render its direct calculation impractical. For this reason, a smaller matrix that has the same eigenvectors and eigenvalues must be found.

Several methods exist, but the one used in this study is based on the method developed by Schmid (2011). In this approach, first the singular value decomposition of V_1^{n-1} is computed:

$$V_1^{n-1} = U\Sigma W^* \tag{4.8}$$

with V_1^{n-1} a $m \times (n-1)$ matrix, U is $m \times m$, Σ is $m \times (n-1)$ and W^* is $(n-1) \times (n-1)$. By re-injecting this expression of V_1^{n-1} in the basic equation 4.6, and rearranging the expression, the following equation is obtained:

$$U^*AU = U^*V_2^nW\Sigma^{-1} = \tilde{S} \tag{4.9}$$

This $(n-1) \times (n-1)$ matrix $\tilde{S}$ can thus also be computed fairly directly from the data set and since the two matrices $\tilde{S}$ and A are similar, they have the same eigenvalues. These eigenmodes and eigenvalues Y and Λ of $\tilde{S}$ are computed, giving after re-injection and rearrangement of equation 4.9:

$$V_2^n = (UY)\Lambda Y^{-1}\Sigma W^* = \Psi\Lambda B \tag{4.10}$$

Using the last notation for this decomposition, the initial data set is decomposed into a series of $n-1$ modes with three distinct components, as described in figure 4.6. The i^{th} mode is described by:

- its spatial shape, given by the i^{th} column of Ψ, ψ_i. The amplitude of each mode is computed so that its L_2 norm is 1.
- its temporal frequency $\lambda_i = log(\mu_i F_s)$, with $\mu_i = \Lambda_{i,i}$ and F_s the sampling frequency. Please note that since λ_i is a complex number, it gives both a mode frequency f_i and an exponential decrease rate.
- its temporal evolution, given by the i^{th} line of B. Since the spatial shapes ψ_i are normalized in the L_2 norm, it also contains information on the relative amplitudes of the modes.

Since the matrix B contains both the relative amplitude of the modes alongside the temporal fluctuations, a solution must be found to extract the relative amplitude of the modes alone. In order to do so, another decomposition can be found in the literature (Jovanović et al. (2014)) and is particularly useful when trying to build reduced models (*i.e.* reconstructions with only the most important modes). This decomposition is in the following form:

$$V_2^n = \Psi D_\alpha V_{and} \tag{4.11}$$

with:

- Ψ the same matrix as before, giving the spatial shape of the modes.
- D_α a diagonal matrix containing the relative amplitudes α_i of all the modes at the first time step.
- V_{and} a Vandermonde matrix describing the temporal evolution of the modes.

By construction, the Vandermonde matrix is:

$$V_{and} = \begin{Bmatrix} 1 & \mu_1 & \cdots & \mu_1^{n-2} & \mu_1^{n-1} \\ 1 & \mu_2 & \cdots & \mu_2^{n-2} & \mu_2^{n-1} \\ \vdots & \vdots & & \vdots & \vdots \\ 1 & \mu_{n-1} & \cdots & & \mu_{n-1}^{n-1} \end{Bmatrix} \tag{4.12}$$

This ensures that the temporal dynamic of each mode is respected, and that the relative amplitudes α_i at the first time step of the modes are only contained in the diagonal terms of D_α.

In the present study, the amplitudes of the various modes are obtained by simply using the pseudo-inverse of V_{and} and the matrices obtained from the first described DMD algorithm:

$$V_2^N = \Psi D_\alpha V_{and} = \Psi \Lambda B \qquad \Rightarrow \qquad D_\alpha = \Lambda B V_{and}^{-1} \tag{4.13}$$

However, more complex approaches to compute the α_i coefficients can be used, especially if the goal is to build a reduced order model, as developed in the article that used the Vandermonde decomposition (Jovanović et al. (2014)).

To better visualize the modes and their repartition, it can be useful to represent them as a spectrum. However, since the modes have a frequency, but also an amplitude which can vary in space (because of the spatial shape ψ_i), a norm for ψ_i must be chosen. As suggested in the previous descriptions, the historical L_2 norm was chosen in this work. Since the data used is composed of real numbers, sets of symmetrical modes with respect to the frequency are obtained, like when doing a Fourier transform. For each mode at a given positive frequency f, the same mode appears at a negative frequency $-f$. As this is not the case for modes with a frequency of 0 Hz, care must be taken when computing spectra. More precisely, the results presented from now on will correspond to an amplitude of $2\alpha_i$ when the corresponding frequency is non-zero, and of α_i for f=0 Hz.

Another problem to take into account when making a spectrum representation, is the temporal evolution of the relative amplitudes. As written before, the computed modes have indeed an exponential growth ratio because of the modulus of the associated eigenvalue μ_i. In practice, this leads to a problem when considering only the values α_i, which are the amplitudes at the beginning of the signal: the DMD algorithm typically finds several strongly unsteady modes, with a very high value for α_i but which quickly vanish. On the

opposite, the modes relevant to the instability are not expected to have a strongly variating amplitude in our case. It was thus chosen here to consider the relative amplitudes of the modes at the last time step to obtain the most representative spectrum of the system's dynamics.

The way the DMD algorithm is used to obtain a spectrum representative of the dynamics is summarized in the following diagram:

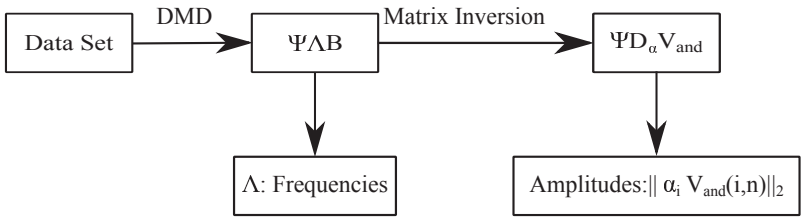

Figure 4.7: *Calculations made to obtain a spectrum with the DMD.*

4.3.1 Limitations of the DMD

The main drawback of the DMD algorithm is its sensitivity to noise, especially since it relies heavily on the last image of the set used to compute the modes. This may not be a problem when using the DMD on simulation data, but on experimental results this can be an important limitation.

Another point to be wary of comes from the choice for the modes' temporal evolution made when computing the DMD. In the most classic cases a sinusoidal shape is imposed for the temporal evolution of the mode, each mode corresponding to a single frequency. For this reason, the DMD may be more capable of discriminating two modes with close frequencies than the POD (Frederich and Luchtenburg (2011)). However, this choice can lead in particular cases to a lesser fidelity of the decomposition if the underlying phenomenon is not sinusoidal. This has been studied by Duke et al. (2011), where it was shown in particular that for a studied signal with a sawtooth or square waveform, the precision of the results of a DMD decomposition is significantly lower than for a sinusoidal signal. A way of mitigating this last effect would be to chose as a basis for decomposition not a sinusoid, but a periodical function with a waveform closer to the one expected. Implementing the matrix decompositions using such a different base may however prove to be more difficult.

Equally linked to the basic assumptions of the DMD is the exponential growth term, which can be both a benefit and a drawback. If the studied phenomenon has such a growth component, then the DMD could very well capture it. However, in practice this growth factor can be a hindrance. Even for constant modes a growth (or decrease) in amplitude over time will be found. The

amplitudes at the first snapshot, given by the matrices obtained from the calculations, can be very different from the actual relative amplitudes since some modes will be found with a very strong initial amplitude, but vanish in a few snapshots. This is the main reason why, as written in the previous subsection, the mode amplitudes considered in the present study are taken at the last snapshot: it prevents taking into account evanescent modes.

If there is indeed an expected temporal evolution of the amplitudes of a given mode, then the DMD in itself is not enough. It would thus be recommended to proceed using a strategy similar to the one developed by Sayadi et al. (2015): first use the DMD algorithm to obtain a mode base, then determine the most prevalent modes (either already known or using for example the sparsity promoting DMD developed by Jovanović et al. (2014)), and finally compute the optimal amplitudes for those modes, with values that can change in time and linked by a model. As no such strong temporal evolution was expected in the instability studied here, it was not deemed necessary to apply such a technique.

Finally, the DMD can require less fields than the POD to obtain a good approximation of the described flow, since less modes are required to describe certain phenomenons (Frederich and Luchtenburg (2011); Bistrian and Navon (2014)). This is at the same time an advantage and potential source of error. If a limited number of instants is used for the DMD, there is indeed a chance that the chosen set of temporal measurements may not be representative of the studied flow. The influence of this number of points will be discussed later in this chapter.

4.4 Extended and Stacked Dynamic Mode Decomposition

Two methods intended to obtain dynamic information from the DMD when information from several diagnostics are available will be presented in this section. These two methods are not equivalent, and should give different results in most cases.

4.4.1 Stacked DMD

One of the ways to look at the possibilities given by the Dynamic Mode Decomposition when data of different types is available, is to try and perform a stacked DMD. In this case, when building the matrices V_1^{n-1} and V_2^n, the different data types for each time step are combined in a single matrix. For example, if data from an image set V_{im} with m pixels and a microphone V_p is

available, the data vectors are built as:

$$\begin{aligned} V(1:m) &= V_{im} \\ V(m+1) &= V_p \end{aligned} \tag{4.14}$$

The type of matrix obtained is illustrated in figure 4.8.

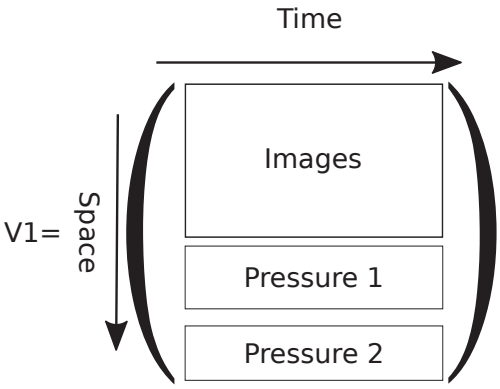

Figure 4.8: *Organization of the data from different diagnostics in the Stacked Dynamic Mode Decomposition, here with one set of images and two microphones.*

The created matrices are then used to look for DMD modes for the global system, as explained in section 4.3. Since the modes correspond to the combination of two or more data types, the amplitude content for each type of data used is different. For example, with two different variables, two mode series and their amplitudes can be defined from the computed modes:

- For the images, modes of shape $\psi_{im,i} = \Psi_{1:m,i}$ and amplitude $\|A_{im}(i)\| = \|\Psi(1:m,i)\alpha_i V_{and\,i,n-1}\|$.
- For the microphone, a mode of shape $\psi_{p,i} = \Psi_{m+1,i}$ and amplitude $\|A_p(i)\| = \|\Psi_{m+1,i}\alpha_i V_{and\,i,n-1}\|$.

It has to be noted that it is then important to find a proper scale for the different data types used when combining them to create the matrix V: since the modes found by the Stacked DMD approximate the overall dynamics of the system as described by the matrix, the relative scaling of the various types of data could play a role in the results obtained.

4.4.2 Extended DMD

As one can see from the previous part, the method of calculation of dynamic modes from the DMD is similar to the calculation of POD modes. As explained in the state of the art concerning this method (in the Introduction), there has already been several studies using a so-called Extended POD. The Extended DMD is based on the very same principle: the modes obtained from the DMD

on a given variable form a basis, on which projections can be made. In the case of the Extended DMD, data from other variables is used to know what part of the signal has the dynamics described by the previously computed modes.

As seen in section 4.3, the DMD algorithm gives for a set of n data points, a series of modes from the SVD decomposition of the $n-1$ first images V_1^{n-1}, and $n-1$ last images V_2^n. This decomposition can be expressed as:

$$V_2^n = \Psi D_\alpha V_{and} = \Psi D \tag{4.15}$$

where Ψ is the matrix containing the modes' spatial shape, and $D = D_\alpha V_{and}$ a matrix containing the temporal information, as well as part of the amplitude information. More precisely, in our case, each mode ψ_i has a norm of 1, so only the information on the shape of the mode is contained in it. The information on the relative amplitudes is thus entirely contained in D too, but if the matrix Ψ is not normed it could contain part of the information on the relative amplitudes of the modes.

As when calculating an Extended POD, the Extended DMD is looking for modes in the data set P_2^n, which is a different variable acquired simultaneously to the main one. These modes are contained in a matrix β, which must verify:

$$P_2^n = \beta D \tag{4.16}$$

The modes β_i contained in the columns of matrix β then follow the same dynamics as the modes ψ_i from the original data set. Their relative amplitude however can change, as each mode β_i does not have the same norm. The amplitude for each of the so-called extended modes is then given as:

$$\|A_{ext}(i)\| = \|\beta_i \times B_{i,n-1}\|_2 \tag{4.17}$$

4.5 Precision and accuracy of the DMD: verification on a synthetic signal

4.5.1 Synthetic images generation

In order to confirm the precision and accuracy of the DMD algorithm, and more specifically the frequency and amplitudes found for the average and main mode in the processed signal, a synthetic signal is created. It is designed to approximate the type of data that will have to be processed afterwards, so consists in a series of artificial images with the same size as those used in the DMD (149×101 pixels), filled as follow:

$$\begin{aligned} U_{ij} &= 12 + 3sin(2 * \pi f t + 2\chi_i \pi) + \beta_{ij} \qquad in \quad "flame" \\ U_{ij} &= 3 + \beta_{ij} \qquad in \quad "ORZ" \end{aligned} \tag{4.18}$$

In this equation, U_{ij} is the value of the signal at pixel i and time step j, χ_i is a random number between 0 and 1, and β_{ij} is a noise component set as a random number between -2 and +2. The "flame" region covers approximately 85% of the image, while the "ORZ" zone covers the 15% remaining. The values for the sinus' amplitude, and the average values in the ORZ and "flame" zones, were chosen to obtain similar ratios to those found on the first DMD tests performed on the experimental data, specifically at ϕ=0.94. Similarly, the noise's amplitude was chosen so as to obtain a value of signal to noise ratio similar to what was observed experimentally (by calculating the PSD at several points in the flame at ϕ=0.94). The frequency f was chosen as 212 Hz (the approximate frequency of the main mode for two of the three experimental conditions). It must be noted that the frequency is set with a fixed value, while in the experimental signals, fluctuations with time are expected. Finally, the time step t set to be the same as in the experiments (corresponding to a 7 kHz acquisition rate). To illustrate these results, a PSD study in both the flame and ORZ region of a synthetic signal and an experimental one at ϕ=0.94 are presented in figure 4.9. The PSD was computed using 1024 points, using a hanning window. With a 50% overlap, 7 windows were used in each case. Both synthetic and experimental data set were the same size. The amplitudes have been computed in dB, defined here as $10log_{10}(A/max(A))$, with A the signal taken at the point of interest in the flame or ORZ zone. In the ORZ, the synthetic signal exhibits a higher noise than the experimental signal. In the flame zone, the amplitude of the peak for the instability is of the same relative value to the average. The noise however has a different repartition: in the synthetic signal, the white noise produces a flat spectrum, while in the real signal the noise amplitude decreases at higher frequencies.

4.5.2 Outline of the parametric study

A whole set of DMD calculations is performed with different image series inside the generated movie. The goal was to ascertain the accuracy and precision of the results from the DMD algorithm computed with various sets of parameters, which were expected to impact the results. These parameters are:

- the data set used
- the number of cycles within the signal
- the number of images per cycle

The first condition is especially important when considering experimental images: the specific image set used may be too noisy, or unfortunately be acquired during a brief amount of time when the dynamics of the observed system are not clearly present. As the DMD tries to approximate the last image of the set using the others, the choice of images is expected to have a strong impact on the results. Because of this, 32 DMD with different images

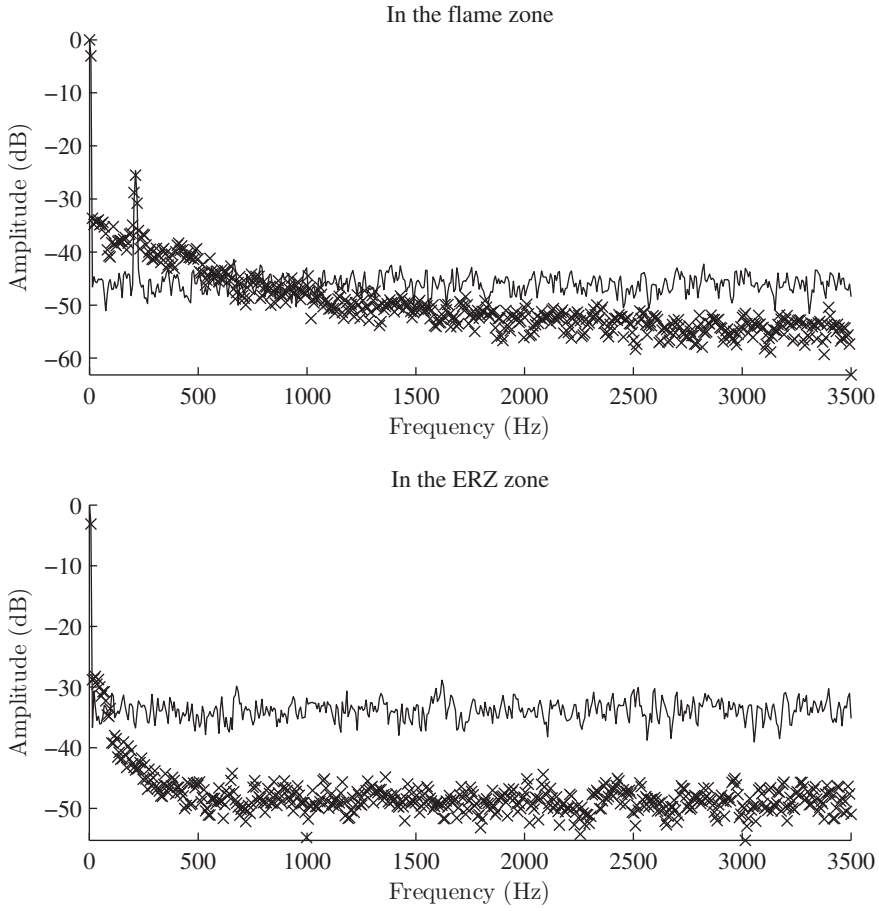

graphicx package

Figure 4.9: *Comparison of PSD results for a synthetic image (black line) and an experimental image (crosses). The amplitudes were normalized on the average value of the signal at the point considered.*

were made for each condition.

The second condition is also important: the main advantage of the DMD compared to phase averaging (and potentially POD), is that it does not require a high number of images to obtain relevant information on the observed system's dynamics. But as the DMD's average frequency resolution is the same as the frequency resolution obtained from a Fourier transform in the same conditions, a high number of cycles may allow to obtain better results as more modes are used to describe the signal.

Lastly, the number of images per cycle can be important. The DMD needs a high enough acquisition frequency to be able to describe the dynamics properly (to prevent aliasing, the Shannon criterion must be respected at the very least), but the sampling rate's impact on the results must be clarified. The DMD was thus used on the original set of data, but also on sub-sampled set of images.

In order to check the influence of these various parameters, different simulations were made. The number of cycles used varied between 1 and 33, and the number of points per cycle changed by sub-sampling between 3.3 and 33 (with the original acquisition frequency of 7 kHz). A list of 32 images was selected in the total simulated signal to be used as the last image in the various calculations. This means that for each set of conditions, 32 DMD calculations were made, with a given last image to ease the comparison between the different results if necessary. These 32 images are in practice two set of 16 images homogeneously sampled: one with the last image selected every 200 images from the original film, from index 1000 to 4000 and the other using the next image: from index 1001 to 4001. This was done to allow the study of the DMD sensitivity to the last image if necessary, as this provides 16 pairs of data set where only the first and last images are different.

4.5.3 Results of the study

The first criterion for the DMD results' analysis is the accuracy and precision at which the frequency of any given mode is found. The results obtained for the frequency on the synthetic signal are given in figure 4.10. From these results, it can be seen that whatever the sampling rate used, if more than 1.5 cycles are taken the results are remarkably good, with an error on the average on 32 DMD calculations of at most 1 Hz, and a standard deviation of less than 1% in each of these batches. Even with the lowest number of samples used, 1.5 cycles at 3.3 points/cycle (corresponding to 5 images), the error found on the frequency is only 12 Hz. It can be noted that when increasing the number of cycles taken in the input signal, the average seems to converge to the exact value (212 hz), and the standard deviation decreases. The sampling rate does not seem to have

a strong impact on the results in the present conditions (the Shanon criterion is always respected). If the modes are ordered by frequency, and the i^{th} mode corresponds to the instability, then the local frequency resolution is defined as:

$$\delta f = f_{i+1} - f_{i-1} \tag{4.19}$$

It is interesting to compute the ratio between this frequency resolution and the frequency resolution δf_{PSD} obtained on a PSD using the same signal. This ratio is plotted in figure 4.10. This relative local frequency resolution has on average the same evolution as the frequency: the higher the number of cycles used for the computation, the more stable the result with regards to the acquisition rate. However, the standard deviation of the results found for a given acquisition rate rises with the number of cycles. This is not expected to have a strong impact on the results: the adjacent modes can have a very low amplitude, and thus the high variation observed at high number of cycles used (leading to a higher number of computed modes) can be linked to the presence of negligible modes very close in frequency to the instability. A similar remark can be made concerning the value of the local resolution: the local resolution seems to be consistently 15% to 20% higher than the resolution for a PSD. This is probably due to the tendency of the DMD to sometimes give modes with very close frequencies, resulting in higher values elsewhere. Another explanation is that the main phenomena attracts most of the energy of the signal in a spectral region and therefore, previous and next modes are more distant than average. However, this lower than expected local resolution does no have a strong impact on the results: as the DMD does not generate uniformly spaced modes, the main mode's frequency is indeed consistently found with a precision much lower than the frequency resolution would suggest.

Another criterion to evaluate the DMD results' quality is to compare the value obtained for the average to the true average (i.e. computed directly from the images used). For the estimation of the average, care must be taken: the first thought would be to take the amplitude of a mode at 0 Hz. This would however lead to sometimes inaccurate results. The DMD will indeed usually give several modes with a 0 Hz frequency (typically 2 modes). If in most cases one of the two has an amplitude negligible compared to the other, in some instances it is not the case. Thus, only taking one of the modes could lead to an important error (with the experimental images used in this study, in some cases up to 40%). Another point to take into account, not found in the results from synthetic images analysis, is that sometimes the mode with the amplitude corresponding to the average is not detected at 0 Hz but at a very low frequency (lower than δf_{PSD}). It is thus important to look for the mode with the maximum amplitude on a slightly larger range. It can be noted however, that in these particular cases, it might be better to outright reject the result if looking for a DMD representative of the system:

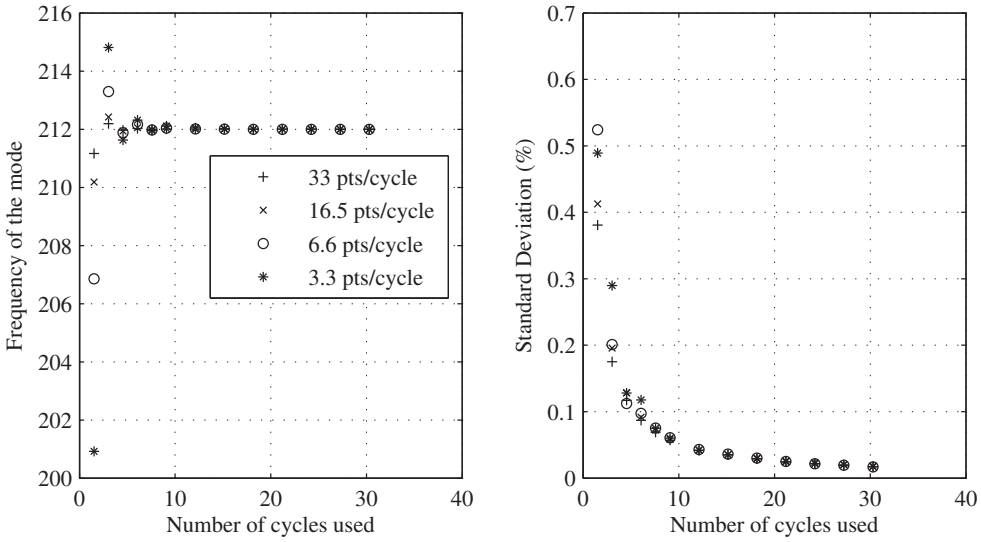

(a) Frequency found for the main mode

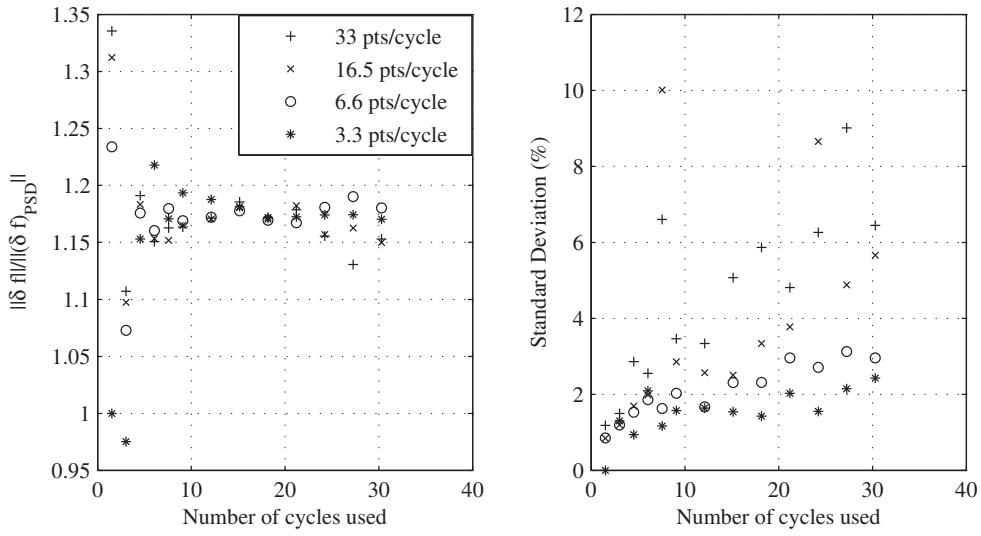

(b) Local frequency resolution (relative to the average resolution)

Figure 4.10: *Frequency accuracy and precision using the DMD on the synthetic signal: frequency found for the mode, and local frequency resolution around it.*

calculations showed that on all the DMD made on data from the ϕ=0.82 case sampled at 7 kHz, 8% of the DMD results contained no strong mode at 0 Hz, but at a low frequency instead. But 70% of these cases lead to an error on the evaluation of the average greater than the standard deviation for their calculation settings. In the present case where overall precision of the DMD algorithm was tested, no such rejection was taken into account. The average given by the DMD was taken as the sum of the highest mode found on a [-δf_{PSD}/2;δf_{PSD}/2] range, and all the modes found at a 0 Hz frequency, taking into account the sign of the corresponding spatial vector for the latter (as the smaller constant modes can either add or subtract to the principal one).

The results found for the amplitudes of the average and of the instability mode on the synthetic case are presented in figure 4.11. The average of image set is always found with very good precision, with less than 0.1% of standard deviation and less than 0.1% error on the average of the 32 calculations made at each setting. The amplitude of the mode corresponding to the instability, relative to this computed average, is presented in the second graph. The results are only really accurate if more than 10 cycles are used for computing the DMD, independently from the sampling rate, as the theoretical result is 0.0828.

The last indicator of the results' quality that was studied is the signal to noise ratio. This was defined as the ratio between the amplitude of the mode corresponding to the main instability, and the average amplitude on a ±50 Hz band around it (excluding that central value). This definition was taken to allow for a consistent criterion among all the calculations, even with widely varying acquisition frequency and number of data points used. The fairly large band was chosen for two reasons. First, in some cases the DMD can find a mode with an abnormally low amplitude next to the main mode, so only using the adjacent modes for the calculations can lead to excessively high ratios (over 1 million...) and is not representative of the spectra obtained. The second reason for such a large range is to be able to use this definition for a number of cycles as low as 8. Computing the noise amplitude of the signal to noise ratio from the average on a wider frequency band could allow to look at the signal to noise ratio for DMD computed using less than 8 cycles, but as the results on frequency and amplitude of the instability found by such DMD computations are not reliable, it was not deemed necessary. The results obtained on the synthetic signal are shown in figure 4.12. This is the first case where the sampling rate seems to matter: the higher the sampling rate, the higher the signal to noise ratio, but also the higher the standard deviation obtained. This is particularly true for the DMD computed using the original 33 points/cycle image set, which exhibit a signal to noise ratio greater by more than a factor 2 compared to the DMD results using the lowest acquisition rate. There is however a larger dispersion of the results in each batch than for the other quality criteria, with up to 12% of standard deviation.

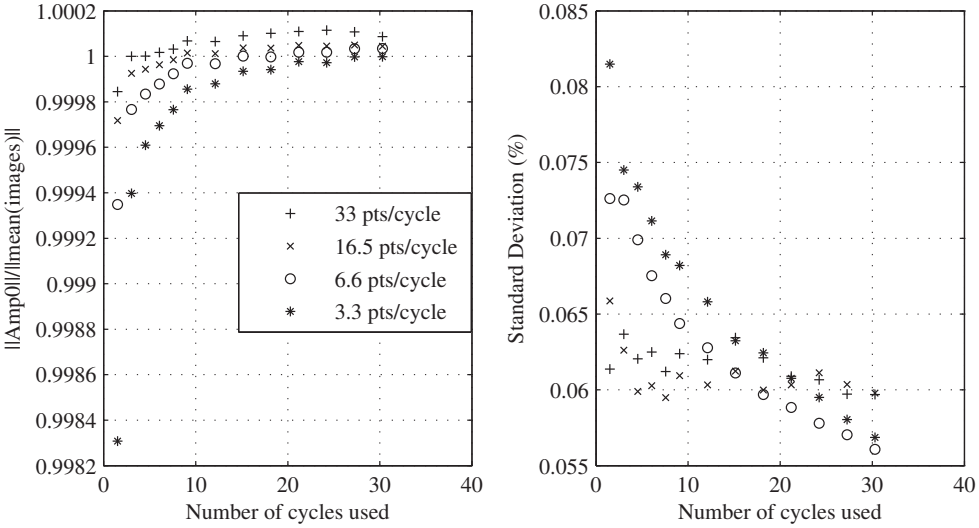

(a) Amplitude of the 0 Hz and very low frequency components compared to the average.

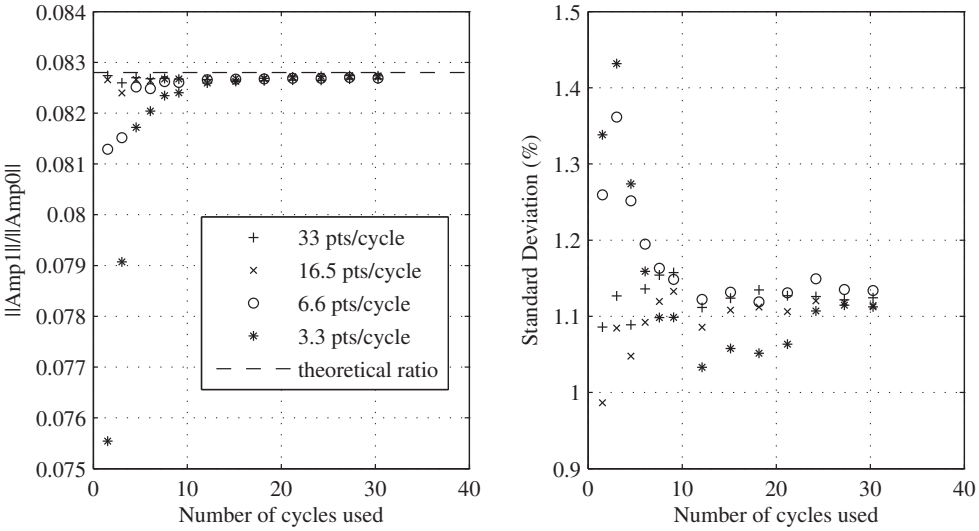

(b) Relative amplitude of the main mode

Figure 4.11: *Values found for the average of the signal, and mode amplitude using the DMD on synthetic images compared to the average.*

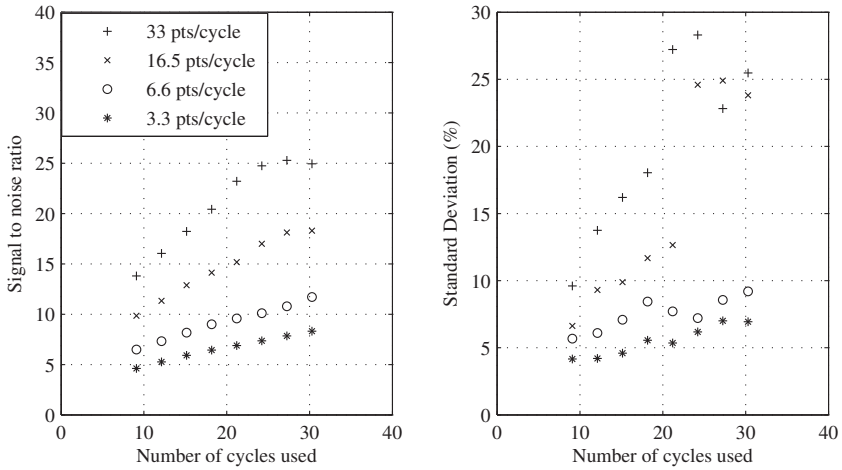

Figure 4.12: *Average and standard deviation of signal to noise ratio as a function of the number of cycles used in the DMD calculation*

From this parametric study, it can be concluded that the DMD can give quantitative information with synthetic signals. In order to obtain accurate results, it seems that a minimum of 5 cycles must be used to compute the DMD, independently from the sampling rate. As the only metric used here that seems dependent on the sampling rate is the signal to noise ratio, it is still interesting to have a high sampling rate, but this does not seem to impact the dynamics obtained. For the frequency as well as the amplitudes, there is clearly a convergence of the DMD results towards the correct solution when using more cycles in the sample signal. It can thus be noted that for more than 10 cycles, the benefits are very low.

4.5.4 Conclusion: recommendations on the DMD

This synthetic case, using a single mode with known amplitude and frequency, allowed to obtain information on how to conduct a DMD analysis on such systems, and gave insight on the way to proceed. It seems that the sampling rate only weakly impacts the results' quality, as excellent precision was achieved with a sampling rate as low as 3.3 points/cycle. The number of cycles used in the input signal is the determining factor. For frequency as well as amplitude, the DMD seems to converge on the solution with an increasing number of cycles: the average on several DMD computations comes closer and closer to the exact solution, and the dispersion of the DMD results using different input image set also decreases.

When evaluating the quality of a DMD result, it is important to check whether or not the input signal's average is recovered. If there is no strong mode at 0 Hz but a very low frequency mode pair instead, it may be preferable to outright reject the results, as the average will usually be recovered with a higher error. The next step is to compare the frequency found to the expected value (from a PSD on a sample signal for example). If the number of cycles used is too low, a bigger error on any single DMD can be expected, as even though the average on several DMD is not strongly impacted by the number of cycles used, the standard deviation is.

In this synthetic case, even with a low number of cycles in the input data set (1.5 cycle was the minimum tested), the results are quite excellent. The underlying signal however presented a single purely harmonic peak without any jitter or change in amplitude over time. The computation using real experimental data cannot be expected to give such a good precision. Since the results seem to start converging for more than 8 cycles, it seems best to use at least as many cycles when computing the DMD.

Lastly, an idea that can come from this parametric study to try and offset this expected degradation of the precision, is to proceed to an averaging of the results on the desired characteristics, somewhat similarly to a periodogram averaging approach. Due to the irregular repartition of the modes in the frequency domain, a true periodogram approach, made on the whole spectrum, may be impractical. However, averaging the amplitudes and frequencies on the important features can be expected to lead to better results than a single calculation. This will be further detailed when looking at the results on the experimental images and comparing them with the phase averaging results in section 4.7.2, as such an approach was attempted.

4.6 Dynamics of the flame from chemiluminescence imaging

From the results of the parametric study done in the previous section, it turns out that the DMD seems to be fairly independent of the acquisition frequency (as low as 3.3 points/cycle), but that the number of cycles used in the process is important. Even more so, a single DMD may not be enough to obtain quantitative information on the system's dynamics.

In order to have access to more quantitative values, one can think about using an approach similar to a periodogram: averaging the results obtained by several DMD calculations on different parts of the total signal to obtain better results. Due to the irregular repartition of the modes in the frequency domain, a true periodogram approach, made on the whole spectrum, may be impractical. Ho-

wever, averaging the amplitudes and frequencies on the important features can be expected to lead to better results than a single calculation.
The validity of this approach can be partly seen in the results from the parametric study on the synthetic signal: the average of the different characteristics of the mode give consistently good results, even when the standard deviation can be quite high. However, several differences between the synthetic signal used in the preliminary parametric study and the actual measurements can be noted. As was visible in figure 4.9, the noise in experimental results is different from the white noise implemented in the synthetic signal, and this difference could have an impact on the DMD results. Moreover, the synthetic signal was constructed using a pure sinusoid with a constant amplitude and frequency, but the experimental results should be expected to show variations in both amplitude and frequency.
For these reasons, a similar parametric study of the DMD using actual experimental images needs to be conducted to confirm that the DMD parameters' influence is indeed the same as with the synthetic case, and to understand the underlying burner's dynamics.

4.6.1 Results of the parametric study on experimental results

In this section, the results from the parametric study in the same conditions as the synthetic case will be presented on two of the cases investigated: ϕ=0.82 and 0.94. The third case, ϕ=0.74, being similar to ϕ=0.82 will not be presented. For each equivalence ratio, and each value of acquisition frequency and number of cycle used, 32 DMD calculations were conducted, the same number as in the study using a synthetic signal.

First, the results when looking at the frequency of the main instability are presented in figure 4.13. While the case at ϕ=0.82 does present the expected evolution with a convergence towards a single frequency value (212 Hz), this is less clearly marked for the ϕ=0.94 case: the standard deviation, as well as the dispersion observed for the average on each DMD batch, is more than tripled when compared to the other case.

Secondly, the amplitude corresponding to the signal's average found in the DMD, compared to the average of the images used is presented in figure 4.14. This gives good results: the average is constantly found with a 2% accuracy, while the standard deviation on the measurements slightly increases with the number of cycles used in the input data. This is very probably due in good part to the data used for the DMD calculations. In every set of 32 DMD computations, the same 32 last images were used. But if more than 6 cycles were used, then an overlap between some of the data set exists as the last image used is taken every 200 images in the original data set. This

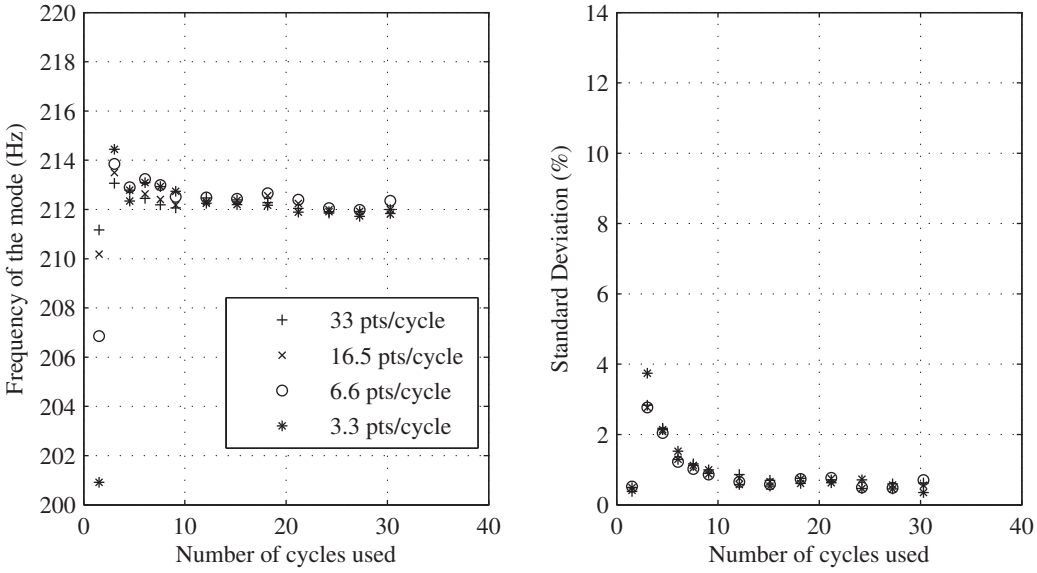

(a) ϕ=0.82

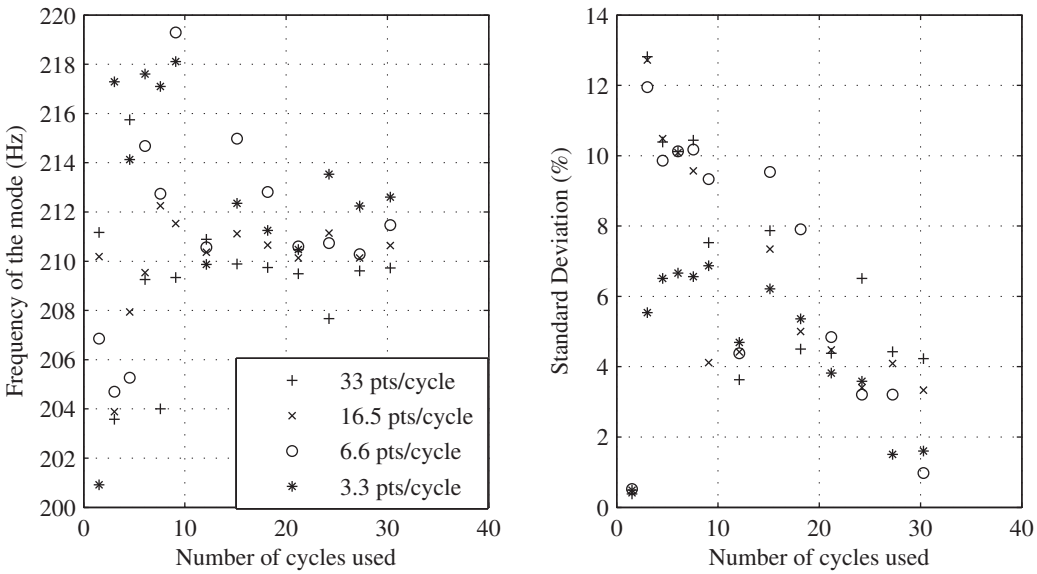

(b) ϕ=0.94

Figure 4.13: *Frequency obtained for the main mode using 32 DMD on two different injection conditions on the burner, using 32 DMD.*

means in particular, that the higher the number of cycles used the higher the overlap between the different image series, and thus the higher the number of times these problematic images are used in the DMD calculations. It is also interesting to note that for the amplitude, it is the ϕ=0.82 case that exhibits a higher standard deviation. This could be due to the lower signal level in the lean cases, that could lead to a lower accuracy of the DMD algorithm. The fact that the flame is much more stable at ϕ=0.94 also certainly plays a role in these results.

Lastly, the main mode's amplitude relatively to the input signal's average found by the DMD algorithm is shown in figure 4.15 for the various settings. For both injection conditions, there is a slight decrease of the average on each batch, together with an increase in the standard deviation when increasing the number of cycles in the input data. A difference with the results from the synthetic signal's study is that the sampling rate seems to have a moderate impact on the results: a higher sampling rate is also linked to a higher amplitude for the mode, and a higher standard deviation. The increase observed with the number of cycle is of the order of 10%, while the change due to the sampling rate is similar, with the exception of the cases where 33 points/cycles are used at ϕ=0.94.

From these results, it can be concluded that the considerations obtained from the synthetic signal's study seem to hold true for the experimental broadband emission images. The study of the system's physics will thus be conducted using input data containing 12 cycles per set, as this leads to a good compromise: there are enough cycles to ensure the precision on the average of the images and frequency on the main mode, while limiting the dispersion of the results from different image set. No frequency sub-sampling is used since it may have an impact on the results obtained.
For each equivalence ratio, 32 different DMD set are computed, as in the present parametric study.

4.6.2 Main modes obtained

From the previous subsection and the parametric study on a synthetic signal, it was shown that the results from DMD made with 12 cycles would lead to the most pertinent results to describe the flame's dynamics. In this section, the results obtained from such DMD calculations at the 3 different equivalence ratios are discussed.

First, it is interesting to look at typical spectra obtained from single DMD calculations, as presented in figure 4.16. The modes' amplitudes presented in this figure are normalized by the 0 Hz mode's amplitude for that DMD computation. In the cases ϕ=0.74 and 0.82, the DMD primarily detects

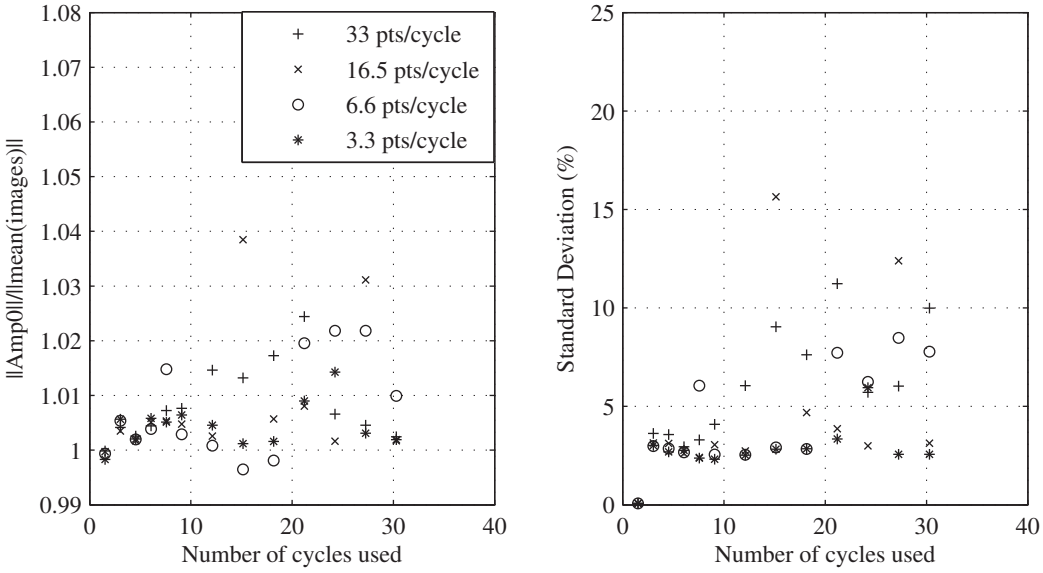

(a) ϕ=0.82

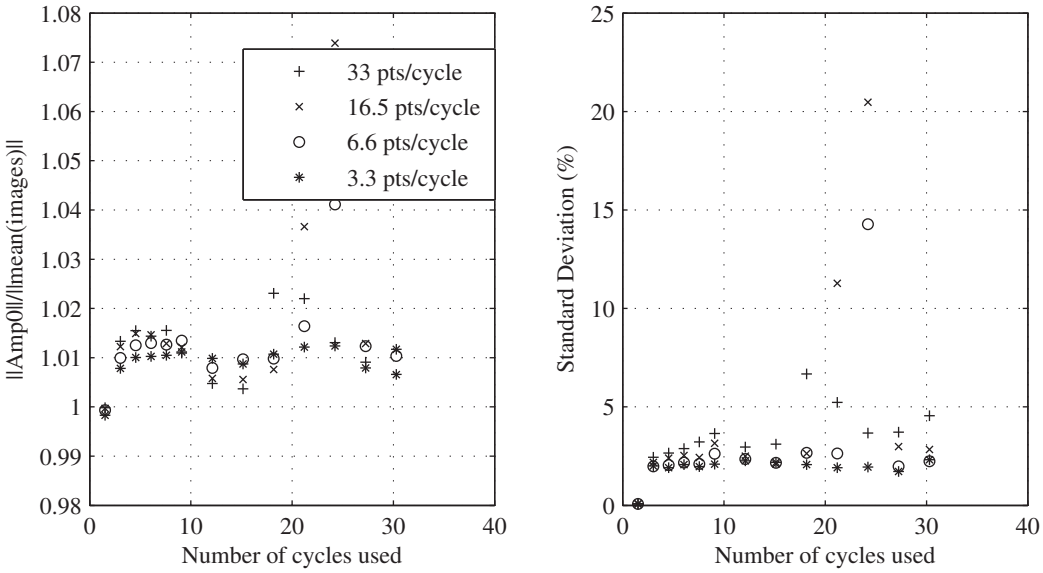

(b) ϕ=0.94

Figure 4.14: *Amplitude for the main mode, relative to the average measured by the DMD, using 32 DMD.*

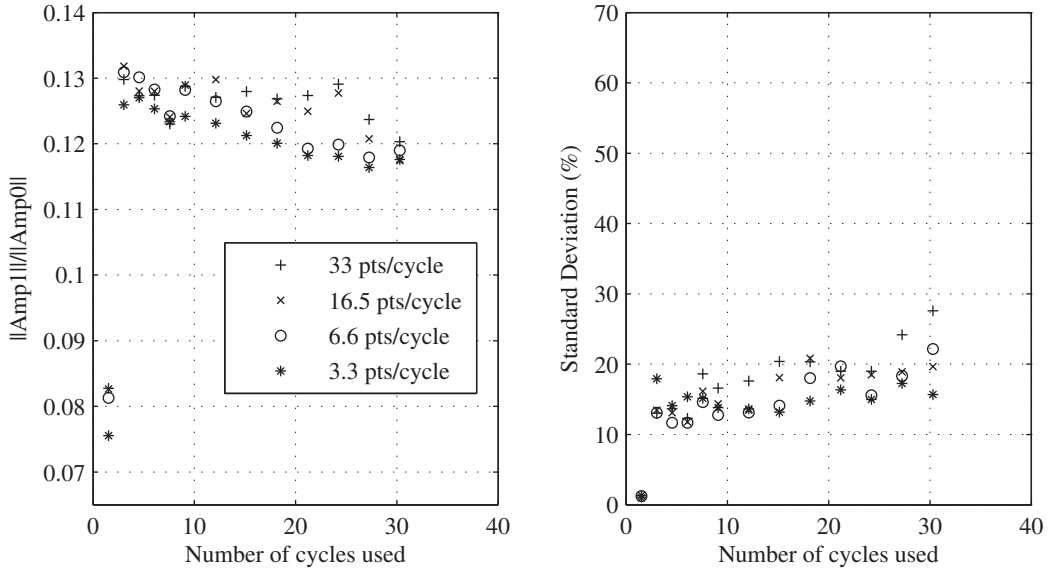

(a) ϕ=0.82

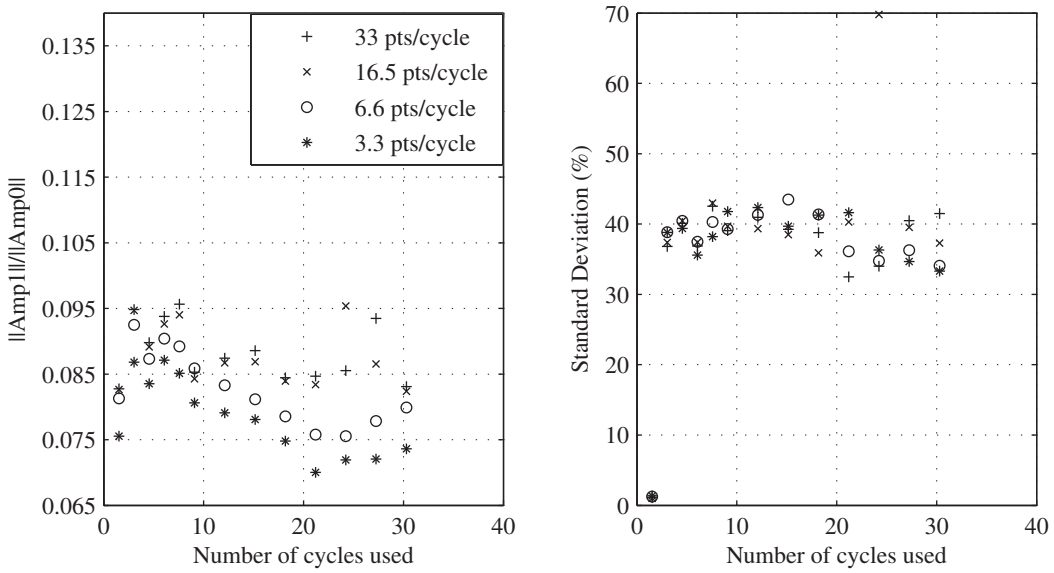

(b) ϕ=0.94

Figure 4.15: *Amplitude of the doubled frequency mode relative to the main mode's amplitude, using 32 DMD.*

content at the frequency of the main oscillation, its double and potentially the triple of its value. The visibility of that last peak depends on the data set used. For ϕ=0.94, only a peak at the main instability frequency is visible. The signal to noise ratio in these conditions is lower than for the other equivalence ratios, and thus the secondary peak may still be there, but drowned in the other modes.

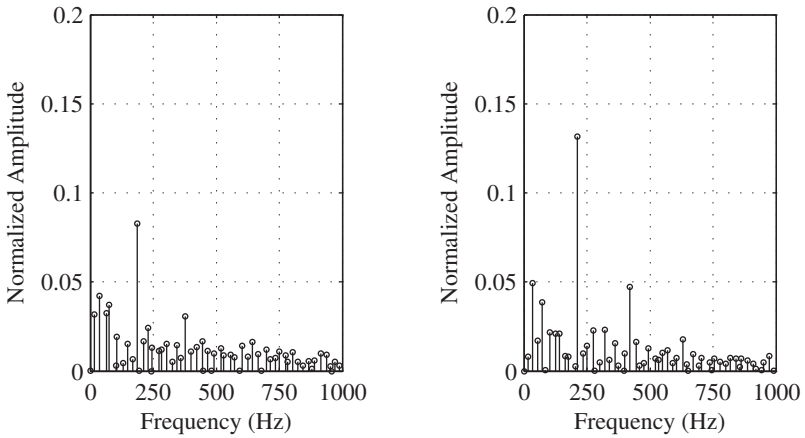

(a) ϕ=0.74 (b) ϕ=0.82

(c) ϕ=0.94

Figure 4.16: *Typical one-sided spectra obtained from DMD calculation on experimental images. The normalized amplitudes are given relative to the 0 Hz component.*

As no other mode appears strongly on the spectra obtained, only the modes at the main frequency and its double are presented in detail. The most important mode at 0 Hz has the same structure as the average of the images when all modes at 0 Hz are taken into account and its amplitude compared to the average of the images is not different by more than 10%. When reconstructing the temporal

evolution $mode_i$ of the i$^{\text{th}}$ mode ψ_i it is necessary to take:

$$mode_i(n\Delta t) = \mathrm{Re}(\psi_i \alpha_i V_{and_i}) = \mathrm{Re}(\psi_i \alpha_i \mu_i^{n-1}) \tag{4.20}$$

It follows that the spatial structure of $mode_i$ oscillates between the two values $\mathrm{Re}(\psi_i)$ and $\mathrm{Im}(\psi_i)$, which represent a phase difference of 90° in the cycle. The results obtained for the main mode in each of the three test cases are presented in figure 4.17. For the three injection conditions, there is a convected pattern, that is very similar to the two most energetic modes obtained by using the POD on the same image set (as seen in figure 4.1), although with a lower amplitude. In the ϕ=0.74 case, the first positive pattern for the real part is at z=10-30 mm, with a negative pattern for z=40-80 mm approximately. The imaginary part on the other hand, exhibits a positive fluctuation for z=0-20 mm, and a negative one for z=30-50 mm. Similarly, in the ϕ=0.94 case, a negative pattern for z=15-35 mm is followed by a positive pattern for z=40-60 mm in the real part of the mode, while the imaginary part has them at z=0-20 mm and z=30-50 mm respectively. This shows that the 90° temporal difference between real and imaginary part also corresponds to a 90° spatial difference in the structure, depicting the convection of a single structure with the flow. So only one DMD mode is required to describe a common phenomenon in flow structures, where the POD needs two (see figure 4.1). The two lean cases exhibit a very similar structure, with approximately one and a half cycle of the spatial instability within the field of view. When ϕ=0.94, the structure is more closed (as is expected from the average shape of the flame), but also seems to have a lower wave-length: almost two full oscillations are observed instead of one and a half. In all three cases, the structure is a pulsation of the flame, both in intensity and its opening angle. These results confirm the type of dynamics that was obtained with phase averaging on the same images. However, obtaining such results using the DMD requires much less images (especially if the exact amplitude of the intensity fluctuations is not required), and is not dependent on a simultaneous pressure fluctuation measurement. The DMD analysis tends to prove that the structure is indeed present in the signal from the flame itself, and is not for example the result of oscillations occurring at a multiple of that frequency.

The results obtained for the mode at a double frequency (f$\simeq$400 Hz, depending on the equivalence ratio) are presented in figure 4.18. The first thing to note on these spatial structures is the difference in size of the observed fluctuations with the main mode: for a double temporal frequency, the spatial shape of the mode is composed of roughly half-size structures.

As far as the amplitudes are concerned, the results presented in these figures were obtained by multiplying the mode ψ_i by its amplitude $\alpha_i \lambda_i^{n-1}$. These are thus the results obtained for this particular set of images in terms of pixel intensity. As was written in the introduction of this section, to obtain a better

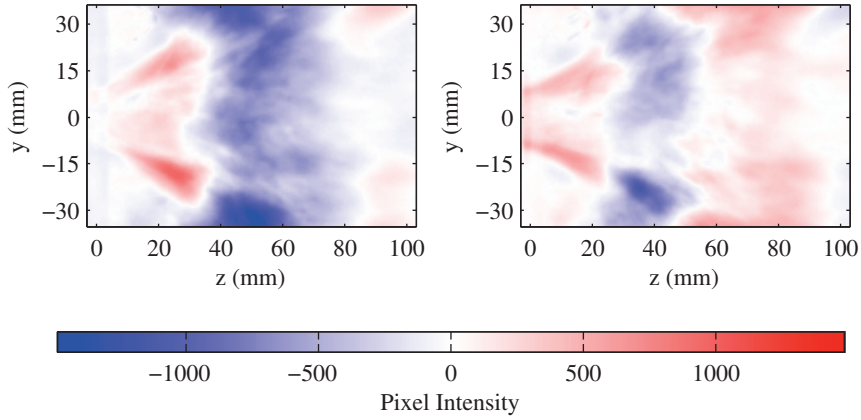

(a) ϕ=0.74

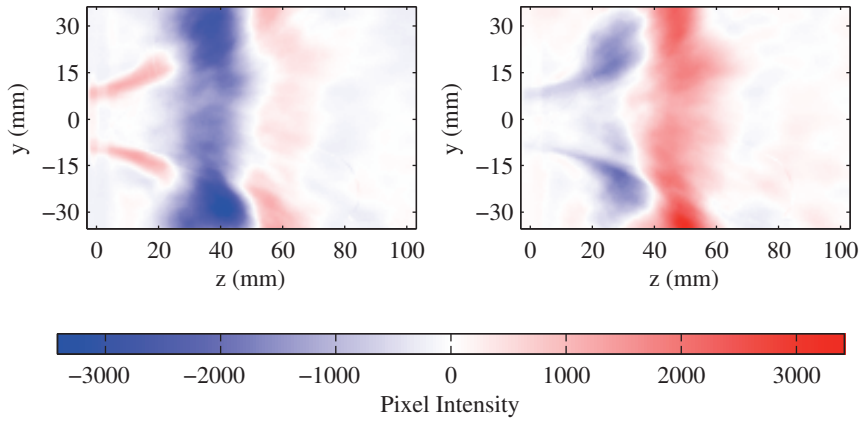

(b) ϕ=0.82

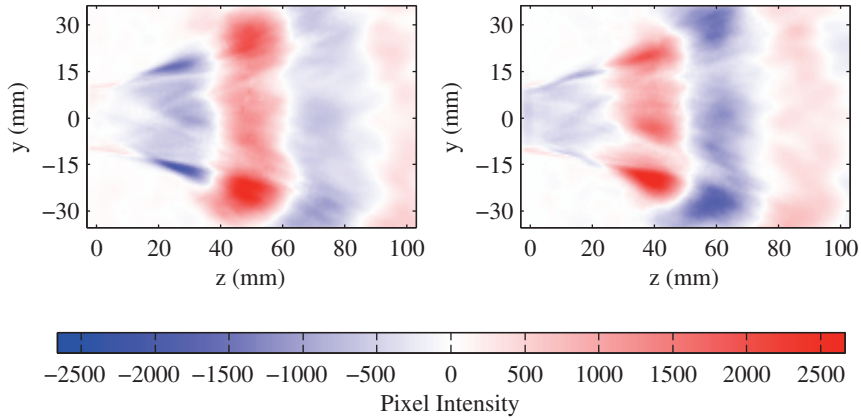

(c) ϕ=0.94

Figure 4.17: *Instantaneous structure of the main mode as detected in experimental data: real part on the left, imaginary part on the right. The corresponding spectra can be seen in figure 4.16*

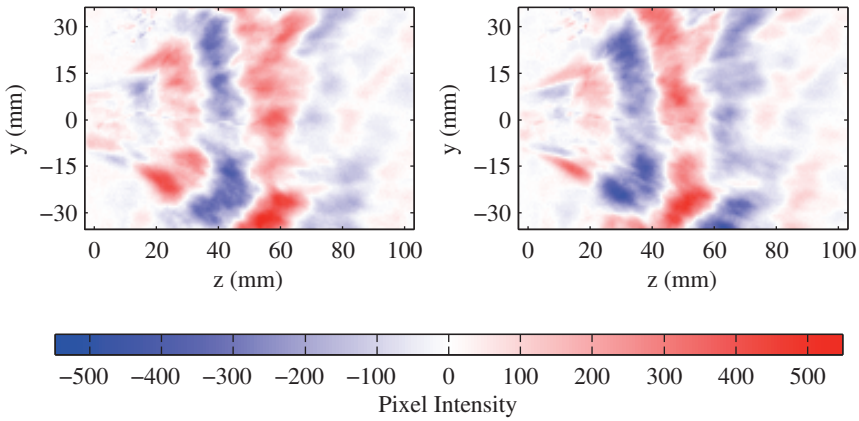

(a) ϕ=0.74

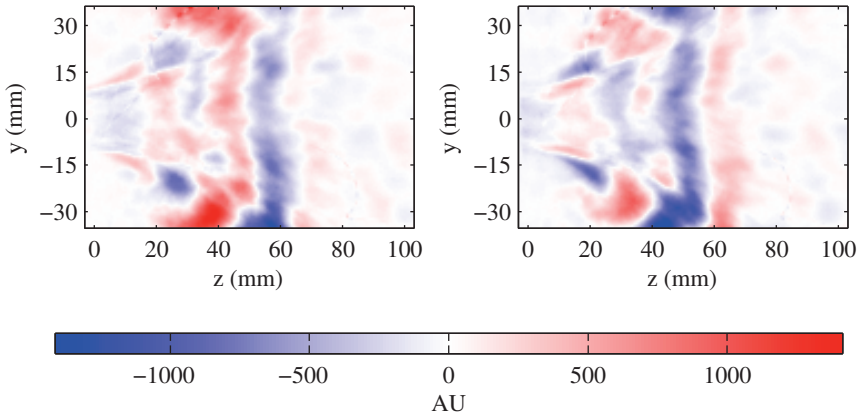

(b) ϕ=0.82

Figure 4.18: *Structure of direct emission intensity measured at the doubled frequency (f≃400Hz) from the experimental data: real part on the left, imaginary on the right. ϕ=0.94 not presented as the mode is not clearly present.*

Equivalence ratio	0.74	0.82	09.4
F_1 (Hz)	191	212	211
$\frac{Amp1}{Amp0}$	8.8%	12.5%	8.6%
signal to noise ratio	10.7	16.5	10.3
F_2 (Hz)	391	423	415
$\frac{Amp2}{Amp0}$	3%	3.45%	2.36%
signal to noise ratio	3.8	4.6	2.8

Table 4.1: *Characteristics of the two main modes observed on DMD, computed with 400 images at 7 kHz (approx. 12 cycles).*

value for the mode's amplitude in this study (where the dynamics are stable), it is preferable to compute several sets of DMD on different images (with the same DMD parameters), and to average the results. This was done for the three equivalence ratios studied here, and the results are summarized in table 4.1. The frequency found for the main mode is the same as what was observed on PSD calculations using pressure or OH* emissions. The relative amplitude of the main instability mode is the highest at 12.5% for the ϕ=0.82 case, while for the other two cases, very close amplitudes are found at about 8.5% of the average value. The doubled frequency mode's amplitude is overall around 3% of the average, but with a much lower signal to noise ratio. These amplitudes, as was described in section 4.3, are using the L_2 norm of the spatial structure, and thus are representative of the energy content of the modes.

The results from DMD calculations thus show that the frequency found for the main instability are coherent with the previous methods. It allows to show the shape of the associated mode, similarly to the phase average (a detailed comparison between the two is made in setion 4.7.2). The advantage of the DMD here is that it allows to know that these results are not forced by the averaging method but are indeed present in the system. The other main advantage is the possibility to clearly detect lesser components: the double frequency for example would be very difficult to observe by phase averaging because of the much stronger content at the main instability, which would drown out that signal.

This study on rapid imaging of the flame showed that the DMD detects oscillations at the frequencies that were expected from the PSD study on the pressure signals acquired in the injector and chamber, confirming the validity of the phase averaging presented in section 3.6.2. And since these pressure signals were taken as the reference for the phase averaging, it can be interesting to also compute the corresponding extended DMD on the pressure signals, which will allow to obtain a common phase reference between DMD and phase averaging, and thus to compare results given by the two methods.

4.7 Adding information from other signals: EDMD

4.7.1 Examples of spectra obtained

As described in section 4.4.2, using the results of DMD calculations from the flame's high speed imaging, a set of corresponding modes can be computed for any simultaneously acquired data from another sensor. In the present case, this means that pressure and OH* emissions can be projected onto the DMD modes from direct imaging, to quantify the coherent fluctuations of these two state variables.

Since the Extended DMD is a projection of another data set on a given DMD series of modes, it suffers from the same drawbacks as the DMD itself: there can be a non negligible variation depending on the data set used in the same test run. For this reason, the same approach is taken: after confirming the general shape of the signal, the features of the relevant modes are extracted by averaging their properties over 32 DMD repetitions. These are the same DMD set as used during the parametric study of the DMD on synthetic and experimental images: two series of 16 DMD calculations, the first using as last image the images 1000 to 4000 (every 200 images), and the second the images 1001 to 4001.

Typical spectra obtained by calculating the EDMD on the pressure signal inside the injector are given in figure 4.19. They were obtained using the DMD results in figure 4.16. It is clear from these spectra that as expected, the pressure signal has a main component close to either 190 Hz (ϕ=0.74 case), or 212 Hz (in the two other cases). It can also be noted that there seems to be a bump of higher amplitude for the modes directly around the main instability than for the broadband imaging spectra. This could mean that the EDMD decomposition of the pressure also detects the broadband noise that is seen in standard PSD analysis, albeit on a short sample. A more precise comparison will be made in the next section.

The results on the EDMD analysis of the OH* emissions measured by the photomultiplier are presented in figure 4.20. As was seen with the microphone signal, the content is concentrated at the frequency of the instability, with components at low frequency still high.

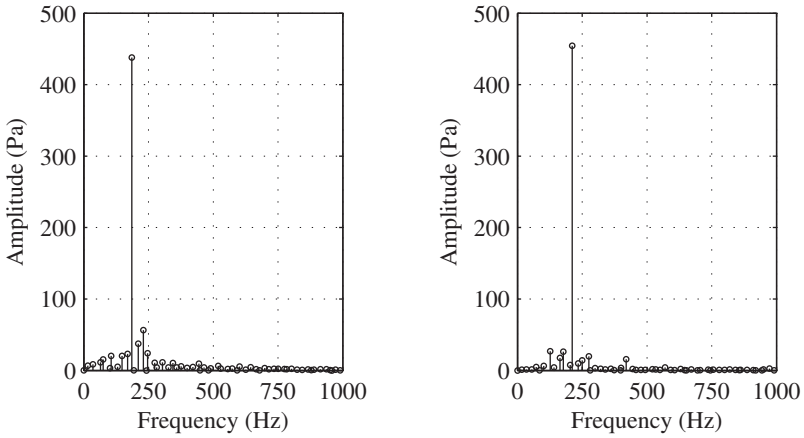

(a) ϕ=0.74 (b) ϕ=0.82

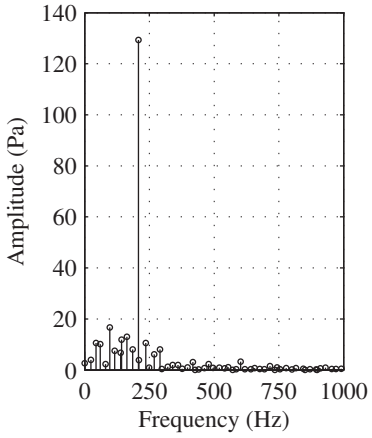

(c) ϕ=0.94

Figure 4.19: *Typical one-sided spectra obtained for the EDMD from the pressure signal inside the injector using the high-speed imaging basis (using the same data set as for the DMD presented in section 4.6.2).*

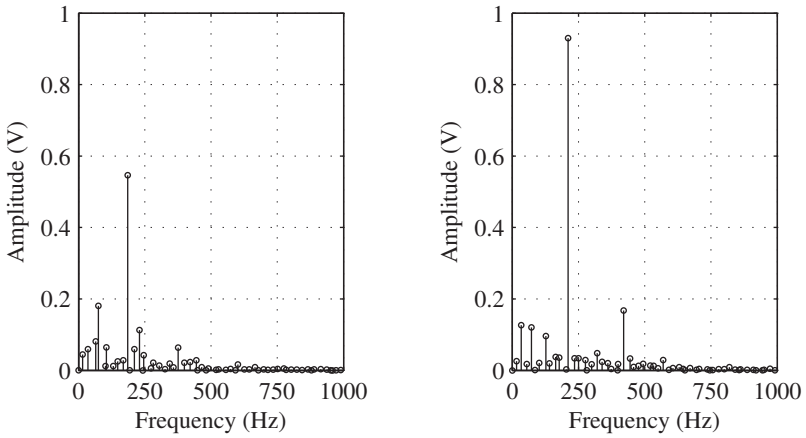

(a) ϕ=0.74 (b) ϕ=0.82

(c) ϕ=0.94

Figure 4.20: *Typical one-sided spectra obtained for the EDMD from the PMT signal using the high speed images as basis.*

4.7.2 Detailed analysis: comparison with classic analysis results

As the pressure inside the injector has already been studied in detail in previous chapters, a comparison of the results can be made. In particular, the following will be detailed:

- Comparison of EDMD spectrum with a Fourier analysis spectrum obtained on the same data set.
- Comparison of the amplitude of the main oscillation with all the post-processing techniques used.

The EDMD gives a series of sinusoidal modes for the pressure, much like the Fourier analysis and the PSD do. The main difference in this case is the subsequent distribution of the mode's frequencies. It is thus interesting to monitor the differences between the spectra obtained with both EDMD and PSD. As the levels of pressure in the signal have a strong difference, the sound pressure level of each mode will be calculated. To do so, the Fourier reference will be the PSD estimate with only one square window. The values for the EDMD spectrum are an estimation: since the modes are sinusoidal, the rms is easily computed from the amplitude, and the sound pressure level for each mode is then:

$$P_i = 20log_{10}\left(\frac{A(i)/\sqrt{(2)}}{20e^{-6}}\right) \tag{4.21}$$

From these calculations, and a set as before, the spectra obtained are presented in figure 4.21. While the instability's amplitude is well captured, on most other points the EDMD gives lower amplitudes. This results in a lower energy in the EDMD than measured using the PSD estimate. This is in good part due to the choice for the amplitude calculation: the real amplitude found by the DMD (and the EDMD) is also a function of time. Since most of the unstable modes computed by the DMD have a decreasing amplitude with time, taking the last time-step as a reference leads to underestimating their amplitude, and thus their energy content. So while this choice is the most useful in identifying stable modes, which have the most chances to have physical meaning and govern the dynamics of the system observed, it would be unwise to consider the whole spectrum, as its energy content is lower than the actual signal. For this reason, only the values at the main components really have a meaning and will be considered thereafter.

The results of a comparative analysis of the modes' amplitude are presented in table 4.2. The PSD results were obtained using the pressure signal on the whole test, but subsampled at 7 kHz (the pressure used for the EDMD). The PSD was calculated using hanning windows of 1024 points length and a 50% overlap, giving a resolution of 6.8 Hz and 7 windows. In order to deduce the

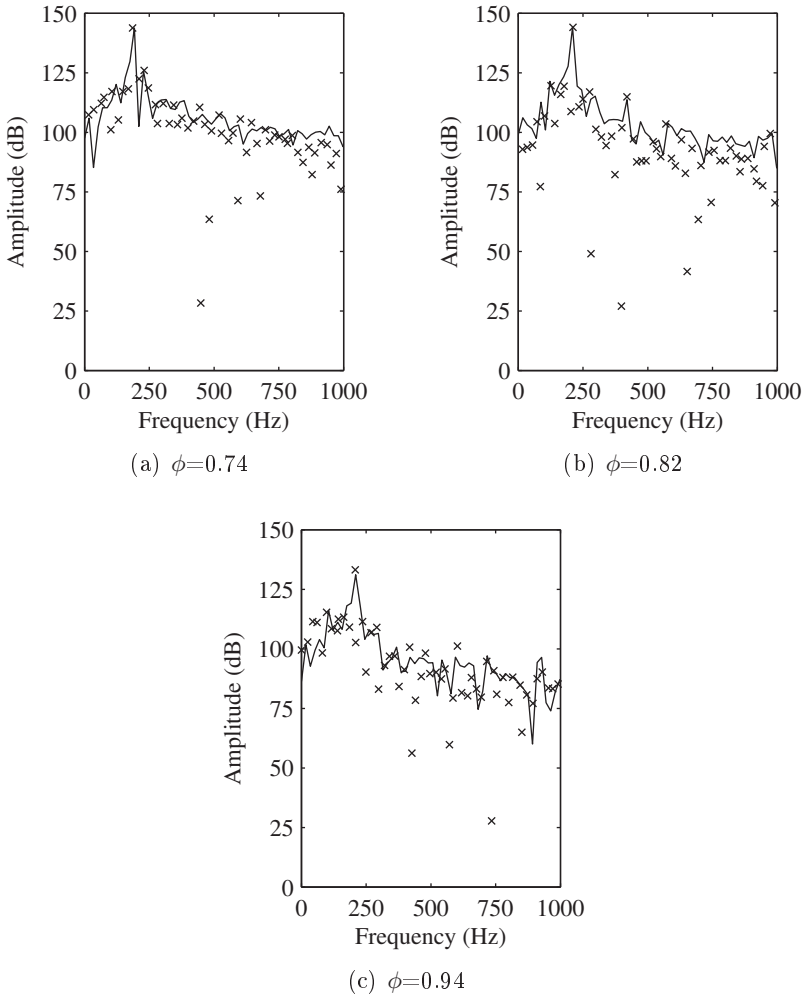

(a) ϕ=0.74

(b) ϕ=0.82

(c) ϕ=0.94

Figure 4.21: *Comparison of results obtained from EDMD on pressure (crosses) for a projection on a base obtained using direct imaging, and PSD estimate on the same data points.*

Equivalence ratio	0.74	0.82	09.4
F_1 (Hz)	191	212	211
$Amp_1(Pa)$	400	433	78
$Amp_{1\,PSD}(Pa)$	419	428	77
$Amp_{1\,phase\,average}$	434	446	93
F_2 (Hz)	390	424	416
$Amp_2(Pa)$	12	9	2
$Amp_{2\,PSD}(Pa)$	13	9	NA

Table 4.2: *Characteristics of the two main modes observed on the EDMD applied to the injector pressure signal, computed with 400 images at 7 kHz (approx. 12 cycles).*

amplitude from the PSD, a correction of the windowing's effect on the PSD must be implemented. To do so, the method described by Schmid (2012) was used. The energy contained at the peak corresponding to the i$^{\text{th}}$mode is:

$$Energy_i = P_i \frac{f_{res} NG}{CG^2} \tag{4.22}$$

with P_i the value given by the PSD, f_{res} the frequency resolution, and NG and CG are correction factors dependant on the windowing function. TFor the hanning window used here, the values are CG=0.5 and NG=0.375. Once the energy in the monofrequential mode is computed, the amplitude is simply deduced:

$$Amp_i = \sqrt{Energy_i}\sqrt{2} \tag{4.23}$$

The results from the two evaluations are close (within 5%) for the main mode. For the double frequency mode, the results are less similar however, and for ϕ=0.94, no peak is visible at these frequencies for the PSD. The phase average on the same data set gives even higher amplitudes. The closest results are obtained for ϕ=0.82, with only 2.9% difference. At ϕ=0.74, the difference between the EDMD evaluation and the phase average amplitude is 8.5%, and at ϕ=0.94, it goes up to 20%.

It has now been established that the EDMD on the pressure inside the injector gives good results in terms of finding the frequency and amplitude of the fluctuations corresponding to the combustion instability. Another property that must be verified is the phase difference between the different signals: pressure, broadband emissions and OH* emissions. The basis for comparison is easy to obtain: by construction, the signal at the n$^{\text{th}}$ time step for the pressure P and

any other signal V is:

$$\begin{aligned} V_n &= \mathrm{Re}\left(\sum_i \psi_i \alpha_i \mu_i^{n-1}\right) \\ P_n &= \mathrm{Re}\left(\sum_i \beta_i \alpha_i \mu_i^{n-1}\right) \end{aligned} \tag{4.24}$$

From this, it comes that the phase for the i$^{\text{th}}$ mode of the pressure signal at that time step is the phase angle of $\beta_i \alpha_i \mu_i^{n-1}$. The phase difference between the modes on V and P is then $angle(\psi_i \alpha_i \mu_i^{n-1}) - angle(\beta_i \alpha_i \mu_i^{n-1})$. In order to make a comparison with the phase average calculations, a phase of 0° must correspond to a zero ascending pressure inside the injector, which corresponds to a phase angle of 270° for the exponential term. It can then be deduced that the average cycles obtained from the EDMD for the i$^{\text{th}}$ mode are of the shape:

$$\begin{aligned} V_{i,average} &= \mathrm{Re}\left(|\psi_i \alpha_i \mu_i^{N-1}| e^{i(\omega\theta + angle(\psi_i \alpha_i \mu_i^{N-1}) - angle(\beta_i \alpha_i \mu_i^{N-1}) + 270)}\right) \\ P_{i,average} &= \mathrm{Re}\left(|\beta_i \alpha_i \mu_i^{N-1}| e^{i(\omega\theta + 270)}\right) \end{aligned} \tag{4.25}$$

for the pressure P and any other diagnostic V, with N the index of the last image used in the DMD. Using this formula, phase differences between the pressure inside the injector and in the chamber, as well as with the OH* emissions measured by a PMT can be obtained. The results are presented in table 4.3, where the phase between each variable and the pressure inside the injector is compared to the value found by the cross power spectral density method. For the cross power spetral density, the results given is the result from the calculation, with the resolution of the method as an error bar. As the EDMD does not really have a fixed resolution, it was chosen to take the maximum difference to the average value on the 32 different computed EDMDs for each value of ϕ as the amplitude of the error bar. This difference in choice for the expression of the methods' resolution explains the higher values for the EDMD. The results for both methods are in good agreement, confirming the validity of the EDMD approach.

The next step is the comparison of the spatial shape of the main mode as obtained by DMD to the phase average. More precisely, as the reference pressure is available for all individual DMD calculations, it is possible to compute a periodo-DMD of the images which can then be compared to the phase average computed on the same images. To compute the periodo-DMD, the phase reference from the injector pressure is used: knowing the phase difference between the microphone and the chemiluminescence signals for each individual mode, the mode is reconstructed at a phase corresponding to 0° for the microphone for each individual DMD (including the amplitude), and then

Equivalence ratio	0.74	0.82	0.94
phase $P_{chamber}$ (EDMD)	-29°±6°	-63°±6°	-43°±27°
phase $P_{chamber}$ (cpsd)	-35°±3°	-63°±3°	-45°±3°
phase $OH*$ (EDMD)	-75°±10°	-109°±5°	-92°±26°
phase $OH*$ (cpsd)	-80°±3°	-110°±3°	-100°±3°

Table 4.3: *Phase difference between various signals and the pressure inside the injector, measured either by the EDMD (with extrema values indicated) or cross power spectral density methods.*

an average of these modes is computed to obtain the periodo-DMD.

The results obtained are presented in figure 4.22. On the left side is given for each injection condition the periodo-DMD mode obtained as described in the previous paragraph. On the right side are given the fluctuations of the phase average: it is the phase average minus the global mean of the signal. This is necessary to compare the two results, as the periodo-DMD was only used for the main mode, and so it does not include the average of the signal.

What can be seen from the results in figure 4.22 is that both methods are again in good agreement: both the mode's shape and amplitude are similar with the two different methods. This seems to confirm that the DMD gives excellent results on the instability observed here.

The periodo-DMD was calculated here by using the reference pressure signal acquired at the same time as the high speed images to deduce the arbitrary phase difference between the modes obtained by the various DMD calculations (as the reference phase for each DMD calculation is the signal's phase at the first time step for the input data set). Another way of computing this average would be to take the zero-phase of one DMD as the reference point, and then deducing the phase difference between this DMD calculation and all the others by correlation. Indeed, by calculating the values of the mode at various phase angles, and considering that the same dynamics are described by all the DMDs, the phase difference is the phase value that gives the highest correlation with the reference frame. The periodo-DMD can then be obtained by averaging the modes as obtained by all the DMD calculations, taking into account these phase differences. This would be required if no extra variables would be recorded simultaneously.

4.7.3 Variability of the measurements: a physical explanation

As developed in section 4.6, the variability obtained on the DMD computations are much higher on the experimental images than they were in the synthetic

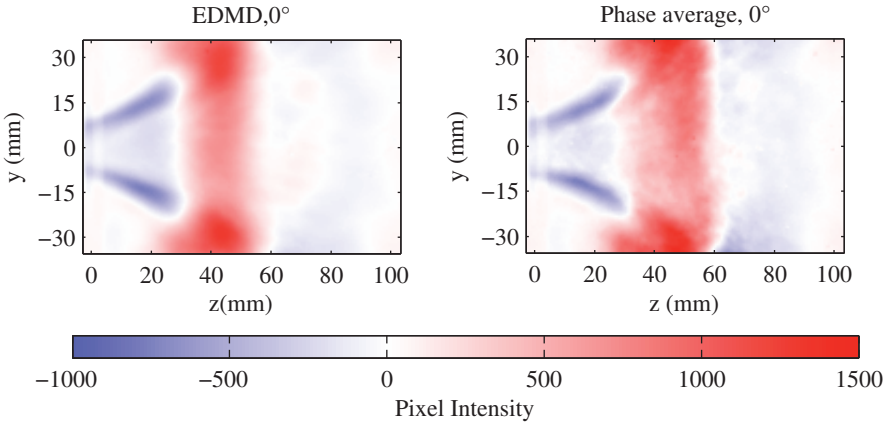

(a) ϕ=0.74

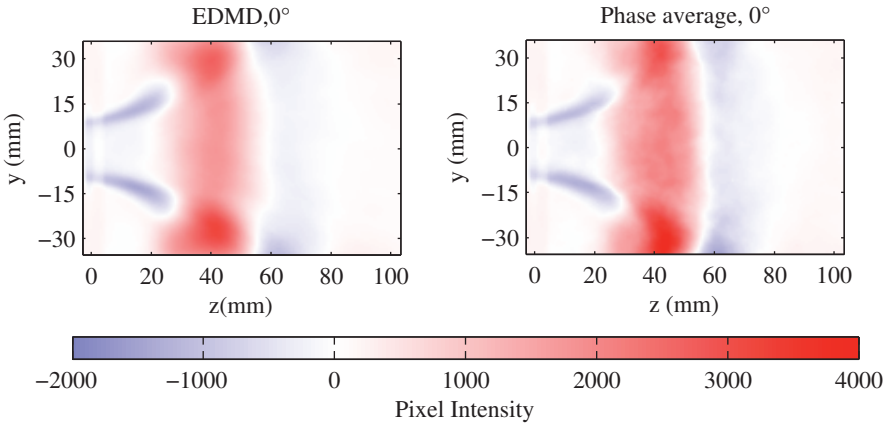

(b) ϕ=0.82

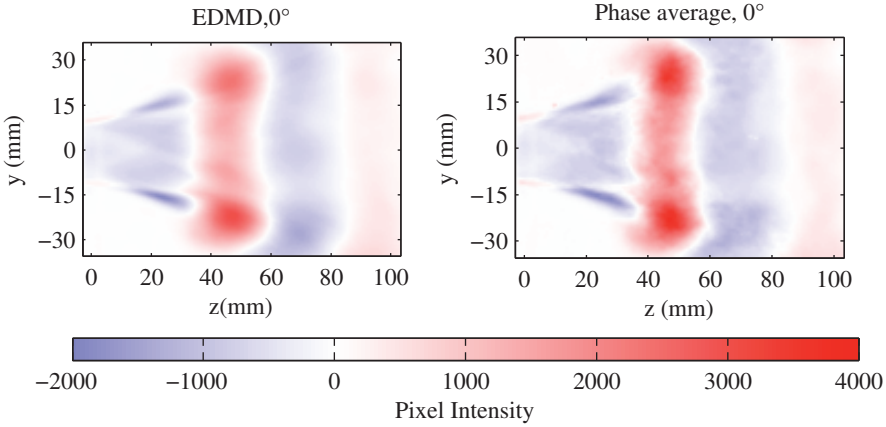

(c) ϕ=0.94

Figure 4.22: *Comparison of results obtained by doing a periodo-DMD (left) and phase average (right) on the high speed images of the flames, for each equivalence ratio condition. Periodo-DMD obtained from 32 individual DMD calculations.*

case. This is partly due to the difference in the data's nature. In particular, the instability in the synthetic case was constructed as purely monofrequential and with a constant amplitude. From what can be observed in the pressure fluctuations of the signal however, this is not the case for the experimental instabilities.

In particular, the main cycle's amplitude varies with time. To evaluate if these variations are the cause of the greater dispersion of amplitude obtained by the DMD on experimental data, in a first step the superposition of the pressure signal and of the mode amplitude for the same signal as found by the EDMD for microphone M1 are presented in figure 4.23. For each EDMD computed in this study, the amplitude of the main instability is indicated by a cross placed at the time-step of last data point used for the calculation. As a reference, a horizontal bar was placed at the top of each graph. The length of this bar is the length of the data set used in the EDMD computations. These results show that the variations detected on the amplitude of the EDMD (and very probably on the DMD as well) are linked to the variations in amplitude of the oscillation in the data used. When a strong variation in the amplitude is present in the base data itself, it is also translated in the EDMD results, as is the case for example when looking at the results for ϕ=0.94: there are EDMD computed at times when the fluctuation's amplitude is high (at index 1000 for example), and at times when it is low (indexes 1600 and 1800).

In a second step, a more thorough analysis was made. For each EDMD performed, the amplitude of the last oscillation in the data set used was extracted for both microphones as well as the photomultiplier. The EDMD amplitude can then be compared directly to the actual pressure oscillation amplitude for each data set, to better understand the precision of the method. Results are presented in figure 4.24 for the pressure data, and 4.25 for the chemiluminescence They show that the dispersion can be important: more than 40% of difference between the EDMD value and the last oscillation's amplitude can be found. Unexpectedly, it's the case ϕ=0.94 where the EDMD seems to correspond the most to the actual oscillation amplitude, as was already visible in figure 4.23. This can come as a surprise, since one could expect that the constant amplitude EDMD computed here would have more trouble describing the variations in time of the amplitude characteristic of this injection condition. This still holds true for ϕ=0.82, but with more discrepancies than in the former case. Lastly, for ϕ=0.74, the EDMD seems to register correct values when the amplitude of the oscillations is high, but underestimates the amplitude when the oscillation is weaker. The results for the analysis of chemiluminescence, presented in figure 4.25, show an inversion of the trend observed in pressure signals: the ϕ= 0.74 and 0.82 cases show an agreement between EDMD and measurement of the last amplitude in the sample used, while for ϕ=0.94, the EDMD tends to underestimate the amplitude.
The values measured by the EDMD can show an important deviation from

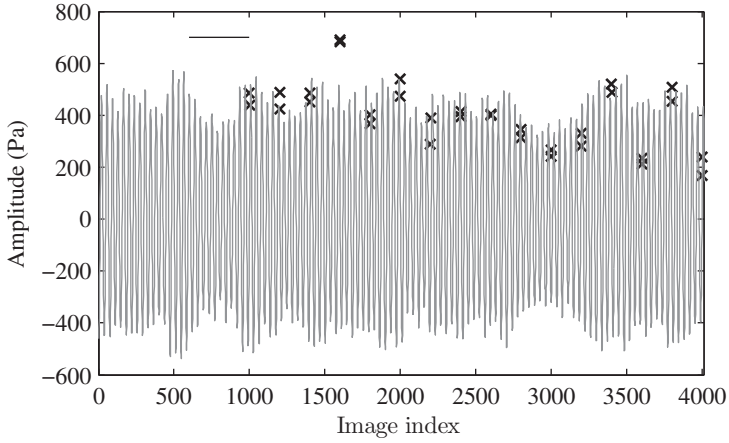

(a) ϕ=0.74

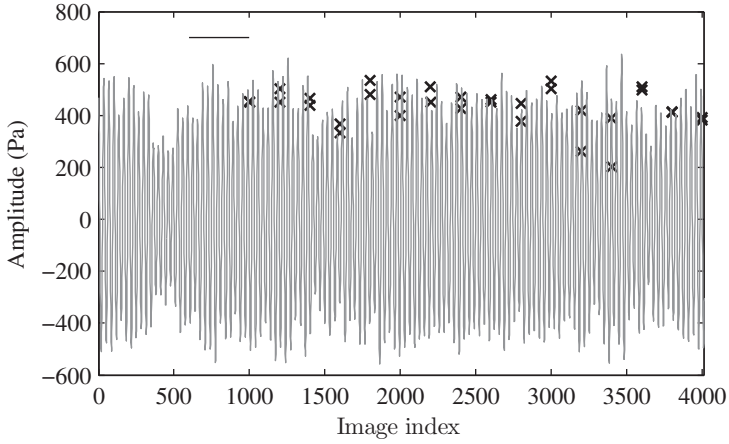

(b) ϕ=0.82

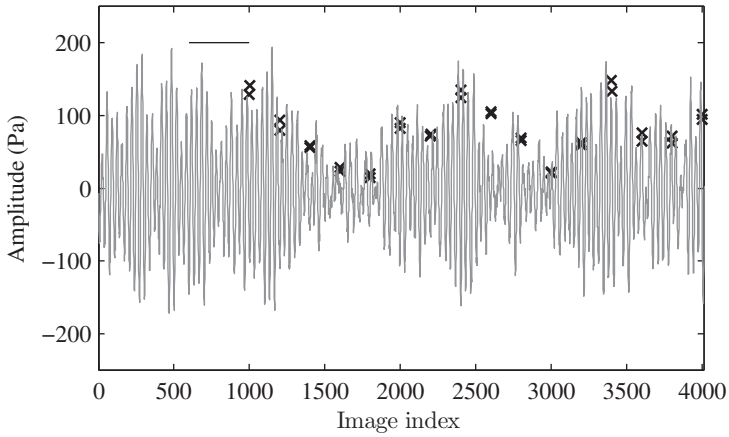

(c) ϕ=0.94

Figure 4.23: *Pressure signal inside the injector for the three injection conditions, and the EDMD amplitudes detected depending on the data sets used (indicated by crosses). The cross is placed at the index of the last data point used for the EDMD calculation, and a line plotted at the top of each graph represent the length of the data set used.*

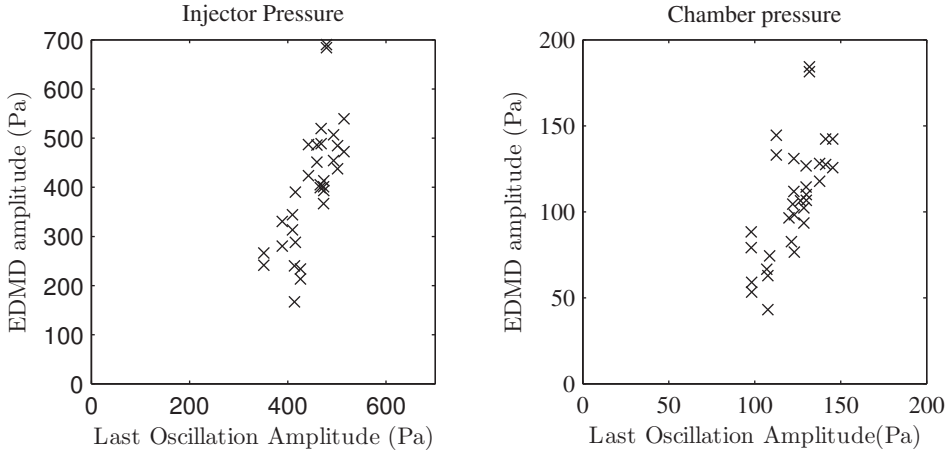

(a) ϕ=0.74

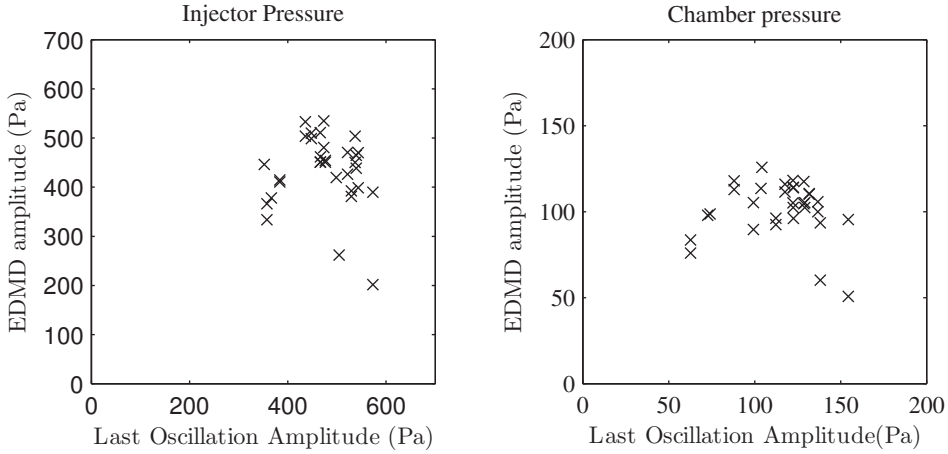

(b) ϕ=0.82

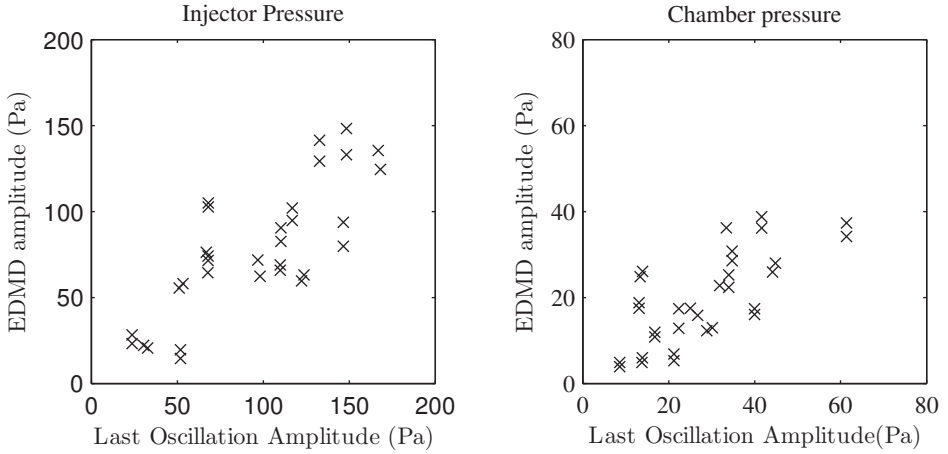

(c) ϕ=0.94

Figure 4.24: *Amplitude found by the DMD as a function of the amplitude at the last oscillation in the dataset for both microphones.*

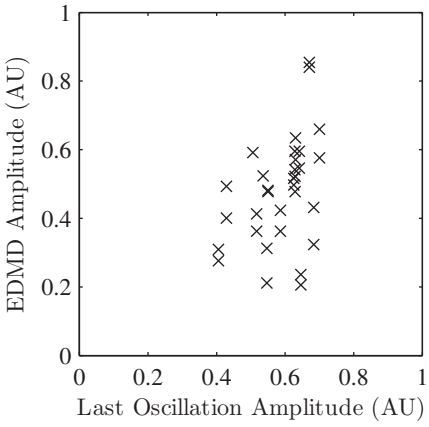

(a) ϕ=0.74

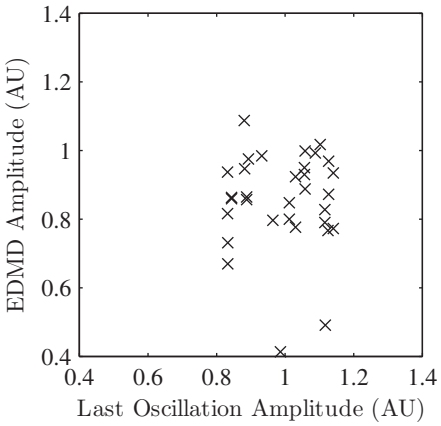

(b) ϕ=0.82

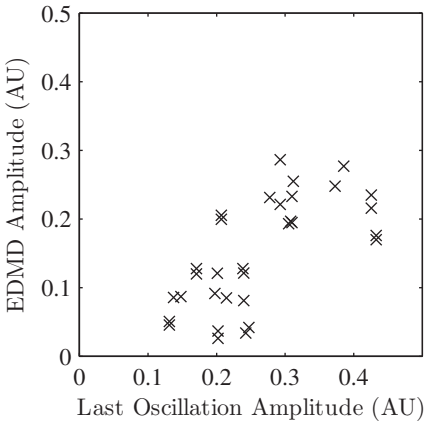

(c) ϕ=0.94

Figure 4.25: *Amplitudefound by the DMD as a function of the amplitude at the last oscillation in the dataset for the photomultiplier.*

ϕ		0.74	0.82	0.94
$P_{injector}$	Average	12.6%	11.8%	10.7%
	Max	44.0%	48.3 %	35.3%
	Min	0.9%	0.7 %	2.27%
$P_{chamber}$	Average	12.6%	11.7%	13.8%
	Max	45.8%	46.8%	37.2%
	Min	1.5%	0.3%	4.9%
$OH*$	Average	14.1%	12.0%	12.5%
	Max	47.7%	48.1%	40.4%
	Min	0.8%	0.4%	1.7%

Table 4.4: *Difference between amplitudes found by the EDMD for data set with only 1 data point offset between them (16 pairs available for each ϕ value).*

the actual amplitude in the underlying signal, but as was stated before, two series of DMD with only a slight difference in the data set used were analyzed: there is only one point shift between them, as indicated by the paired crosses visible in the graphs. Thanks to these two series using very close data set, it can be seen that even a minor difference in data points can result in fairly important variations on the amplitude detected: most of the pairs of crosses visible in figure 4.23 exhibit a noticeable difference, which in some cases can become quite important, as illustrated here by the EDMDs computed using data sets using last index 3200 and 3201, or 3400 and 3401 of the ϕ=0.82 case. A more thorough analysis was conducted by measuring the relative difference in amplitude for the main mode for each of the 16 pairs of DMD available for each value of ϕ. The results presented in table 4.4 show that the difference is indeed substantial: for the three diagnostics used in EDMD computation, a shift of only one point in the data set leads on average to more than 10% difference in the resulting amplitude, with a maximum difference systematically over 40%. This does confirm the importance of the last data point used in DMD computations, as this is the main difference in the data set used in this comparison.

The DMD and EDMD results must thus be taken with a bit of care: the data used has to be representative of the system, but even if the underlying physics are the same, a variation of more than 10% in the amplitude of a strong mode can be found with a minor variation in the data set used (a difference of 2 data points in the present case). This is another reason to recommend the averaging of several DMD's results if the goal is to obtain quantitative information.

4.8 Conclusion

The Dynamic Mode Decomposition proved to be an adequate post-processing technique for analyzing the combustion instability. It proved to be very accurate on a synthetic signal representing a simplified version of the expected dynamics of the system (less than 1% error on all characteristics of the dynamics used), and in cases having sinusoidal dynamics at a fixed frequency, fairly low data quantity and acquisition rate should be required: 10 cycles acquired at 3.3 points/cycle seem sufficient to extract the information. However, using experimental data proved more difficult, as it is prone to noise and fluctuations in both amplitude and frequency of the instability governing the dynamics of the system. More precisely, it appears that an upper limit on the number of cycles used is also present here: more than 20 cycles result in greater dispersion of the results of the DMD depending on the image set used. The Extended Dynamic Mode decomposition allowed to obtain the pressure and OH* emissions linked to the fluctuations of the direct images of flame, and confirmed the results obtained by the phase average and statistical analysis.

A comparison between the DMD and the POD results on the same 400 images for each equivalence ratio showed that, if the two most energetic POD modes seem to correspond to the DMD mode at the main instability frequency, the similarities end there. The POD modes present a rich content in the frequency domain, rendering their interpretation difficult. In particular, several modes show strong content both around 200Hz and 400 Hz, and no POD mode could be found that would account for the majority of the energy repartition at 400 Hz, rendering the analysis of the fluctuations at that frequency impossible using the POD in the same conditions as the DMD.

From this study using the DMD and EDMD, the instability's evolution with the equivalence ratio is confirmed. At low equivalence ratios, a strong pulsation of the flame can be observed, accompanied by vortex shedding. This vortex shedding is strongly marked and already influencing the flame's shape at the injector. When the equivalence ratio is increased to 0.82, the same dynamics are conserved, with similar amplitudes. The frequency of the instability gets higher, reaching a frequency close to 212 Hz. The results obtained at ϕ=0.94 suggest that for this value, the vortex shedding gets closer and closer spatially, and has an influence that is further downstream. This translates into lower amplitudes for the pressure fluctuations generated, while the angle of the flame and the chamber axis decreases. Therefore, the combustion instability in all these conditions can be described by a mode with similar characteristics, and thus can be supposed to have the same underlying driving mechanisms, but the mode's characteristics (frequency, amplitude, spatial repartition) change with the injection conditions.

Conclusion

The goal of this thesis work was to develop a reusable strategy for the analysis of combustion instability in partially-premixed swirl flames, using the CESAM burner as an example. In particular, the post-processing strategy used very common statistical analysis methods and phase averaging, but also a more recent development in the identification of coherent structures, the Dynamic Mode Decomposition.

General Conlclusion: Post-processing strategy

First, a statistical study should be used to have a basic understanding of the underlying mechanics. In the case of combustion instability, the pressure signals are the first to be analyzed, but an estimation of the heat release rate is also important. Fourier transform analysis or a Power Spectral Density should be used to check the instability's characteristics, in particular if the frequency content presents one or several peaks. For example, in the previous study of the CESAM burner (Lamraoui (2011)), using a doubled mass flow at similar equivalence ratios than in the present study led to a bimodal instability, where several modes linked to the injector tube or the combustion chamber were simultaneously present while in this study the instability appears at a single frequency. Cross power spectral density can also be used to obtain an estimation of the phase differences between the various physical quantities available.

Then, once one or several predominant modes are detected, phase averaging can be used. This method however will only give good results if there is one clearly dominant mode, otherwise the phase averaging at one frequency could take into account the influence of the content at other frequencies. The use of phase averaging is particularly necessary if one of the diagnostics used has a very low acquisition rate, as was the case in this study with PLIF measurements at 10 Hz for an instability around 200 Hz. Care must be taken not to filter too much the reference signal when computing phases, as this could lead to erroneous cycle detection.

If time resolved 2D fields can be acquired, a modal analysis tool such as the POD or the DMD should be used. The POD gives structures that may be difficult to interpret since their temporal evolution can be quite complex, but the method is well known and gives interesting results. In the present study, the POD was used as a basis for comparing the results obtained using the more recent and less studied DMD. The DMD's main advantage over POD is the modes' ease of interpretation: their temporal evolution is sinusoidal, and the convection of a given structure is described by only one mode, whereas the POD would need two. In the case of the DMD, a sensitivity study should be made to ensure how many cycles of the expected instability must be used when computing the decomposition. In the present case, 8 cycles seemed to be the minimum, independently from the acquisition frequency used. The calculation on a single data set gives very good results as far as frequency and spatial shape are concerned, but the modes' amplitude is more subject to error or uncertainties. In order to obtain better accuracy and precision, the recommended approach is thus to compute several DMD on different sets of data points, and then compute the average of the modes' characteristics. If several diagnostics are used simultaneously, two approaches can be adopted to take advantage of the additional information. In the first approach, different data types can be used as a base to compute the decomposition (DMD as well as POD). The main difficulty would be to find the proper scaling factors to prevent one diagnostic overwhelming the other(s) if the global dynamics of the system are desired. The other approach, is to project the data points from the other diagnostics on the mode base obtained from the main data set. This is the approach taken in this study, where pressure and chemiluminescence signals were projected on the DMD base from high speed imaging of the flame.

The phase averaging and modal decompositions lead to a better understanding of the instability cycle in itself, and can take advantage of simultaneous acquisition. Phase averaging is for the moment the only method available to reconstruct a mode from very low frequency diagnostics, provided a reference signal at high frequency is simultaneously acquired. Recently, efforts have been made to develop methods based on the DMD algorithm that could use data at low acquisition frequency as input, and thus could lift this particular limitation. If the acquisition rate of images (or vector field) is high enough, modal decomposition methods should be preferred, as they do not force the dynamics of a different signal on the results, but use the data itself. Both the POD and DMD have their own limitations however. POD needs several modes to describe simple underlying dynamics (in particular, at least two modes to describe the convection of a flow feature), and since it prioritizes the energy content of the modes, in some cases a coherent flow feature may have its importance in the dynamics of the phenomenon underestimated. The DMD on the other hand, forces the modes to have a sinusoidal behavior, which can be problematic if the underlying dynamics do not have such evolutions.

General Conclusion: Flame dynamics

The statistical analysis of the acquired acoustic pressure signals allowed to ascertain that a single acoustic mode dominated burner' dynamics for the mass flow rates used in the study, regardless of the equivalence ratio and staging tested. This allowed to have a first understanding of the instability's evolution with the equivalence ratio, and to chose three particular injection conditions that seemed interesting as they delimited a change in that evolution. Indeed, at low equivalence ratios the mode's amplitude is constant, and its frequency rises with the fuel's injection rate. At higher equivalence ratios however (but still in lean conditions), the frequency obtained is constant, and the amplitude decreases with an increase of equivalence ratio. This change in the evolution was studied in detail by choosing the 3 injection conditions ϕ=0.74, 0.82 and 0.94. The first and last ones are the most extreme values in the usable injection conditions of the burner at the considered mass flow rate, and ϕ=0.82 is the value at which the change in the evolution was observed. Further analysis showed that as could be expected, there are fluctuations in the heat release rate, broadband emissions of the flame, and in temperature inside the chamber at the mode's frequency, exhibiting a high coherence with pressure fluctuations.

In a second step, effort were made to obtain equivalence ratio fluctuations from acquired data. This measurement is based on the absorption of an infrared laser by fuel molecules in the fresh gases. Due to the burner's geometry, the laser had to be placed outside of the injector, where the flame and burned gases are present. It was thus necessary to determine fluctuations in the length of fresh gases crossed by the laser beam, especially since the strong flame movement suggest that this length should change during an instability cycle. In order to determine these fluctuations, OH PLIF images were used. Since only one mode is overwhelmingly prevalent and the PLIF was acquired at a low frequency together with a high speed reference pressure signal, phase averaging post-processing was conducted. In order to validate this phase averaging approach, it was used on most acquired signals. This allowed to confirm the phase difference between the various physical quantities studied, which were previously obtained by cross power spectral density. In a second step, the evolution of the Inner Recirculation Zone of the flow was analysed using the OH PLIF images acquired in radial planes. This showed that contrary to first expectations, the two lean conditions do not exhibit a radial symmetry: the radial profile of IRZ is a rotating ellipse. Its rotation rate however seems to be around half the instability frequency's, suggesting that a precession phenomenon unseen on the pressure signals may occur there. The higher equivalence ratio has a more standard behavior: the IRZ is almost circular,

with two small inwards recesses near the horizontal plane. The orientation of these slits changes with the distance to the injector. The evolution of the IRZ's surface, as well as axial PLIF imaging and broadband emissions of the flame indicate that in the lean cases, a vortex is rolled and convected downwards from the injector, causing a strong transversal opening and closing of the V-shaped flame. In the richest case, this vortex is only visible far from the injector, and has a much lesser impact. In all three cases, a pattern of temperature fluctuations convected in the combustion chamber was measured with the BOS system. Finally, estimations of the length of fresh gases crossed by the IR laser were attempted. Two methods were tested: one using radial PLIF results, and one using axial images. However in both cases the results have a high uncertainty, and thus the values obtained for the equivalence ratio are to be taken with caution. In particular, the average equivalence ratio could not recovered properly. The results however do suggest that in the two leanest cases strong equivalence ratio fluctuations can occur, while for ϕ=0.94 their amplitude is much lower.

Lastly, the high speed imaging of the flame was studied using the DMD, and in a lesser measure, the POD. This method is interesting if time resolved 2D fields are available, since it can give good information on the system's dynamics using only a very limited amount of data points, and quantitative results can be achieved if several DMD computations are averaged. As a parametric study showed that less than 8 cycles in the data set used would not give satisfactory results, the DMD was computed using 12 cycles in the present case. When considering fluctuations at the instability's main frequency, DMD and POD gave results very similar to the phase averaging, which was expected since both pressure (used as a reference for phase averaging) and broadband emissions of the flame are highly correlated at that frequency. Since the DMD and POD do not use pressure as a reference however, it confirmed that no strong bias was introduced by the phase averaging method. The DMD showed slightly more interesting results that the POD. The analysis of the DMD modes' amplitudes does indeed show a secondary peak at two times the main instability's frequency, while no POD mode describing such an evolution could be found: all modes mainly vary at the instability's frequency. By computing the Extended DMD, which consists in projecting data taken simultaneously to the images used in the DMD computation on the modes obtained, the pressure and heat release rate were also studied. The results of the Extended DMD on the main instability mode for all the diagnostics used, in amplitude as well as in phase, are in good agreement with phase averaging results, confirming the method's validity.

In conclusion, the CESAM burner exhibits a strong thermoacoustic instability around 200 Hz for all stable points with an air mass flow rate of 7.6 g/s and a staging of 50%. For low equivalence ratio values (ϕ<0.82), the pressure

fluctuations' amplitude is the strongest, with the phase difference between the fluctuations in the injector tube and the chamber rising with ϕ. This is accompanied by a strong vortex roll-up from the injector, causing transversal fluctuations of the flame. The IRZ is elliptical, with a rotation that seems to be around 100 Hz, suggesting a different mechanism than the main instability may be at play. The literature suggests that it could be due to the precession of vortexes in the IRZ (O'Connor and Lieuwen (2012)), which could not be observed using the diagnostics employed in the present study. For ϕ=0.94, the phase difference between the pressure in the injector and in the chamber is down to values obtained at the lowest equivalence ratio used, but the fluctuations have a much lower amplitude. The vortex-roll up is much less marked, and the flame seems stable near the injector. The IRZ there is almost circular, and oscillates around a central position during an instability cycle. The phase difference between the heat release rate and pressure fluctuations in the chamber is almost constant and around 45° for all three injection conditions, giving a positive Rayleigh criterion. Temperature fluctuations in the chamber were observed being convected in all three cases. Results from equivalence ratio measurements, even though not entirely reliable, suggest a strong fluctuation in the two lean cases exhibiting a high amplitude instability, and a lower fluctuation in the low amplitude case.

Perspectives

The present study exhibited the presence of a strong instability mode in the CESAM burner, that stabilizes at high equivalence ratios. The evolution of pressure, chemiluminescence from OH radicals, and the geometry of the flame were obtained quantitatively, along with qualitative results on temperature fluctuations in the chamber, and an estimation of equivalence ratio fluctuations. Ideally, a PIV study or similar would allow to obtain the velocity field to check whether or not the velocity at the injection plane is constant during the cycle, as well as the presence of precessing vortexes in the IRZ. However, the uncooled chamber of the present configuration is a problem: it limits the time available for measurements, but most importantly, it prevents access to thermally stabilized conditions which would improve the measurements' repeatability. Moreover, for the strong instability present for the lowest equivalence ratio, the flame almost impacts the walls during some parts of the cycle. A larger chamber may then be preferable to reduce the wall's effects on the instability observed.

The method used to make absorption based equivalence ratio measurements unfortunately did not work as well as intended. This is due to the flame's configuration (mostly present at the limit of the IRZ), which unfortunately led

to a weakly defined frontier between the fresh gases and the ORZ. Since the method relies on a precise measurement of the absorption length, a configuration with an M shaped flame, where both external and internal limits of the fresh gases are clearly defined, should give much better results. This method could then allow to use this absorption based technique in configurations where no plenum is present.

Concerning the DMD, there are several ways to improve on the current approach. The main problem at the moment is obtaining quantitative results. In the present case, even though the mode describing the instability is strongly prevalent and fairly stable, its amplitude fluctuates with time, causing fluctuations in the DMD mode's amplitude, independently from other factors. The use of a higher number of data points could be a solution, but the results obtained here suggest that a bigger data set does not necessarily give better results, as the dispersion obtained on several DMD calculations was similar when using 10 cycles or more. Another development linked to these concerns is the evolution with time of the modes. At the moment, the DMD algorithm never gives modes with a truly constant amplitude, even in the case of a purely sinusoidal synthetic signal. This is due to the exponential growth factor resulting from the eigenvalue calculations, which is left unmodified at the moment in the following steps of the post-treatment. A way to correct this may be to further develop an approach where the mode's amplitude is allowed to vary in time, similarly to the approach taken by Sayadi et al. (2015). In that case, an assumption on the relation between the most pertinent modes describing the system's dynamics is made, but this type of approach may allow to obtain a better description of the modes, including their amplitude fluctuations.

Appendix A

Influence of parameters in the phase average calculation

In this appendix, the effects of the filtering of the reference signal and of the method for phase determination on the computed phase averages will be detailed. This will justify the final choice of a filtering at ±50 Hz around the peak frequency, and use a zero-level detection for the phase.

A.1 The two methods of phase determination tested: Hilbert transform and zero-level detection

In a signal with a strong oscillation at a given frequency, the phase of any given point can be taken relatively to a reference signal M. This phase is defined for each time stamp t of a cycle as:

$$\theta = \frac{t - t_0}{\Delta t} * 360 \tag{A.1}$$

with t_0 the beginning of the cycle, taken arbitrarily in this study as the point where the signal goes from negative to positive values. Another possibility to obtain the signal's phase, is to use the Hilbert transform:

$$\theta = angle(Hilbert(M)) \times \frac{180}{\pi} + 90 \tag{A.2}$$

where the factors outside of the Hilbert transform are there to ensure a result in degrees with the reference phase of 0 degrees as before.

If the reference signal is perfectly sinusoidal, the two methods will give the same result. However, the Hilbert transform method is very sensitive to noise, which is unfortunately unavoidable when using experimental data. In order to illustrate the differences eventually existing between the results of the two methods, a comparison of the phases found using one of this study's acquired

signals was conducted. The figure A.1 is a scatter plot of the phases obtained with the two methods, when using the microphone reference signal filtered at ± 50 Hz around the peak value. It shows that for the two cases with a strong instability, the two methods indeed give very similar results. When ϕ=0.94 however, the presence of cycles at very low amplitude and with a shape somewhat far from a sinusoid, even on the filtered signal, creates differences between the two.

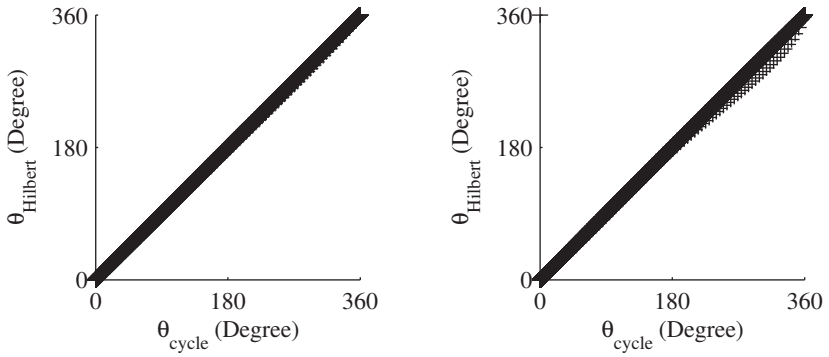

(a) ϕ=0.74

(b) ϕ=0.82

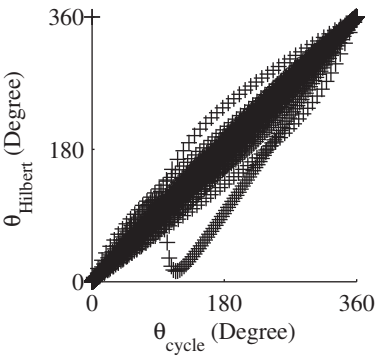

(c) ϕ=0.94

Figure A.1: *Illustration, for the three injection conditions, of the difference between a phase computing from the Hilbert transform, and the cycle detection methods, on the signal filtered wit a bandpass at ± 50 Hz around the peak pressure frequency.*

Since the instability at ϕ=0.94 shows substantial differences between the two methods, a choice has to be made. As the Hilbert transform methods suppose that the underlying signal is sinusoidal (which is not strictly the case here), and is more sensitive to noise, the instantaneous cycle detection method was chosen. Another advantage of this method, presented in chapter 3 section 3.3, is that when computing an instantaneous frequency, it is possible to

reject detected cycles with a frequency too far from the desired value. This is especially useful when treating the ϕ=0.94 case: the part of the signal with low amplitudes, even after filtering, can exhibit variations leading to cycles with an instantaneous frequency well out of the filter's range.

A.2 Influence of the filtering

In order to obtain better detection of the cycles, a filtering of the initial signal is necessary. However, the filter's width is of prime importance: if a very narrow filter is used, then the filtered signal's dynamic can be forced on a sinusoid at the filter's frequency, possibly modifying the shape of the obtained phase average (even though the amplitude values used are from the non filtered signal).

In order to obtain the influence of the filter's width, a systematic study was conducted. Phase values for a given signal were computed on the raw signal at first, and then after filtering with various bandwidths. The effect of the filters used is shown in figure A.2. The most severe filter at ±10 Hz barely encompasses the main peak, while other less restrictive filters take into account the broadband component of the flame noise at various degrees.

The scatter plots of the phases computed from a filtered/non-filtered signal are presented in figure A.3. The filtering's effect on the phase computed using experimental signals acquired at equivalence ratios ϕ=0.74 and 0.82 is minimal, with a dispersion getting bigger with more severe filtering. For the equivalence ratio ϕ=0.94 the effect is similar, but the presence of data points for which filtering or not has a great impact on the computed phase has to be noted. This phenomenon at high equivalence ratio can be attributed to parts of the signal where the oscillation's amplitude is low.

From these results, it seems that filtering is mainly interesting in the case ϕ=0.94, where looking at the temporal signal indicates that erroneous values will be found without it. However, care must be taken not to filter too much, in order to keep the dynamics of the real oscillation cycle intact. As a means of visualizing the effect of that filtering on the phase average obtained, the repartition of the data points in the cycle, as well as the corresponding phase average are presented in figure A.4. Since the results for equivalence ratios ϕ=0.74 and 0.82 are similar, only the results obtained for the latter are presented. As can be seen from those graphs, filtering has an effect on the repartition of the pressure values along the cycle. If no filtering is applied, as expected there is almost only points with pressure fluctuations at 0 Pa for phases at 0° and 360° per the definition of the phase used in the study. The

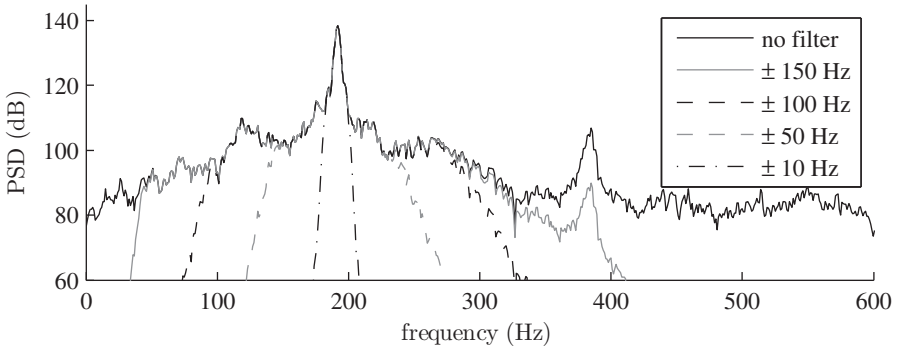

(a) ϕ=0.74

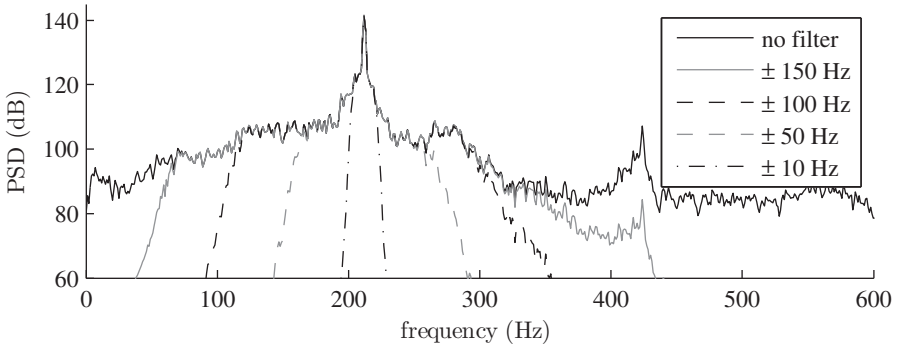

(b) ϕ=0.82

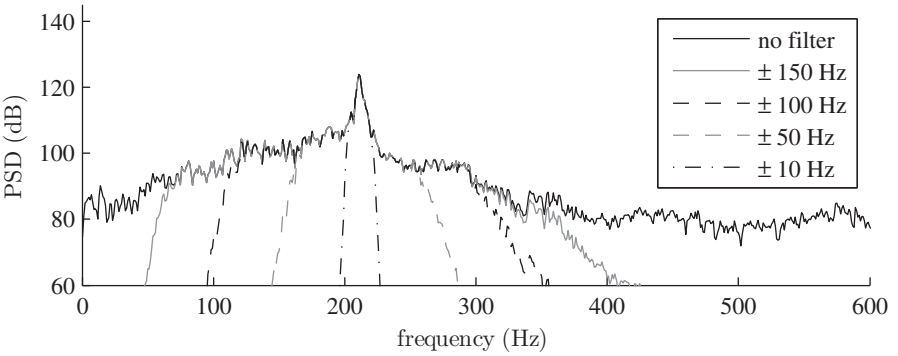

(c) ϕ=0.94

Figure A.2: *Visualization of the filters tested on the PSD of the reference microphone signal, for the three injection conditions.*

instantaneous cycles detected seem to have broadly the same shape, and vary in amplitude. When using a filter however, the narrower the filter used, the more cycles in instantaneous data appear to have a similar amplitude, but

Equivalence ratio	0.74	0.82	0.94
Unmodified signal	5.5%	8.9%	58.6%
± 100 Hz	4.3%	6.8%	51.1%
± 50 Hz	0.5%	1.28%	24.6%
± 10 Hz	0.2%	0.2%	2.0%

Table A.1: *Rejection rate of the points when calculating the phases for phase averaging, depending on the bandwidth of the filter applied beforehand.*

with shifted average pressures: the pressure at phase 0° and 360° is more often different from the average pressure. For the equivalence ratio ϕ=0.94 however, the need for filtering can be seen at first glance: without it, at any point during the cycle pressure fluctuations at 0 Pa can be obtained.

If the validation criterion that the instantaneous frequency for a cycle must be less than 10 Hz apart from the expected value is added, the effect is mainly seen on the injection condition ϕ=0.94. For this particular point, its effect can be important in term of rejection rate: if no filtering is applied to detect the cycles and compute the phases, almost 60% of the available data points can be rejected. The criterion's effect is presented in table A.1. From these results, it can be concluded that even though for ϕ=0.74 and 0.82 no preliminary filtering seems necessary, the ϕ=0.94 case needs it in order to not lose half of the data points.

The figure A.5 shows the effect of that elimination criterion on the distribution of points: those that are rejected also mainly correspond to cases where the amplitude at non-zero phases is very low, or even in phase opposition to what would be expected, especially if no preliminary filtering was made. In the case of a signal already filtered at ±50 Hz, no important impact on the distribution's shape seems to happen.

Finally, the figure A.6 shows for the three injection conditions the effect of the filtering on the computed phase average. In all cases, the signal was filtered, and the rejection criterion applied. The phase average was computed with a 7.5° large bin size (so with a better phase resolution than showed in the rest of the study). The results show that even though filtering seemed to change the repartition of the points among the phases, the effect on the phase average is almost negligible for ϕ=0.74 and ϕ=0.82. For ϕ=0.94, the filtering's effect is a reduction of the amplitude obtained, but if the filtering is kept at more than ±50 Hz, the effect is still minimal.

A.3 Conclusion

The cycle detection method for the phase computation was chosen over the Hilbert method because at injection condition ϕ=0.94, the presence of non sinusoidal cycles, even in the filtered signal, could lead to erroneous values for some points' computed phase.

From this study of the different parameters used for computing the phase average of the signals, it can be concluded that the use of a filter with a $\pm$50 Hz bandwidth, coupled with the elimination of cycles with an instantaneous frequency more than 10 Hz apart form the central frequency seemed to offer the best compromises. The filtering and rejection criterion ensure that the number of erroneous cycles used in the phase average is kept to a minimum while keeping a good portion of the initial points and not affecting too greatly the repartition of the phases and phase average.

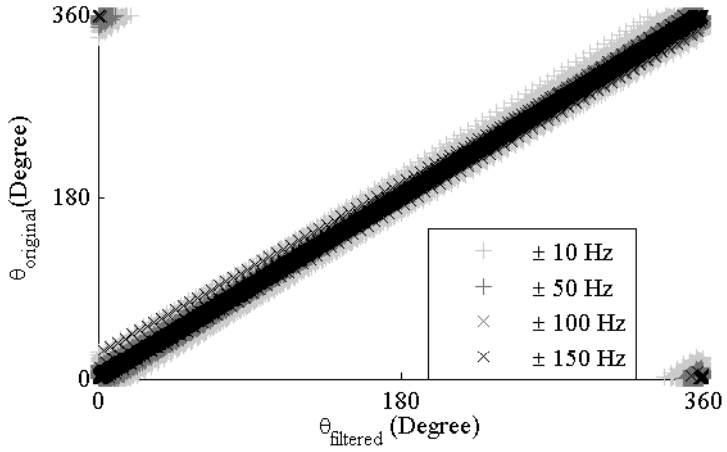

(a) ϕ=0.74

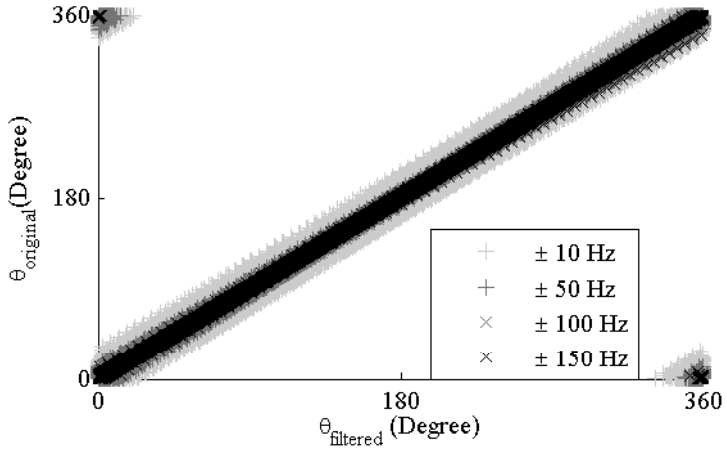

(b) ϕ=0.82

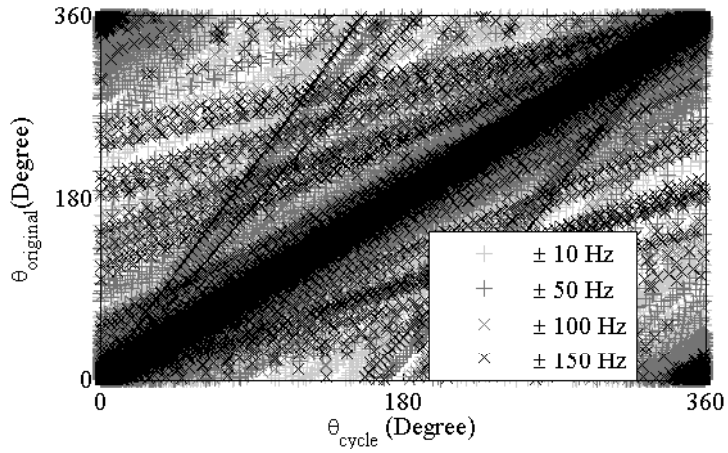

(c) ϕ=0.94

Figure A.3: *Scatter plots of the phase obtained from a filtered reference signal, compared to the phase obtained from the unmodified signal.*

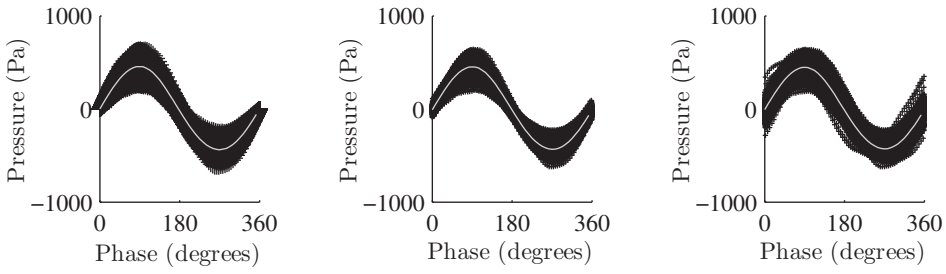

(a) ϕ=0.82, no filtering (b) ϕ=0.82, ±50 Hz filter (c) ϕ=0.82, ±10 Hz filter

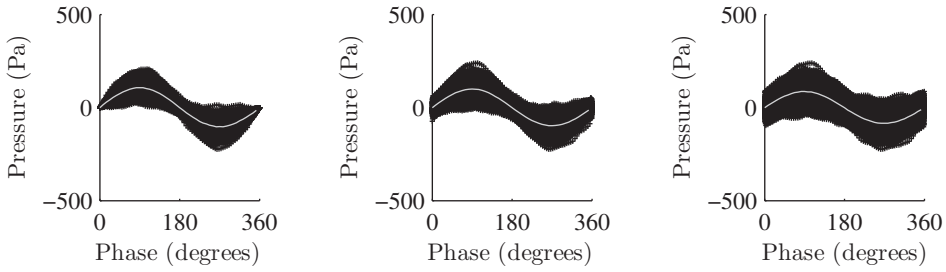

(d) ϕ=0.94, no filtering (e) ϕ=0.94, ±50 Hz filter (f) ϕ=0.94, ±10 Hz filter

Figure A.4: *Effect of signal filtering on the phase average of the pressure signal inside the injector. The line in gray is a phase average computed using bin of 7.5° width, while in black crosses are shown the individual points used in that phase average.*

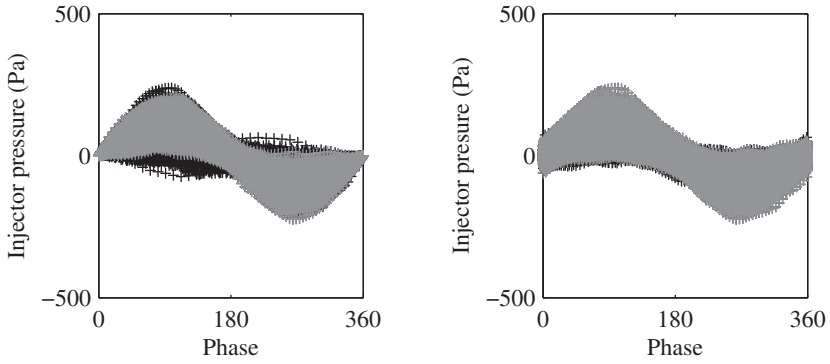

(a) ϕ=0.94, no filtering (b) ϕ=0.94, ±50 Hz filter

Figure A.5: *Effect of the elimination of points in cycles with an instantaneous frequency further than 10 Hz from the expected value. Points without rejection are shown in black, and after rejection in gray.*

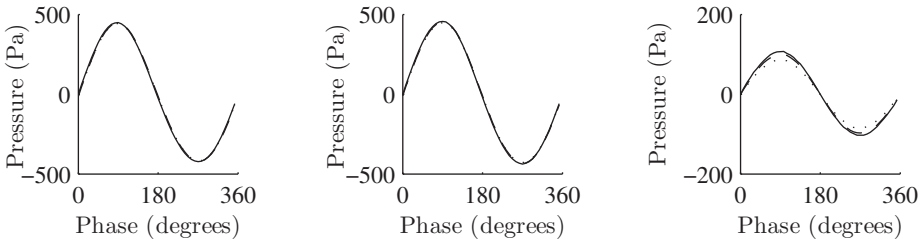

(a) ϕ=0.74 (b) ϕ=0.82 (c) ϕ=0.94

Figure A.6: *Effect of the filtering on the phase average obtained (with elimination of abnormal frequencies). The continuous line shows the results without filtering first, the dashed line with a ±50 Hz filter, and the dotted line with a ±10 Hz filter.*

Appendix B

Repeatability of the measurements

In this part, the statistics on the pressure signals acquired inside the injector will be detailed, as they were used as the reference to compare all the other measurement types. In particular, the distribution of the pressure amplitude, frequencies will be shown for the same injection conditions, and during a single test.

B.1 General information

Counting all the test runs made for each of the equivalence ratio, there is a total of 60 runs for each injection condition available. This should allow to obtain meaningful statistics on the measurements' repeatability. As the acquisition rate of the microphone signals was the same for all the tests, this parameter is not a problem. But the acquisition lengths depends on the diagnostics used simultaneously, and thus to ensure that the same number of windows was used when computing the PSD, only the first 4 seconds of each signal were used in the following results.

B.2 Dispersion of the frequencies

First, the dispersion of the main mode's frequency will be presented. It was obtained through a PSD analysis with a frequency resolution of 1 Hz. The figure B.1 presents the histograms obtained for each injection condition. For all of them, the pressure spectrum presents a peak at a stable frequency. For ϕ=0.82, almost all the values are contained in a $\pm$2 Hz band. There is a slightly higher dispersion for the ϕ=0.94 case, but as the instability is weaker in that case, it also presents the most overall variation between cases as will be seen with all other statistics shown here. Lastly, for ϕ=0.74, the repartition of the frequencies obtained is flatter. This can be explained by the fact that it is the

only equivalence ratio used that is in the range where the instability's frequency varies with the equivalence ratio: small fluctuations in the average equivalence ratio between one test run and another are expected to have an impact on the frequency obtained, which is less true for the two other cases.

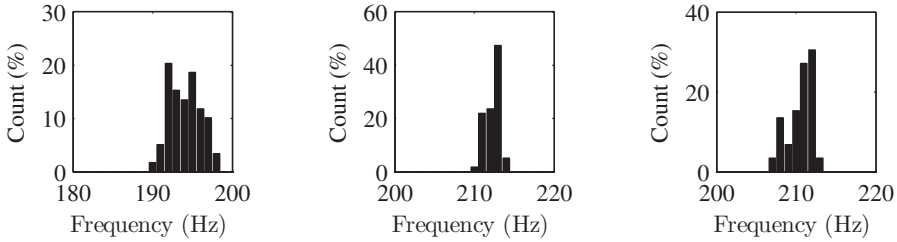

(a) ϕ=0.74 (b) ϕ=0.82 (c) ϕ=0.94

Figure B.1: *Histogram of the repartition of the frequency found for the main mode, using a PSD with a resolution of 1 Hz on the pressure inside the injector.*

B.3 Dispersion of the amplitudes

The variability of the amplitudes, as well as the relation between the amplitude of the modes inside the injector and chamber will be considered in this part. First, the figure B.2 presents a scatter-plot of the amplitude repartitions for the two modes. The amplitudes obtained from the PSD spectrum of the pressure signal in both microphones are clearly linked: no variation observed in the chamber isn't accompanied by a similar variation in the injector, which tends to confirm the coherence of the mode in the two cavities.

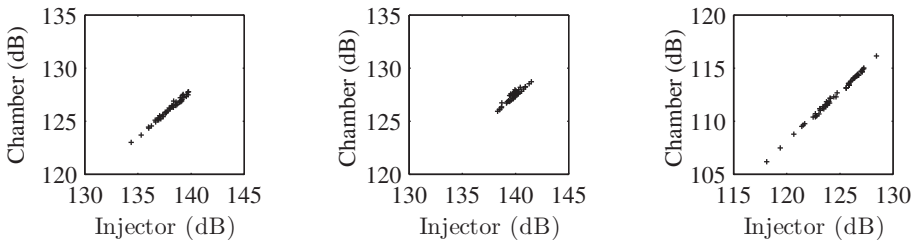

(a) ϕ=0.74 (b) ϕ=0.82 (c) ϕ=0.94

Figure B.2: *Scatter-plot showing the variability between different test runs in the peak amplitude in the spectrum of the pressure inside the combustion chamber, in relation with the amplitude inside the injector.*

The main mode's amplitude repartition when looking at the peak pressure is presented in figure B.3. This shows that for each equivalence ratio condition,

a variation of about ±2 dB in the amplitude can be expected. The richest injection condition gives the least stable amplitudes, with a more flattened profile.

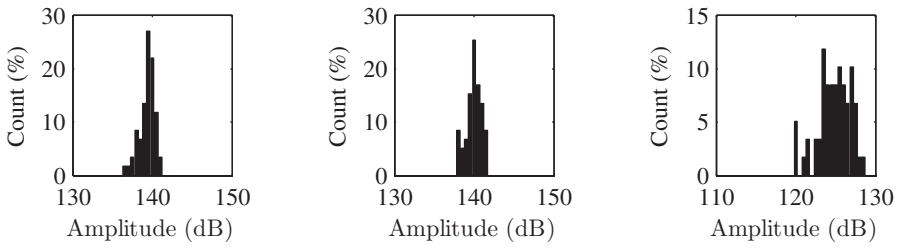

(a) ϕ=0.74 (b) ϕ=0.82 (c) ϕ=0.94

Figure B.3: *Histogram of the repartition of amplitude obtained for the peak pressure in the injector.*

In order to see what kind of variation occurs during a single test, the amplitudes of each cycle for the microphones was computed during a single test run. The detection of the cycles was done using the same method as when computing the phases in the phase average algorithm (based on the detection of the zeros in the cycle), and the amplitude is defined as the peak to peak value for each half cycle in the signal. The signals shown here are 4 seconds long. First, in the figure B.4, the values obtained for each half cycle in the chamber and injector are compared. For the three cases, a repartition that seems centered around a line was obtained. This once again confirms the relationship between the pressure in the two cavities of the burner. At first glance it seems that the shapes are more elongated the higher the equivalence ratio. But that could also be an effect of the pressures involved, which vary significantly between the conditions. In order to be able to simply compare the results, a non-dimensional variable c was chosen for each pressure signal. It is defined for each amplitude value amp of the pressure data signal M as:

$$c(M) = \frac{amp}{2\sqrt{(}2)rms(M)} \tag{B.1}$$

As such, this criterion compares the instantaneous amplitude for each half cycle to the expected value $2\sqrt{(}2)rms(M)$ it would have if the pressure signal was only composed of a constant sinusoidal oscillation at a single frequency. The figure B.5 shows the results of the calculation of c for each equivalence ratio condition. The resulting distribution is centered around a line parallel to the one giving the same value in both chamber and injector: the tendency of the pressure in both chamber and injector to be at similar values relatively to the expected oscillation amplitude is confirmed. Having the burner set at a higher equivalence ratio elongates the distribution along its symmetry axis, and less so in the orthogonal direction. This means that, as was suggested by

looking at the correlation between the microphones in chapter 3, the coherence between the pressure inside the injector and chamber is good, for all three injection conditions.

One last remark concerns the comparison between the variation fomr one test to another, and the variations observed inside one test. By computing instantaneous SPL values from the peak to peak amplitudes on half cycles (done by supposing the signal is monofrequential), it appears that for the most stable case of ϕ=0.74, the variation during a test rub is of $\pm$3.5 dB in the chamber and $\pm$3 dB in the injector. This can be compared to the $\pm$2 dB at the peak amplitude found between different tests, showing that the dispersion inside a single continuous instability is greater than between two different repetitions.

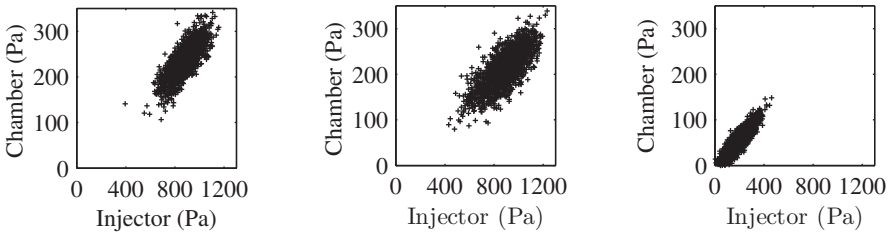

(a) ϕ=0.74 (b) ϕ=0.82 (c) ϕ=0.94

Figure B.4: *Scatterplot showing the repartition of half-cycle amplitudes for the pressure signals inside the injector and chamber.*

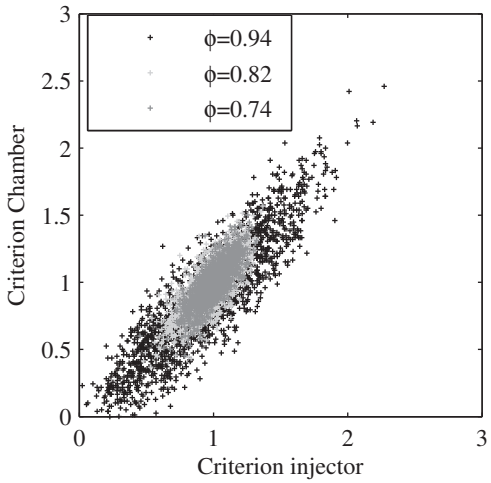

Figure B.5: *Scatterplot showing the adimensional variable c defined in equation B.1.*

B.4 Phase difference between the pressure signals

Finally, the repartition of the phase difference between the pressure signals in the injector and chamber for all the test runs will be analyzed. The phase difference presented here is only between the registered signals, and as such does not take into account the effect of the waveguides linking the microphones to the burner. As this effect is the same for any injection condition, and the same across all tested equivalence ratios, it would be enough to add to the values given here the correction caused by the difference of temperature and length between the waveguides in the two microphones. The figure B.6 presents the results obtained across the experiments. From these histograms it comes that the variation between measurements can vary by ±5° around a central value, with a higher dispersion in the case ϕ=0.94 as usual. As the microphone signals are acquired at 16 kHz and the cycle frequencies used to compute the phase shifts are in the 192-212 Hz range, a precision of 4° is to be expected in these measurements. The variation observed is thus quite good, as it seems to be partly du to the precision limits of the system.

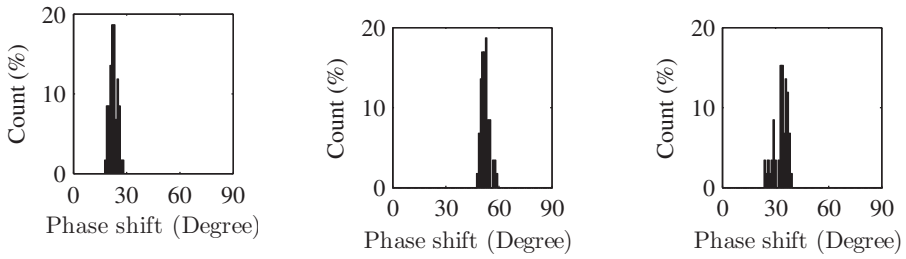

(a) ϕ=0.74 (b) ϕ=0.82 (c) ϕ=0.94

Figure B.6: *Histogram of the phase difference between the pressure signals from the microphones. Please not that these values do not take into account the necessary correction due to the waveguide introduced delays.*

References

Alekseenko, S. V., P. a. Kuibin, V. L. Okulov, and S. I. Shtork (1999, March). Helical vortices in swirl flow. *Journal of Fluid Mechanics 382*, 195–243. *(p. 3)*

Allen, M. G. (1998). Diode laser absorption sensors for gas-dynamic and combustion flows. *Measurement Science and Technology 9*(4), 545. *(p. 7)*

An, X., A. W. Caswell, J. J. Lipor, and S. T. Sanders (2011). Determining the optimum wavelength pairs to use for molecular absorption thermometry based on the continuous-spectral lower-state energy. *Journal of Quantitative Spectroscopy and Radiative Transfer 112*(14), 2355–2362. *(p. 7)*

Arroyo, M. P., S. Langlois, and R. K. Hanson (1994, May). Diode-laser absorption technique for simultaneous measurements of multiple gas-dynamic parameters in high-speed flows containing water vapor. *Appl. Opt. 33*(15), 3296–3307. *(p. 7)*

Atcheson, B., W. Heidrich, and I. Ihrke (2009). An evaluation of optical flow algorithms for background oriented schlieren imaging. *Experiments in Fluids 46*(3), 467–476. *(p. 8)*

Ballester, J. and T. García-Armingol (2010). Diagnostic techniques for the monitoring and control of practical flames. *Progress in Energy and Combustion Science 36*(4), 375 – 411. *(p. 4, 5)*

Barbosa, S., P. Scouflaire, and S. Ducruix (2009). Time resolved flowfield, flame structure and acoustic characterization of a staged multi-injection burner. *Proceedings of the Combustion Institute 32*(2), 2965 – 2972. *(p. 43)*

Beér, J. and C. Howarth (1969). Radiation from flames in furnaces. *Symposium (International) on Combustion 12*(1), 1205 – 1217. *(p. 6)*

Berkooz, G., P. Holmes, and L. J. L. (1993). The proper orthogonal decomposition in the analysis of turbulent flows. *Annual review of Fluid Mechanics 25*, 539–75. *(p. 11)*

Bistrian, D. A. and I. M. Navon (2014). Comparison of optimized Dynamic Mode Decomposition vs POD for the shallow water equations model reduction with large-time-step observations. *International Journal for Numerical Methods in Fluids*. *(p. 129)*

Böhm, B., C. Heeger, R. L. Gordon, and A. Dreizler (2011). New perspecti-

ves on turbulent combustion: Multi-parameter high-speed planar laser diagnostics. *Flow, Turbulence and Combustion 86*(3-4), 313–341. *(p. 4)*

Bolshov, M. a., Y. a. Kuritsyn, V. V. Liger, and V. R. Mironenko (2011). Development of diode laser absorption spectroscopy method for determining temperature and concentration of molecules in remote object. *Optics and Spectroscopy 110*(6), 848–856. *(p. 7)*

Borée, J. (2003). Extended proper orthogonal decomposition: a tool to analyse correlated events in turbulent flows. *Experiments in Fluids 35*(2), 188–192. *(p. 11)*

Bourgouin, J.-F., D. Durox, J. P. Moeck, T. Schuller, and S. Candel (2013). Self-sustained instabilities in an annular combustor coupled by azimuthal and longitudinal acoustic modes. In *ASME Turbo Expo 2013: Turbine Technical Conference and Exposition*, pp. V01BT04A007–V01BT04A007. American Society of Mechanical Engineers. *(p. 2)*

Boxx, I., M. Stöhr, C. Carter, and W. Meier (2010). Temporally resolved planar measurements of transient phenomena in a partially pre-mixed swirl flame in a gas turbine model combustor. *Combustion and Flame 157*(8), 1510–1525. *(p. 4)*

Brown, D. M., P. M. Sandvik, J. B. Fedison, J. Hibshman, and K. S. Matocha (2008). Determination of lean burn combustion temperature using ultraviolet emission. *Sensors Journal, IEEE 8*(3), 255–260. *(p. 7)*

Candel, S. (2002). Combustion dynamics and control: Progress and challenges. *Proceedings of the Combustion Institute 29*, 1–28. *(p. xvii, 2)*

Correa, S. M. (1998). Power generation and aeropropulsion gas turbines: From combustion science to combustion technology. *Symposium (International) on Combustion 27*(2), 1793 – 1807. *(p. 1)*

Dioc, N. (2005). *Etude expérimentale des mécanismes d'instabilité dans un brûleur à injection étagée : application aux turbines à gaz*. Ph. D. thesis, Ecole Centrale Paris. *(p. 15, 42)*

Docquier, N. and S. Candel (2002). Combustion control and sensors: a review. *Progress in Energy and Combustion Science 28*(2), 107 – 150. *(p. 4)*

Docquier, N., F. Lacas, and S. Candel (2002). Closed-loop equivalence ratio control of premixed combustors using spectrally resolved chemiluminescence measurements. *Proceedings of the Combustion Institute 29*(1), 139 – 145. *(p. 5)*

Ducruix, S., T. Schuller, D. Durox, and S. Candel (2003). Combustion Dynamics and Instabilities: Elementary Coupling and Driving Mechanisms. *Journal of Propulsion and Power 19*(5), 722–734. *(p. 2, 6)*

Duke, D., J. Soria, and D. Honnery (2011, December). An error analysis of the dynamic mode decomposition. *Experiments in Fluids 52*(2), 529–542. *(p. 13, 128)*

Duwig, C. (2010, April). Extended proper orthogonal decomposition for analysis of unsteady flames. *Flow, turbulence and combustion 84*(1), 25–47. *(p. 11)*

Dyne, P. (1953). Optical methods for the determination of combustion temperatures. *Journal of the American Rocket Society 23*(3), 165–169. *(p. 6)*

E.D. Iffa, A. A. and A. Malik (2011). Gas flame temperature measurement using background oriented schlieren. *Journal of Applied Sciences 11*(9), 1658–1662. *(p. 8)*

Farooq, A., J. B. Jeffries, and R. Hanson (2008a). Co2 concentration and temperature sensor for combustion gases using diode-laser absorption near 2.7 μm. *Applied Physics B 90*(3-4), 619–628. *(p. 7)*

Farooq, A., J. B. Jeffries, and R. K. Hanson (2008b). In situ combustion measurements of h 2 o and temperature near 2.5 μm using tunable diode laser absorption. *Measurement Science and Technology 19*(7), 075604. *(p. 7)*

Frederich, O. and D. M. Luchtenburg (2011). Modal analysis of complex turbulent flow. In *The 7th International Symposium on Turbulence and Shear Flow Phenomena (TSFP-7)*. *(p. 128, 129)*

García-Armingol, T., Y. Hardalupas, A. Taylor, and J. Ballester (2013, November). Effect of local flame properties on chemiluminescence-based stoichiometry measurement. *Experimental Thermal and Fluid Science*. *(p. 5)*

Gillet, B., Y. Hardalupas, C. Kavounides, and a. M. K. P. Taylor (2004). Infrared absorption for measurement of hydrocarbon concentration in fuel/air mixtures (MAST-B-LIQUID). *Applied Thermal Engineering 24*(11-12), 1633–1653. *(p. 6)*

Goldhahn, E. and J. Seume (2007). The background oriented schlieren technique: sensitivity, accuracy, resolution and application to a three-dimensional density field. *Experiments in Fluids 43*(2-3), 241–249. *(p. 8)*

Haber, L., U. Vandsburger, W. Saunders, and V. Khanna (2001). An experimental examination of the relationship between chemiluminescent light emissions and heat-release rate under non-adiabatic conditions. Technical report, DTIC Document. *(p. 20)*

Hardalupas, Y., M. Orain, C. S. Panoutsos, A. M. K. P. Taylor, J. Olofsson, H. Seyfried, M.Richter, J. Hult, M. Aldén, F. Hermann, and J. Klingmann (2004). Chemiluminescence sensor for local equivalence ratio of reacting mixtures of fuel and air (flameseek). *Applied Thermal Engineering 24*(11-12), 1619 – 1632. Industrial Gas Turbine Technologies. *(p. 5)*

Hendricks, a. G., U. Vandsburger, W. R. Saunders, and W. T. Baumann (2005). The use of tunable diode laser absorption spectroscopy for the measurement of flame dynamics. *Measurement Science and Technology 17*(1), 139–144. *(p. 7)*

IEA (2014). Co_2 emissions from fuel combustion. Technical report, International Energy Agency. *(p. 1)*

Jovanović, M. R., P. J. Schmid, and J. W. Nichols (2014). Sparsity-promoting dynamic mode decomposition. *Physics of Fluids 26*(2). *(p. 126, 127, 129)*

Keshav, S., Y. Utkin, and I. V. Adamovich (2010). Feedback combustion control using chemi-ionization probe in supersonic flow of combustion

products. *Journal of Propulsion and Power 26*(1), 67–73. *(p. 5)*

Keshav, S., Y. G. Utkin, M. Nishihara, A. Bao, J. W. Rich, and I. V. Adamovich (2008). Studies of chemi-ionization and chemiluminescence in supersonic flows of combustion products. *Journal of Thermophysics and Heat Transfer 22*(2), 157–167. *(p. 5)*

Kim, K. T. and D. a. Santavicca (2013, August). Interference mechanisms of acoustic/convective disturbances in a swirl-stabilized lean-premixed combustor. *Combustion and Flame 160*(8), 1441–1457. *(p. 5)*

Klingbeil, A. E., J. B. Jeffries, and R. K. Hanson (2006). Temperature- and pressure-dependent absorption cross sections of gaseous hydrocarbons at 3.39 μm. *Measurement Science and Technology 17*(7), 1950–1957. *(p. 32)*

Klingbeil, A. E., J. B. Jeffries, and R. K. Hanson (2007). Tunable mid-IR laser absorption sensor for time-resolved hydrocarbon fuel measurements. *Proceedings of the Combustion Institute 31 I*, 807–815. *(p. 6)*

Klingbeil, A. E., J. M. Porter, J. B. Jeffries, and R. K. Hanson (2009). Two-wavelength mid-ir absorption diagnostic for simultaneous measurement of temperature and hydrocarbon fuel concentration. *Proceedings of the Combustion Institute 32*(1), 821–829. *(p. 6)*

Lamraoui, A. (2011, July). *Investigating combustion noise and instabilities in a gas turbine combustor : acoustic propagation and flame dynamics.* Theses, Ecole Centrale Paris. *(p. 15, 18, 42, 167)*

Lamraoui, A., F. Richecoeur, S. Ducruix, and T. Schuller (2011). Experimental analysis of simultaneous non-harmonically related unstable modes in a swirled combustor. In *ASME 2011 Turbo Expo: Turbine Technical Conference and Exposition*, pp. 1289–1299. American Society of Mechanical Engineers. *(p. 42)*

Lee, J. G., K. Kim, and D. A. Santavicca (2000). Measurement of equivalence ratio fluctuation and its effect on heat release during unstable combustion. *Proceedings of the Combustion Institute 28*, 415–421. *(p. 5)*

Legrand, M., J. Nogueira, A. Lecuona, S. Nauri, and P. a. Rodríguez (2009, nov). Atmospheric low swirl burner flow characterization with stereo PIV. *Experiments in Fluids 48*(5), 901–913. *(p. 3)*

Leroux, R. and L. Cordier (2016). Dynamic mode decomposition for non-uniformly sampled data. *Experiments in Fluids 57*(5), 94. *(p. 12, 125)*

Li, H., S. D. Wehe, and K. R. McManus (2011). Real-time equivalence ratio measurements in gas turbine combustors with a near-infrared diode laser sensor. *Proceedings of the Combustion Institute 33*(1), 717–724. *(p. 5)*

Lieuwen, T. (2003). Modeling premixed combustion-acoustic wave interactions: A review. *Journal of Propulsion and Power 19*(5), 765–781. *(p. 2)*

Lieuwen, T., H. Torres, C. Johnson, and B. T. Zinn (2001). A mechanism of combustion instability in lean premixed gas turbine combustors. *Journal of engineering for gas turbines and power 123*(1), 182–189. *(p. 2)*

Luque, J. and D. R. Crosley (1999). Lifbase: Database and spectralsimulation program (version 2.1.1). *SRI International Report MP 99-009*. *(p. 23)*

Meier, W., I. Boxx, M. Stöhr, and C. D. Carter (2010, may). Laser-based investigations in gas turbine model combustors. *Experiments in Fluids 49*(4), 865–882. *(p. 5)*

Meier, W., P. Weigand, X. Duan, and R. Giezendannerthoben (2007, July). Detailed characterization of the dynamics of thermoacoustic pulsations in a lean premixed swirl flame. *Combustion and Flame 150*(1-2), 2–26. *(p. 5)*

Mizukaki, T., K. Wakabayashi, T. Matsumura, and K. Nakayama (2014). Background-oriented schlieren with natural background for quantitative visualization of open-air explosions. *Shock Waves 24*(1), 69. *(p. 8)*

Moeck, J. P., J.-F. Bourgouin, D. Durox, T. Schuller, and S. Candel (2012a). Investigation of precessing-vortex-core–flame interaction based on tomographic reconstruction techniques. In *ASME Turbo Expo 2012: Turbine Technical Conference and Exposition*, pp. 1213–1224. American Society of Mechanical Engineers. *(p. 3)*

Moeck, J. P., J.-F. Bourgouin, D. Durox, T. Schuller, and S. Candel (2012b, aug). Nonlinear interaction between a precessing vortex core and acoustic oscillations in a turbulent swirling flame. *Combustion and Flame 159*(8), 2650–2668. *(p. 3)*

Moos, R., N. Izu, F. Rettig, S. Reiß, W. Shin, and I. Matsubara (2011). Resistive oxygen gas sensors for harsh environments. *Sensors 11*(4), 3439–3465. *(p. 4)*

O'Connor, J., V. Acharya, and T. Lieuwen (2015). Transverse combustion instabilities: Acoustic, fluid mechanic, and flame processes. *Progress in Energy and Combustion Science 49*, 1e39. *(p. 2)*

O'Connor, J. and T. Lieuwen (2012). Recirculation zone dynamics of a transversely excited swirl flow and flame. *Physics of Fluids 24*(7). *(p. 81, 85, 171)*

Omega (2015). Thermocouple response time. http://www.omega.com/temperature/Z/ThermocoupleResponseTime.html. *(p. 6)*

Pastor, E., A. Rigueiro, L. Zárate, A. Gimenez, J. Arnaldos, and E. Planas (2002). Experimental methodology for characterizing flame emissivity of small scale forest fires using infrared thermography techniques. In *Fourth International Conference on Forest Fire Research & Wildland Fire Safetyâ€™.(Ed. DX Viegas)(Millpress: Luso, Portugal).* *(p. 6)*

Providakis, T. (2012). *Étude de la dynamique de flamme swirlé dans un injecteur diphasique multipoints étagé.* Ph. D. thesis, Ecole Centrale Paris. *(p. 24)*

Providakis, T., P. Scouflaire, L. Zimmer, and S. Ducruix (2010). Time-resolved PIV measurements applied to a non-reactive dodecane-air mixture in a two-staged multi-injection burner. pp. 5–8. *(p. 3)*

Raffel, M. (2015). Background-oriented schlieren (bos) techniques. *Experiments in Fluids 56*(3). *(p. 7)*

Raffel, M., J. T. Heineck, E. Schairer, F. Leopold, and K. Kindler (2014). Background-oriented schlieren imaging for full-scale and in-flight testing. *Journal of the American Helicopter Society 59*, 1 – 9. *(p. 8)*

Raffel, M., C. Tung, H. Richard, Y. Yu, and G. Meier (2000). Background oriented stereoscopic schlieren (boss) for full scale helicopter vortex characterization. In *In 9th international symposium on flow visualization*, pp. 23–24. *(p. 8)*

Regitz, S. and N. Collings (2008). Fast response air-to-fuel ratio measurements using a novel device based on a wide band lambda sensor. *Measurement Science and Technology 19*(7), 075201. *(p. 4)*

Richard, H., M. Raffel, M. Rein, J. Kompenhans, and G. Meier (2002). Demonstration of the applicability of a background oriented schlieren (bos) method. In *Laser Techniques for Fluid Mechanics*, pp. 145–156. Springer Berlin Heidelberg. *(p. 8)*

Richecoeur, B. F., L. Hakim, A. Renaud, and L. Zimmer (2012). DMD algorithms for experimental data processing in combustion. pp. 1–11. *(p. 122)*

Rieker, G. B., J. B. Jeffries, R. K. Hanson, T. Mathur, M. R. Gruber, and C. D. Carter (2009). Diode laser-based detection of combustor instabilities with application to a scramjet engine. *Proceedings of the Combustion Institute 32 I*(1), 831–838. *(p. 7)*

Rieker, G. B., H. Li, X. Liu, J. B. Jeffries, R. K. Hanson, M. G. Allen, S. D. Wehe, P. a. Mulhall, and H. S. Kindle (2007). A diode laser sensor for rapid, sensitive measurements of gas temperature and water vapour concentration at high temperatures and pressures. *Measurement Science and Technology 18*(5), 1195–1204. *(p. 7)*

Rowley, C. W., I. Mezić, S. Bagheri, P. Schlatter, and D. S. Henningson (2009, December). Spectral analysis of nonlinear flows. *Journal of Fluid Mechanics 641*, 115–127. *(p. 12, 122)*

Sayadi, T., P. J. Schmid, F. Richecoeur, and D. Durox (2015, March). Parametrized data-driven decomposition for bifurcation analysis, with application to thermo-acoustically unstable systems. *Physics of Fluids 27*(3). *(p. 129, 172)*

Scarpato, A., S. Ducruix, and T. Schuller (2012). A novel design method for robust acoustic dampers with perforated plates backed by a cavity operating at low and high strouhal numbers. In *ASME Turbo Expo 2012: Turbine Technical Conference and Exposition*, pp. 885–895. American Society of Mechanical Engineers. *(p. 16)*

Scarpato, A., N. Tran, S. Ducruix, and T. Schuller (2012). Modeling the damping properties of perforated screens traversed by a bias flow and backed by a cavity at low strouhal number. *Journal of Sound and Vibration 331*(2), 276–290. *(p. 16)*

Schadow, K. and E. Gutmark (1992). Combustion instability related to vortex shedding in dump combustors and their passive control. *Progress in Energy and Combustion Science 18*(2), 117–132. *(p. 2)*

Schmid, H. (2012). How to use the fft and matlabâ€™s pwelch function for signal and noise simulations and measurements. Technical report, FHNW/IME,. *(p. 156)*

Schmid, P. J. (2010, July). Dynamic mode decomposition of numerical and experimental data. *Journal of Fluid Mechanics 656*, 5–28. *(p. 12, 122, 125)*

Schmid, P. J. (2011, February). Application of the dynamic mode decomposition to experimental data. *Experiments in Fluids 50*(4), 1123–1130. *(p. 12, 122, 126)*

Schmid, P. J., D. Violato, and F. Scarano (2012, February). Decomposition of time-resolved tomographic PIV. *Experiments in Fluids 52*(6), 1567–1579. *(p. 12, 122)*

Schwarz, H., L. Zimmer, D. Durox, and S. Candel (2010). Detailed measurements of equivalence ratio modulations in premixed flames using laser rayleigh scattering and absorption spectroscopy. *Experiments in Fluids 49*(4), 809–821. *(p. 5)*

Seume, J., N. Vortmeyer, W. Krause, J. Hermann, C.-C. Hantschk, P. Zangl, S. Gleis, D. Vortmeyer, and A. Orthmann (1997). Application of active combustion instability control to a heavy duty gas turbine. In *ASME 1997 Turbo Asia Conference*, pp. V001T05A007–V001T05A007. American Society of Mechanical Engineers. *(p. 2)*

Sharpe, S. W., T. J. Johnson, R. L. Sams, P. M. Chu, G. C. Rhoderick, and P. A. Johnson (2004). Gas-phase databases for quantitative infrared spectroscopy. *Applied Spectroscopy 58*(12), 1452–1461. *(p. 32)*

Shimura, M., M. Tanahashi, T. Miyauchi, G.-M. Choi, and D.-J. Kim (2009, November). Combustion measurement of thermoacoustic oscillating flames by diode-laser absorption spectroscopy sensors. *Thermochimica Acta 495*(1-2), 95–100. *(p. 7)*

Smith, G. P., D. M. Golden, M. Frenklach, B. Eiteener, M. Goldenberg, C. T. Bowman, R. K. Hanson, W. C. Gardiner, V. V. Lissianski, and Z. W. Qin (2000). GRI-Mech 3.0. *(p. 76)*

Spearrin, R., W. Ren, J. Jeffries, and R. Hanson (2014). Multi-band infrared co2 absorption sensor for sensitive temperature and species measurements in high-temperature gases. *Applied Physics B 116*(4), 855–865. *(p. 7)*

Steinberg, a. M., I. Boxx, M. Stöhr, C. D. Carter, and W. Meier (2010). Flow-flame interactions causing acoustically coupled heat release fluctuations in a thermo-acoustically unstable gas turbine model combustor. *Combustion and Flame 157*(12), 2250–2266. *(p. 3)*

Stöhr, M., I. Boxx, C. Carter, and W. Meier (2011, January). Dynamics of lean blowout of a swirl-stabilized flame in a gas turbine model combustor. *Proceedings of the Combustion Institute 33*(2), 2953–2960. *(p. 4)*

Stöhr, M., R. Sadanandan, and W. Meier (2009). Experimental study of unsteady flame structures of an oscillating swirl flame in a gas turbine model combustor. *Proceedings of the Combustion Institute 32 II*, 2925–

2932. *(p. 3)*

Stöhr, M., R. Sadanandan, and W. Meier (2011, June). Phase-resolved characterization of vortex-flame interaction in a turbulent swirl flame. *Experiments in Fluids 51*(4), 1153–1167. *(p. 3, 11)*

Stopper, U., M. Aigner, H. Ax, W. Meier, R. Sadanandan, M. Stöhr, and A. Bonaldo (2010, April). PIV, 2D-LIF and 1D-Raman measurements of flow field, composition and temperature in premixed gas turbine flames. *Experimental Thermal and Fluid Science 34*(3), 396–403. *(p. 5)*

Syred, N. (2006, January). A review of oscillation mechanisms and the role of the precessing vortex core (PVC) in swirl combustion systems. *Progress in Energy and Combustion Science 32*(2), 93–161. *(p. 3)*

Taylor, P. and P. Foster (1974). The total emissivities of luminous and non-luminous flames. *International Journal of Heat and Mass Transfer 17*(12), 1591 – 1605. *(p. 6)*

Todoroff, V. (2013). *Mesure d'un champ de masse volumique par Background Oriented Schlieren 3D. Étude d'un dispositif expérimental et des méthodes de traitement pour la résolution du problème inverse*. Ph. D. thesis. Thèse de doctorat dirigée par Le Besnerais, Guy et Millan, Pierre Dynamique des fluides Toulouse, INPT 2013. *(p. 37)*

Tomita, E., N. Kawahara, M. Shigenaga, and A. Nishiyama (2004). In situ Measurement of Fuel Concentration of Hydrocarbon near Spark Plug in an Engine Cylinder by 3.392.MU.m Inflamed Laser Absorption Method (Discussion of Applicability with Homogeneous Methane-Air Mixture). *Transactions of the Japan Society of Mechanical Engineers Series B 70*(690), 511–517. *(p. 5)*

Tragut, C. and K. Härdtl (1991, jun). Kinetic behaviour of resistive oxygen sensors. *Sensors and Actuators B: Chemical 4*(3-4), 425–429. *(p. 4)*

Tran, N. (2009, April). *Influence of inlet acoustic boundary condition on large amplitude combustion instabilities : design of a robust impedance control system*. Ph. D. thesis, Ecole Centrale Paris. *(p. 15, 42)*

Tu, J. H., C. W. Rowley, J. N. Kutz, and J. K. Shang (2014). Spectral analysis of fluid flows using sub-nyquist-rate piv data. *Experiments in Fluids 55*(9), 1805. *(p. 12, 125)*

Vasudeva, G., D. R. Honnery, and J. Soria (2005). Non-intrusive measurement of a density field using the background oriented schlieren (bos) method. In *Proc. Australian Conf. Laser Diagnostic in Fluid Mechanics & Combustion*. *(p. 7)*

Venkatakrishnan, L. and G. Meier (2004). Density measurements using the background oriented schlieren technique. *Experiments in Fluids 37*(2), 237–247. *(p. 8)*

Zhou, H., L. Xiaoliang, Q. Li, and K. Cen (2011). Temperature measurements using the background oriented schlieren technique. *Proceedings of the CSEE 5*, 012. *(p. 8)*

ÉCOLE DOCTORALE
Sciences mécaniques et énergétiques, matériaux et géosciences (SMEMAG)

Titre : Développement d'une stratégie de post-traitement pour l'analyse de la combustion prémélangée : à une flamme turbulente swirlée.

Mots clés : Combustion, Instabilité, DMD, POD, post-traitement, LIF, PIV

Résumé : Une des pistes majeures pour obtenir des turbines à gaz moins polluantes est l'utilisation de chambres de combustion fonctionnant en régime prémélangé pauvre. Cependant, dans de tels régimes de fonctionnement, la flamme obtenue est cependant plus facilement sujette aux instabilités thermo-acoustiques.

Dans cette thèse, un brûleur étagé swirlé fonctionnant au propane a été employé pour illustrer une méthode d'analyse de la combustion prémélangée. Cette installation a été étudiée à l'aide de diagnostics classiques (micros, PLIF, film à haute cadence de la flamme).

La stratégie de post-traitement développée dans cette thèse utilise par contre des outils eux aussi classiques (PSD, moyenne de phase) mais aussi une méthode d'analyse avancée, la Décomposition en Modes Dynamiques. Celle-ci est notamment étudiée em détail afin d'en cerner les avantages et les limitations dans le cadre de l'analye des instabilités de combustion.

Title : Post-processing Strategy Development for Premixed Combustion Analysis: Application to Turbulent Swirled Flames

Keywords : Combustion, Instability, DMD, POD, post-processing, LIF, PIV

Abstract : One of the major ways of reducing pollutant emissions in gas turbines is using combustion chambers with lean premixed mixtures. However, in such operating conditions the flame is more susceptible to thermo-acoustic instabilities.

In the present work, a propane-fed swirled burner using two injection stages is used to illustrate a post-processing strategy for premixed combustion analysis. This model burner has been studied using classic diagnostics (microphones, PLIF, highspeed imaging).

The strategy developed in the present work uses both classic postprocessing tools (PSD, phase averaging) and an advanced method, the Dynamic Mode Decomposition. In particular, this method is studied in detail and compared to more lassic ones in order to clearly point its advantages as well as its shortcomings when used to study combustion instabilities.

Université Paris-Saclay
Espace Technologique / Immeuble Discovery
Route de l'Orme aux Merisiers RD 128 / 91190 Saint-Aubin, France